Faculty of Applied Engineering
Research group of Applied
Electrochemistry & Catalysis
(ELCAT)

Towards stable Cu-Ag bimetallic nanoparticles to boost the electrocatalytic CO_2 reduction

This thesis is submitted in fulfilment of the requirements for the degree of Doctor in Applied Engineering at the University of Antwerp defended by Lien Pacquets

Promotor(en):
Prof. dr. Ing. Tom Breugelmans
Prof. dr. Sara Bals

Antwerp, 2022

The candidate was financially supported by the Research Foundation Flanders (FWO).

De kandidaat werd financieel gesteund door het Fonds voor Wetenschappelijk Onderzoek Vlaanderen (FWO).

Faculty of Applied Engineering
Research group of Applied
Electrochemistry
& Catalysis (ELCAT)

Towards stable Cu-Ag bimetallic nanoparticles to boost the electrocatalytic CO_2 reduction

Lien Pacquets

Members of the Jury

Prof. dr. ir. Pieter Billen	President of the jury University of Antwerp
dr. ir. Nick Daems	Secretary of the jury University of Antwerp
Prof. dr. Ing. Tom Breugelmans	Promotor University of Antwerp
Prof. dr. Sara Bals	Promotor University of Antwerp
Prof. dr. Maria Ibáñez	External jury member IST Austria
Prof. dr. ir. Jon Ustarroz	External jury member L'Université libre de Bruxelles

Acknowledgements

When I was 15 years old, I decided I would become a chemist one day. From that moment on, I started my journey in order to fulfill this dream. I will never forget the day I told my teacher that I wanted to do a PhD. Little did I know that this dream would become reality. And what a hell of a journey it has been… After four years of hard work, I'm about to finish my PhD, which was one of the hardest things I've ever faced. Therefore, I would like to take the opportunity to tank everyone that supported me throughout this journey.

First of all, I would like to express my gratitude to my promotors Tom and Sara, who gave me the opportunity to start my PhD. You always believed in me and challenged me to do better. I want to thank you for guiding me, reading and correcting my work and helping me to obtain my FWO SB grant. In addition I would like to thank Nick for the guidance throughout my PhD and for the many hours of brainstorming together.

I also want to thank my colleagues of ELCAT. The group has grown significantly since I started my PhD at ELCAT. Thank you all for your help and creating a nice working atmosphere, it was a pleasure working with you. Special thanks to Kevin and Jonathan for designing the cover of my thesis. Additionally, I want to specifically thank Sander. We both joined ELCAT when it was still named ART. Thank you for the many early coffee breaks and assistance during my PhD as well as being my mental coach when I needed it.

Let me also thank the colleagues of EMAT for taking the time to answer my questions and helping me at the microscope. To Daniel who collaborated with me during the last part of my PhD. Thank you for your refreshing insights and support.

Ik zou graag mijn familie en vrienden bedanken die mij door de jaren heen gesteund hebben. Om mij bij te staan bij de moeilijke beslissing om drastisch van studierichting te veranderen en in mij te blijven geloven op momenten dat ik het echt nodig had.

Bedankt mama en papa om deze droom voor mij mogelijk te maken door mij financieel en mentaal te steunen. Dank u Bart, Anke en Tibo jullie slaagden er telkens weer in om mijn gedachten te verzetten. Ook wil ik graag mijn grootouders, bedanken voor hun onvoorwaardelijke liefde en steun.

Tot slot zou ik graag mijn vriend Robin willen bedanken. Woorden schieten te kort wanneer ik wil beschrijven hoeveel jij voor mij betekent. Jij bent mijn steun en toeverlaat. Bedankt om uren naar mijn uiteenzettingen over mijn doctoraat te luisteren. Deze 2 jaar met jou waren een geweldig avontuur, dat we er nog veel samen mogen meemaken.

Lien

Summary

Ever since the industrial revolution, the emission of greenhouse gasses dramatically increased. The increase in human activity, such as the combustion of fossil fuels, resulted in major changes in CO_2 concentrations, with levels currently rising above 400 ppm. Many scientists are currently exploring different strategies to capture and reuse this CO_2. One of many strategies is the electrochemical conversion of CO_2 to value added products, such as carbon monoxide, formic acid, methane, ethylene and ethanol. As renewable energy will gain even more importance in the future, its implementation as an energy source is a great opportunity to electrochemically convert CO_2 in a green manner. In particular the conversion of CO_2 towards CO is of high interest because, together with formic acid, it creates the most economic value per mole of electrons generated. Compared to formic acid, a great demand of CO in the chemical industry already exists.

Nevertheless, at the moment, the electrochemical CO_2 reduction (eCO_2R) is not yet industrially viable, mainly due to high energy costs and the lack of good electrocatalysts. Attempts to improve the electrocatalyst performance are mainly directed to the introduction of the morphology, size and bimetallic effect. Over the last couple of years, nanosized bimetallic have emerged as promising candidates. It is believed that bimetallic enhancement effects are behind the improved performance of these electrocatalysts when compared to the monometalic counterparts. Although widely investigated, there are still some remaining issues and/or open questions. As such, the development of a robust and straightforward synthesis method, to obtain a good control over morphology, size and composition, remains absent. The synthesis of electrocatalysts is key in determining which properties are beneficial for the CO_2 reduction towards CO. Additionally, these electrocatalysts are designed to be implemented in electrolyzers and therefore have to maintain long-term performance. Nevertheless, fundamental insight into their resistance towards electrochemical stress remain underexplored.

This work is devoted to the optimization of a synthesis method towards reproducible electrocatalysts, enabling the investigation of the structure-performance relationship of bimetallic electrocatalysts and gather further insides into their degradation mechanism. Hence, the combination of electron microscopy, spectroscopy and (electro)chemical techniques enables the further optimization of these electrocatalysts.

Firstly, the synthesis of Cu (nano)particles on a rough substrate through electrodeposition is explored. The effect of substrate surface pre-treatment and electrodeposition parameters on the particle morphology and size is investigated. Using this approach, Cu (nano)particles with various sizes could be obtained. In order to reduce the Cu particle size up to the sub-10 nm range and ameliorate their monodispersity, a thermal decomposition method is implemented. By using galvanic displacement, various Cu-Ag bimetallic nanoparticles could be designed. Probing their composition-selectivity profile showed that increasing the Ag concentration improved the production of CO and suppressed hydrogen. The CO production is boosted by using Cu@Ag core-shells compared to Cu/Ag nanodimers and is promoted even more by changing the type of electrolyte.

Second, the implementation of the Cu-Ag bimetallic nanoparticles caused the electrocatalyst to degrade. Nevertheless, the exact degradation pathway remained unclear. Therefore, the early stages of the degradation were investigated by mapping structural changes of Cu@Ag core-shell nanoparticles in 3D after applying electrochemical stress. Results show that a two-step degradation mechanism is at play, where initially an inverted Ag@Cu core-shell is obtained by Cu leaching with the subsequent sintering of the Ag cores as the second degradation step. Since these core-shell suffer from degradation, the possibility of a carbon layer serving as a degradation inhibitor is explored.

In general, the product selectivity can be tuned by using different Cu-Ag bimetallic nanoparticles synthesized through a robust method. The unique degradation pathway of Cu@Ag core-shell nanoparticles has led to the proposition of a more accurate stabilization strategy. These findings can contribute significantly in the quest for improved electrocatalysts for the CO_2 reduction.

Samenvatting

Sinds de industriële revolutie is de uitstoot van broeikasgassen drastisch toegenomen. Dit heeft geleid tot grote veranderingen in de CO_2-concentraties aangezien steeds meer fossiele brandstoffen werden verbrand. Deze concentraties stijgen momenteel boven de 400 ppm. Veel wetenschappers onderzoeken momenteel verschillende strategieën om deze CO_2 af te vangen en opnieuw te gebruiken. Een van de vele strategieën is de elektrochemische omzetting van CO_2 in hoogwaardige, zoals koolstofmonoxide, mierenzuur, methaan, ethyleen en ethanol. Aangezien hernieuwbare energie in de toekomst nog aan belang zal winnen, is de toepassing ervan als energiebron een uitgelezen kans om CO_2 op een groene manier elektrochemisch om te zetten. Met name de omzetting van CO_2 in CO is van groot belang omdat dit, samen met mierenzuur, de meeste economische waarde per mol opgewekte elektronen oplevert. In vergelijking met mierenzuur is er in de chemische industrie reeds een grote vraag naar CO.

Toch is de elektrochemische reductie van CO_2 momenteel nog niet industrieel toepasbaar, vooral wegens de hoge energiekosten en het gebrek aan goede elektrokatalysatoren. Strategieën om de prestaties van de elektrokatalysator te verbeteren zijn voornamelijk gericht op de introductie van de morfologie, de grootte en het bimetaaleffect. De laatste jaren bleken bimetallische verbindingen veelbelovende kandidaten. Men gelooft dat bimetallische versterkingseffecten aan de basis liggen van de verbeterde prestaties van deze elektrokatalysatoren in vergelijking met de monometallische tegenhangers. Hoewel er veel onderzoek is verricht naar deze elektrokatalysatoren, zijn er nog steeds enkele onopgeloste problemen en/of open vragen. Zo ontbreekt de ontwikkeling van een robuuste en eenvoudige synthesemethode, om een goede controle over morfologie, grootte en samenstelling te verkrijgen. De synthese van elektrokatalysatoren is van cruciaal belang om te bepalen welke eigenschappen gunstig zijn voor de reductie van CO_2 naar CO. Bovendien zijn deze elektrokatalysatoren ontworpen om te worden toegepast in elektrolyzers en moeten zij dus op lange termijn blijven presteren. Fundamentele inzichten in hun resistentie tegen elektrochemische stress blijven echter onderbelicht.

Dit werk is doelt op de optimalisatie van een synthesemethode voor reproduceerbare elektrokatalysatoren, die het mogelijk maakt de structuur-performantieverhouding van bimetallische elektrokatalysatoren te onderzoeken en meer inzicht te krijgen in hun

afbraakmechanisme. De combinatie van elektronenmicroscopie, spectroscopie en (elektro)chemische technieken maakt de verdere optimalisatie van deze elektrokatalysatoren mogelijk.

Ten eerste wordt de synthese van Cu (nano)deeltjes op een ruw substraat door elektrodepositie onderzocht. Het effect van de voorbehandeling van het substraatoppervlak en de elektrodepositieparameters op de deeltjesmorfologie en -grootte wordt onderzocht. Met behulp van deze aanpak kunnen Cu (nano)deeltjes met verschillende afmetingen worden verkregen. Om de Cu deeltjesgrootte te reduceren tot sub-10 nm en hun monodispersiteit te verbeteren, wordt een thermolyse methode toegepast. Door gebruik te maken van galvanische uitwisseling, konden verschillende Cu-Ag bimetallische nanodeeltjes worden ontworpen. Onderzoek van hun samenstelling-selectiviteitsprofiel toonde aan dat verhoging van de Ag-concentratie de productie van CO verbeterde en waterstof onderdrukte. De CO-productie wordt verhoogd door Cu@Ag core-shells te gebruiken in vergelijking met Cu/Ag nanodimeren en wordt nog meer bevorderd door het type elektrolyt te veranderen.

Ten tweede veroorzaakte de implementatie van de Cu-Ag bimetallische nanodeeltjes een degradatie van de elektrokatalysator. Niettemin bleef het exacte degradatieroute onduidelijk. Daarom werden het beginstadia van de degradatie onderzocht door het in kaart brengen van structurele veranderingen van Cu@Ag core-shell nanodeeltjes in 3D, na toepassing van elektrochemische stress. De resultaten tonen aan dat de degradatie in twee stappen gebeurt. In eerste instantie wordt er een omgekeerde Ag@Cu core-shell gevormd door Cu leaching met de daaropvolgende sinteren van de Ag kernen als de tweede degradatie stap. Aangezien deze core-shells nanodeeltjes degraderen tijdens de elektrochemische CO_2 reductie, wordt de mogelijkheid onderzocht van een koolstoflaag die als een beschermende laag fungeert.

In het algemeen kan de productselectiviteit worden afgestemd door verschillende Cu-Ag bimetaal nanodeeltjes te gebruiken die via een robuuste methode zijn gesynthetiseerd. Het unieke degradatie mechanisme van Cu@Ag core-shell nanodeeltjes heeft geleid tot het voorstel van een meer accurate stabilisatiestrategie. Deze bevindingen kunnen een belangrijke bijdrage leveren in de zoektocht naar verbeterde elektrokatalysatoren voor de CO_2 reductie.

Table of contents

Nomenclature

COP26	UN climate change conference
EU	European Union
CO	Carbon monoxide
eCO_2	Electrochemical CO_2 reduction
H_2	Hydrogen
NPs	Nanoparticles
FE	Faradaic efficiency
EASA	Electrochemical active surface area
CO_2RR	CO_2 reduction reaction
UV-VIS	Ultraviolet-visible spectroscopy
SEM	Scanning electron microscopy
(S)TEM	(Scanning) transmission electron microscopy
HRSTEM	High resolution scanning transmission electron microscopy
GC	Gas chromatography
	Glassy carbon
HPLC	High-performance liquid chromatography
XPS	X-ray photoelectron spectroscopy
CA	Chronoamperometry
CP	Chronopotentiometry
CV	Cyclic voltammetry
WE	Working electrode
RE	Reference electrode
CE	Counter electrode
HER	Hydrogen evolution reaction
RHE	Reversible hydrogen electrode

SHE	Standard hydrogen electrode
R	Reductant
O	Oxidant
HAADF	High angle annular dark field
BF	Bright field
DF	Dark field
EDS	Energy dispersive X-ray spectroscopy
FEG	Field emission gun
EM	Expectation maximization
TDPA	Tetradecylphosphonic acid
GDE	Gas diffusion electrode
MSA	Methane sulfonic acid
IPA	Isopropanol
TFA	Trifluoroacetate
TOA	Trioctylamine
IAE	Isoamyl ether
MQ	Milli Q
OCP	Open circuit potential
NL	Nucleation loop
ICP-MS	Inductive coupled plasma mass spectrometry
NCs	Nanocrystals
PSD	Particle size distribution
AEM	Anion exchange membrane
FID	Flame ionization detector
FIB	Focused ion beam dual beam microscope
EELS	Electron energy loss spectroscopy
CEM	Cation exchange membrane
DEMS	Differential electrochemical mass spectrometry

List of symbols

E	Potential (V)
E_{ref}	Measured potential with respect to the used RE (V)
E_{RHE}	Potential expressed with respect to the RHE (V)
$E_{CP,exp}$	Measured potential during experiment (V)
E_{CI}	Measured potential during current interrupt (V)
E_p	Peak potential (V)
E_n	Nucleation potential (V)
E_g	Growth potential (V)
i	Current (A)
$i_{CP,exp}$	Applied current during experiment (A)
i_{CI}	Applied current during current interrupt (A)
$i_{p,c}$	Peak current (A)
IR	Potential losses due to ohmic resistance (V)
iR	Uncompensated resistance (Ω)
Q	Charge (C)
Q_n	Nucleation charge (C)
Q_g	Growth charge (C)
n	Mol (mol)
z	Transferred electrons
F	Faraday's constant (96 485 C mol^{-1})
FE	Faradaic efficiency (%)

PART I

Introduction

CHAPTER 1:

General introduction

This chapter provides a general introduction of the relevance of electrochemistry in the current climate crisis. The importance of electrocatalysis as a decarbonization strategy is highlighted along with the illustration of the basic concepts. In addition, the enhancement strategies are elaborated. To conclude, the state-of-the-art for Ag and Cu-Ag bimetallic catalyst for the CO_2 reduction is summarized.

1.1 Global decarbonization

Ever since the industrial revolution, the emission of greenhouse gasses dramatically increased. These gasses allow light to pass through, but trap some of the earth's generated heat. This heat capture is to some extent necessary to provide life on earth as we know it [1]. Nevertheless, the increase in human activity such as the combustion of fossil fuels, land clearing and agriculture, resulted in the excessive production of greenhouse gasses [2], [3]. The CO_2 concentration in the atmosphere is currently rising above 400 ppm, which equals a 47 % increase compared to pre-industrial levels (280 ppm). Due to the accumulation of CO_2 in the atmosphere, more heat is preserved. As a consequence, in 2020, we experienced one of the warmest years ever recorded, with a global average temperature of 1.2 °C above the pre-industrial level. This average temperature is likely to increase further to above 1.5 °C between 2030 and 2052 at the current rate of 0.2 °C per decade [4]. This increase could have a disastrous impact on the climate such as a rise in global sea levels due to melting of the ice caps and melting of the permafrost. Additionally, anthropogenic climate change has contributed to more pronounced heat extremes and global intensification of precipitation during the last decades [5]. To oppose the effects of global warming, 196 countries signed a treaty, the so-called Paris agreement in 2015. Its goal is to limit the forecasted temperature increase to only 2 °C (preferably 1.5 °C) above pre-industrial levels, to limit the disastrous impact this will have on our climate to a maximum [6]. More recently, at the UN climate change conference (COP26), 200 countries agreed on the Glasgow Climate pact. This pact focusses on mitigation (reducing emissions), adaption (helping those impacted by climate change, finance (enabling countries to reach their climate goals) and collaboration (working together to achieve the goals) [7]. Therefore, the European Union (EU) endorses initiatives to cut down greenhouse gas emissions along with the elimination of already present greenhouse gasses in order to reach carbon neutrality by 2050 [8].

To combat global warming, countries look towards changes in energy supply, industrial processes and transportation. The industry could reduce its emissions by improving the energy efficiency of chemical processes and by implementing green energy-based heating and cooling systems, both strategies imply a reduction in CO_2 emissions by 4.6 Gt CO_2 per year by 2030. Additionally, carbon capture and storage is predicted to cause a reduction in CO_2 emissions by 1.22 Gt CO_2 per year by 2030. The transport sector, combining automobile and aviation sector, need to increase fuel efficiency along with making a shift to electric vehicles and/or changes in fuel supply and improved infrastructure in order to reduce CO_2 emissions by approx. 3.3 Gt CO_2 per year by 2030.

Since energy production is the largest contributor to the emissions of greenhouse gasses. Several decarbonization strategies are in play here as well, including energy efficiency improvements, transition of fossil fuels and the generation of energy through low/zero greenhouse gas emission technologies such as renewable energy [3]. The latter received increased interest compared to earlier years and is estimated to supply 20-30 % of the world's primary energy by 2040, compared to the current 15 % [9]. Wind and solar energy sources combined will become the largest electricity producers worldwide, accounting for 87 % of the total energy supply by 2050 [10]. Recently published studies show the possibility of obtaining a completely renewable energy system by 2050 [11], [12]. These prospects point out the major transition of our primary energy supply, which in 2015 was still mainly ruled by fossil coal, oil and gas, accounting for 28 %, 29 % and 27 %, respectively. These sources will die out and will be replaced by primarily solar and wind and will account for 69 % and 18 %, respectively across the power, heat and transport sectors. Additionally, hydropower, biomass and geothermal energy will also contribute to this renewable energy system, albeit to a lesser extent. The speed of this transition is largely related to the cost of these renewable sources compared to their fossil counterparts [13].

Unfortunately, renewable energy sources such as solar and wind are accompanied by a time-dependent energy production. This means that the energy produced by one of these sources varies in function of time because they depend on the weather circumstances (conditions and period of the day/year) which brings along fluctuations in power delivery to the grid [14]. Consequently, they result in the inescapable misfit between energy supply and demand [15], since the energy will also be produced on off-peak moments of energy demand. Therefore, decarbonization by introducing these renewable energy sources, to phase out non-sustainable technologies, induces the need for grid balancing. Since the power grid can only absorb an additional 10 % of its capacity and with the prospect of the increasing share of renewables, integration of energy storage technologies becomes unavoidable [16]. Energy storage allows untapped renewable energy to be conserved, making this approach of high interest. It is predicted that the energy storage will account for 23 % of the electricity demand and 26 % of the heat demand [11].

Different energy storage possibilities are mentioned in latest studies about renewables, such as electricity energy storage (power-to-power), thermal energy storage (power-to-heat), gas- and liquid energy storage (power-to-chemicals) [17]. A combination of all three storage possibilities will be necessary to ensure a smooth transition to a renewable world.

Electricity energy storage is ensured by the use of batteries. Their substantial cost reduction over the past few years and the coming years (i.e. further decrease by two thirds of their cost in 2016 by 2040) has attracted the attention of the industry. Batteries, on the contrary to other current technologies, have the benefit to switch between withdrawing and injecting electricity while also having the ability to alter their input, depending on the demand or consumption at that certain point in time [10]. This makes them very flexible and highly interesting to store (renewable) electricity. Nevertheless, these systems are currently still expensive and bring along a certain complexity.

Thermal energy storage uses energy to cool down or heat up media which can be used in heating or cooling systems. This approach is also devoted to upgrading steam and waste heat to improve its efficient re-use. Heat production by using electricity becomes more attractive than the traditional heat sources such as natural gas because of the low electricity price. Electricity driven heat pumps can upgrade waste streams to usable temperature levels for implementation in industry [17].

Chemical energy storage is a very promising approach in storing excess of energy. The use of electricity to produce chemicals is referred to as electrosynthesis; Here a catalyst (electrocatalysis) is used to convert a feedstock to value added products, which as such serves as an energy carrier. The electrochemical conversion of reactants has the advantage of being very selective towards different products since these can be tuned by the potential applied to the system and the type of catalyst used. There is no need for external activation of the system, since the catalyst is activated by the electrons. Since this is a selective technique and the reaction takes place at the catalyst surface by means of an electron transfer, the use of reducing agents and other products can be mainly prevented. As the catalyst is a solid electrode, it can easily be removed and replaced, facilitating the processing of the products. Additionally, this conversion can take place at ambient conditions (room temperature and atmospheric pressure), which is beneficial compared to traditional chemical processes, which require high temperatures and pressures. All these combined advantages emphasize the great potential of this technique. Finally, this approach opens up ways towards new chemicals, along with the transformation of already existing routes. These chemicals can be used as building blocks in the chemical industry. As such, electrolysis allows to produce them in a sustainable manner [17].

A chemical energy storage approach with great prospects is the electrochemical conversion of CO_2. This reaction has received great interest because it combines the storage of excessive energy together with the elimination of CO_2 from the atmosphere. This reaction allows the production of a variety of products amongst them are important chemicals such as methane, carbon monoxide (CO), formic acid and ethylene.

One of the main reasons behind the increasing attention for the electrochemical CO_2 is the "cap-and-trade" policy installed by the EU to urgently reduce CO_2 emissions. This policy restricts the amount of CO_2 emitted by companies. The EU sells allowances, which enables a company to emit CO_2 without being fined. The amount of allowances reflects the amount of CO_2 a company is allowed to emit. Nevertheless, these permits are becoming increasingly expensive and the number of permits will decline with an annual rate of 2.2 % [18]. Emitting more CO_2 than allowed, results in a fine of 100 euros per ton excess [19]. This evolution forces companies to improve their processes and reduce their CO_2 emissions. These prospects will thus facilitate the investment in carbon capture and conversion facilities and their implementation. As such, CO_2 is captured and can subsequently be electrochemically converted, with renewable energy, to valuable products [20]–[22].

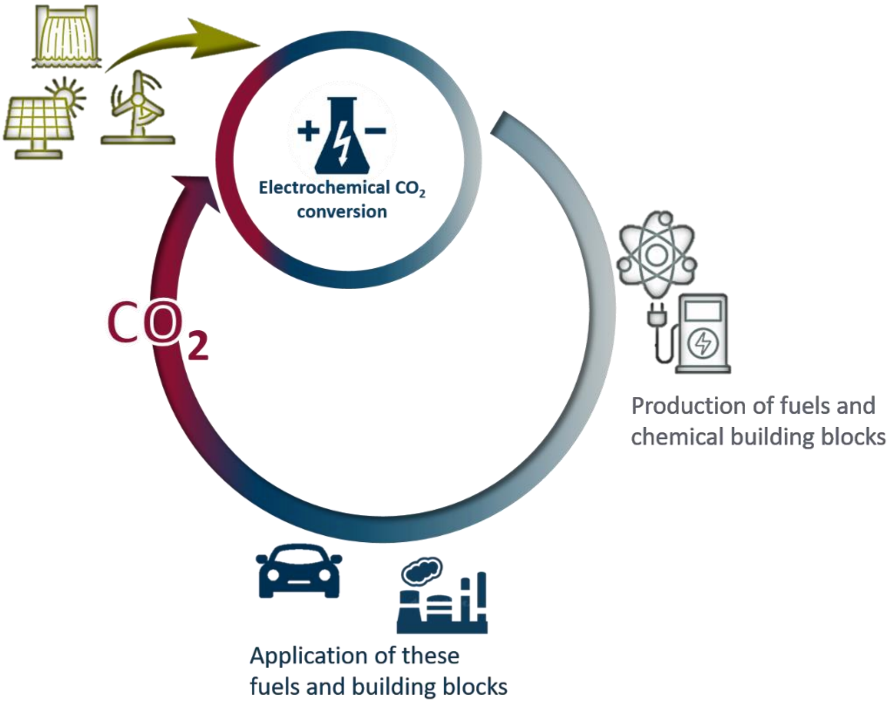

Figure 1-1: Carbon neutrality due to capture and conversion of CO_2 using renewable energy sources.

This strategy tackles both the high CO_2 concentrations in the atmosphere and the need for renewable energy storage possibilities at the same time. Implementing this approach allows us to obtain a circular economy, as presented in Figure 1-1.

1.2 Electrocatalysis

As previously mentioned, the need for a more sustainable future has driven policy makers to look for alternative routes to produce energy and chemicals and thereby reducing its greenhouse gas emissions. One promising approach is to convert CO_2 to value added products/building blocks by means of electrocatalysis. This technique facilitates the conversion of a reactant over a catalyst by using an electric potential to activate the reaction. Despite its great potential, electrocatalysis is rather new and underexplored in the current chemical industry, but it has been on the rise during the last decades.

Electrocatalysis and heterogeneous catalysis share a common base, since both techniques rely on the use of a catalyst to lower the activation barrier of the reaction and as such speed up the reaction. Additionally, both approaches include reactions at an interface where the catalyst itself remains unchanged after the reaction(s). However, using electrocatalysis, an electrochemical potential serves as an energy supply, whereas in heterogeneous catalysis, heat is used. Previously, electrocatalysis suffered from the absence of detailed insights into the reaction mechanism, due to the underdevelopment of the required spectroscopical and theoretical techniques. Understanding electrocatalysis becomes even more challenging when considering the more complex solid/liquid interface, caused by the appearance of ions, electric fields and charged interfaces [23]. Over the last decades, computational surface analysis techniques advanced rapidly, leading to new insights and unraveling complex solid/liquid interfaces, which ultimately allowed to determine the CO_2 reduction mechanism for different catalytic species.

An electrochemical reaction takes place by means of an electron transfer. When considering this electron transfer, one must take into account the interactions of the reactant with both solvent and electrode. Depending on the strength of one interaction compared to the other, two distinct pathways are plausible. If the interactions with the electrode are relatively weak, compared to the solvent interactions, the reactant is located at several Ångstroms from the electrode surface, this process is referred to as an outer sphere reaction. More precisely, the ligand and solvent shell keep the reacting center away from the electrode. The surrounding solvent must reorient during reaction (since reactant and product carry different charges) and as such, always limits the reaction compared to the fast electron transfer. Here, the type of metal that is used, does not play an important role, since the electrode merely serves as an electron reservoir, meaning no catalysis takes place at its surface as there is no direct interaction with the reactant [23], [24].

If the interactions of the reactant with the electrode are stronger compared to the solvent-reactant interactions, the reactant adsorbs to the surface and loses part of its solvation shell, which is referred to as an inner sphere reaction. The adsorption can either be weak or strong, depending on the metal that is used, enabling catalysis and is depended on the energy of its d-band center (a d-band arises from the energy splitting pattern occurring in a molecule). The higher the energy level of the d-band, the stronger the chemisorption that occurs [25]. The reaction rate depends strongly on the type of catalyst material that is used and can differ about eight orders of magnitude between the best and worst catalyst. Additionally, the electronic level of the reactant can be shifted by the solvent (fluctuations in their orientation) and the applied potential [24], such that a reaction can take place.

The bonding of the reactant with the catalytic surface was first described by Sabatier [26]. The principle states that some kind of binding between reactant and catalyst is necessary in order for a reaction to occur. It is of utmost importance that the binding is neither too weak, since the catalyst needs to be able to activate the reactant, nor too strong in order to prevent poisoning of the catalyst surface. Ideally, the reactant binds with intermediate strength. Later on, Balandin found that this relationship resulted in a volcano-type curve. This so-called volcano plot expresses the catalytic activity in function of binding energy [27]. The catalyst which situates at the top of the volcano curve, possesses a reactant/catalyst bindings strength which is equal to the binding between the atoms in the reactant molecule. The top of the volcano curve results in zero thermodynamic overpotential.

Figure 1-2 (A) presents a volcano plot for the electrochemical CO_2 reduction (eCO_2R), where the activity (y-axis) is expressed as the partial current density of the CO production. As the Sabatier principle dictates that the catalyst material which binds nor too strong, nor too weak with the key intermediate, will lead to a maximum in activity, is evidenced here. In case of the *COOH intermediate (which is a key intermediate for the production of CO), Au possess the most ideal binding energy and is therefore most suited to produce CO (in terms of activity). Although Au lies closest to the ideal bonding strength, the electronic properties of a metal can be altered in order to shift to more ideal bonding strengths, which will be discussed in more detail in section.

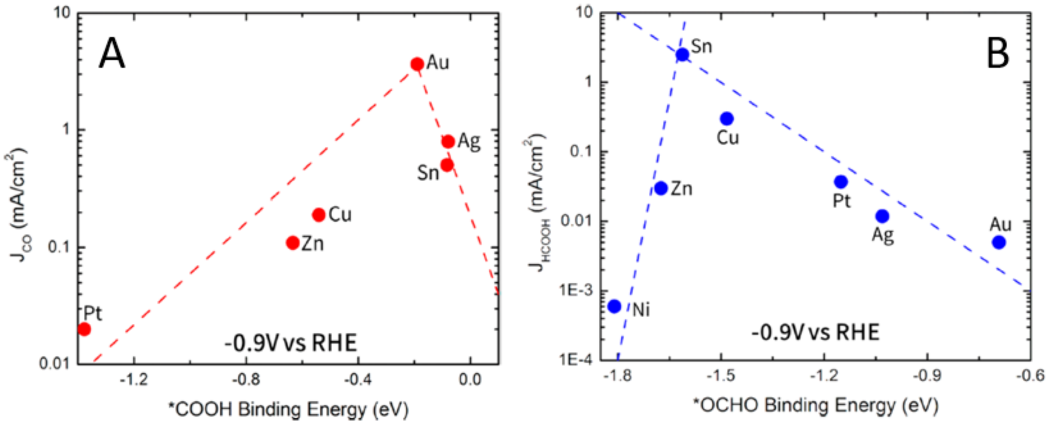

*Figure 1-2: (A) Volcano plot representing the partial current density for CO production vs. binding strength of the *COOH intermediate and (B) Volcano plot representing the partial current density for HCOOH production vs. binding strength of the *OCHO intermediate* [28]

Considering Figure 1-2 (B), several catalyst materials are evaluated for the production of HCOOH. As HCOOH is produced through another key intermediate (*OCHO), the classification of the metals seems to be quite different, compared to Figure 1-2 (A). Whereas Sn binds *COOH the weakest, it shows to be most suited for the reduction of CO_2 towards HCOOH, through *OCHO as key intermediate.

1.3 Catalyst design for the electrochemical CO_2 reduction

The eCO_2R was studied for the first time in 1870 by Royer [29]. Afterwards, the number of publications increased every year, especially during the last few years where it increased exponentially. The eCO_2R is an electrochemical reaction where CO_2 is converted by applying a potential or current. The eCO_2R can generally be written as:

$$m\,CO_2 + n\,(e^- + H_2O) \rightarrow product + n\,OH^- \qquad 1.1$$

Considering the eCO_2R, a big concern is related to the high stability of CO_2 due to its symmetry and its low polarity. In order to be bond to the catalyst surface, the CO_2 molecule needs to reorient the carbon and oxygen atoms in the molecule, as shown in Figure 1-3.

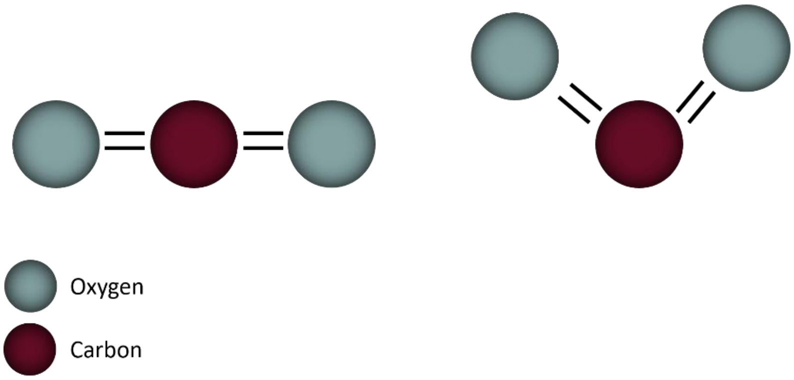

Figure 1-3: Reorientation of carbon and oxygen within a CO_2.

Here, electrocatalysts play a crucial role, since they chemically bond with the CO_2 molecule. Subsequently, a $CO_2^{\bullet-}$ radical anion or other reaction intermediates are formed, which are stabilized by the electrocatalyst, leading to a reduced overpotential [30]. With the right electrocatalyst, it is possible to reduce CO_2 to products such as CO with low overpotentials.

Consequently, the research on catalyst design is of utmost importance and the amount of studies have tremendously increased over the last decades in an attempt to improve the CO_2 reduction reaction performance. One of the pioneers in the thorough investigation of the eCO_2R was Yoshio Hori. He evaluated the eCO_2R on various electrodes (with a specific focus on the use of Cu electrodes [31]–[34]) and was one of the founders who divided the electrocatalysts into four main groups, depending on the final product [35]. The first group encloses the metals that do not give products descending from CO_2, such as Ni, Fe, Ti and Pt. As they bind the CO_2 intermediate to strong, hydrogen (H_2) is the main product generated at these electrodes. The second group includes the metals that are able to generate formate, such as Pb, Hg, Sn, Cd, In and Tl. The third group consists of metals that primarily produce CO (Au, Ag, Zn, Pd and Ga). Finally, the fourth group encloses only one metal, Cu. Cu is a unique metal since it is able to convert CO_2 into higher carbon chain products [35].

In order to explain the differences between the four electrocatalyst groups, many research has been devoted to the mechanistic study of the eCO_2R on these metals [36]. Despite the fact that the reaction mechanisms are still not fully understood (especially for the CO_2 reduction involving more than two electrons), main trends can be observed. For instance, the production of CO (involving two electrons) is established by hydrogenation of an oxygen atom in a (carbon bonded) CO_2 molecule, whereas formate is formed by the hydrogenation of a carbon atom in an (oxygen bonded) CO_2 molecule. Higher carbon products can be produced through C-C coupling. Various reaction pathways are presented in Figure 1-4.

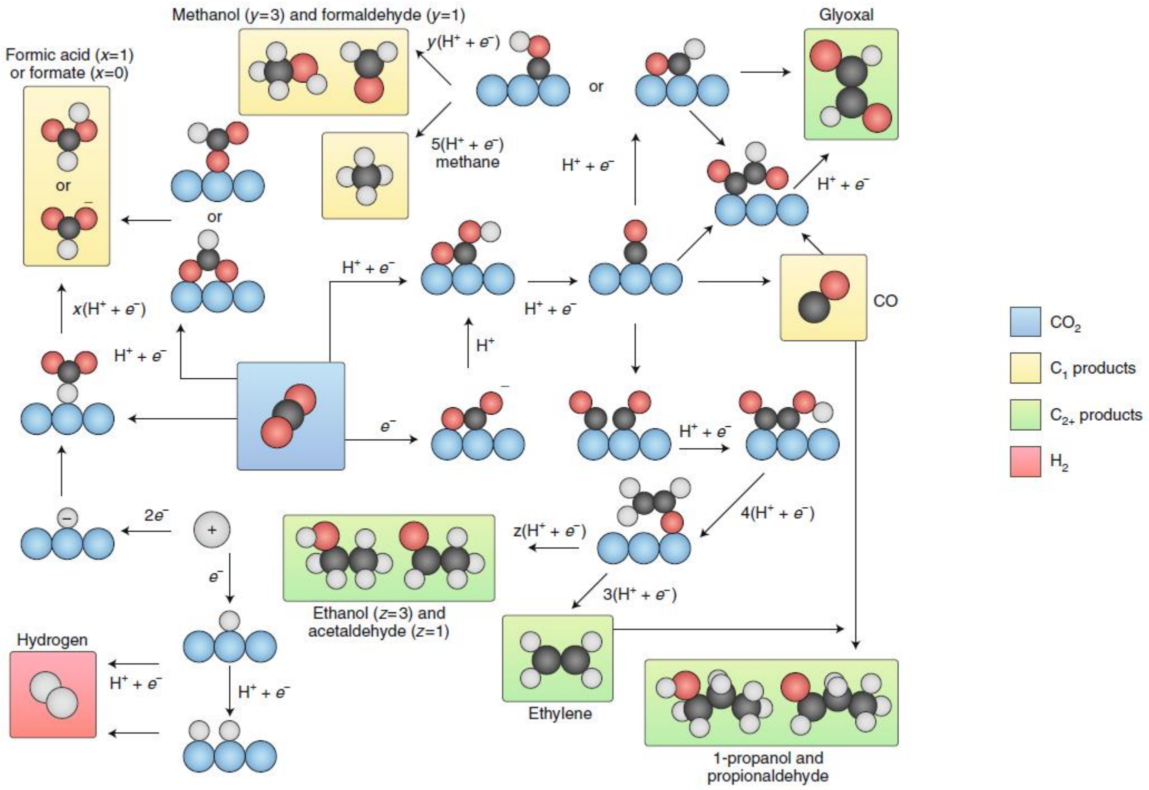

Figure 1-4: Overview of the CO_2 reduction pathways for the different reaction products. Black spheres, carbon; red spheres, oxygen; white spheres, hydrogen; blue spheres, (metal) catalyst [30].

Numerous experimental and computational efforts have been made to detect [37]–[39] and validate [40]–[42] intermediates during the eCO_2R. Despite the efforts, unraveling the behavior of monometallic electrocatalysts remains challenging. The complexity of the eCO_2R mechanism is displayed by the fact that several products share, to different extends, the same intermediate and reaction pathway. Moreover, an additional dimension to this problem is given by incorporating a second (or third,…) metal into the electrocatalyst, since the different materials in the structure can influence each other significantly (a detailed description is provided in section 1.3.3).

The urge of obtaining a more profound understanding of the eCO_2R on electrocatalysts has boosted the research on this topic even more, resulting in new reaction pathways and divergence between the proposed routes [43]. Therefore, this thesis will focus on obtaining a more thorough understanding of eCO_2R on bimetallic (more precisely Cu-Ag as a case study) electrocatalysts. Cu-Ag bimetallic structures were preferred, since Ag is known to already have an excellent performance for the eCO_2R and Cu a favored metal for the production of higher chain carbon products. Combining these two metals will enable us to investigate the effect of Ag on the product distribution during the eCO_2R on Cu. Consequently, the focus of the following literature review, will be on Ag and Cu-Ag bimetallic catalysts for the electrochemical production of CO from CO_2.

1.3.1 Reaction mechanism of the CO_2 reduction on Cu-Ag bimetallic surfaces

Many studies have been devoted to unravel the CO_2 reduction mechanism on Cu-Ag bimetallic surfaces [44]–[50]. It has been experimentally proven that the product distribution can be altered upon addition of Ag atoms into a Cu catalyst. The mechanism can be divided into two categories: (i) tandem effects and (ii) ligand and strain effects, which are represented in Figure 1-5.

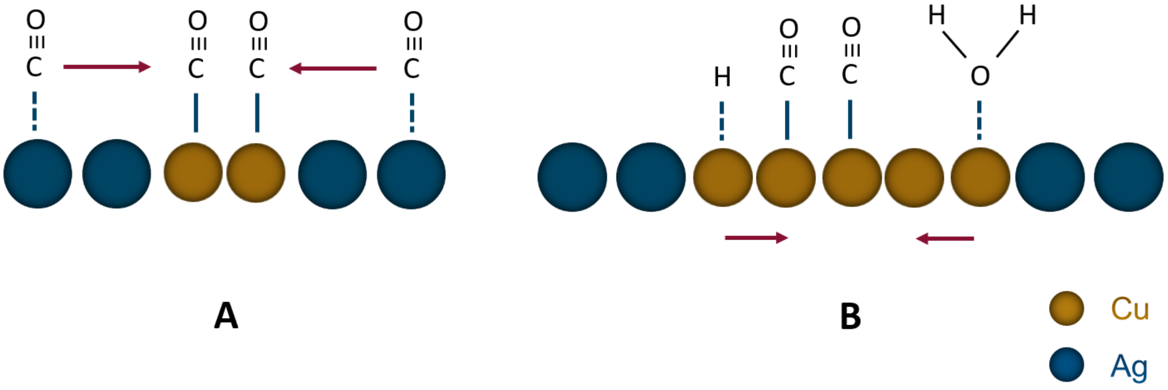

Figure 1-5: (a) tandem effects and (b) ligand and strain effects altering product distribution of the CO_2 reduction

First, the CO_2 molecules need to chemisorb onto the Ag surface through the C atom, leading to the formation of the key intermediate $*CO_2^-$ by injection of an electron from the electrode to the anti-bonding orbital of the CO_2 molecule. It is important to note that depending on the final product, CO_2 binds preferably through its C (formation of CO, and C_2 and C_3 products) or O (formation of formic acid) atom and would thus result in a different mechanism [51]. This adsorption is mostly known as the rate-determining step during the eCO_2R. Subsequently, *COOH is formed by water-assisted protonation of the $*CO_2^-$.

Thereafter, *COOH reacts to *CO through a water-assisted H transfer [36]. This mechanism is comparable to that of bare Ag.

Afterwards the spillover or tandem effect can occur because of the different binding energies of CO [52]. Since CO binds relatively weak to Ag, it will detach from the surface and be attracted to the Cu surface, which exhibits a stronger binding energy for CO compared to Ag. This increases the chances of C-C coupling and will improve the production of C_2 products over C_1 products [53], [54].

In addition to the spillover effect, the presence of Ag atoms accompanies the occurrence of strain, leading to a decrease in oxophilicity [55]. This would favor the binding of CO over H_2O, explaining the decrease in hydrogen production and an increased C_2 product formation, typically observed on Cu-Ag catalysts [54].

1.3.2 Size and morphology affecting the intrinsic catalyst activity

As the volcano plot already indicated, a theoretical optimum can be obtained, where a specific binding strength results in the highest activity for a given reaction. Every metal yields a different interaction with the reactant, resulting in a different activity towards the specific reaction. The affinity of the reactant towards the catalyst can be altered by changing the properties of the materials. In literature, different approaches are described such as, size effect [56], [57], faceting [58], [59], support effect [60], [61], surfactant [62]–[64] and alloying [65]–[67]. All approaches mentioned above, which change the intrinsic properties of the catalyst, are referred to as enhancement effects. This work will focus on the size and bimetallic effect.

When bulk materials are downsized to the nanometer range, the surface-to-volume ratio is increased, leading to a change in catalytic behavior owing to the increased contribution of surface atoms at the nanoscale [68]. The changes in catalytic behavior are caused by the altered electronic properties of these downsized structures. These changes in properties originate from the shift in position of the d-band center compared to the Fermi level [69]. By decreasing particle size, the band width changes which induces a shift in d-band center and consequently changes the adsorption of reaction intermediates at an electrocatalyst surface. Taking Au NPs as an example, a narrower d-band width results in a higher CO adsorption coverage and therefore a higher reactivity compared to its bulk metal [70]. In other studies where thin layer electrocatalysts are investigated, they assign the narrower d-band to the fewer atoms present within these layers [71], [72].

In addition, decreasing particle size, causes an increase in ratio of edge, corner and surface atoms and/or the presence of structural defects, which influence the binding energy of the reactant/intermediate, as such altering the reaction [73], [74]. Considering Cu NPs, increased edges and steps compared to surface atoms lead to more negative chemisorption energies of *CO intermediates, improving the C-C coupling and therefore altering the product distribution. These effects contribute to the altered activity of the catalyst and an optimal particle size can be found for a specific metal and a specific reaction.

One of the key factors in low cost CO_2 reduction towards CO is the efficiency of the catalyst performance. Ag catalysts have been known to be one of the most effective monometallic catalysts to selectively reduce CO_2 towards CO, but the high catalyst cost made them less appealing. Different strategies have been proposed in order to lower the catalyst costs. One potential approach is the downscaling of the catalyst's size. The transition to the nanoscale seemed to be beneficial to lowering the capital costs along with increasing the activity.

Salehi-Khojin et al. [75] investigated the effect of Ag nanoparticles (NPs) on the CO_2 reduction towards CO. They changed their size between 200 nm and 1 nm and found that decreasing the size of the Ag particles below 200 nm, resulted in an increased activity for the Ag particles. Decreasing the size further down to the nanoscale, an optimum was observed at 5 nm, displaying the highest partial current densities towards CO at the same applied potential. Later, Kim et al. [61], investigated the effect of supported Ag NPs (between 3 nm and 10 nm) on the eCO_2R, compared to normal Ag foil at the same potential. They confirmed the optimum to be 5 nm, where the lowest overpotential towards CO and the highest partial current density could be obtained. Below 5 nm, the faradaic efficiency (FE) towards CO decreased.

Besides the size effect, the morphology plays an important role. Indeed, by changing the morphology of the catalyst, different facets become dominant, potentially changing the catalytic properties. Therefore, single crystal Ag catalysts with different dominant facets have been studied. For example, Nagahiro et al. [32] found that the catalytic activity of single crystal facets of Ag catalysts decreased according to Ag(110) > Ag(111) > Ag(100).

Ag(110) facets show a lower energy barrier for the formation and stabilization of the COOH intermediate, which is the most important intermediate in the production of CO.

Later Yang et al., demonstrated a strong dependence of Ag catalysts morphology for the electrochemical reduction of CO_2 towards CO. They unambiguously showed that cubic Ag catalysts favor CO reduction compared to octahedral Ag catalysts, by 20 % (FE) [58]. Triangular Ag nano-plate catalysts also showed improved CO production over similarly sized Ag NPs and bulk Ag, with an FE of 96,8 % in addition to showing a substantial durability of 7 days. They hypothesize this is due to the improved edge-to-corner ratio and the presence of the Ag(100) facet, which requires less energy to initiate the rate-limiting step.

In addition to well-designed catalyst structures, catalysts with high porosity can also be of interest because of their potentially high electrochemical active surface area (representing the area accessible for the electrolyte and participating in the charge transfer; EASA). Indeed, Hsieh et al. [76] discovered a 32-fold increase in activity (normalized by surface area) for Ag nano-corals as compared to plain Ag foils. Furthermore, Lu et al. [57] synthesized nanoporous Ag catalysts, which showed a 150-fold increase in surface area and a 20-fold increase in activity towards CO production, compared to polycrystalline Ag catalysts. The improved activity was due to the superior stabilization of the *COOH intermediate on the highly curved surface.

To conclude, tuning the size and morphology can have major effects on the activity of the eCO_2R. Therefore, the focus of this work will be to synthesize spherical nanoparticles, preferably with a size below 10 nm, since both the surface-to-volume ratio and the electronic effects come into play and are optimal in this size range.

1.3.3 Bimetallic effect

In addition to the effect of size reduction, the interaction of the catalyst with the reactant can also be changed by the addition of a second or third metal into the catalyst. An additional metal causes metal-metal interactions to occur, providing properties that were originally absent in their single phase metals. Additionally, adding extra elements might be cost beneficial, since the introduction of a second (less expensive) metal reduces the amount of the expensive metal that is required. The findings of these unexpected characteristics has led to extensive research concerning possible applications. Bimetallic electrocatalysts have shown to be very promising candidates in the further optimization of the eCO_2R, which originates from their unique interface effects [65], [77]–[79].

Tremendous efforts have been made in the fundamental understanding of the different mechanisms that are at play and alter the electrochemical reaction as compared to the single metal. These can be divided in ligand, strain and ensemble effects [80].

Ligand effect

Upon doping the catalyst with an extra metal, the activity of the initial catalyst can be enhanced. This effect is called the ligand effect and originates from the shift in d-band center [81]. A shift in d-band center can greatly benefit the interaction of the surface with the reactant/intermediate. A stronger bonding between the catalytic surface and the adsorbates relates to the upward shift of the d-band relative to the Fermi level and can be induced by the addition of another metal [82].

Bimetallic structures can have several configurations as presented in Figure 1-6. First, the metal interactions can take place within the same particle where the different metals are uniformly mixed (Figure 1-6(A)). Second, the interaction can take place at the interface between the two metals where either a core-shell (Figure 1-6 (B)) or a dimer (Figure 1-6(C)) can be formed [83].

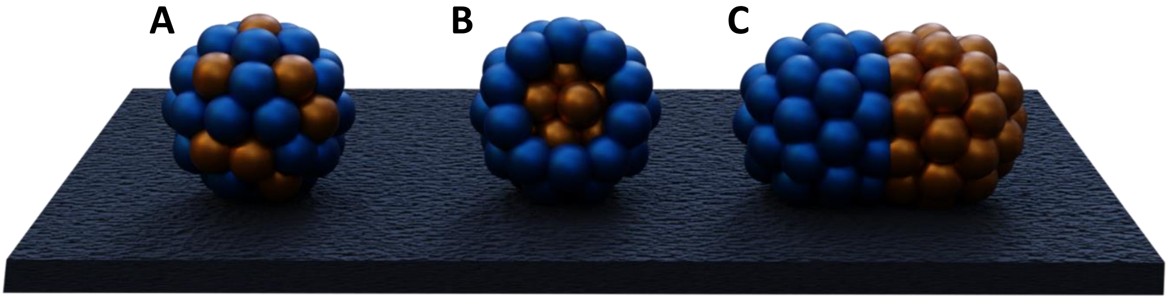

Figure 1-6: Graphical representation of bimetallic configurations such as (A) Me-Me alloyed, (B) core-shell: the core contains a less noble metal than the shell and the shell is preferably a few atomic layers thick and (C) dimers: this configuration consists of two separate metal particles connected by a common interface (not to scale)

Considering core-shell nanoparticles, a metal core is totally covered by another metal shell. As the metal core is encapsulated by a second metal. This kind of structure enables the protection of the interior of the structure from the surrounding environment. One example is the use of Cu NPs as a core material, as it can be protected from oxidation by covering the NPs with another metal shell. In addition, the core metal will influence the properties of the metal in the shell by altering its electronic environment [84]. Changing the electronic environment leads to a shift in d-band center with respect to the Fermi-level, which is key when considering the reactivity of bimetallic electrocatalysts [85]. As for nanodimers, two different metals are separated by a distinct interface, where totally different properties of the two parts can exist [86]. This multi-functionality can result in a tandem reaction such as described for Cu-Ag bimetallic electrocatalysts in 1.3.1. Here, a key intermediate is generated on the Ag surface and subsequently adsorbs on the Cu surface, which will be converted to higher carbon products. These structures have great potential in electrocatalysis owing to the ability to boost/tune their performance based on their composition, structure, size and shape.

Cu-Ag bimetallic catalysts gained more interest over the last years because of their excellent performance for the eCO_2R towards CO [64], [87], as well as higher carbon chains [88]–[90], depending on the amount of Cu present at the surface. Catalysts combining these two metals can have two effects (ligand and strain effect) contributing to the changes in electronic structure, and therefore resulting in altered electrocatalytic selectivity and activity. By introducing Ag to a Cu surface, heteroatom bonds changes the electronic environment, giving rise to changes in the electronic structure caused by the ligand effect.

Strain effect

Activity enhancement can also be induced by strain effects [91], [92], which are related to the changes in electronic properties of the metal by shifting the d-band center [25], [93]. Strain will occur when a misfit between the lattice constant of the different metals is present. Tensile strain results in an upshift in d-band center, causing a stronger interaction with the adsorbates, whereas compressive strain leads to a downshift and therefore a weakening of the interactions with the adsorbates [93]. For the CO_2 reduction reaction (CO_2RR) to CO the case of Cu and Ag is particularly interesting as a large misfit of over 12 % exists (Ag has a larger interatomic distance than Cu), giving rise to strain. Indeed, Chang et al. [66] investigated the effect of Cu overlayers in Ag@Cu structures on the CO_2RR and found that tensile surface lattice strain enhanced the CO adsorption on the surface.

Thin films with interphase miscibility show increased activity and selectivity towards carbonyl products. It is hypothesized that this is due to the decreased surface binding energy of oxygen-containing intermediate species [67]. A decrease in hydrocarbons and HER upon increasing Ag concentration was also noticed. This was, according to theoretical calculations, due to the weakening of the binding energy of H*.

Cu/Ag nanodimers are a first step towards Cu@Ag core-shells. Huang et al. [94] investigated the difference of nanodimers compared to their monometallic parents. Cu/Ag nanodimers with equal Cu and Ag NP size are accompanied by an increase in ethylene production and suppression of hydrogen compared to the monometallic Cu. The CO production was decreased compared to monometallic Ag. This study also showed a good balance between Cu and Ag is key to an optimal ethylene production.

Cu@Ag core-shell NPs were synthesized in literature and used for the conversion of CO_2. Zhang et al. [95] found that by introducing a layer of Ag onto Cu NPs, the product distribution was effected. They varied the Ag concentration between 11.2 % and 24.2 % and noticed a volcano-type relationship between the Ag concentration in the core-shell and the selectivity towards C_2 products. Upon increasing the concentration of Ag from 11.2 % to 15 %, C_2 production is promoted and the selectivity increased. Nevertheless, further increase in Ag concentration, and thereby shell thickness, the selectivity towards C_2 products decreased substantially. The decrease in C_2 products was accompanied by an increase in CO formation. These results clearly indicate a delicate balance exists between Cu core and Ag shell for the eCO_2R. They speculate a tandem reaction is the foundation of this findings, where CO_2 is firstly converted to CO at the Ag surface and then further reduced to higher chain chemicals on the Cu surface. As this becomes more and more difficult as the Ag shell thickens, more and more CO is produced. Kuhn et al. [90], also investigated Cu@Ag core-shell NPs within the same size-range. A shell thickness of 0.1 nm increased the C_2 concentration with a relevant selectivity difference towards ethylene at low overpotentials compared to bare Cu and Cu@Ag core-shells with a shell thickness of 0.3 nm. They hypothesize that the C-C coupling on sub-10 nm Cu NPs is boosted at low overpotentials by the addition of Ag atoms causing a strain effect, and as such an electronic tuning of the Cu-Ag interface and an increased CO* concentration at the surface as a consequence.

<u>Ensemble effect</u>

Finally, the ensemble effect arises when a reactant needs more than one atom to bind to the catalyst surface. Replacing one atom with another metal can severely weaken the bond of the catalyst with the reactant. In this respect, Wang et al. [96] investigated the ensemble effect of Pd on Au. They found that depending on the ensembles (monomer, dimer, trimer) of Pd present at the surface, the binding strength of the CO intermediate can be altered. the dimer ensemble seemed most suited and balanced the *COOH and *CO adsorption most efficiently.

In conclusion, incorporating Ag into a Cu structure alters the properties of the Cu and as such, tunes the final product during the eCO_2R. Despite the many efforts of synthesizing Cu-Ag bimetallic structures and exploring the effects of different Ag concentration in this electrocatalysts, a thorough understanding of the bimetallic electrocatalyst performance is still lacking. This is especially the case for bimetallic electrocatalysts with a particle size below 20 nm. This thesis aims to establish a more in-depth understanding of the composition-selectivity relationship of Cu-Ag bimetallic nanoparticles. Accordingly, a straightforward synthesis method will be developed in order to fine-tune the Cu-Ag bimetallic structures and explore their capabilities towards the eCO_2R.

CHAPTER 2:

Scope and outline

This chapter provides the objectives along with the strategy and the outline of this doctoral work.

2.1 Objectives

As discussed in Chapter 1, global decarbonization to combat global warming is becoming more urgent every day. One of the possible solutions is the electrochemical reduction of CO_2 to value added products. Regardless of the exponentially increasing literature reports on the eCO_2R over bimetallic electrocatalysts, their behavior and the influence of an additional metal on a core metal is not fully understood yet. As the morphology, size and composition is key in altering the performance of bimetallic electrocatalysts, the development of a reliable synthesis method is indispensable.

As such, **the aim of the doctoral work is to optimize the synthesis route towards reproducible electrocatalysts, unveiling structure-performance relationships and unraveling the restructuring pattern in order to improve these electrocatalysts for the eCO_2R.** In order to reach these goals, it is important to find a straightforward and reproducible method to produce the electrocatalyst. Characterization will be performed by combining electron microscopy, spectroscopy and (electro)chemical techniques to evaluate the parameters of interest in obtaining a good electrocatalyst. The information that can be obtained in this manner enables the further optimization of these electrocatalysts.

2.2 Strategy

In order to obtain a more thorough understanding of the behavior of bimetallic electrocatalysts, Cu and Ag will be selected as an example. Ag is already intensively studied and produces solely CO, whereas Cu is known to be capable of reducing CO_2 towards various high end products.

Cu-Ag bimetallic nanoparticles will be synthesized using electrodeposition, thermal decomposition and galvanic displacement. Through this approach, Cu-Ag electrocatalysts (with altered Cu:Ag composition and structure) will be acquired. These structures will be characterized by scanning electron microscopy (SEM), transmission electron microscopy (TEM), ultraviolet-visible spectroscopy (UV-VIS) and electrochemical analysis. The Cu-Ag series, containing different Cu:Ag compositions, will be analyzed in an hybrid flow cell. The gas –and liquid flow will be analyzed by gas chromatography (GC) and high-performance liquid chromatography (HPLC).

Subsequently, the electrochemical stability of Cu@Ag bimetallic core-shell electrocatalysts will be studied, and their morphological changes will be analyzed using electron tomography. The structural changes will be linked to the performance during the eCO_2R, accordingly. The effect of a carbon layer (with altering thickness) on the stability and promotion of the eCO_2R will be explored. The carbon layer will be characterized by TEM, Raman spectroscopy and X-ray photoelectron spectroscopy (XPS).

2.3 Outline

The experimental work in this dissertation, can be divided into two mean parts: (i) the synthesis of Cu and Cu-Ag bimetallic (nano)particles and their application for the electrochemical CO_2 reduction and (ii) the stability investigation of Cu@Ag core-shell nanoparticles. The schematic representation of the outline is given in Figure 2-1.

In Part I, an introduction into this dissertation is given in Chapters 1-3. Here, a general introduction into the field of electrochemistry and its applications, along with a theoretical background and the used techniques are discussed. The electrochemical CO_2 reduction is investigated, with the aim of obtaining a reliable synthesis method for preparing sub-10 nm Cu-Ag bimetallic nanoparticles and investigating their behavior and electrochemical restructuring pathways.

Part II describes the synthesis of Cu-Ag bimetallic nanoparticles and their behavior in a CO_2 electroreduction environment. In Chapter 4, monometallic Cu (nano)particles on rough substrates were synthesized using single and double pulse electrodeposition. Here, the effect of the substrate pre-treatment and double pulse parameters on the morphology and size, respectively, was investigated. In order to reduce the particle size up to the sub-10 nm scale, an organic synthesis approach was investigated to obtain reproducible batches. Additionally, a second metal was incorporated for the synthesis of Cu-Ag bimetallic nanoparticles, to push the CO selectivity even higher. These topics are addressed in Chapter 5. Finally, in Chapter 6, the performance of the Cu-Ag bimetallic nanoparticles has been extensively studied under CO_2 operating conditions to investigate the effect of (i) the electrocatalyst structure, (ii) the electrolyte on the product selectivity during the electrochemical CO_2 reduction (iii) a carbon black carrier.

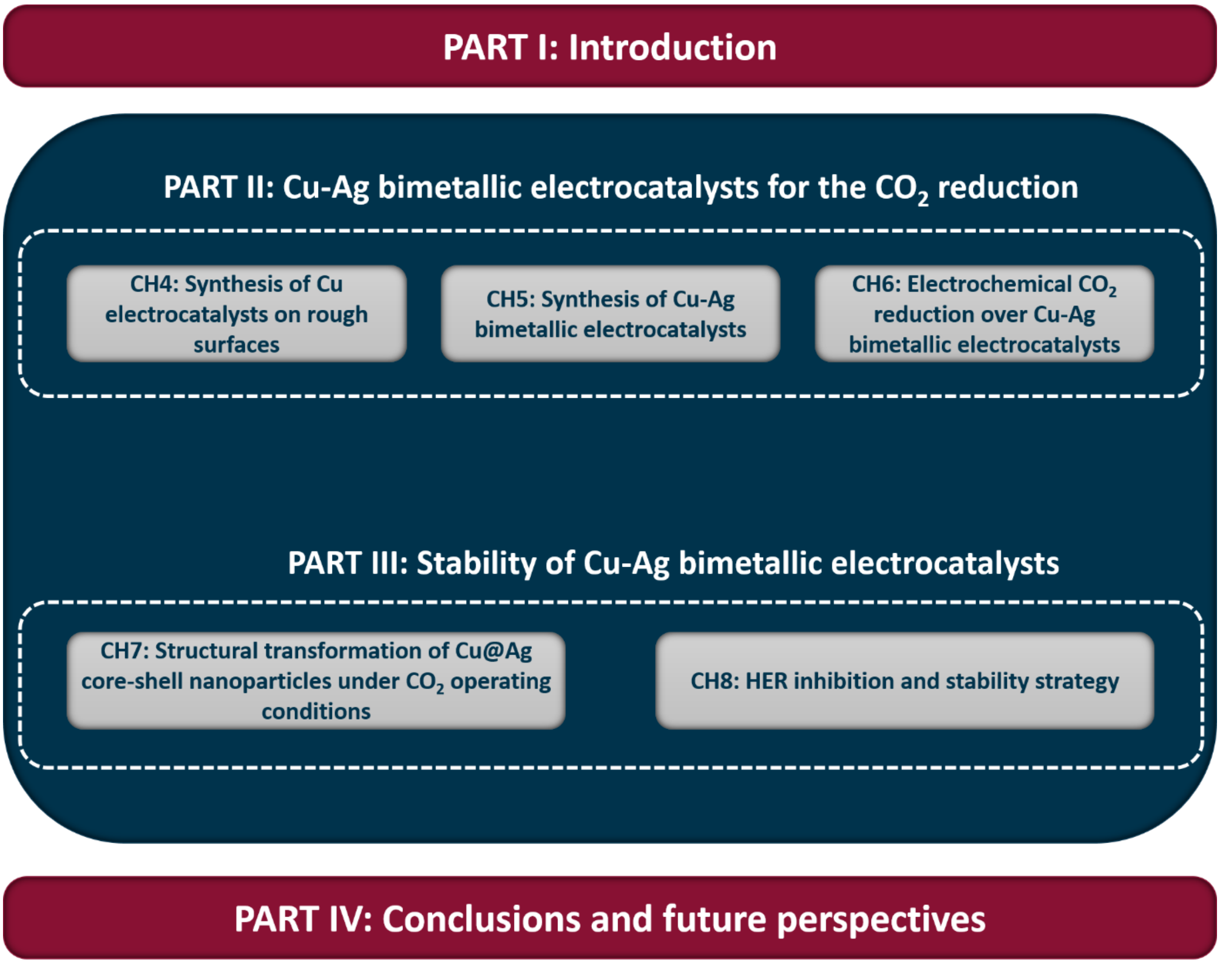

Figure 2-1: Schematic outline of the doctoral work

Part III consists of 2 chapters. Since the stability of core-shells is still not investigated in detail, structural transformation pathways remain unclear. Therefore, we devoted Chapter 7 to unraveling the electrochemical destabilization mechanism of Cu@Ag core-shell nanoparticles after different reaction times and under varying conditions. The morphological changes were studied using electron tomography and were linked to the electrocatalyst performance. As electrocatalysts suffer from degradation during an electrochemical experiment, a strategy for boosting their electrochemical stability was proposed by protecting the active layer (Ag layer was used as a benchmark) with a carbon layer.

To summarize this work, the main conclusions from the experimental work in Part II and Part III will be given in part IV along with a perspective for future research lines.

CHAPTER 3:

Theoretical background

This chapter provides the theoretical background of the electrochemical, the surface analysis techniques and the electrocatalyst synthesis techniques used further on in this work.

3.1 Electrochemical techniques

In this work, electrochemical techniques such as chronoamperometry (CA), chronopotentiometry (CP) and cyclic voltammetry (CV) are used. Cyclic voltammetry is used to characterize the catalyst and for degradation analysis, whereas chronoamperometry is used for electrodeposition. Chronopotentiometry is used during the eCO_2R experiments. A more detailed description of the experimental parameters is provided in the respective chapters. The outline of this section has been based on references [97]–[99].

3.1.1 Chronoamperometry (CA)

Chronoamperometry (CA) is a pulse technique where a potential step is applied to the working electrode (WE) vs. a reference electrode (RE). When a potential is applied to the working electrode, the value is shifted from a potential where no reaction occurs, to a potential where an electrochemical reaction takes place. This applied potential is accompanied by a current response, which is monitored in function of time (Figure 3-1). CA is often used to study the kinetics of an electrochemical reaction.

In this dissertation, CA will be used to deposit Cu onto a substrate (Chapter 4). By applying a negative potential, the Cu ions in the electrolyte deposit onto the WE. By variations in the applied potential and duration of the experiment, the Cu deposition can be altered (discussed in more detail in section 3.3).

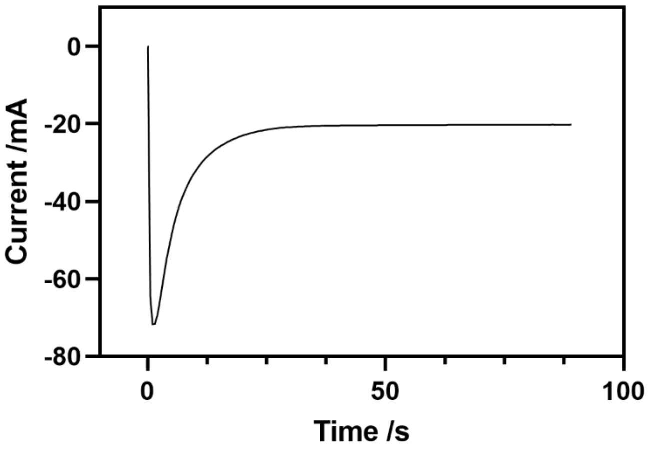

Figure 3-1: Current response of a CA experiment.

When a potential is applied to the electrode surface, the corresponding current will consist of a capacitive contribution and a faradaic contribution. The capacitive current is due to the charging of the electrochemical double layer. The faradaic current is provoked by the reduction of Cu on the WE surface.

3.1.2 Chronopotentiometry (CP)

Chronopotentiometry (CP) is an electrochemical technique where a current step is applied between the WE and the counter electrode (CE) and the potential response is monitored. Considering an electrochemical system where redox species are present, the application of a negative current corresponds to the reduction of these species at a certain potential with a constant rate. The potential value is characteristic for each reactant in the system. When applying a current, the potential is shifted until it is negative enough for an electrochemical reaction to occur. In this study CP is used in a flow system where a continuous CO_2 flow is provided at the electrocatalyst surface and therefore sufficient reactant is ensured at the electrode in order to prevent depletion. Nevertheless, the eCO_2R is performed using an aqueous electrolyte, which often results in the competing hydrogen evolution reaction (HER).

Since a constant current is applied throughout the experiment, the electrolyte resistance (ohmic resistance) is also constant. This resistance between reference and working electrode causes a potential drop, referred to as the ohmic drop. The application of a current simplifies the correction for this ohmic drop since this potential drop is equal to the product of the current and the ohmic resistance. In addition, the eCO_2R is pH dependent and therefore the measured potential is often expressed with respect to the reversible hydrogen electrode (RHE, equation 3.1).

$$E_{RHE} = E_{ref} + 0.210V + 0.059 \cdot pH + IR \tag{3.1}$$

Where E_{RHE} is the potential expressed with respect to the RHE, E_{ref} is the measured potential with respect to the used RE, 0.210V is the potential of the RE (Ag/AgCl 3 M KCl) with respect to the standard hydrogen electrode (SHE), 0.059pH is the pH dependent factor and IR is the correction factor of the ohmic losses.

The potential difference between CP experiment and the iR-drop measurement was divided by the current difference of the two, which corresponds to the uncompensated resistance as expressed below.

$$iR = \frac{E_{CP,exp} - E_{CI}}{i_{CP,exp} - i_{CI}} \tag{3.2}$$

Where iR is the uncompensated resistance, $E_{CP,exp}$ and E_{CI} are the potentials from the CP experiment and the current interrupt, respectively. $i_{CP,exp}$ and i_{CI} are the currents applied during the CP and current interrupt experiment, respectively.

3.1.3 Cyclic voltammetry (CV)

Cyclic voltammetry (CV) is one of the most commonly employed techniques in electrochemistry. It is often used for the preliminary study of an electrochemical system. Cyclic voltammetry is a reversal technique, a linearly varying potential is imposed to the working electrode starting from the initial potential (E_i) until the switching potential (E_{min}). When reaching this point, the potential is reversed and swept to E_{max}.

Figure 3-2 shows the potential sweep and the corresponding cyclic voltammogram. During the forward scan of a CV experiment, the reduction of species in the electrolyte or the electrode itself occurs. Reversing the scan means that the reduced products from the previous scan will be oxidized.

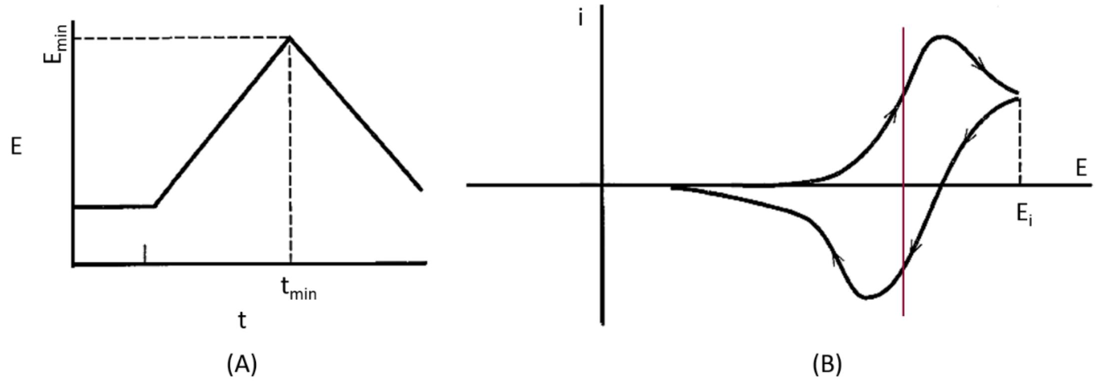

Figure 3-2: Illustration of (A) cyclic potential variation and (B) the corresponding cyclic voltammogram

At the beginning of the CV measurement, only O (oxidant) is present and the sweep direction will therefore be to the negative potential range, reducing O to R (reductant). This leads to a depletion of O at the surface of the electrode, since they are being reduced to R. As the experiment proceeds, the concentration of O is further depleted upon (negatively) increasing the potential, eventually reaching a peak current ($i_{p,c}$). This current is dictated by the delivery of O via diffusion from the bulk to the electrode, which increases the larger the concentration difference between bulk and electrode. The diffusion layer at the electrode, containing the reduced species R, then starts to expand at more negative potentials, making mass transport of O to electrode more difficult. The diffusion rate of O becomes slower, resulting in a decrease in current upon scanning to more negative potentials. Reaching the switching potential, the scan is reversed and R will be oxidized to O during this scan. At the half way potential (indicated by the red line in Figure 3-2) observed between the oxidation and reduction peak, the concentration of O and R are equal. Upon further scanning, the rate of diffusion of R starts to slow down and a depletion in current is again observed due to the slower diffusion. During this experiment, two peaks can be observed, corresponding to the oxidation peak (the peak at positive currents) and the reduction peak (the peak at negative currents). A process is reversible when the two peak potentials (E_p) are separated by a maximum of 57 mV. For quasi reversible systems, a larger potential difference between the peaks is observed and in case of an irreversible system, only one peak is visible.

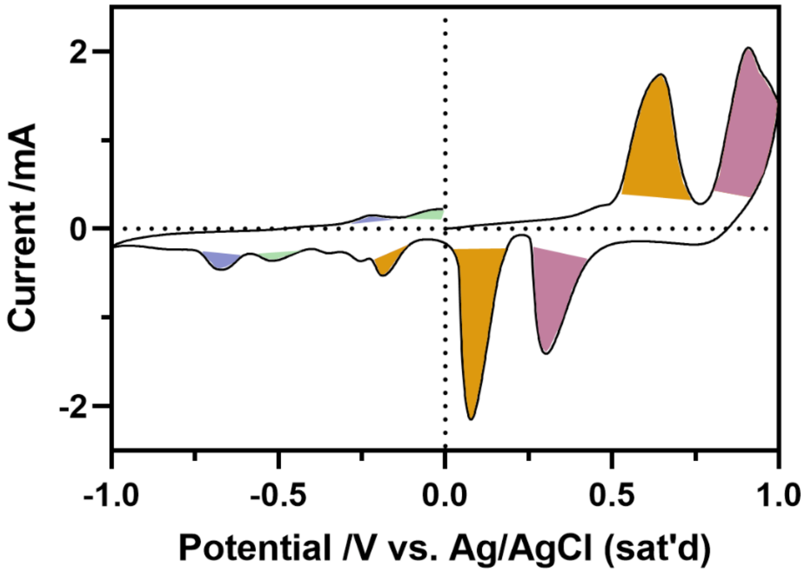

Figure 3-3: Cyclic voltammogram of a Cu-Ag bimetallic electrode. The potential is swept between -1 V and 1 V vs. Ag/AgCl (sat'd) in a 0.5 M NaOH solution with a scan rate of 50 mV s^{-1}.

In this work, cyclic voltammetry was used for several studies. First, this technique was used to qualitatively indicate the presence of different elements in the catalyst and served as a supporting technique for other characterization methods such as electron microscopy (discussed in 3.2 in more detail). As every metal possesses its own specific reduction/oxidation potential, this technique can be used to identify different metals on an electrode as shown in Chapter 7 and 8. Figure 3-3 demonstrates a CV of a Cu-Ag bimetallic electrode. The different oxidation states of both Cu and Ag can be deduced. The oxidation and reduction peaks indicated in purple and green represent the Cu/Cu_2O and the CuO/Cu_2O, respectively. The Ag/Ag_2O and AgO/Ag_2O are highlighted in orange and pink, respectively. Given the fact that Ag is a more noble metal compared to Cu, it tends to be less prone to oxidation.

Generally, the potential is swept with scan rates of 20 mV s^{-1} to 1 kV s^{-1}. At high scan rates, the electrochemical system is not able to establish an equilibrium. This implies that besides the faradaic current (due to the reaction of the species/electrode), a capacitive current is also generated by the occurrence of an electrochemical double layer. The charge of this double layer changes upon sweeping the potential.

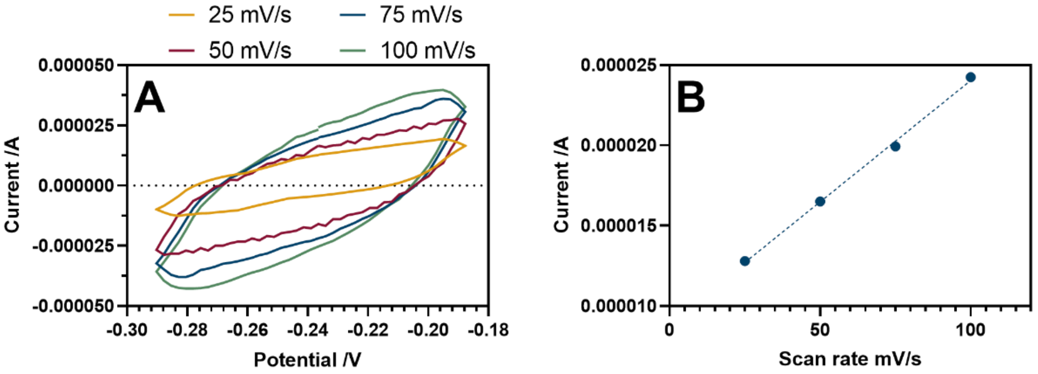

Figure 3-4: : Capacitance graph presenting the (A) CV measurement at scan rates ranging from 100 mV s^{-1} to 25 mV s^{-1} and (B) scan rate dependence of the charging current.

Performing CV measurements within a range where no reaction occurs, only the capacitive current is measured (Figure 3-4 (A)). Repeating the measurement at different scan rates, allows us to plot the current vs. scan rate (Figure 3-4(B)). The slope of this curve gives an indication on the EASA, which can be used to compare electrocatalysts of the same metal (Chapter 4).

3.1.4 Faraday’s law of electrolysis

The law of Faraday dictates that the amount of chemical produced is proportional to the amount of charge transferred.

$$Q = nzF \tag{3.3}$$

Where, Q is the transferred charge, n is the amount of product formed in mol, z is the amount of electrons and F is the Faraday’s constant. In order to calculate the faradaic efficiency (FE) during the eCO_2R, an accurate measurement of the reaction products is necessary. Therefore, the outlet gas stream is sampled and measured by gas chromatography (GC). Considering the eCO_2R, multiple reactions occur simultaneously (conversion of CO_2 to multiple products, competing HER) as a result of which the total transferred charge needs to be divided among the different reaction products. Computing the FE illustrates the amount (in %) of the charge is consumed by a certain reaction product (i).

$$FE_i = \frac{n_i z_i F}{i} * 100\ \% \tag{3.4}$$

Where n_i is the amount of moles of product generated, z_i is the number of electrons transferred per mole product, i is the total current supplied the system.

3.2 Structural characterization techniques

In this work surface characterization techniques such as scanning electron microscopy (SEM), high angle annular dark field scanning transmission electron microscopy (HAADF-STEM) and electron tomography are used. The outline of this section was based on references [100]–[110].

3.2.1 Scanning electron microscopy (SEM)

In this work, electrocatalysts are synthesized at the nanoscale, which unavoidably leads to the need for a high spatial resolution to image these catalysts. An optical microscope is insufficient for imaging nanoscale materials, since it is limited by the diffraction of light in the visible range. In order to be able to image sub-micron scale materials, an electron microscope can be used. One commonly used technique is scanning electron microscopy, denoted as SEM. This technique is used to analyze the surface of the catalyst material.

A schematic representation of such an electron microscope is given in Figure 3-5. A SEM microscope encompasses the electron gun, electromagnetic lenses, a vacuum chamber with the sample stage and a selection of different detectors. The amount of current of a finely focused electron beam, interacting with the sample, determines the magnitude of the signals emitted from the sample. In addition, the size of this finely focused electron beam governs the resolution of the scanning electron microscope.

The electron gun is located at the top of the instrument column and acts as an electron generator (electron source). Electron guns can consist of either a thermionic source (produces electrons when heating tungsten or lanthanum hexaboride crystals), or a field-emission source (produces electrons when a large potential is applied to a fine tungsten needle). The latter is most frequently employed, since this source yields more monochromatic electrons compared to the thermionic sources. This means higher resolution and current density of electrons. The gun consist of a fine tungsten needle and an anode set. This anode serves as an extractor and accelerator for the electrons. Voltages between 1 kV and 30 kV are used. The gun operates under ultra-high vacuum (10^{-8} Pa) to avoid scattering of electrons.

Below the gun, a series of lenses are located including condenser and objective lenses. These lenses are used to focus the electron beam, generated by the electron gun. Since the beam generated in the gun is about 50 µm in size, its diameter needs to be reduced by 100 or 5000 fold to obtain a diameter of 0.5 µm to 10 nm in order to be useful for imaging. This large demagnification requires at least two condenser lenses. A direct current runs through these lenses and by varying this current, the desired demagnification can be obtained.

In order to control the number of electrons along with the angular width of the electron beam and the lens defects, apertures are installed. Spray apertures are used to block off-axis electrons, while beam-limiting apertures are used to reduce angular width and current of the electron beam. Small apertures will result in a small probe size and low beam current. This will increase the resolution but decrease signal strength. The radii of these apertures vary between 10 µm and 500 µm. Along with the electron gun, the entire system operates under high vacuum, to minimize scattering of the electrons in the beam.

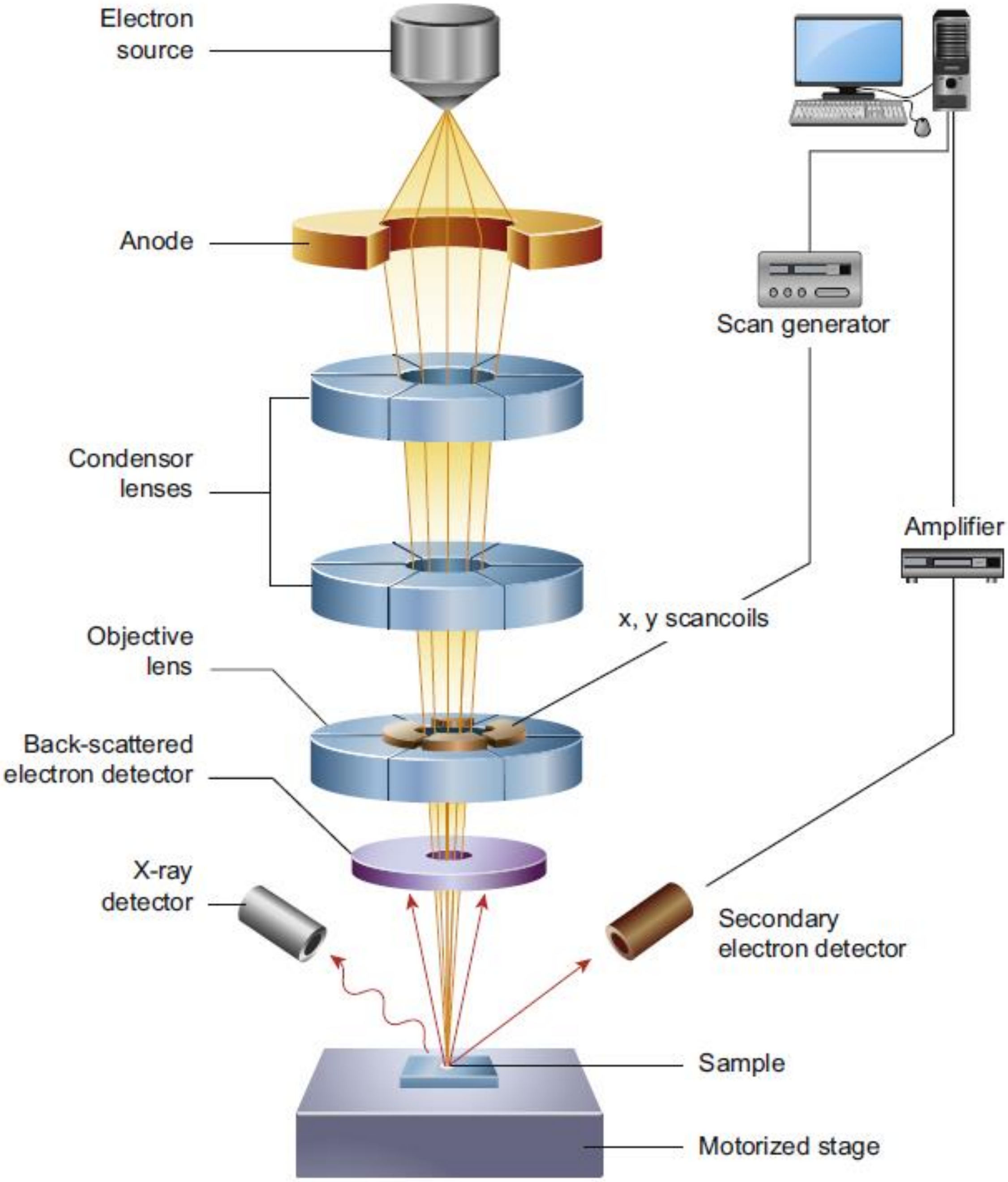

Figure 3-5: Illustration of a SEM with its core components [100]

The focused electron beam is scanned point by point across the material of interest with the scan-coils or deflection coils and the scan generator (providing the pattern on the specimen). When the electrons from the beam enter the sample, elastic or in-elastic interaction can occur. Elastic scattering takes place when primary electrons (electrons from the electron beam) get deflected into a new direction (deviating from the initial path of the electron beam) by the atomic nuclei, without losing energy. The probability of high angle elastic scattering increases when heavier atoms are analyzed, due to their stronger positive charge. The tendency of an electron to undergo elastic scattering decreases with increasing beam energy, since the energy is more likely to overcome this positive charge of atomic nuclei. These elastic scattered electrons are also referred to as backscattered electrons and can be used for SEM imaging.

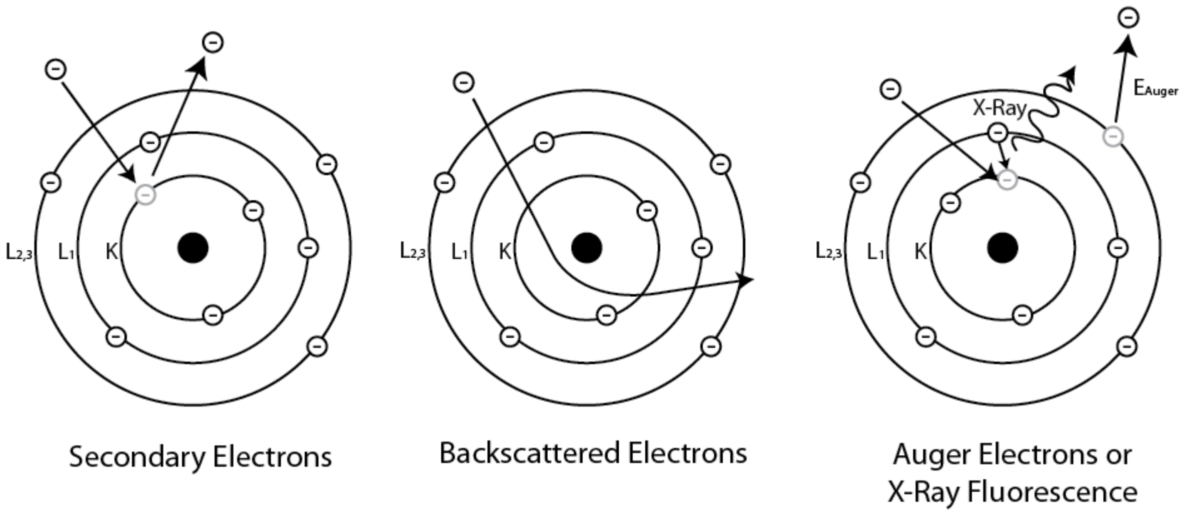

Figure 3-6: Schematic representation of electron interactions occurring when primary electrons penetrate the sample in SEM

On the contrary, inelastic scattering occurs when the energy of a primary electron is reduced by interacting with the specimen atoms. These interactions can cause ejection of weakly bound outer-shell electrons from the specimen atoms to form secondary electrons or ejecting of tightly bound inner shell electrons, which eventually result in the formation of characteristic X-rays (explained in more detail in 3.2.3). The different electron interactions are depicted in Figure 3-6.

In this thesis, SEM is used as important characterization method for the investigation of the morphology, particle density/distribution on the substrate of the synthesized catalyst in Chapters 4 and the imaging of the electrocatalyst surface in Chapter 8.

3.2.2 Scanning transmission electron microscopy (STEM)

Scanning transmission electron microscopy (STEM) is a very powerful technique to investigate nanostructures and obtain morphological and structural information. While

SEM can reach a resolution of up to 10 nm, STEM offers atomic resolution. Compared to SEM, where the electron beam is emitted from the surface of the specimen, STEM uses higher acceleration voltages of up to 300 kV, enabling the transmission of electrons through a sample, provided it is sufficiently thin (maximum thickness of ~100 nm). STEM imaging is performed in a transmission electron microscope (TEM) in STEM mode and is illustrated in Figure 3-7.

A STEM microscope consists of several parts, starting with the gun (not shown in Figure 3-7). In most modern STEM microscopes, a field emission gun (FEG) is used analogous with SEM, albeit more powerful (due to the higher energy of the electrons). After the electrons leave the FEG cathode, they are accelerated by the anode to their final kinetic energy before they reach the sample. Demagnification of the electron beam is achieved by the condenser system consisting of condenser lenses and an aperture in sequence. A fine probe (<< 1nm) is scanned across the sample using deflection coils. Upon scanning the electron beam across the sample, a variety of scattered signals can be detected as a function of probe position. The scattered electrons can be detected in bright-field (BF) or dark-field (DF) mode, depending on the angle of investigation.

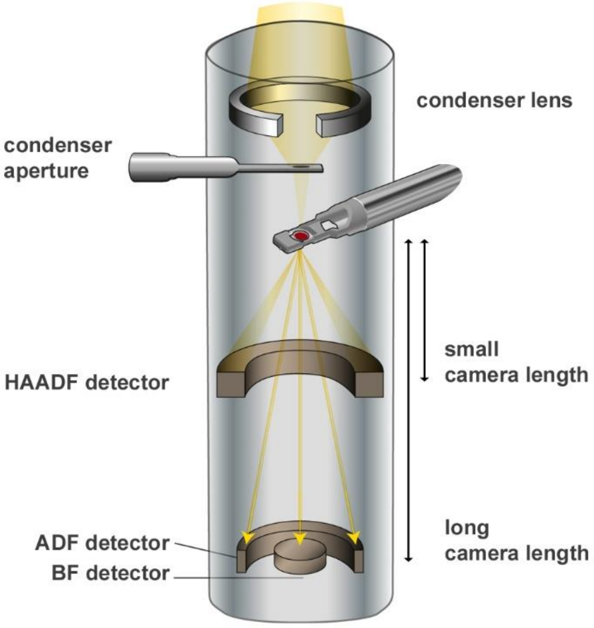

Figure 3-7: Schematic illustration of a TEM in STEM mode [111]

When electrons are scattered at relatively low angles with respect to the optic axis (< 10 mrad), they are detected by the bright-field detector. The annular dark-flied detector is used for the detection of electrons at higher angles (10 mrad – 50 mrad), followed by the high angle annular dark-field detector that collects electrons at the highest angles (> 50 mrad). The collection of electrons at different angles can be achieved by adjusting the physical camera length of the detector and increases from the HAADF to ADF to BF detector. Since the HAADF detector collects high angle scattered electrons which pass closer to the atomic nucleus in the sample due to Rutherford scattering and contain elemental information, its signal is proportional to the thickness of the sample and Z^n, with Z the atomic number, and $1.6 < n < 2$.

3.2.3 Energy dispersive X-ray spectroscopy (EDS)

Energy dispersive X-ray spectroscopy (EDS) is a technique which is used for the elemental analysis. When an electron beam interacts with the sample, the electrons from the inner shell can be excited and ejected from that shell. This creates a vacancy and leaves the atoms in a higher energy state. This energy can be lowered by transition of an electron from a higher energy shell. The excess of energy will be released accordingly and can translate itself in two ways. Firstly, a characteristic X-ray can be emitted and its energy is equal to the energy difference between the two shells and is as such characteristic for a specific element (a schematic representation is given in Figure 3-6). Secondly, an Auger electron can be emitted to release the atom's energy excess. In this process, the shell energy difference is used to eject an outer shell electrons, referred to as the Auger electron, instead of emitting an X-ray.

In combination with SEM imaging, an elemental map can be obtained by measuring an EDS spectrum for each pixel. It can also be combined with STEM, as illustrated in Figure 3-8, where a HAADF-STEM image is shown, along with the EDS map of Cu and Ag. Overlaying the Cu and Ag map show the presence of Ag at the Cu nanoparticle surface.

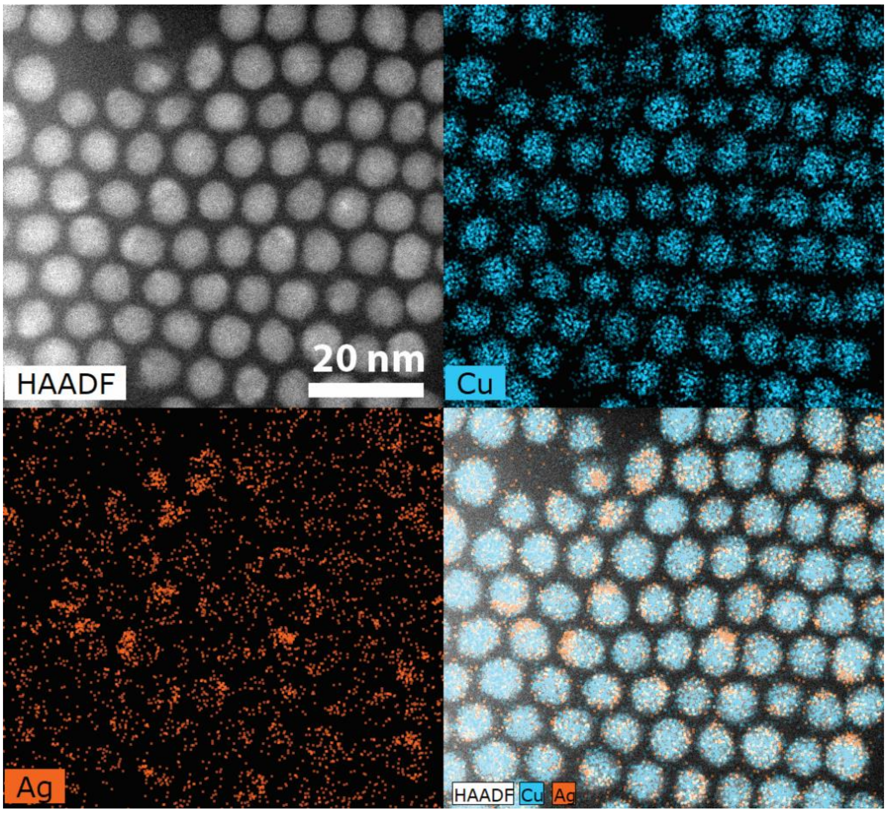

Figure 3-8: EDS mapping of Cu-Ag bimetallic nanoparticles

3.2.4 Electron tomography

Despite the fact that atomic resolution can be reached using STEM, characterization of nanoparticles is still hampered because conventional STEM imaging only provides 2D images of a 3D object. These 2D projections complicate the interpretation of the morphology when more complex structures are analyzed and can lead to wrong conclusions. A lego sculpture, referred to as A B C, by John V. Muntean, is shown in Figure 3-9 represents this concept. Here, a projection of a 3D object is taken under different angles, where every angle leads to another projection. It gives the impression, the object is an A, B or C, but in fact it is none of them. This problem also arises with analyzing nanomaterials during 2D STEM imaging. A possible solution to this problem is to use electron tomography to reconstruct a 3D image using 2D images obtained over different angles.

Figure 3-9: Magic angle lego sculpture A B C, by John V. Muntean

An electron tomography experiment is conducted by acquiring 2D projections over an angular range as large as possible (typically ± 80°), starting at the angle closest to -80°. These projections should meet the projection requirement, where the intensity in the image is a monotonic function of a property of the sample [112]. Therefore, imaging of the sample is often performed in HAADF-STEM mode, since the intensity of a HAADF-STEM image scale proportionally with Z^n and the thickness of the sample. Additionally, highly crystalline materials with a high atomic number are strongly scattering and often used in catalyst research, which makes HAADF-STEM most suited.

The 2D projections of the samples are collected with an increment of 1° or 2° and is schematically presented in Figure 3-10. After acquiring the series, the projections are aligned to a common tilt axis to eliminate any shift between the images. Finally, the series is used to reconstruct a 3D image of the specimen of interest by using a mathematical algorithm (Figure 3-10).

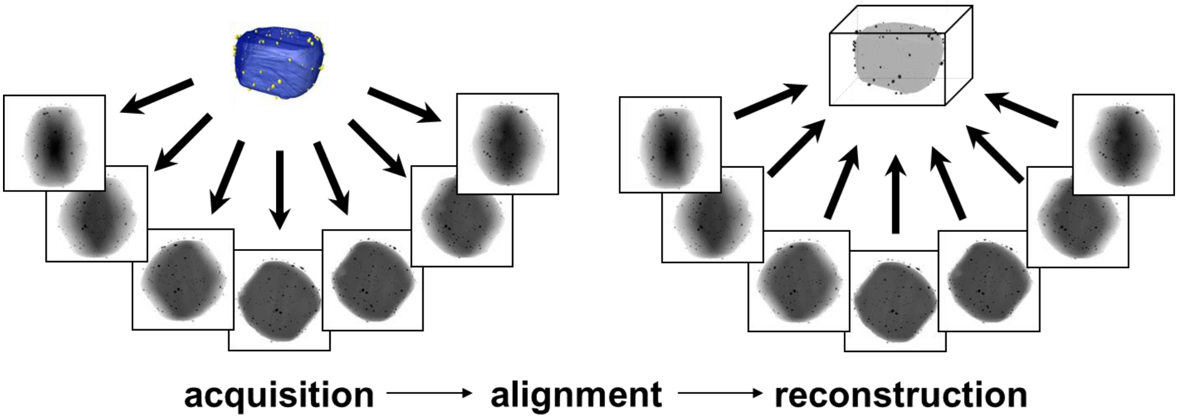

Figure 3-10: Illustration of an electron tomography experiment where 2D images under different angles are acquired, aligned and the 3D images is reconstructed

Tomography was first described by Johan Radon in 1917 [113]. Mathematically, the reconstruction is based on the Radon transform, R, is an integral transform. Here, the Radon transform can be obtained by taking the line integral of an object f(x,y) through all possible lines L with unit length ds.

$$Rf = \int_L f(x,y)ds \tag{3.5}$$

Experimentally, the Radon transform represents the acquirement of the projections of an object under different angles. The inverse Radon transform of the projections represents the original object f(x,y). Since a limited amount of projections are taken, the inverse transform will always be imperfect. Different reconstruction methods can be used. An iterative technique referred to as expectation maximization (EM) is used in this work.

The EM algorithm estimates the probability of the calculated 3D structure being the unknown object, given the acquired tilt-series. This algorithm is based on the Bayes theorem (Equation 3.6).

$$\mathbb{P}(\Theta|p) = \mathbb{P}(p|\Theta)\frac{\mathbb{P}(\Theta)}{\mathbb{P}(p)} \tag{3.6}$$

Where $\mathbb{P}(\Theta|p)$ is the probability of Θ being the unknown object, given its projections p, $\mathbb{P}(p|\Theta)$ is the probability of observing the projections p, given Θ and is referred to as a-priori probability or likelihood. $\mathbb{P}(\Theta)$ and $\mathbb{P}(p)$ defines the probability distribution of Θ and p, respectively. An estimate of the object Θ can now be reconstructed by maximizing the probability (Equation 3.7).

$$\hat{\Theta} = arg\,\max_{\Theta}\mathbb{P}(\Theta|p) \tag{3.7}$$

In practice, the log of the probability is maximized (Equation 3.8).

$$\Theta" = arg\,\max_{\Theta} log\big(\mathbb{P}(\Theta|p)\big) \tag{3.8}$$

In principle, the EM algorithm retrieves the unknown object Θ by maximizing the log of the probability. Therefore, the algorithm operates in two steps, namely the expectation (E) step and the maximization (M) step. During the E-step, the expected value of the log-likelihood is calculated, given the projections p and the current parameter estimate of Θ. Subsequently, the log-likelihood is maximized by adjusting those parameters in the M-step.

In this work, electron tomography is used to characterize Cu@Ag core-shell nanoparticles in Chapter 7. The degradation process of Cu@Ag core-shell nanoparticles is visualized and linked to the product distribution during the eCO_2R experiments.

3.3 Electrocatalyst synthesis techniques

A meticulous method for obtaining catalysts with certain specifications is a key aspect for studying and employing them in several electrocatalytic applications. As previously mentioned, the material of the catalyst can have an influence on the conversion efficiency of a reactant. Furthermore, the morphological characteristics can severely influence the selectivity of a reaction. It is highly desired to obtain monodisperse catalyst particles with large EASA and a homogeneous coverage over a large area of the supporting material.

Several techniques such as thermal decomposition and electrodeposition can be used to produce monometallic catalysts. For the introduction of a more noble metal, galvanic displacement can be chosen. These techniques are used in this work to synthesize nanoparticle electrocatalysts for the eCO_2R and are therefore discussed in more detail in what follows.

Electrodeposition is a technique that relies on the application of a constant negative potential or current. Using this technique ensures the direct contact of the catalyst with the support and therefore assures good electrical contact. By applying potential or current pulses, metal ions in the solution will be converted at the charged surface into their metal form and subsequently grow into nanoparticles.

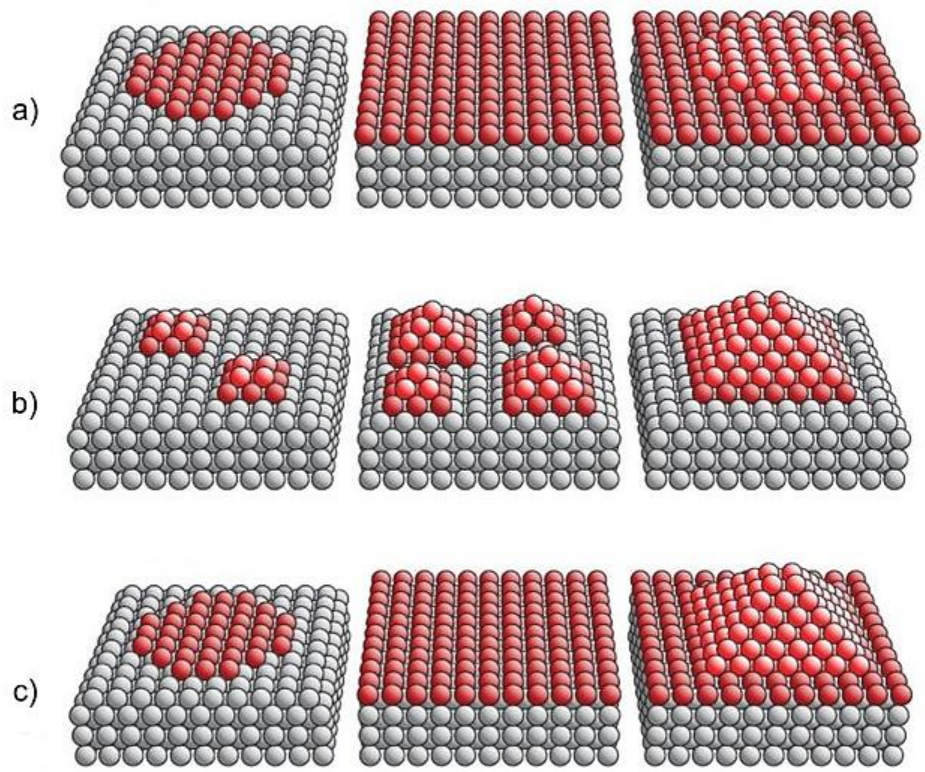

Figure 3-11: Illustration of the growth modes (not to scale); (a) Frank-van der Merwe, (b) Volmer-Weber and (c) Stranski-Krastanov

The growth of a particle can proceed through three different modes, as presented in Figure 3-11. The first type is the Frank-van der Merwe (or layer-by-layer) growth mode, where the crystallographic misfit between the substrate and the deposit is negligible. This results in strong interaction of the substrate with the deposit. If the crystallographic misfit becomes significant, the deposition of several monolayers is initiated, but due to the occurrence of strain, the growth of 3D crystals (which are unstrained) becomes favorable. This is called Stranski-Krastanov growth mode. Increasing the misfit even further, the interaction between substrate and deposit becomes unfavorable and the metal-metal interactions become more pronounced. This results in the 3D island growth and is called the Volmer-Weber growth mode [114]. The latter is preferred when nanoparticles with high surface-to-volume ratios are desired, which is thus preferred for our purpose.

The challenge this technique faces, is to separate nucleation and growth in time, such that small and monodisperse particles can be obtained. For this reason, it is important to make a distinction between single – and dual pulse electrodeposition. During the single pulse deposition, the nucleation and growth takes place at the same time. This can possibly lead to the deposition of particles with different sizes.

In order to gain more control during electrodeposition, the dual-pulse mode was introduced. Here, two subsequent pulses are applied, separating nucleation and particle growth (Figure 3-12).

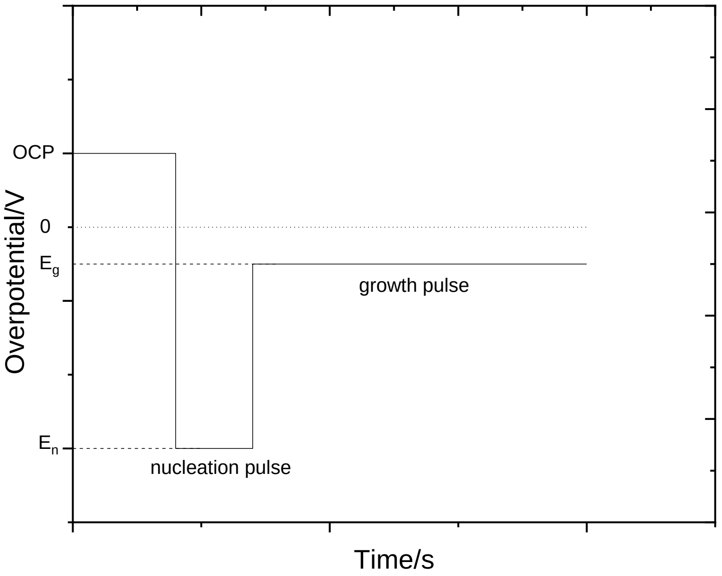

Figure 3-12: Scheme of dual-pulse electrodeposition.

During the first pulse, a negative potential is applied for a short amount of time, leading to deposition of nuclei on the surface. Subsequently, in the second pulse, a less negative potential for a longer amount of time is applied. This enables the nuclei to grow but no new nuclei to form. This approach allows an improved control over the monodispersity of particles because one is able to fine-tune the deposition by varying nucleation and growth potential and nucleation and growth time. The use of electrodeposition has increased over the last years because it provides many tunable parameters such as applied potential or current, time, temperature and electrolyte composition. The disadvantage upon using this technique is the influence of the substrate on the deposition quality [115]. The roughness can have a great influence on the reproducibility, as will be discussed in Chapter 4.

Thermal decomposition is used as a synthesis technique where a compound breaks down upon heating. This happens at high temperatures, since most of these reaction are endothermic as heat is required to break bonds. In this study, a metal precursor along with a capping agent are dissolved in an organic solvent. The capping agent regulates the growth of the particles and by adjusting the ratio of capping agent vs. precursor, the particle size can be adjusted. Additionally, the binding strength between capping agent and precursor influences the monodispersity of the particles [116]. In this study, tetradecylphosphonic acid (TDPA) is used to ensure monodispersity of the particles. During the synthesis, TDPA and Cu form an intermediate polymer lamellae (Figure 3-13, due to nano-segregation of the ligand [117]–[119]), which is crucial for size focusing and monodispersity, indicating the fundamental role of TDPA in the pre-nucleation stage.

The synthesis is a very robust method owing to the slow growth rate that is achieved when using TDPA as a surfactant as compared to others [120]. This slow growth rate originates from the strong binding abilities of TDPA with the Cu-precursor.

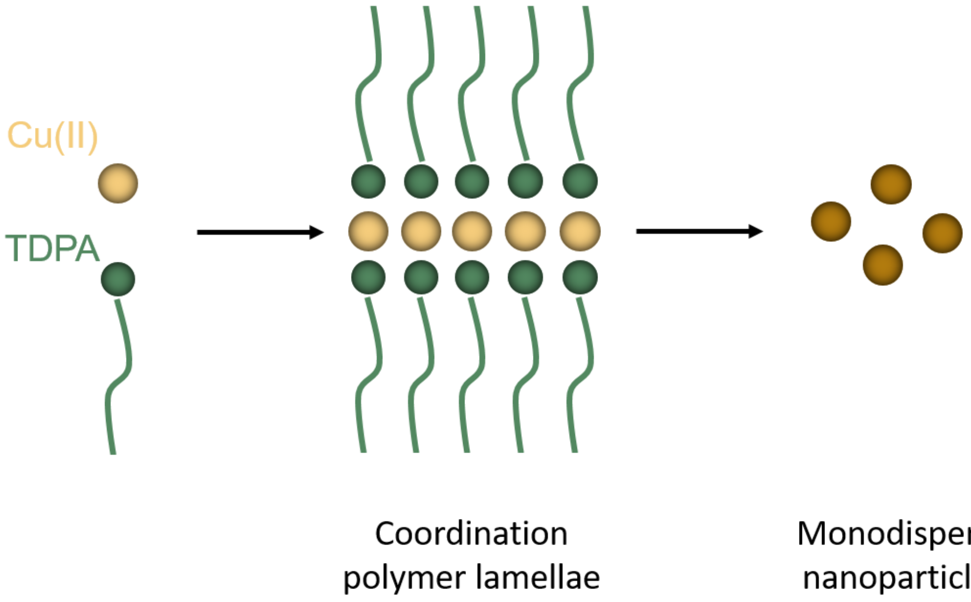

Figure 3-13: Formation of polymer lamellae during the thermal decomposition

This method is widely used because it is a straight forward and robust method and the synthesis can easily be upscaled making this an attractive route. The advantage compared to electrodeposition is the absence of a substrate and therefore the synthesis of the catalysts is not influenced by its nature.

Galvanic displacement is a natural occurring process and takes place when a base metal is replaced by an ion (present in the solution) having a higher reduction potential than the metal ion which is being replaced [121].

Galvanic displacement is used in this study to cover Cu NPs with an Ag shell (Figure 3-14). Cu atoms at the surface are being replaced by Ag ions in the solution. This means that Cu (E^0 = 0.34 V) metal atoms are oxidized and dissolved and Ag (E^0 = 0.779 V) ions are reduced and deposited onto the remaining Cu NP surface.

$$Cu \rightarrow Cu^{2+} + 2e^- \tag{3.9}$$

$$2Ag^+ + 2e^- \rightarrow 2Ag \tag{3.10}$$

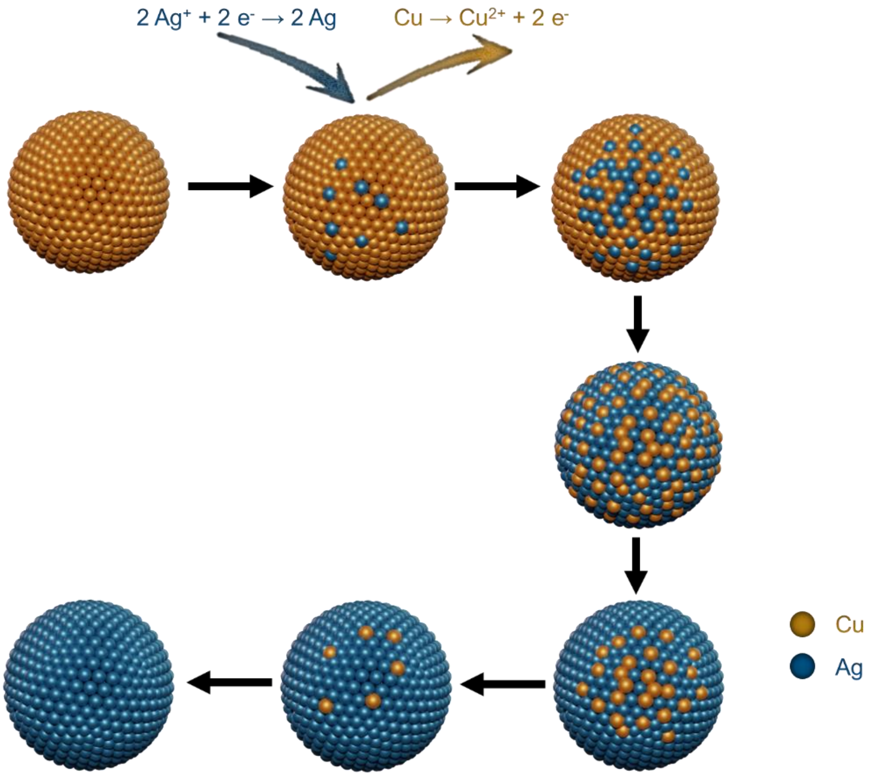

Figure 3-14: Illustration of the principle of galvanic displacement between Cu and Ag

Galvanic displacement allows the synthesis of thin bimetallic interfaces. Since Cu and Ag are almost immiscible, it enables the synthesis of nanodimers and core-shell catalysts.

PART II

Cu-Ag bimetallic catalysts for the CO_2 reduction

CHAPTER 4:

Electrodeposition of Cu nanoparticles on rough surfaces

This chapter presents the electrodeposition of Cu (nano)particles on a gas diffusion electrode. The possible effect of pre-treating the GDE with respect to the deposition of a catalyst is investigated. First, the GDE surface is pre-treated with four different solutions to improve its hydrophilicity. The impact of the GDE pre-treatment on the size and morphology of the nanoparticles is then investigated. Additionally, the effect of the dual pulse parameters on the size and distribution will be investigated on the pre-treated GDE. Finally, the stability of electrodeposited Cu, under electrochemical conditions, is compared to spray-painted Cu GDEs.

This chapter has been published as: L. Pacquets, E. Irtem, S. Neukermans, N. Daems, S. Bals, T. Breugelmans, Size-controlled electrodeposition of Cu nanoparticles on gas diffusion electrodes in methanesulfonic acid solution, *Journal of Applied Electrochemistry*, (51) 2021, 317-330.

All electrochemical measurements were performed by Lien Pacquets.

4.1 Introduction

Electrocatalysis related to CO_2 reduction and its potential to combat global warming was described in Chapter 1. It was noted that depending on the catalyst material, the product distribution could be altered [122]. Additionally, the importance of particle size, morphology and alloying was highlighted. The main objective of this PhD research will be to synthesize Cu-Ag bimetallic nanoparticles, since they are known to improve CO production. Therefore it will be important to synthesize monodisperse Cu cores in a reproducible manner, such that they can serve in a later stage as the basis to obtain the Cu-Ag bimetallic nanoparticles. In this chapter, the aim is to synthesize monometallic Cu nanoparticles with a particles size preferably below 10 nm, as within this range, the surface-to-volume ratio and the electronic effects come into play.

The Cu cores will be synthesized by electrodeposition. This technique has drawn a lot of attention because it enables good control over the synthesis process, which is a key factor in catalyst optimization. Using this approach, one or more negative potentials are applied in order to reduce the Cu ions, in the electrolyte solution, into Cu metal on the substrate. By changing the applied potential, the particle size and distribution can be tuned.

In addition to the deposition method, the nature and the structure of the support play an important role in determining the morphology of the nanoparticles. Most of the literature studies report the use of glassy carbon (GC) electrodes as support for copper electrodeposition [123]–[126]. However, for industrial applications (e.g. fuel cells [127] or biosensors [128]), a popular approach is to replace GC electrodes with gas diffusion electrodes (GDEs) [127]–[134]. The advantage of using gas diffusion electrodes (GDEs) instead of glassy carbon relies on its large resulting surface area because deposition inside the carbon paper is also possible. Additionally, it allows a better supply of CO_2 to the catalyst surface. Therefore, we aim to synthesize monodisperse Cu nanoparticles on a rough surface, in a reproducible manner.

Since a GDE is hydrophobic, the surface is pre-treated to increase its hydrophilicity and to improve the deposition of Cu. To elucidate the impact of this pre-treatment and thus hydrophilicity on the Cu deposition, the CV measurements, surface pH and SEM images were analyzed. The effect of the pre-treatment on the nucleation mechanism was analyzed. Subsequently, the size of the Cu (nano)particles was altered by varying the dual pulse parameters and its EASA was compared to single pulse deposited particles. Finally, the stability of the electrodeposited Cu was evaluated compared to spray-painted Cu to investigate the benefit of using electrodeposition as synthesis method.

4.2 Experimental

4.2.1 Chemicals

Copper sulfate pentahydrate ($CuSO_4.5H_2O$, 99 %) was purchased from Riedel-de Haën. Methane sulfonic acid (MSA, 70 % aq. sol.) were purchased from Alfa Aesar. Triton ® X-100 (TX100) was purchased from Acros organics. Nitric acid (HNO_3, 70 % aq. sol.) and sodium hydroxide (NaOH, pellets) were purchased from Chem-lab and Sigma-Aldrich, respectively. All solutions were prepared in ultra-pure water (MQ, Milli-Q grade, 18.2 MΩ cm), previously purged with argon prior to deposition

4.2.2 Electrochemical set-up

The electrodeposition of Cu was performed in a 4-electrode set-up, where a WE (4 cm^2) consisting of carbon paper (Toray paper) was placed in between 2 CEs (8 cm^2) made of carbon paper (Sigracet ® 39 AA). A saturated Ag/AgCl RE was positioned next to the WE. The measurements were performed with a Bio-logic VSP-300. All potentials applied in the experiments were derived from cyclic voltammetry (CV) measurements.

4.2.3 Preparation of the GDE

Before the synthesis of Cu on a GDE, a surface modification of the GDE was applied to ensure a higher hydrophilicity and thus an easier deposition. Therefore, the GDEs were treated with either MQ, 0.1 M acid (HNO_3), 0.1 M base (NaOH) or 10 mM surfactant (TX100) for 24 h at room temperature after which the proper surface treatment was selected for further experiments. The GDEs were washed 3 times with MQ and dried in a desiccator.

The dual pulse experiments, which consisted of 2 consecutive pulses, were carried out in a solution containing 10 mM $CuSO_4$ (as often used in literature [135]–[137]) and 2 M methane sulfonic acid (MSA) (essential to maintain an acidic environment to avoid Cu oxidation and an eco-friendly alternative for the commonly used H_2SO_4, i.e. reduced toxicity and biodegradable [125], [138]–[141]). In the first pulse, the nucleation pulse, the potential is stepped from open circuit potential (OCP, where no reaction occurs) to a potential negative enough to deposit Cu nuclei onto a substrate. In a second pulse, called the growth pulse, the nuclei of the first pulse grow at a potential more positive to the first one (resulting in less driving force), which inhibit the formation of new nuclei. Besides using TX100 during the pre-treatment of the GDE, it can also be added to the deposition solution of Cu. The addition of TX100 into the deposition solution, results in the deposition of Cu inside the HNO_3 pre-treated GDE. This ensured an even better Cu coverage in the interior of the GDE.

Once the optimal pre-treatment was selected, the impact of the deposition parameters, both the nucleation pulse as well as the growth pulse parameters were altered to investigate their impact on the resulting material. At first, the nucleation potential (E_n) was varied between -0.5 V and -1 V. The nucleation charge (Q_n) was kept constant at -28.2 mC (≈ nucleation time of 1 s). The growth potential (E_g) and growth charge (Q_g) were altered between 0.05 V and 0.1 V and -67.5 mC, -135 mC and -270 mC, respectively.

4.2.4 Electrochemical and electrode surface analysis

Differences in pre-treatment of the GDE on the Cu electrodeposition mechanism were first analyzed by CV measurements, within a potential range of -0.7 V and 0.7 V, with a scan rate of 50 mV s^{-1}. Next, the nucleation mechanism of the Cu electrodeposition on pre-treated GDEs was studied using CA experiments. The potential was stepped from the open circuit potential (OCP) to -0.3 V with a charge of 2.18 C. Both experiments were performed in a solution containing 0.1 M $CuSO_4$ and 2 M MSA.

Additionally, the point of zero charge of the GDEs was determined after pre-treatment using the pH drift method, also called the solid addition method [142]. This allowed us to determine whether the surfaces were positively or negatively charged, which led to a possible explanation for the shift in the CV curves that could be observed experimentally. Therefore, solutions of 5 mL of 0.01M NaCl were bubbled with argon to remove the dissolved CO_2. The pH of the solutions was adjusted between 6 and 11 with an increment of 1 using 0.01 M HCl and NaOH. An amount of 15 mg of pre-treated carbon paper was added and the solution was stirred for 24 h. The final pH was plotted against the initial pH. The intersection point of this curve with the reference curve is considered the point of zero charge. The reference curve is a straight line where final pH and initial pH coincide.

An FTIR spectrum of the TX100 pre-treated GDE was recorded between a wavelength of 399 cm^{-1} and 4000 cm^{-1}. The GDE used was pre-treated with a 0.05 M TX100 at 80 °C. This was necessary because the GDE needed to be crunched, mixed with KBr and pressed into a tablet.

The EASA was calculated by performing capacitance measurements using cyclic voltammetry. GDE3 (Table 4-1) was used as an example of the dual pulse technique. As benchmark single pulse electrodeposition was used to calculate the relative EASA and was performed in a 10 mM $CuSO_4$ and 2 M MSA solution (purged with Ar) applying -0.5 V vs. Ag/AgCl sat. to deposit a loading of -0.096 C. Different CV measurements were performed at scan rates going from 150 mV s^{-1} to 25 mV s^{-1} with an increment of 25 mV s^{-1} within a potential range of ± 40 mV vs. OCP. The experiment is also performed on the blank GDEs before depositing any Cu to eliminate the difference in capacitive current between different GDE electrodes. The current obtained during this experiment is subtracted from the measured current after depositing Cu onto the GDE. Hereafter, the current at OCP (of the second cycle) was plotted against the scan rate. The slope of the trendline is a measure of the EASA.

Surface morphology and changes in particle size were studied with a scanning electron microscope (SEM, FEI Quanta 250) at 5 kV using secondary electrons.

4.2.5 Stability test

The stability of electrodeposited Cu on the GDE surface, with a loading of 0.18 mg cm^{-2}, was tested by applying a constant potential of -1.0 V vs RHE for 4 hours in a solution of 0.5 M $KHCO_3$ (saturated with CO_2), using an H-type cell at room temperature. These results were compared to spray-painted Cu on GDE, with a loading of 0.2 mg cm^{-2}. Cu was spray-painted using a solution of Cu (Sigma Aldrich 14-25 µm) and isopropanol (IPA).

After the experiment, the electrolyte samples were diluted 10 times and adjusted to 1 % HNO_3 (Merck, Suprapur). The acidic solutions were analyzed via inductive coupled plasma mass spectrometry (ICP-MS, Agilent 7500).

4.3 Results and discussion

4.3.1 Influence of the pre-treatment of GDE

Figure 4-1 shows the first cycle of the CV experiments for the HNO_3, MQ, NaOH and TX100 pre-treatments. Shifts in the peak potential of Cu are observed, which is a significant indication that the pre-treatment has an effect on the electrodeposition of Cu on GDE. The HNO_3, NaOH and TX100 pre-treatments can be compared to the MQ pre-treatment, which functions as benchmark. The use of HNO_3 results in a positive potential shift, from -0.28 V to -0.22 V, compared to MQ, due to the fact that carboxylic groups are present at the GDE surface after the acid treatment [143]–[145]. These groups could possibly enhance the surface hydrophilicity, leading to a smoother electrodeposition of Cu on these surfaces. For TX100, a negative shift (from -0.28 V to -0.34 V) is observed compared to MQ. NaOH has the same effect as TX100 and again a negative shift (from -0.28 V to -0.32 V) is found.

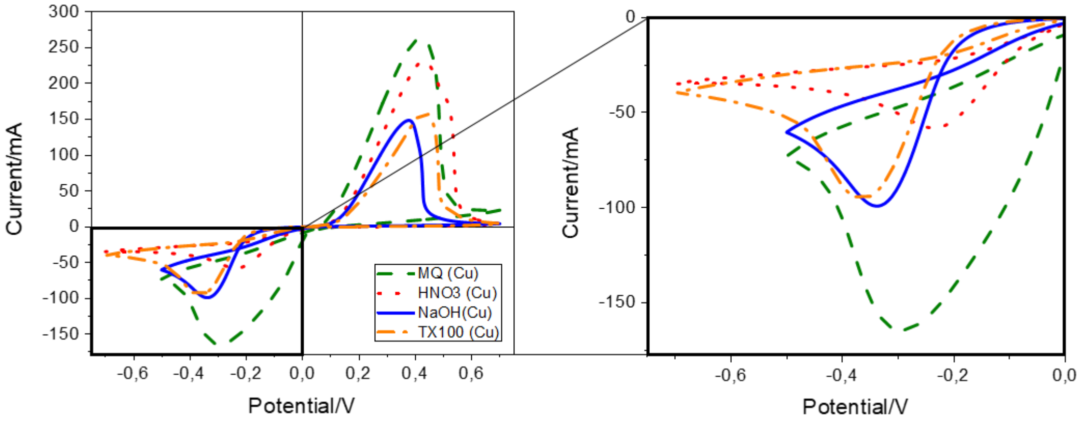

Figure 4-1: First cycle of CV measurements of MQ (dashed), HNO_3 (dotted), NaOH (solid) and TX100 (dash dotted) treatment with a scan rate of 50 mV s^{-1} (potential are plotted vs Ag/AgCl saturated)

Surface pH measurements (Figure 4-2) indicate that when using NaOH and TX100, the point of zero charge is located at pH 8.0 and pH 7.8, respectively. The Cu deposition solution has a pH lower than 1, inducing a positively charged surface, which results in the repulsion of Cu-ions and thus explains the need for a more negative potential to initiate the deposition of metallic Cu. Comparing this to HNO_3, which has a surface pH of 2.7, we can conclude that the surface, in case of HNO_3, will have a negative charge compared to TX100 and NaOH. This could indicate that the copper ions can encounter less repulsion in this case, which confirms the results of the CV measurements, as they indicated that a less negative potential is necessary for HNO_3. To summarize, a positive shift in peak potential is observed when using HNO_3 compared to MQ because of the negatively charged surface of the GDE due to its pre-treatment as such attracting the Cu-ions. The negative shift of TX100 and NaOH can potentially be explained by the more positively charged surface, which causes the repulsion of the positive Cu-ions resulting in the need for a more negative potential to reduce Cu-ions to metallic Cu on the GDE surface. Nevertheless, it should be noted that the roughness of the surface can have a significant effect on the electrodeposition as well. The defects at the surface caused by the roughness can contribute to a difference in nucleation of Cu.

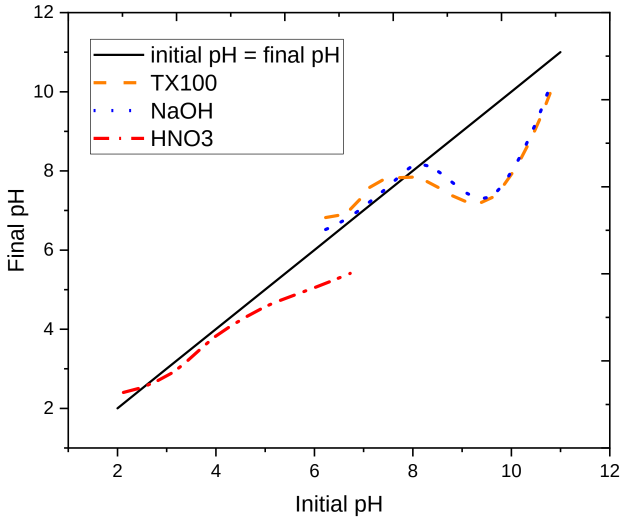

Figure 4-2: Determination of point of zero charge of TX100 (dashed), NaOH (dotted) and HNO3 (dash dotted) pre-treated GDEs in a pH range of 2 to 11 with an increment of 1

In addition to the electrodeposition potential, the current density at the peak potential is an important parameter since it is directly related to the amount of deposited Cu. When comparing these peak current densities for the different pre-treatments, it can be observed that HNO_3 displayed a threefold drop in current density with respect to MQ. In case of NaOH and TX100, only a twofold drop in current density was perceptible. These lower current densities might be caused by the functional groups present at the surface as they can potentially inhibit the interaction of Cu with the surface. We hypothesize that Cu-ions are less abundant in the visinity of the eletrode surface, resulting in a lower current compared to the MQ blank.

In case of NaOH and HNO_3, a shoulder is present on the anodic peak, which would be attributed to the desorption of Cu from the surface after specific adsorption of Cu-ions during the reduction peak. During the CV measurements, a nucleation loop (NL) is present in case of NaOH and TX100. The NL appears in the potential range where nucleation occurs and is characterized by a cross over between the forward and reversed scan and where the current in the reversed scan is higher (more negative) than in the forward scan [146]. This is a typical behavior for the deposition of metallic Cu nuclei on a foreign (in this case GDE) surface and indicates that the deposition of Cu is easier on the already present Cu nuclei in comparison to the bare GDE substrate. The fact that only NaOH and TX100 exhibit such a NL is caused by its positively charged surface, which obviously repels the positive Cu ions. Once some Cu nuclei are formed, deposition will become easier on this growing nuclei explaining this loop. For the HNO_3-treated GDE this NL is not found as the positive Cu ions are attracted to the negatively charged surface making its deposition favorable from the start of the experiment [147].

In order to get a better understanding of the change in morphology, we investigated the nucleation mechanism of the Cu electrodeposition using current-time transient curves. The potential was shifted from an initial value, where no electrodeposition occurred to a potential (-0.3 V) negative enough to induce the electrodeposition of Cu.

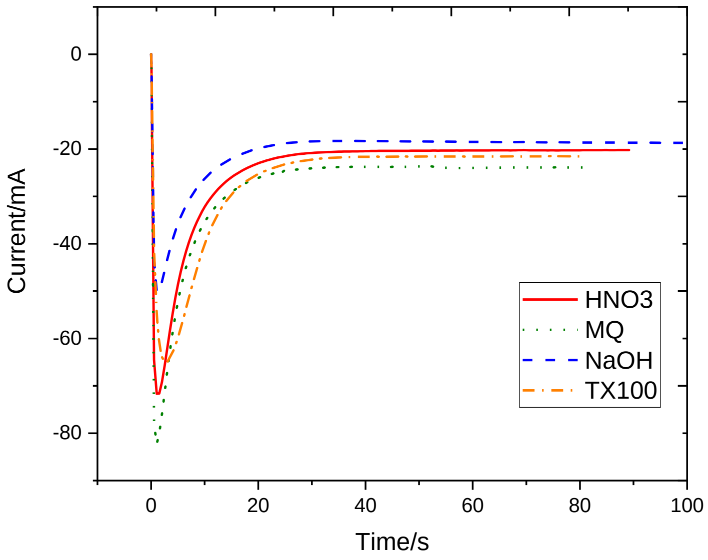

Figure 4-3: Current-time transient curves of Cu electrodeposition on HNO_3 (solid), MQ (dotted), NaOH (dashed) and TX100 (dash dotted) pre-treated GDE

Figure 4-3 shows the current-time transient curves of the Cu electrodeposition using the 4 pre-treatments of the GDEs. The current increases due to the charging of the double layer, the formation of extra nuclei and the increase in size of the nuclei, reaching a maximum in current. A maximum in current is reached within 1 s in case of HNO_3, NaOH and MQ. Using TX100, on the other hand, it took up to 3 s to reach a maximum in current. After this point, diffusion zones start to overlap (deposition rate slows down), which results in a reduced surface area, leading to a decrease in current because of the transition to planar diffusion of Cu-ions to the growing islands [148]–[150]. The difference observed for TX100 in comparison to the other 3 pre-treatments (longer time to maximum current) might indicate the existence of another (slower) nucleation mechanism for TX100, which will be elaborated later on [151].

To determine the nucleation mechanism, the current-time transient curves were normalized and compared to the Scharifker-Hills model [152] using equation 4.1 and 4.2. According to this model, the nucleation can occur either through an instantaneous process or through a progressive route. The following equations describe the nucleation process for 3D nucleation with crystal growth dominated by localized hemispherical diffusion.

$$\left(\frac{i}{i_m}\right)^2 = \frac{1.9542}{\frac{t}{t_m}}\left(1 - e^{-1.2564\frac{t}{t_m}}\right)^2 \textit{(instantaneous nucleation)} \qquad 4.1$$

$$\left(\frac{i}{i_m}\right)^2 = \frac{1.2254}{\frac{t}{t_m}}\left(1 - e^{-2.3367\frac{t}{t_m}}\right)^2 \textit{(progressive nucleation)} \qquad 4.2$$

Where I is the current, I_m is the maximum current, t is time and t_m is the time at the maximum current. As can be observed in Figure 4-4, the transients from the experimentally obtained curves for MQ, HNO_3 and NaOH are in good agreement with the theoretically calculated curve for instantaneous nucleation, although a small deviation for NaOH is observed. This means that for all 3 cases, the nucleation occurs immediately at the beginning of the electrodeposition and no new nuclei are formed during the rest of the experiment. The experimental curve of TX100 overlaps with the progressive model, meaning nucleation proceeds via progressive nucleation, where nuclei are progressively formed throughout the experiment, and thus nucleation also occurs at later stages during the electrodeposition. This can be explained as follows. During the TX100 pre-treatment, long carbon chains are adsorbed on the GDE surface. If we analyze the FTIR spectrum of a TX100 pre-treated GDE in Figure S 4-1, 2 peaks at 2870 cm^{-1} and 2960 cm^{-1} are observed indicating the presence of methyl groups. These methyl groups are present in the TX100 molecule at the end of the molecular structure thus proving the presence of TX100 at the GDE surface. These carbon chains could potentially block the surface, potentially inhibiting the interaction of Cu-ions with the surface. Consequently, Cu-ions are less abundant in the visinity of the eletrode surface. At a high enough deposition time, the transient starts to approach the curve of instantaneous nucleation. At that point, diffusion zones are overlapping and the formation of new nuclei becomes impossible at these zones [153].

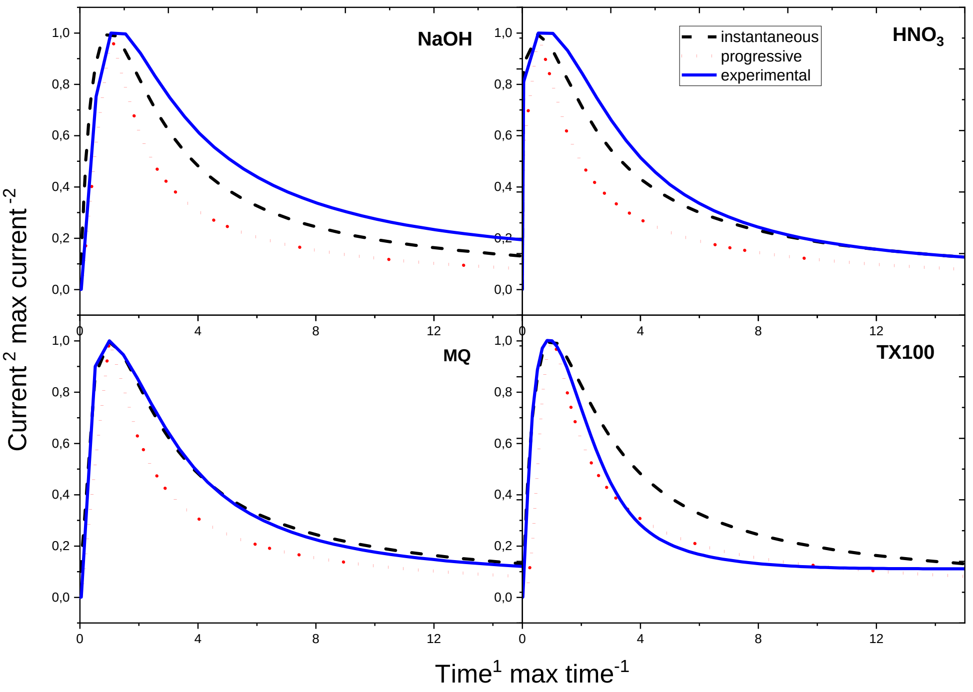

Figure 4-4: Non-dimensional i^2 i_m^{-2} vs. t t_m^{-1} of the current-time transient curves, shown in Figure 4-3, compared to the theoretically calculated curve of instantaneous and progressive nucleation

As evidenced by Figure 4-4, TX100 follows another nucleation mechanism than HNO_3, MQ and NaOH. This is caused by steric hindrance and manifests itself in the growth of alternate morphologies as clearly visible in the SEM images (Figure 4-5). Major changes are perceived between TX100 and the other pre-treatments, which results in the electrodeposition of hemispherical particles (1.7 µm ± 0.04 µm, Figure 4-6 D), consisting of smaller cubic shaped particles (200 nm) as opposed to the spherical shaped particles that were observed for the other pre-treatments (indicated by the arrows). It is clear that the use of TX100 limits the growth in certain directions by preventing certain facets from growing and at the same time promoting the growth of those facets that are not limited by the presence of TX100. This in turn results in the production of specifically shaped particles, or in this case where the growth of cubes is promoted.

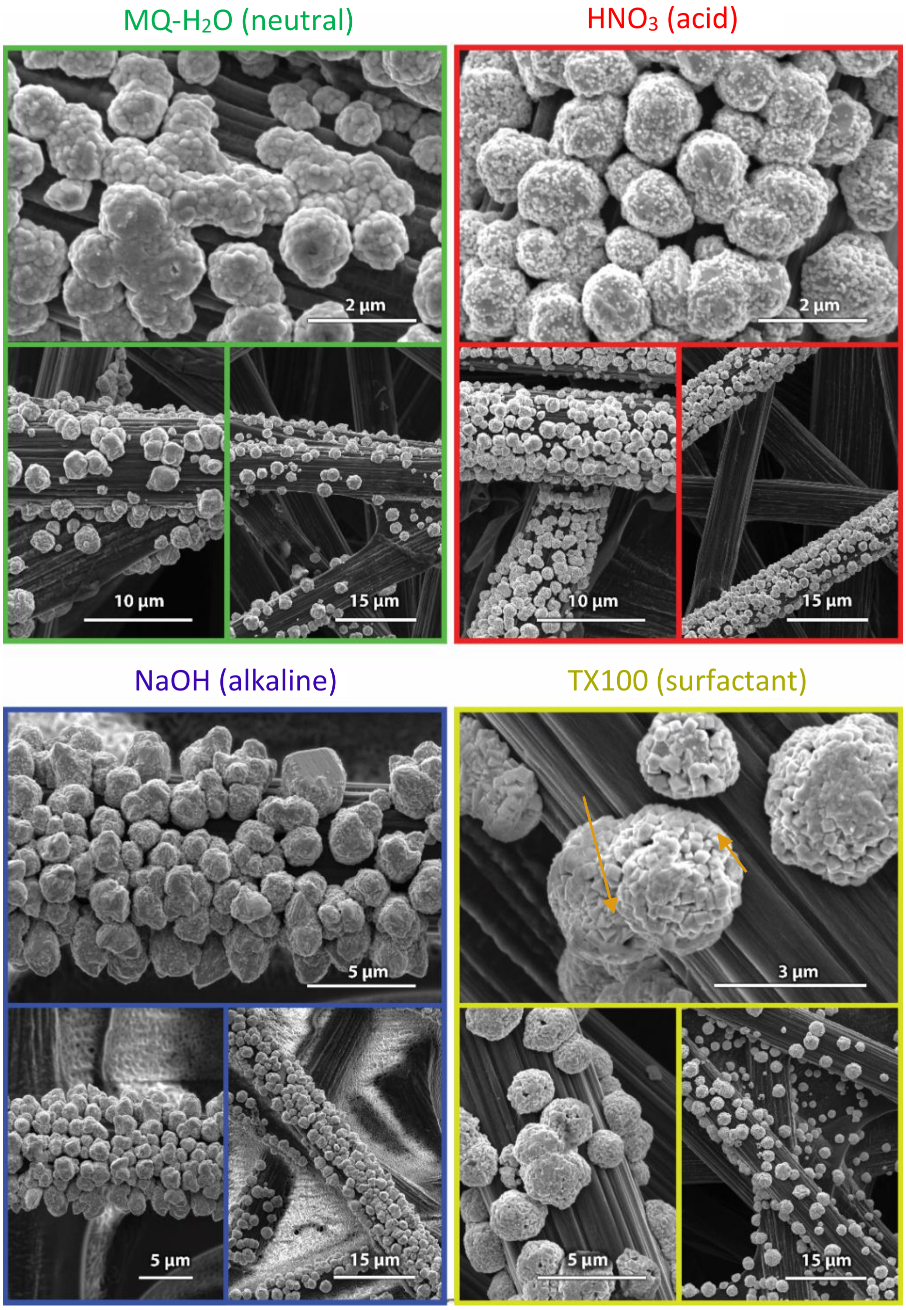

Figure 4-5: Impact of surface pre-treatment on the electrodeposition of copper particles: single pulse electrodeposited Cu on MQ (neutral); HNO_3 (acid); NaOH (alkaline); TX100 (surfactant) pre-treated GDEs. Pre-treatment with MQ leads to particles with a smooth surface and a particle size of 0.8 µm; pre-treatment with HNO_3 results in a more rough surface and a particle size of 1.0 µm; pre-treatment with NaOH gave more edged particles with a size of 1.8 µm; pre-treatment with TX100 resulted in hemi-spherical particles consisting of smaller cubic particles, these particles had a size of 1.7 µm.

In conclusion, while it is clear that TX100 results in a different, progressive, nucleation mechanism the rationale between this behavior is not as clear. We hypothesize, this can have two potential causes. First, as already mentioned before by decreasing the presence of Cu at the substrate, it can be expected that the formation of nuclei is also delayed when using TX100. Second, it is possible that the growth facets, which are blocked from growing by TX100, allow a slower nucleation and thus lead to the progressive process.

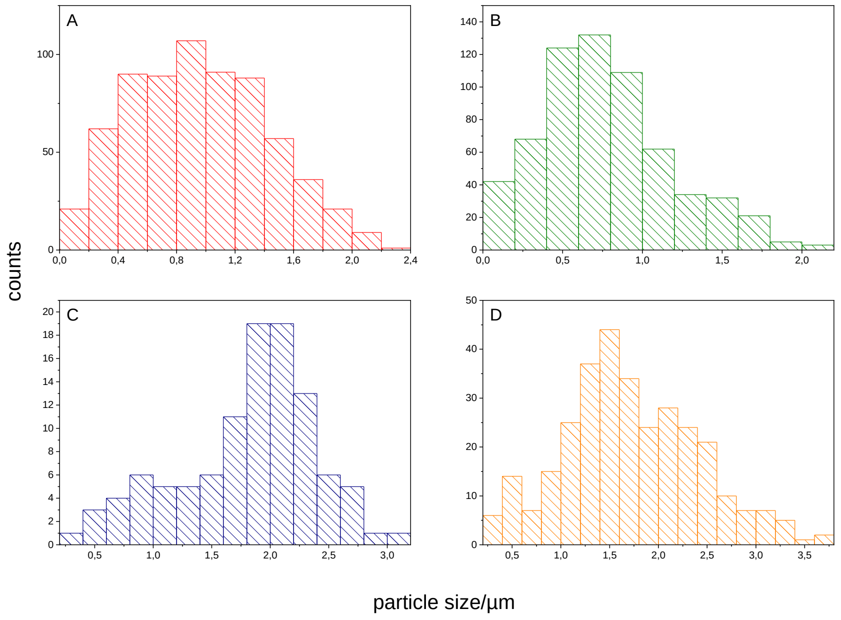

Figure 4-6: Particle size distribution of (A) HNO_3; (B) MQ; (C) NaOH and (D) TX100 pre-treatment

On the contrary, only small changes in morphology exist between the pre-treatments with MQ (0.8 µm ± 0.02 µm, Figure 4-6 B), HNO_3 (1.0 µm ± 0.02 µm, Figure 4-6 A) and NaOH (1.8 µm ± 0.06 µm, Figure 4-6 C), which all proceed through instantaneous nucleation. The particle size using MQ varies slightly compared to HNO_3. The latter gives rise to a more uniform and dense particle distribution. Even more so, it allows deposition of particles on the inner matrix just beneath the surface of the GDE thus results in a better coverage and bigger (active) surface area (Figure S 4-2 and Figure S 4-3). In addition to lower overvoltage requirement, the particles obtained using HNO_3 appear rougher compared to MQ treatment, resulting in an increased surface area which is beneficial for catalytic purposes.

Since the pre-treatment with HNO_3 gives rise to a more homogeneous particle distribution with an increased particle roughness, it was selected as the most optimal pre-treatment and will be further used to investigate the impact of the deposition parameters on the Cu size and distribution.

4.3.2 Dual pulse electrodeposition of Cu on HNO_3 pre-treated GDE

In the first stages of growth it is plausible that the nuclei, formed in the preceding step, grow independently of each other. When the growth evolves, nuclei start to become bigger nanoparticles which eventually can result in the overlap of the diffusion zones of the particles, meaning the particles can no longer grow freely in all directions and will start agglomerating.

The influence of the nucleation potential on the particle size and the particle density is shown in Figure 4-8 A and C. Upon increasing the nucleation potential, more energy is entering the system and more nuclei are deposited at the same time, leading to a greater particle density [137], [148], [154], [155]. More particles are deposited and therefore, the available amount of energy needs to be divided between them, leading to smaller particles. It is clear that the particle density and their size on the electrode surface depend on the nucleation pulse.

Table 4-1: Deposition parameters for the dual pulse deposition of Cu in 10 mM $CuSO_4$ and 2 M MSA

Electrode number	Nucleation potential/V	Nucleation time/s	Growth potential/V	Growth charge/C	Particle size/nm
GDE1	-0.5	1	-0.1	-0.27	148 ± 3
GDE2	-0.75	1	-0.1	-0.27	91 ± 1
GDE3	-0.5	1	-0.1	-0.0675	45 ± 1
GDE4	-0.5	1	-0.1	-0.135	136 ± 3
GDE5	-1	1	-0.05	-0.135	61 ± 2
GDE6	-1	1	-0.1	-0.135	55 ± 1

Comparing GDE1 with GDE2 and GDE4 to GDE6, the average size of the Cu particles is 148 nm (Figure 4-7 A), 91 nm (Figure 4-7 B), 136 nm (Figure 4-7 D) and 55 nm (Figure 4-7 F), respectively.

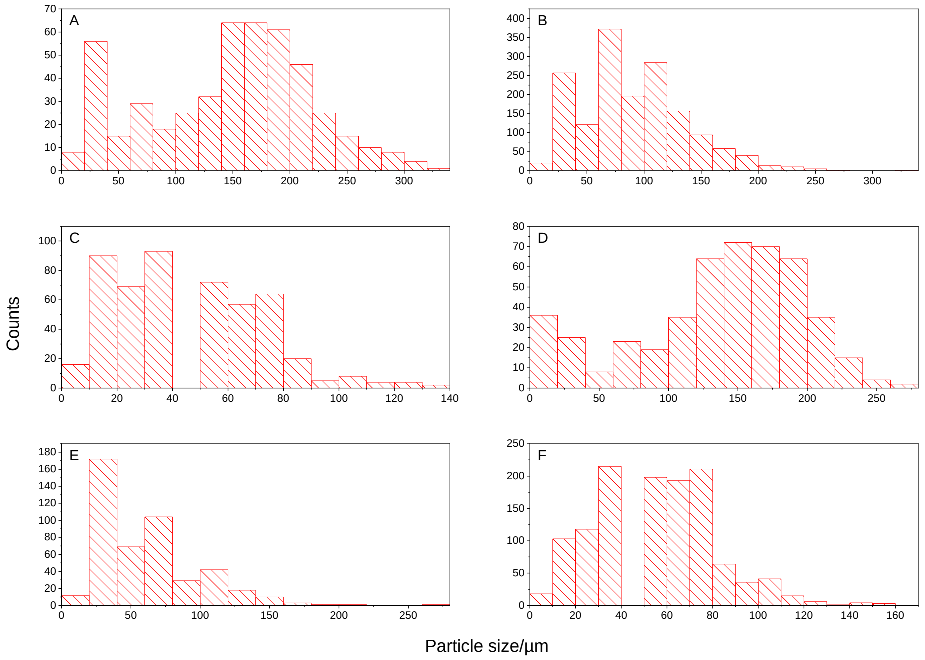

Figure 4-7: Particle size distribution of electrodeposited Cu op HNO_3 pre-treated GDE: (A) GDE1; (B) GDE2; (C) GDE3; (D) GDE4; (E) GDE5; (F) GDE6

This indicates that the particle size decreases with the nucleation potential. Histograms of GDE1, GDE4 exhibit two maxima. This is related with the ability of the particles to aggregate. Small nuclei, which are within a specific radius attract each other, forming first order agglomerates. These same nuclei can also form larger agglomerates, leading to a different particle size [156]. In addition, a higher particle density was observed with a negative increment of the nucleation potential (-0.75 V and -1 V compared to -0.5 V), which partially validates the smaller particle size as the same loading was deposited. Another possible cause for the smaller size is the theory of nucleation and growth of nuclei. This theory states that the radius of a particle is inversely proportional to the nucleation overpotential, meaning more negative nucleation potentials lead to a smaller radius of the nuclei. This is related with the critical nuclei radius, which is larger when using less negative nucleation potentials. As such at more negative potentials, more nuclei will meet the required critical size leading to a higher particle density (and thus smaller particles) on the surface [154], [157]. Smaller nanoparticles are thus obtained using more negative nucleation potentials [158].

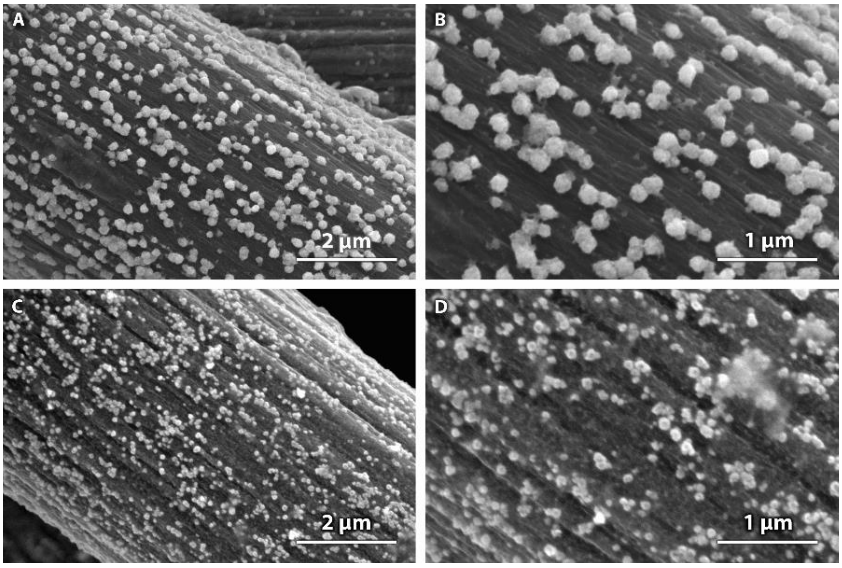

Figure 4-8: SEM images of Cu electrodeposition in MSA on GDE via dual pulse with different nucleation potentials (A, B) GDE1 and (C, D) GDE2

From Figure 4-9 it is clear that the size of the Cu particles alters with the growth charge (which is correlated to the growth time). Considering GDE1, GDE3 and GDE4, the mean radius of the particles enlarged with increasing growth charge (Figure 4-7 A, C and D).

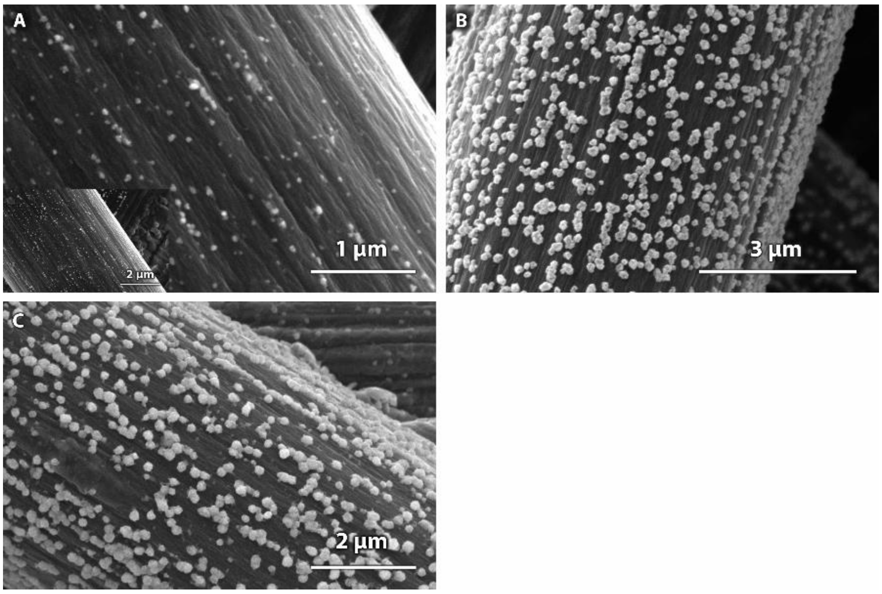

Figure 4-9: SEM images of Cu electrodeposition in MSA on GDE via dual pulse with varying growth charge (A) Qg -0.0675 C, GDE3; (B) Qg -0.135 C, GDE4 and (C) Qg -0.270 C, GDE1

This is straightforward considering that the growth charge is proportional to the duration of the experiment. At larger growth charge, the particles are given more time and energy to grow, ultimately resulting in bigger particles. Using deposition parameters of GDE3, a particle size of 45 nm (Figure 4-7 C) was obtained, which increased up to 148 nm for GDE1, because of the smaller growth potential (and thus larger growth charge) employed, favoring copper ions to deposit on preformed Cu islands.

The mean particle size decreases with an elevation in growth potential, as shown in Figure 4-10. The mean radius of GDE5 and GDE6 decreases from 61 nm (Figure 4-7 E) to 54 nm (Figure 4-7 F), respectively. These experiments were performed using the same growth charge. If we look at the deposition time required to perform these experiments, it shows that using a less negative growth potential, a longer time was needed to deposit the same amount of charge. This would thus mean that by depositing the Cu nanoparticles for the same duration, the nanoparticles will be using -0.05 V compared to -0.1 V. The growth potential is linked to the growth rate. A more negative potential leads to a higher growth rate, which means particles grow faster and during the same amount of time, the particles will thus grow larger as compared to applying a less negative growth potential.

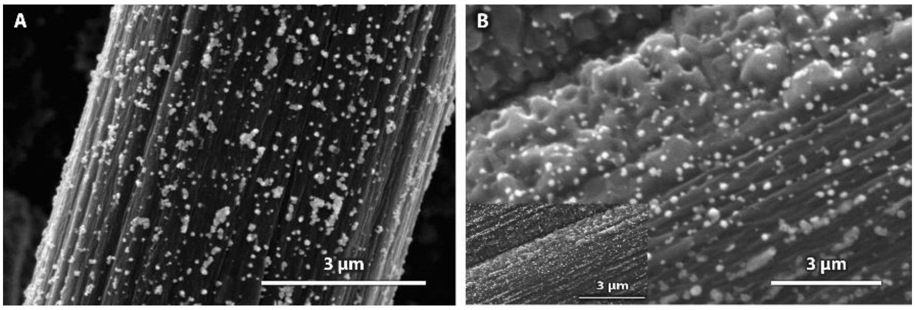

Figure 4-10: SEM images of Cu electrodeposition in MSA on GDE via dual pulse with different growth potentials (A) Eg -0.05 V, GDE5 and (B) Eg -0.1 V, GDE6

Using dual pulse leads to a better control in the electrodeposition of nanoparticles and smaller nanoparticles can be obtained compared to single pulse electrodeposition. This leads to an increased activity of the catalyst. To substantiate this assumption, the EASA of the nanoparticles deposited using single and dual pulse electrodeposition are compared. CV measurements are performed in a range ± 40 mV s^{-1} vs. OCP to make sure no faradaic contribution would be present during the experiment and only a capacitive current was measured. The scan rate varies from 150 mV s^{-1} to 25 mV s^{-1} with an increment of 25 mV s^{-1}. The difference in current at OCP of the second scan is plotted against the scan rate in Figure 4-11. The slope of the trendline using single pulse is 10 times smaller than the slope of the dual pulse technique. Since the slope is an indication of the EASA of the deposited Cu nanoparticles, we can conclude that using dual pulse electrodeposition a bigger surface area is obtained, which will lead to higher activity of the catalyst.

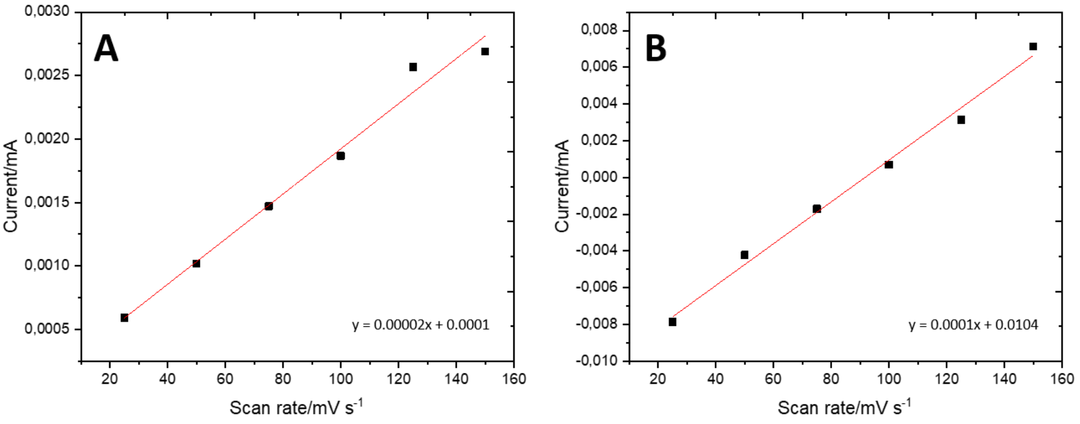

Figure 4-11: Plot of capacitive current against scan rate (A) single pulse; (B) dual pulse electrodeposition in 0.1 M $HClO_4$ *with scan rates going from 150 mv s-1 to 25 mV* s^{-1} *with an increment of 25 mV* s^{-1}

As well-known from literature, the particle size of Cu, deposited on GC, can vary from the nanometer scale [159], [160] to the micrometer range [161]. In this paper, we were able to control the particle size within the same range as literature states for the electrodeposition of Cu on GC, only we are using a rough surface. This has the advantage of increasing the active surface area and by doing so, higher current densities can be obtained.

All dual pulse parameters tested in this research have their own effect on the particle size and the particle distribution. The same trends were observed performing dual pulse electrodeposition of Cu on glassy carbon (smooth substrate).

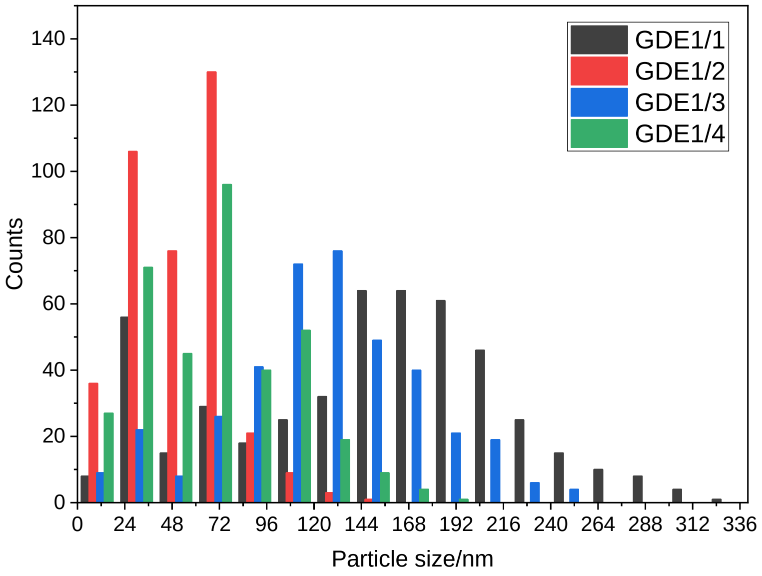

Figure 4-12: Particle size distribution of electrodeposited Cu on HNO_3 pre-treated GDE using GDE1 parameter set

From reproducibility tests (Figure 4-12), it is clear that another parameter, namely the constantly changing surface, plays an important role. This means, because of the rough surface of the GDE, the substrate is not always exactly the same, meaning it is difficult to deposit the particles with the same size upon reproduction. Nevertheless, this research opens perspectives about the electrodeposition of Cu onto rough surfaces. From this research it is clear the effect of the surface cannot be neglected and has to be taken into account.

4.3.3 Stability tests of Cu/GDE

Cu and its oxides are often used as electrocatalysts for CO_2 reduction because of their ability to convert it to higher value added chemicals such as methane and ethylene [123], [162]. This explains why the stability experiments for the Cu/GDEs, synthesized through electrodeposition and spray-painting, were tested under conditions often used in literature when investigating the CO_2 reduction. A potential of -1 V_{RHE} was applied for 4 h in a CO_2-saturated electrolyte containing 0.5 M $KHCO_3$. The electrolyte was tested with the ICP-MS for Cu suggesting possible detachment of Cu and hence instability of the electrocatalyst. When calculating the loss of Cu for the electrodeposited and the spray-painted Cu, 0.16 % and 0.72 % of Cu detached from the surface, respectively. This enables us to conclude that almost no Cu was present in the solution, thus suggesting they were both stable for 4 h under working conditions. However, when compared to each other, the percentage of Cu detaching from the surface when using the electrodeposited Cu was 22 % lower than spray-painted Cu.

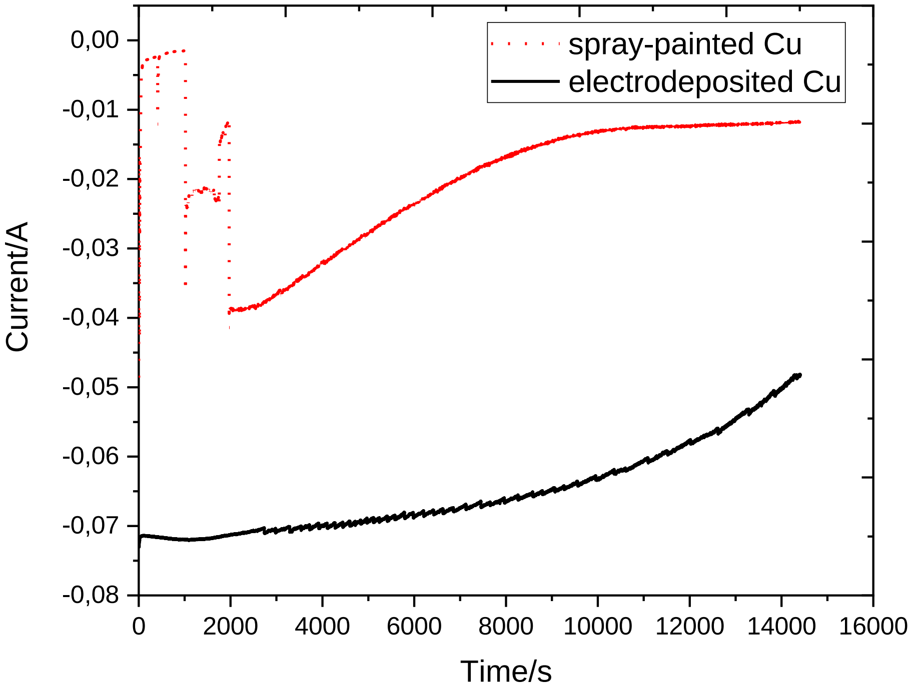

Figure 4-13: Current response for stability testing, comparing electrodeposited Cu (black, solid) and spray-painted Cu (red, dotted) when applying -1 V vs. RHE using a CO_2 saturated electrolyte containing 0.5 M $KHCO_3$

During the first minutes of the experiment using spray-painted Cu, the current decreases (to more positive values) drastically, as shown in Figure 4-13. After 30 min, an extreme current increase (to more negative currents) was observed. A possible hypothesis is that the Cu detaches during the first minutes of the experiment and redeposits after 30 min. This explains the fluctuating graph at the beginning of the experiment.

The reason for the detachment in both cases lies in the production of gases during the experiment, which are visible at the GDE surface. The detachment of Cu in regard to the spray-painted Cu was larger since it is not chemically bonded to the surface of the GDE as it was for electrodeposited Cu. This also explains the sudden drop during the first period of the experiment. Once the detached Cu was redeposited, the current was more stable. Additionally, electrodeposition ensured the deposition of Cu in the inner matrix of the GDE. Nevertheless, the current drops which could be due to the sintering of the NPs.

4.4 Conclusions

This chapter focused on the improvement of Cu deposition onto rough surfaces (e.g. GDE substrates). The results in this chapter indicated that pre-treating the hydrophobic GDE surfaces can potentially affect the Cu electrodeposition. Comparing the nucleation mode of the pre-treatments, TX100 deviated from HNO_3, NaOH and MQ (progressive vs. instantaneous for the other 3) which reflected itself in the SEM analysis. Whereas on TX100 pre-treated GDEs hemispherical particles consisting of smaller cubic-like particles were obtained, HNO_3, NaOH and MQ pre-treated GDEs exhibited more spherical-like particles. In addition, differences in surface charge were acquired: NaOH > TX100 > HNO_3 with decreasing positive charged surface. We hypothesize this could potentially affect the nucleation and growth on pre-treated surfaces. Nevertheless, the roughness of the GDE surface can initiate defects as such that the electrodeposition was affected as well and therefore can potentially contribute to a difference in nucleation of Cu.

Because of the rough surface of the GDEs, it was more difficult to control the electrodeposition of Cu. Reverting to dual pulse can potentially result in an improved control over the Cu deposition, as more parameters can be adjusted. By adjusting the parameters during the nucleation and growth pulse, a particle size of up to 45 nm could be obtained. Despite the improved control and obtaining particles in the nanometer range, reproducing the electrodeposition remained challenging. We hypothesize that this had to do with the roughness of the GDE surface, which impeded the synthesis of (nano)particles within the size range. Therefore, another synthesis approach will be investigated in the following chapter in order to obtain reproducible monodisperse Cu NPs.

4.5 Supporting information

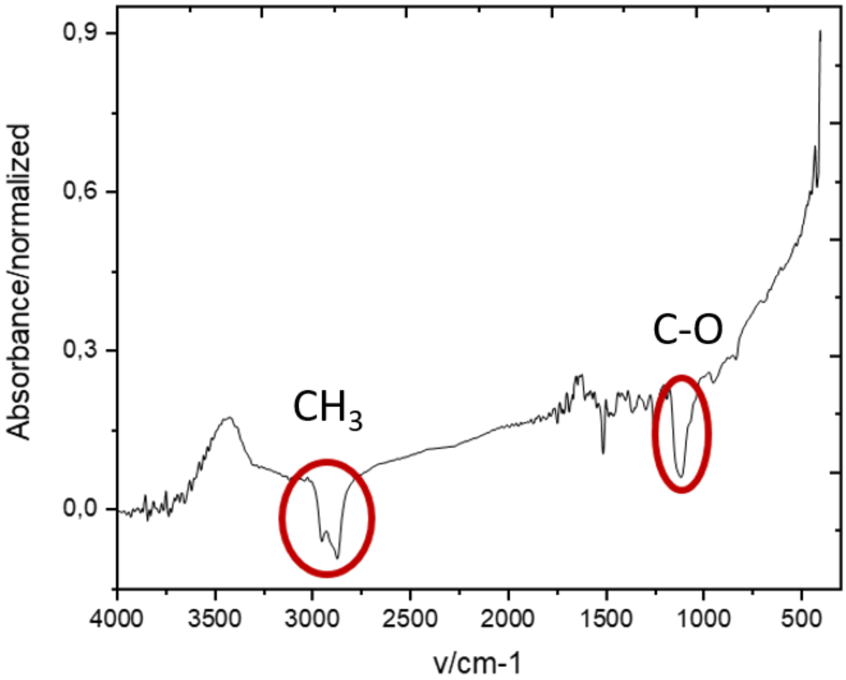

Figure S 4-1: FTIR spectrum of a TX100 pre-treated GDE substrate

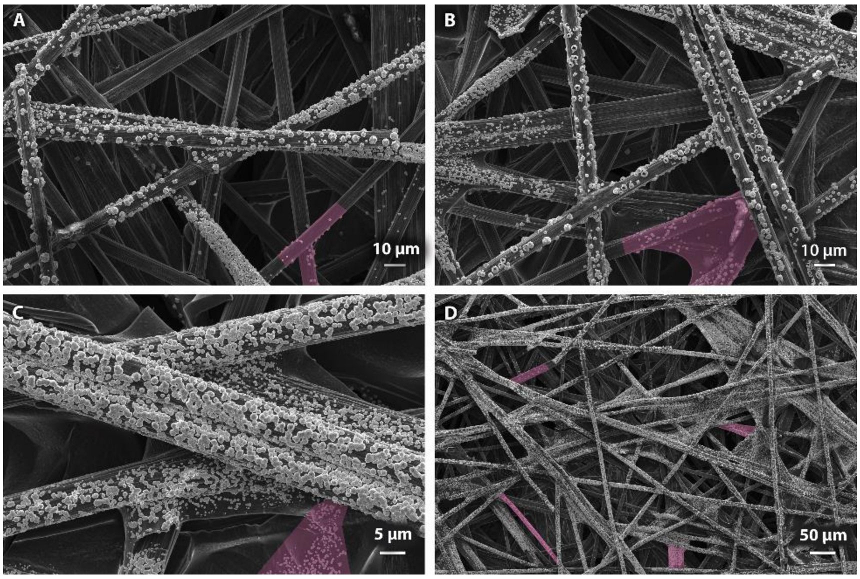

Figure S 4-2: SEM-images of Cu electrodeposition in 0.1 M $CuSO_4$ and 2 M MSA applying -0.3 V on MQ pre-treated GDE

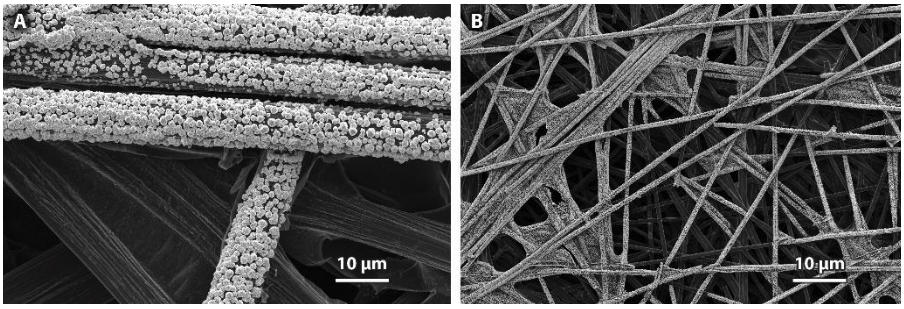

Figure S 4-3: SEM-images of Cu electrodeposition in 0.1 M $CuSO_4$ *and 2 M MSA applying -0.3 V on* HNO_3 *pre-treated GDE*

CHAPTER 5:

Synthesis of Cu-Ag bimetallic electrocatalysts

In this chapter, the synthesis of highly monodisperse sub-10 nm Cu-Ag bimetallic nanoparticles is discussed. Cu core nanoparticles are synthesized through a thermal decomposition method, followed by the galvanic displacement of Cu with Ag, resulting in a Ag shell. The influence of the capping agent-to-Cu ratio on the Cu particle size is investigated. Thereafter, the thickness of the Ag shell is altered by changing the reaction temperature, reaction time and concentration of Ag during the synthesis. Improved heat distribution positively affected the uniformity of the Ag shell.

This chapter is in preparation to be published as: L. Pacquets, D. Choukroun, S. Hoekx, S. Arnouts, C. Li, N. Daems and T. Breugelmans, Synthesis of sub-10 nm Cu-Ag nanodimers and core-shell nanoparticles by thermal decomposition and galvanic displacement, *Journal of nanomaterials*, (2022).

The Cu-Ag bimetallic nanoparticles have been synthesized by Lien Pacquets and Daniel Choukroun.

5.1 Introduction

At present, several methods have been explored for the effective synthesis of Cu cores surrounded Ag shells [163]–[166]. Mostly, complex methods involving toxic reducing agents were used to synthesize Cu cores [167]–[169] and there is still a need for more environmental friendly synthesis routes. Despite the increasing interest in Cu-Ag bimetallic particles, also the formation of the Ag shell remains challenging. Synthesis is often performed in water [170]–[172], potentially harming the metallic Cu core through oxidation, or shell formation occurred too fast hampering control over the shell thickness [173]–[175]. Alternatives to galvanic displacement were also reported and these typically required higher temperatures, as such inducing the self-nucleation of Ag [176]. Unfortunately, the currently available methods for Cu-Ag nanoparticles yield aggregation and broad size-distributions with instable shell formation are common [163], [164]. Therefore, it is important to design a route to obtain a robust process at which monodisperse core-shell nanoparticles with homogeneous Ag distribution across the shell can be synthesized.

In Chapter 4, it was shown that the size of Cu (nano)particles could be controlled by altering the double pulse parameters during electrodeposition. Despite electrodeposition being a straightforward method, monodispersity could not be obtained due to the rough surface of the GDE. In this chapter, we report a facile multi-step synthesis method for Cu-Ag nanodimers and core-shells based on the thermal decomposition of Cu-precursor that is different compared to common literature. In this manner, it became possible to obtain monodisperse sub-10 nm Cu NPs in a reproducible manner. Subsequently, one or two galvanic displacement reactions were performed in an organic Ag-trifluoroacetate (TFA) solution. As a result, highly monodisperse Cu-Ag NPs with small sizes and different Ag concentrations were obtained. Several parameters were investigated to tune the synthesis towards the desired properties (i.e. monodisperse, variable Cu size, uniform Ag shell, shell thickness). To this end, the influence of the TDPA-to-Cu (Tetradecylphosphonic acid used as capping agent) ratio on the particle size was investigated. Additionally, we investigated the effect of heating and stirring on the uniformity of the shell and the influence of the Ag concentration and the reaction time during galvanic displacement on the Ag shell thickness in Cu-Ag bimetallic NPs. Finally, we also improved the core-shell stability compared to particles typically found in literature by performing multi-step galvanic displacement and using a capping agent and storing solvent that are almost insoluble.

5.2 Experimental

5.2.1 Chemicals

Copper(II) acetate monohydrate (Cu(II)OAc, p.a., Janssen Chimica), Trioctylamine (TOA, 97%, Acros Organics), Ethanol (99.5% Extra Dry, AcrosSeal®, Acros Organics), iso-propanol (99.5%, AcrosSeal® Acros Organics), Tetradecylphosphonic acid (TDPA, 98%, Sigma Aldrich), Isoamyl ether (IAE, 99%, Sigma Aldrich) and silver trifluoroacetate (Ag-TFA, 99.99%, trace metal basis, Sigma Aldrich) were used without further purification unless stated otherwise.

5.2.2 Preparation of Cu nanoparticles

The Cu NPs were prepared using a modified synthesis method based on the approach proposed by Hung [116] and Osowiecki [177]. Since Cu is prone to oxidation when exposed to air, an air-free environment is crucial to ensure the growth of metallic Cu nanoparticles, which is an endothermic process [178]. Typically, 122 mg of Cu(II)OAc was mixed with 16.5 mg, 82.3 mg or 278 mg TDPA (depending on the used ligand to CuOAc molar ratio; ratio 0.1, ratio 0.5 or ratio 1.0, which will be further referred to as Cu0.1, Cu0.5 and Cu1.0, respectively) in 10 mL of TOA (pre-dried with molecular sieves to reduce the water content). Prior to synthesis, the mixture was brought under inert atmosphere using a Schlenk line by evacuating and refilling with Ar for several times. Subsequently, the mixture was heated to 105 °C and retained there for 1 h, while stirring, which ensured the dissolution of Cu(II)OAc and TDPA and eliminated any traces of available water [178]–[180].

Next, the solution was rapidly heated to 180 °C with an increment of ~3 °C min^{-1} and maintained there for 30 min to ensure the reaction of Cu-precursor with TDPA resulting in the formation of an intermediate polymer lamellae (as discussed in Chapter 3). This intermediate is crucial for size focusing and monodispersity, indicating the fundamental role of TDPA in the pre-nucleation stage. The synthesis is a very robust method owing to the slow growth rate that is achieved when using TDPA as a surfactant as compared to others [120]. This slow growth rate originates from the strong binding abilities of TDPA with the Cu-precursor. Eventually, the temperature was further ramped to 270 °C with the same increment of ~3 °C min^{-1} and maintained at this value for another 30 min, inducing the growth of the Cu seeds upon reduction with TOA [181], [182]. After the particle growth, the heating block was removed and the 3-neck flask was quenched by immersing it in water at room temperature. This Cu NP mixture was then transferred under Ar to a glove box (Unilab Pro, MBraun) for particle purification.

The Cu NPs were purified using a 1:1 v/v mixture of ethanol and iso-propanol (cleaning solvent) and was added using a volumetric ratio of 1.25:1 cleaning solvent:reaction solution. Subsequently this mixture was centrifuged for 5-10 min at 5000 rpm and the precipitated Cu NPs were redispersed in hexane. This process was repeated three times and the cleaned Cu NPs were eventually redispersed and stored in hexane or redispersed in IAE as reaction solvent for further synthesis of the Cu-Ag nanocrystals (NCs). In the case of Cu0.1, further work-up was required as NPs with a broad size distribution were obtained. In order to separate the sub-10 nm NPs, centrifugation of the mixture in hexane was performed for 5-10 min at 5000 rpm, where the supernatant, afterwards, contained the desired nanoparticles.

5.2.3 Fabrication of Cu-Ag nanocrystals

Cu-Ag NPs were synthesized by galvanic displacement where Cu surface atoms are replaced by Ag atoms (Figure 5-1).

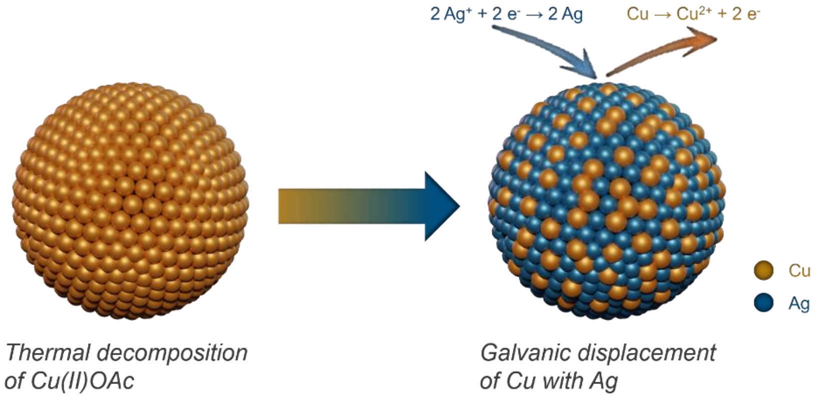

Figure 5-1: 2-step synthesis process starting with the thermal decomposition of Cu(II)OAc followed by the galvanic displacement of Cu with Ag

To achieve the Cu-Ag NPs, the as-prepared Cu NPs were redispersed in IAE, which serves as the reaction solvent during the galvanic displacement. It is an organic non-reducing solvent to avoid homogeneous nucleation of Ag (and as such Ag NP growth), allowing the dissolution of both TDPA-capped Cu NPs and Ag-TFA. The Ag-TFA salt was dissolved in IAE (11 mg in 3 mL) and depending on the original concentration of the Cu NPs solution, different volumes were added to the redispersed Cu NPs. An Ag content of 10-20 at.% (depending on the synthesis) was aimed for. Additionally, the temperature during the galvanic displacement was kept below 120 °C since Ag-TFA thermally decomposes at this temperature and would otherwise yield Ag NPs instead of an Ag shell [183]. The Ag containing solution was gradually added to the Cu NPs containing solution while mixing to ascertain that the local concentration of Ag was kept low enough to prevent oversaturation as this would otherwise lead to homogeneous nucleation of Ag NPs instead of the Ag being used to form a shell around the Cu NPs [177], [184].

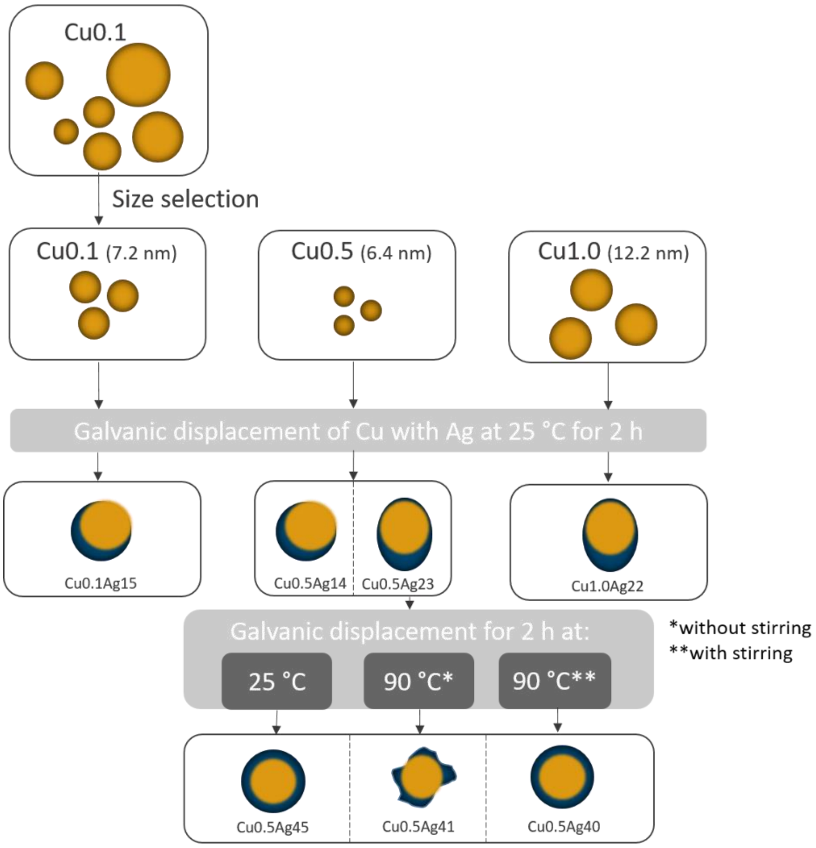

Figure 5-2: schematic representation of the different synthesis performed in this work (not to scale)

The reaction mixture was stirred for 2 h at room temperature using a vortex. Afterwards, the Cu-Ag NPs were purified using the same cleaning method as mentioned in the previous section. The Cu-Ag NPs were eventually redispersed and stored in hexane, except for the Cu-Ag NPs prepared from Cu0.5. These NCs were subjected to a final synthesis step were another Ag-containing solution (20 at% Ag) was added and subsequently heated to 90 °C on a hot plate for 2 h either stirred or not stirred. In this study nanodimers and core-shells were synthesized with different Ag concentration of 14 at%, 15 at%, 22 at%, 23 at%, 41 at%, 45 at% and 40 at% and will be referred as CuXAgY, were X represents the TDPA:Cu ratio and Y the concentration of Ag in at%, respectively. For example Cu0.5Ag41 are Cu@Ag core-shell NPs containing 41 at% Ag and descend from Cu NPs where a TDPA:Cu ratio of 0.5

was used. A schematic representation of the different syntheses performed is depicted in Figure 5-2.

5.2.4 Characterization

UV-VIS spectra were recorded using a Hitachi U-2001 instrument in the range of 300 – 800 nm. All suspensions were diluted 100 to 200 times in hexane. These spectra were a first indication of the presence of Ag.

Oxidation tests were performed to indicate the presence of a full covering Ag shell. For this purpose, all Cu-Ag and Cu suspensions were diluted 100 to 200 times in hexane. In a next step, hexane was removed by evaporation, exposing the particles to air, after which they were redispersed in hexane. If the shell is incomplete this resulted in a change in color of the solution before and after redispersion from dark red (metallic Cu) to green (oxidized Cu). If the Ag shell was fully covering the Cu core, the solution remained dark red.

Quantification of the bulk metal concentrations was conducted using an Agilent 7500 Series Inductively Coupled Plasma Mass Spectrometer (ICP-MS). 100 µL of the as-prepared Cu-Ag and Cu mixtures were digested with aqua regia or nitric acid at 70 °C overnight after which the sample was diluted and analyzed.

Particle size distribution and quantification were deduced from HAADF-STEM images combined with EDS and EELS mapping using an aberration corrected Thermo Fischer Scientific Titan electron microscope operated at 300kV and a Thermo Fischer Scientific Osiris electron microscope operated at 200kV. The TEM samples were prepared by drop casting the as-prepared Cu-Ag and Cu solutions on an ultra-thin film Au TEM grid inside the glove box. These grids were cleaned in a mixture of activated carbon and ethanol to remove the ligands prior to the electron microscopic investigation.

5.3 Results and discussion

5.3.1 Importance of the Ligand-to-Cu ratio on the particle size

In contrast to literature [177], [185], [186], TDPA was elected as surfactant which operated as capping agent, ensuring complex formation of the Cu(II)OAc and allowing stabilization and storage of the as-prepared Cu NPs in organic solvents by preventing post-synthesis agglomeration [187].

In this work, the influence of the TDPA:Cu ratio was investigated employing molar ratios of 0.1, 0.5 and 1.0. HAADF-STEM images of the as-prepared Cu NPs using different TDPA:Cu ratios are provided in Figure 5-3.

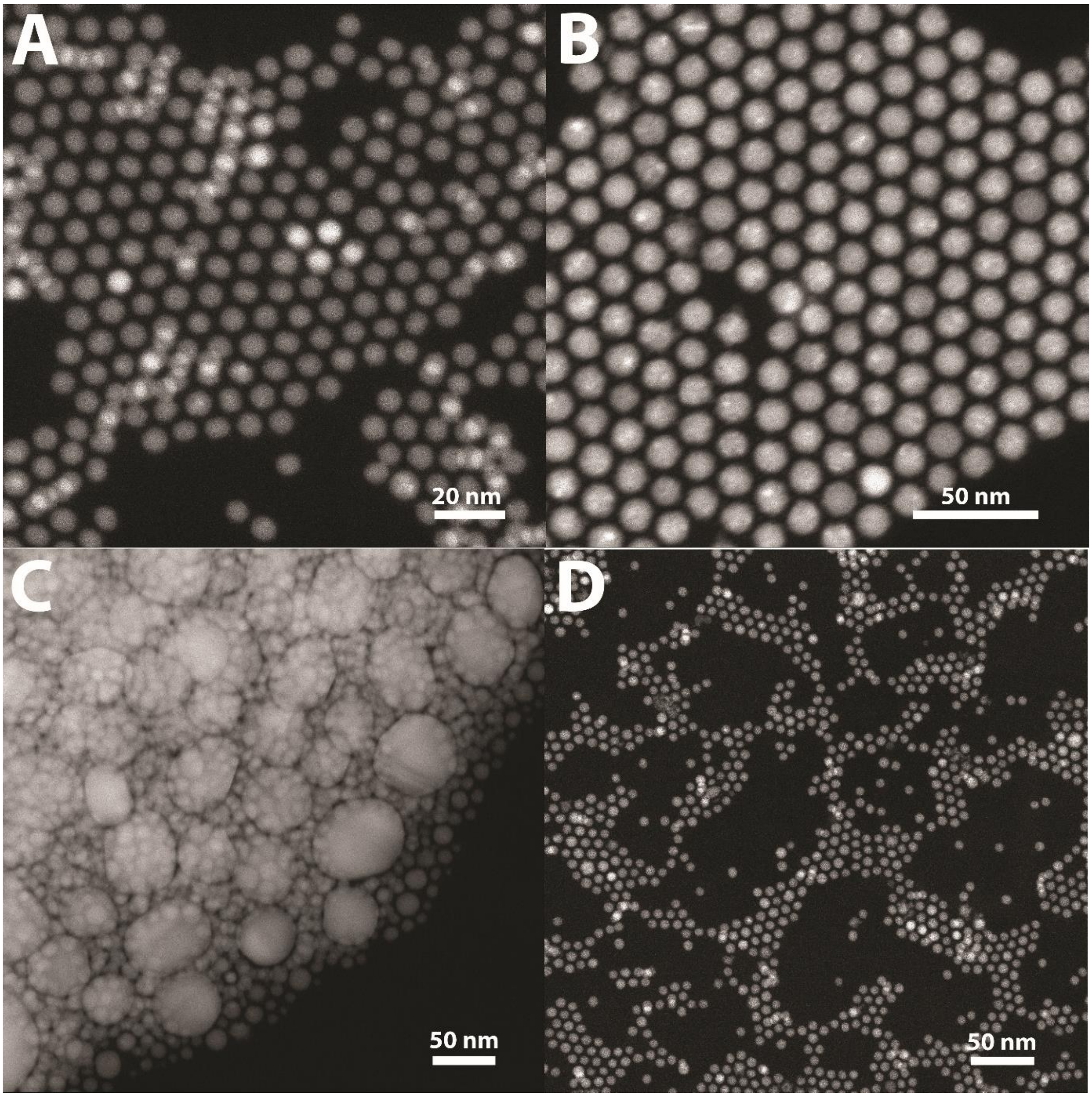

Figure 5-3: As-prepared Cu NPs with a TDPA:Cu ratio of (A) 0.5 and (B) 1.0, (C) 0.1 before size selection and (D) 0.1 after size selection,

By employing different TDPA:Cu ratios, the size of the Cu NPs could clearly be altered. A ratio of 0.5 resulted in particles which were 6.7 nm (Figure 5-4 (B)) in size compared to a ratio of 1.0 which resulted in a mean particle size of 12.3 nm (Figure 5-4 (C)). After the synthesis, a bulk concentration of respectively 1.83 mg mL^{-1} and 1.81 mg mL^{-1} was obtained.

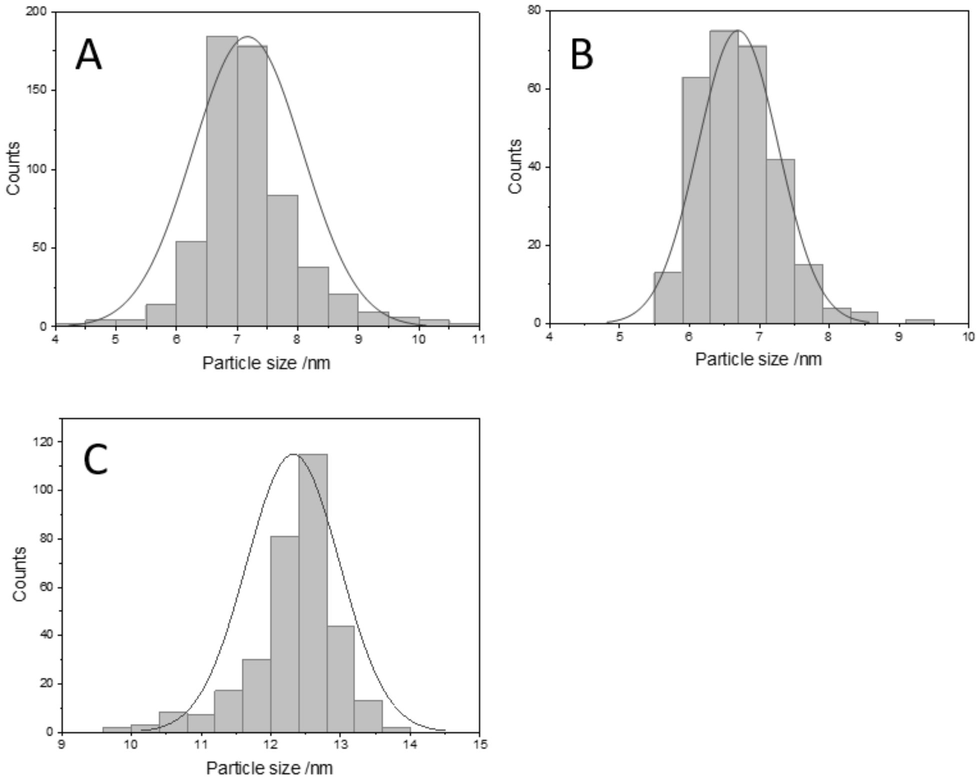

Figure 5-4: Particle size distribution Cu NPs with different TDPA:Cu ratios of (A) R=0.1 (Cu0.1 after size selection, 7.2 nm ± 0.9 nm), (B) R=0.5 (Cu0.5, 6.7 ± 0.6 nm) and (C) R=1.0 (Cu1.0, 12.3 nm ± 0.7 nm).

The use of TDPA as a surfactant in this synthesis has thus led to the formation of small closely packed monodisperse Cu NPs. Nevertheless, a minimum amount of TDPA is required to achieve monodisperse nanoparticles since the use of a TDPA:Cu ratio of only 0.1 leads to the formation of Cu NPs with a broad size distribution from 5 nm – 50 nm (Figure 5-3 (C)). We speculate that the low concentration of TDPA in the pre-nucleation stage led to the formation of incomplete intermediate lamellae polymers. Mantella *et al.* investigated the influence of TDPA on particle size/dispersity [182]. The authors concluded that TDPA was crucial for size focusing because syntheses performed without TDPA led to bigger Cu NPs. A lamellar phase where the Cu-precursor is layered with phosphonate chains was crucial for obtaining the monodisperse Cu NPs as shown in Figure 5-3 (A) and (B). Therefore, reducing the TDPA:Cu ratio below 0.5 resulted in the formation of Cu NPs with different sizes. After an additional centrifugation step removing the NPs above 10 nm with the deposit, monodisperse NPs (7.2 nm; 1.69 mg mL^{-1}) could however be obtained from this synthesis approach as well (Figure 5-3 (D)).

In conclusion, increasing the TDPA:Cu ratio from 0.5 to 1.0 led to an increase in particle size [116], while reducing it below 0.5 resulted in Cu NPs with a broad size distribution due to the insufficient presence of TDPA to form complete polymer lamellae [188]. We hypothesize that the increase in particle size with TDPA content is related to the larger collision probability of single micelles at higher TDPA contents as more micelles will be present in this case. Upon collision, particles merge resulting in the larger mean size of the particles at these higher TDPA contents.

5.3.2 Evolution of the Ag shell growth

In this chapter, Cu-Ag nanodimers and core-shells nanoparticles were synthesized using different concentrations of Ag. Given the fact that Cu and Ag have a positive mixing enthalpy, the formation of bimetallic structures with segregated domains such as core-shells, crescents and dimers are favored. Indeed, as a consequence of the positive mixing energy the separating force will be greater than the interdiffusion force which would otherwise promote the inward diffusion of Ag in the Cu core and thus the formation of alloys.

When Ag-ions were added in a controlled manner to the Cu NPs suspension, galvanic displacement at the pristine Cu NP surface occurred. Initially, the interdiffusion of Cu to the surface and Ag to the core, driven by entropy, was high, while the segregation driven by the positive enthalpy of mixing remained small. The further the galvanic replacement progressed, the more the unfavorable mixing energy started to prevent Ag from diffusing further into the NP until eventually, the mixing energy balanced the interdiffusion force and a shell started to form.

Cu/Ag nanodimers were synthesized through galvanic displacement of Cu0.1 (size-selected), Cu0.5 and Cu1.0 by dropwise addition of an Ag-TFA/IAE solution at room temperature. After two hours of synthesis, the morphology and elemental composition of the as-prepared Cu-Ag bimetallic nanostructures were investigated by HAADF-STEM and STEM-EDS, as illustrated in Figure 5-5.

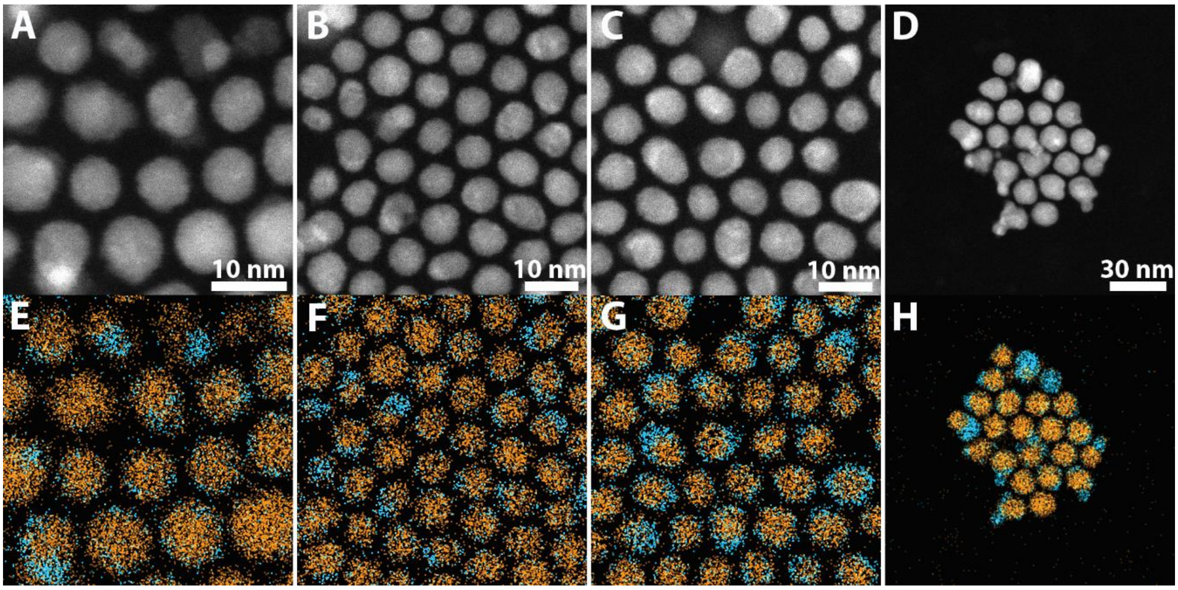

Figure 5-5: HAADF-STEM images of (A) Cu0.1Ag15, (B) Cu0.5Ag14 (C) Cu0.5Ag23, (D) Cu1.0Ag22 and there corresponding EDS maps in (E), (F), (G) and (H) where orange and blue represent Cu and Ag, respectively

The HAADF-STEM images in Figure 5-5 (A-D) show particles at high magnification. The use of HAADF-STEM enabled to correlate the contrast observed in the image, with the atomic number Z of the materials in the nanoparticles. The atomic numbers of Cu (29) and Ag (47) are apart, which means that high intensity areas can be linked to increased Ag concentration and the lower intensity areas to presence of Cu. The nanoparticles were seemingly segregated and formed nanodimer-like structures. Nevertheless, one should consider the potential presence of remaining diffraction contrast. Therefore, the corresponding EDS-maps (Figure 5-5 (E-H)) were investigated as well. They confirmed the nanodimer-like structure, which gets more distinct when the concentration of Ag is increased. The Cu-Ag bimetallic series contained 15 %, 14 %, 23 % and 22 % Ag (measured with EDS and expressed in at%) in Cu0.1Ag15, Cu0.5Ag14 Cu0.5Ag23 and Cu1.0Ag22, respectively. These nanodimer structures originate from a difference in lattice constant between Cu and Ag leading to a very unfavorable interphase among Cu and Ag [189]. Indeed, considering the large lattice misfit of ~12,6 % between Cu and Ag, it is highly likely that strain will occur by deposition of Ag onto Cu [190]. This strain can be reduced by defects into the Ag shell or by 3D island growth. The latter mechanism will dominate when a mismatch larger than 5 % occurs [190], which explains why nanodimers are formed under these conditions.

Differences in particle size and composition were obtained during the syntheses. This is for example clear when comparing Cu0.5Ag14 and Cu0.5Ag23 (the corresponding UV-VIS spectra are presented in Figure S 5-1). Both samples originated from the same Cu0.5 batch and were prepared in the same manner except for the added amount of Ag-TFA. For the latter, the Ag content during the synthesis was doubled. Similar observations were made when comparing Cu0.1Ag15 and Cu1.0Ag22. As a consequence and as expected, increasing the Ag concentration led to a higher (although not proportionally) Ag content in the specific nanodimers, which is also in accordance to literature [184].

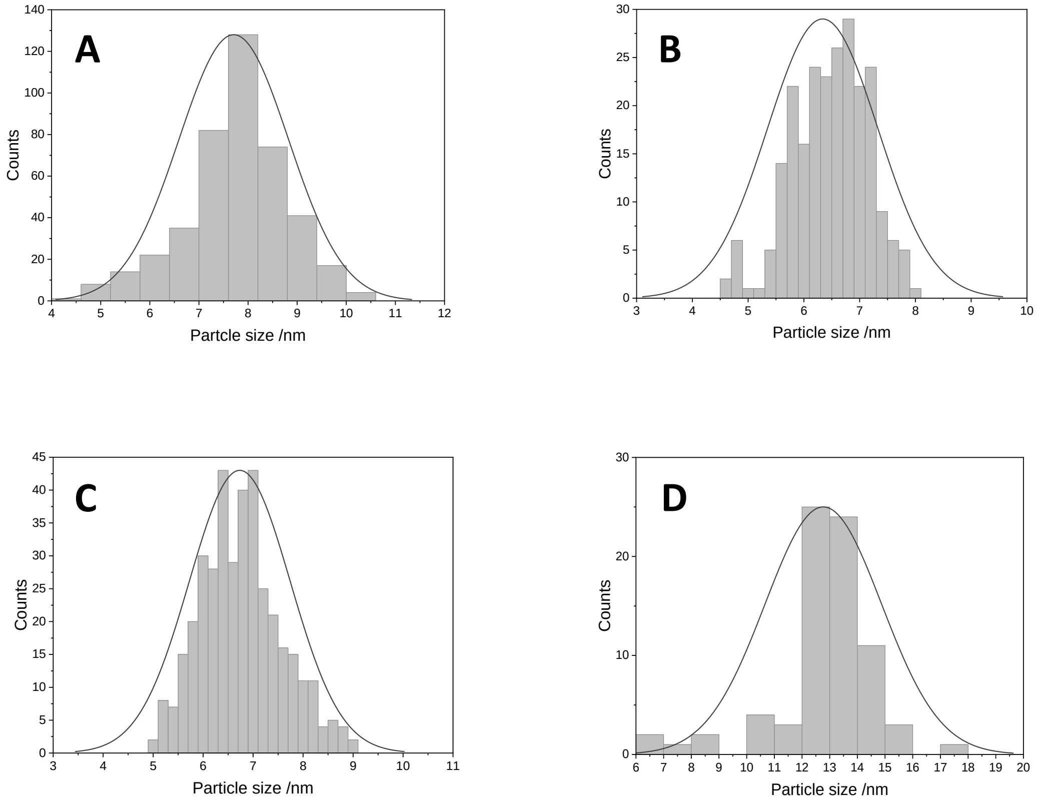

Figure 5-6: Particle size distribution of (A) Cu0.1Ag15 (7.7 nm ± 1.1 nm), (B) Cu0.5Ag14 (6.3 ± 1.0 nm), (C) Cu0.5Ag23 (6.7 nm ± 1.0 nm) and (D) Cu1.0Ag22 (12.8 nm ± 2.1 nm).

Except for Cu-Ag bimetallic structures originating from Cu1.0 (initial Cu NP size above 10 nm), all NPs were sub-10 nm. The particle size distribution (PSD) was calculated and is presented in Figure 5-6. These results confirm that particles with a narrow size distribution (± 1 nm) could be obtained through this synthesis procedure.

Figure 5-7 represents the Cu@Ag core-shells Cu0.5Ag41 and Cu0.5Ag45, which were prepared with Cu0.5Ag23 as substrate, and performing an additional galvanic displacement at 90 °C and room temperature, respectively. This extra step resulted in the production of a core-shell structure, which was primarily confirmed by performing an oxidation test (see experimental). The absence of the green color in both Cu0.5Ag41 as well as Cu0.5Ag45 after the oxidation test ensured the total coverage of the Cu surface by Ag and thus the formation of Cu@Ag core-shell NPs (Figure S 5-2).

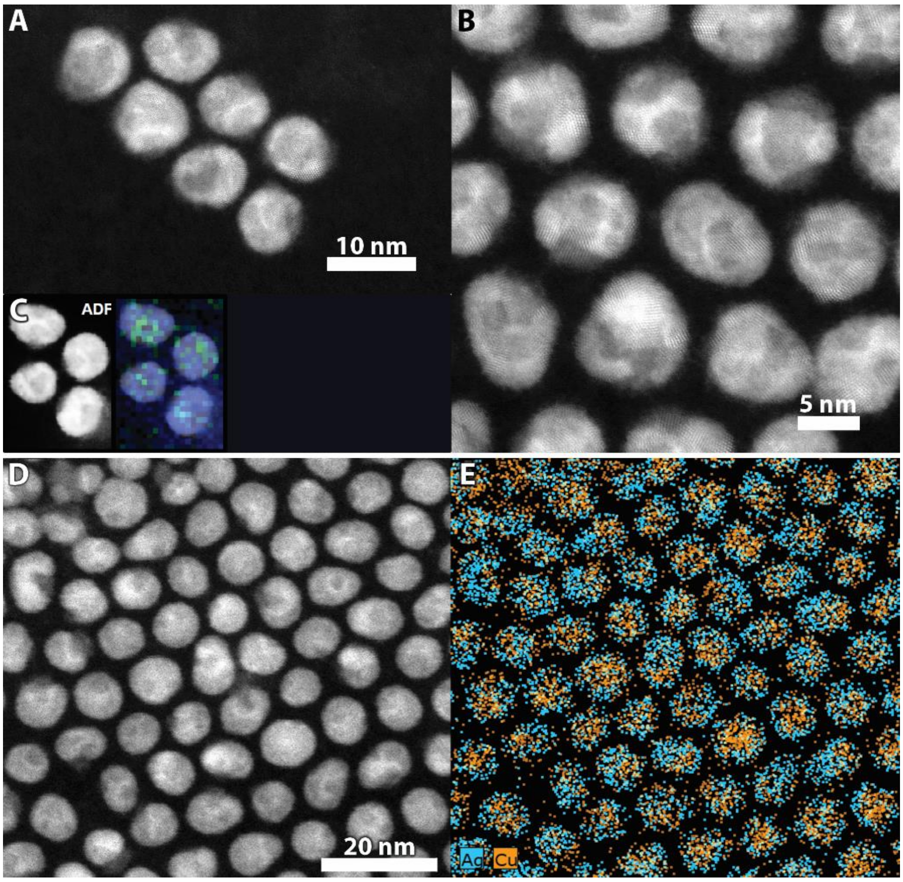

Figure 5-7: HAADF-STEM images of (A, B) Cu0.5Ag41 and its corresponding EELS map depicted in (C). HAADF-STEM images of (D) Cu0.5Ag45 and its corresponding EDS map presented in (E).

Notably, Cu0.5Ag41 (Figure 5-7 (C)) contains a more pronounced ‘spotty’ Ag shell compared to Cu0.5Ag45 (Figure 5-7 (E)). This signifies that at room temperature, a more uniform shell coverage was obtained, in contrast to the inhomogeneous Ag shell produced at 90 °C without stirring. We hypothesize that this descends from the increased mobility rate of Ag at the surface, leading to more heterogeneity in the core-shells, which in turn is a consequence of the faster nucleation and dissolution rate at elevated temperatures [191].

Finally, it is clear that an elevated reaction temperature did not necessarily lead to a significant increase in incorporation of Ag in the shell.

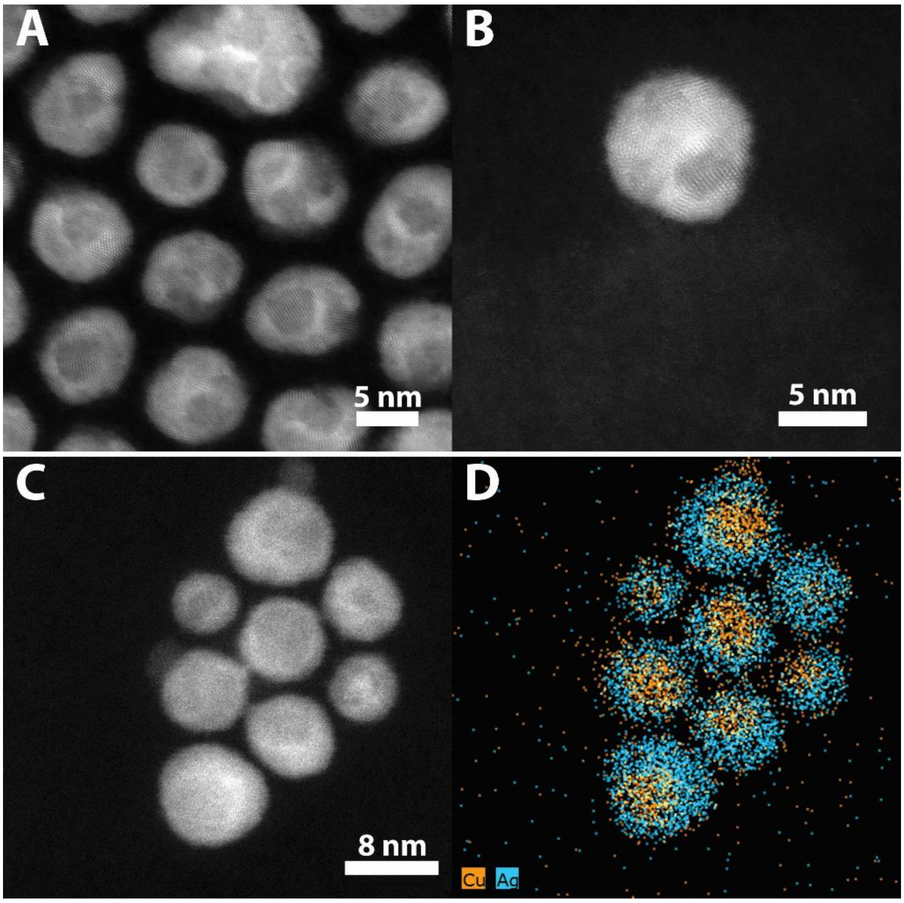

Figure 5-8: HAADF-STEM images Cu@Ag core-shells synthesized at 90 °C (A, B) without stirring (Cu0.5Ag41) and (C) with stirring (Cu0.5Ag40) with its corresponding EDS map presented in (D)

Finally, in an attempt to improve shell homogeneity also at higher temperatures, the synthesis of Cu0.5Ag41 was repeated but including stirring during the step at 90°C. As was clear from Figure 5-8 and was discussed above, an increase in temperature (in the absence of stirring) results in a less uniform shell. From Figure 5-8, it can be observed that Cu0.5Ag40 has a more homogeneous distribution of Ag along the surface as the heat was distributed more homogeneously during this step.

Comparing the PSD of the three Cu@Ag core-shells depicted in Figure 5-9, core-shells of 7.6 nm, 7.7 nm and 7.8 nm for Cu0.5Ag41, Cu0.5Ag45 and Cu0.5Ag40 could be synthesized, respectively.

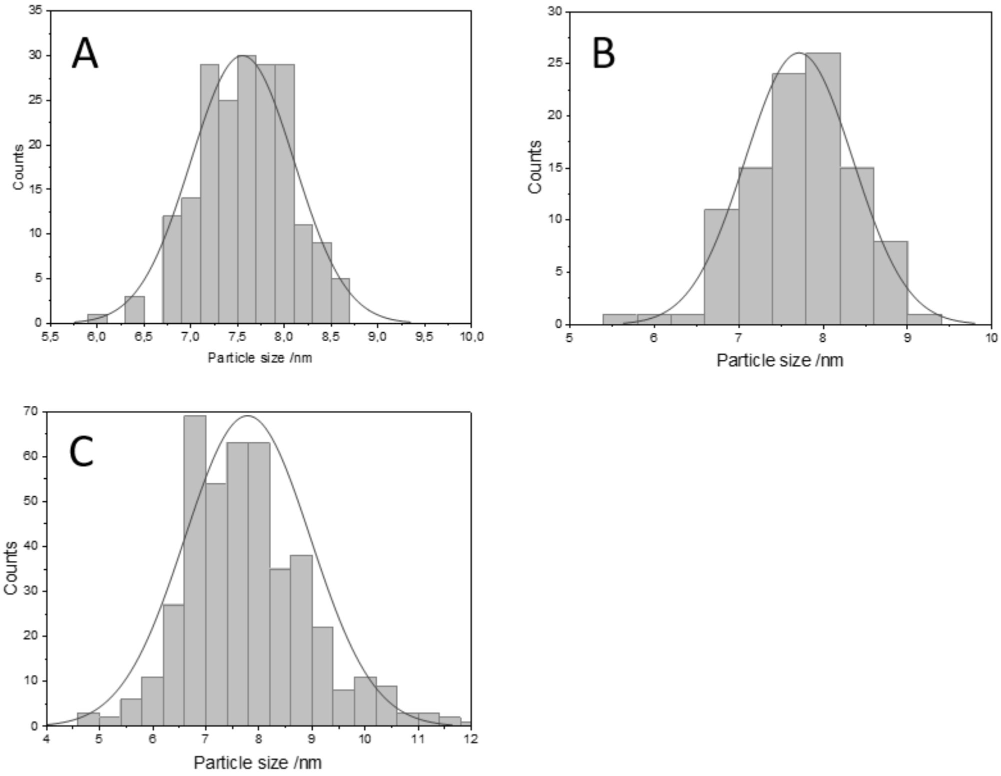

Figure 5-9: Particle size distribution of (A) Cu0.5Ag41 (7.6 nm ± 0.6 nm), (B) Cu0.5Ag45 (7.7 ± 0.6 nm) and (C) Cu0.5Ag40 (7.8 nm ± 1.2 nm).

To conclude, different Cu/Ag bimetallic nanodimers could be synthesized depending on the concentration of Ag-TFA used during the galvanic displacement. By performing a second galvanic displacement step, a core-shell structure could be obtained. Additionally, at elevated temperatures it was discovered that stirring greatly improves the homogeneity of the Ag shell.

5.3.3 Formation of stable Cu@Ag core-shell nanoparticles

As previously mentioned, a large lattice misfit exists between the two metals Cu and Ag resulting in strain which makes core-shell formation highly unfavorable. This is also the reason why this configuration is known to suffer from long term stability issues. As described by Muzikasky et al. [192], they observed Ag leaching from Cu@Ag core-shell after 12 months. The analysis revealed the formation of small Ag NPs surrounding the original Cu@Ag core-shell NPs when the Ag shell synthesis (galvanic displacement) was performed at room temperature. They speculate that an increased stability could be obtained after performing the galvanic displacement at elevated temperatures of 75 °C due to the improved interdiffusion resulting in an increased roughness at the Cu/Ag interface.

These authors used a comparable synthesis method as the Cu0.5Ag45 batch that was synthesized in this paper. Only here, the galvanic displacement was performed in two subsequent steps and also the Ag-precursor was different. After 12 months the core-shell structure was maintained as is clear from Figure 5-8 (D) and (E). Compared to literature, where Ag leached from the shell, our Cu@Ag core-shell nanoparticles revealed to be much more stable [192]. We hypothesize this could have to do with one or more of the following characteristics. (i) The larger amount of Ag present at the surface, i.e. 45 at% compared to 25 at% in literature [192]. The presence of an increased amount of Ag in the shell could be able to release the strain in the core-shell resulting in a more stable core-shell configuration as depicted in Figure 5-8 (D) and (E). (ii) The use of TDPA as surfactant, known to be an excellent stabilizing agent [120], can result in an increased stability. (iii) Our Ag shell synthesis is based on two subsequent galvanic displacement steps, which ensure the formation of a stable intermediate during the first step, followed by the formation of a core-shell in the second and last step of the synthesis procedure. This intermediate nanodimer is favored due to the large misfit between Cu an Ag lattices [86], [193]. In summary, we tuned the synthesis of Cu@Ag core-shell NPs such that the NPs remained stable for over 12 months without leaching of Ag, which is an improvement compared to literature.

5.4 Conclusions

In summary, a robust and straightforward synthesis method was developed to obtain highly monodisperse Cu-Ag bimetallic nanodimers and core-shell nanoparticles containing different amounts of Ag. By modifying several synthesis parameters (i.e. TDPA:Cu ratio, Ag concentration, reaction time, reaction temperature and the influence of stirring), we managed to modify our synthesis approach in such a way that a more uniform Ag shell could be obtained, exhibiting a stability against Ag leaching for over 12 months.

Primarily, varying the TDPA concentration during the thermal decomposition of Cu affected the monodispersity of the Cu NPs. An optimum Cu:TDPA ratio was found at 0.5. Higher ratios resulted in the production of bigger nanoparticles, which exceeded 10 nm. Lower ratios, on the other hand, resulted in NPs with a broad size distribution, which was undesired.

The importance of the initial Ag concentration during the galvanic displacement was also demonstrated. Upon increasing the Ag concentration in the solution, the final Ag content in the Cu-Ag nanodimers increased from 14 at% to 23 at%. A second galvanic displacement step ensured the enrichment of Ag in the shell up to 45 at% and thereby establishing a core-shell structure. Performing the synthesis at elevated temperatures, enabled us to obtain core-shell NPs with an inhomogeneous shell with a Ag concentration up to 41 at%. Improving the heat distribution during synthesis, by stirring the reaction solution, resulted in a more homogeneous Ag distribution in the shell.

Finally, despite the large lattice misfit between Cu and Ag, making these configurations prone to degradation over time, we were able to synthesize Cu@Ag core-shell nanoparticles at room temperature with improved stability compared to literature. We hypothesize this was due to the multiple step galvanic displacement procedure. In the first step an intermediate nanodimer structure was formed which was the most favorable because this led to the highest relief of occupant strain. The second step resulted in a core-shell configuration with high amounts of Ag resulting in improved stability.

5.5 Supporting information

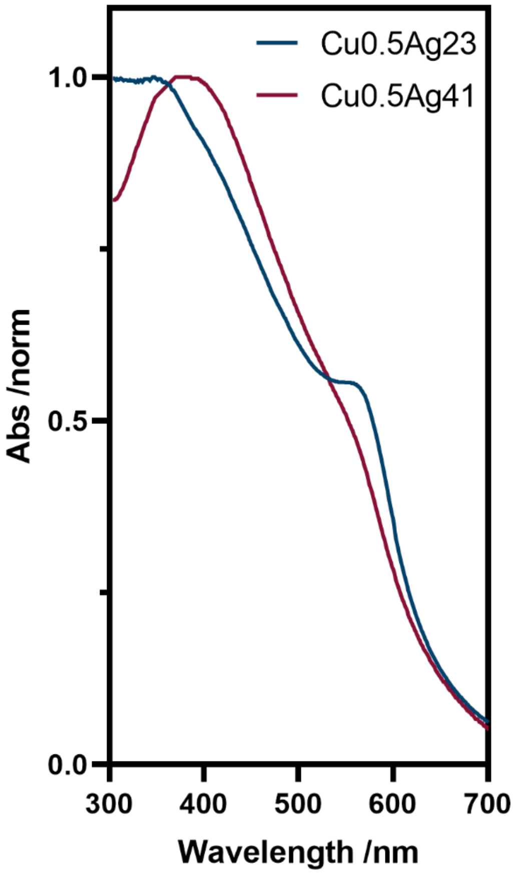

Figure S 5-1: UV-VIS spectra of unoxidized Cu-Ag bimetallic nanostructures where the absorption was normalized against the Ag peak in the spectrum

The optical excitation spectra of Cu0.5Ag23 and Cu0.5Ag41 are represented in Figure S 5-1. It is known from literature that both Cu and Ag feature plasmonic resonances which occur at two significantly different wavelengths. Combining these two metals, the optical behavior can change. Introducing a Ag shell onto a Cu NP, resulted in a redshift in the spectrum when the Ag concentration increased from 23 at% to 41 at%, while the specific Cu peak significantly decreased in intensity.

Figure S 5-2: Cu0.5Ag41 core-shell NPs dispersed in hexane after exposure to air

An oxidation test was performed by evaporating hexane (operated as solvent) from a diluted Cu0.5Ag41 core-shell NPs suspension. After evaporation and exposure to oxygen (air), the solution was redispersed in hexane. Figure S 5-2 presented a suspension of Cu0.5Ag41 core-shell NPs after the oxidation test where the original color was preserved which was a clear indication of the absence of Cu-oxides.

CHAPTER 6:

Electrochemical CO_2 reduction over Cu-Ag bimetallic electrocatalysts

In this chapter, Cu-Ag bimetallic nanoparticles were investigated for the electrochemical CO_2 reduction. The reduction of CO_2 towards CO has been improved by tailoring the Cu-Ag bimetallic nanoparticles and reaction conditions. The morphology of the nanoparticles (core-shells compared to nanodimers), the electrolyte cation and Ag shell concentration have proven to be crucial parameters in the enhancement of the CO production.

This chapter is part of: Daniel Choukroun, Lien Pacquets, Chen Li, Saskia Hoekx, Sven Arnouts, Kitty Baert, Tom Hauffman, Sara Bals, and Tom Breugelmans, Mapping Composition–Selectivity Relationships of Supported Sub-10 nm Cu–Ag Nanocrystals for High-Rate CO_2 Electroreduction, ACS Nano, 2021, 15, 9, 14858–14872

Electrochemical performance measurements have been conducted by Daniel Choukroun. The syntheses have been conducted by Lien Pacquets.

6.1 Introduction

In Chapter 5, highly monodisperse sub-10 nm Cu-Ag bimetallic nanocrystals were synthesized. Nanoparticles with different sizes and shell thicknesses could be obtained. As known from literature, Cu-Ag bimetallic NPs are appealing since they exhibit high faradaic efficiencies towards CO using a reduced amount of Ag compared to monometallic Ag NPs [64]. Additionally, Cu-Ag bimetallic structures are currently also deployed as catalyst for the production of C_2-products [88]–[90], highlighting the great application potential of such catalysts.

Despite the great application potential, Cu-Ag bimetallic electrocatalysts remain under explored. Literature concerning Cu-Ag bimetallic nanocrystals and their performance, is limited and reduces even more when considering sub-10 nm Cu-Ag bimetallic nanoparticles [66], [194], [195]. Therefore, this chapter has been devoted to map the composition-selectivity relationship of unsupported and supported Cu-Ag bimetallic nanocrystals (0 - 41 at% Ag). The influence of the electrolyte cation, the Ag concentration and the difference between a core-shell and nanodimer was investigated.

6.2 Experimental

6.2.1 Chemicals

2-propanol (99.5%, Extra Dry over Molecular Sieve, AcrosSeal® Acros Organics), cesium bicarbonate (99.99%, trace metal basis, Sigma Aldrich), potassium bicarbonate (99.99%, trace metal basis, Sigma Aldrich), Sigracet® 39BC (SGL Carbon), ENSACO®-350G (Imerys Graphite and Carbon), hydrochloric acid (≥37%, TraceSELECT™, Fisher Scientific), nitric acid (≥69%, TraceSELECT™, Fisher Scientific), Selemion® DSVN anion exchange membrane (AGC Engineering Co., Japan),

6.2.2 Synthesis of Cu and Cu-Ag bimetallic nanoparticles

The synthesis has been thoroughly described in Chapter 5 to which the reader is referred for a detailed explanation. All experiments in this chapter have been conducted on these electrocatalysts.

6.2.3 Electrode preparation

Working electrodes (diameter 2.54 cm) were prepared by drop casting particles directly from a Cu-Ag suspension in hexane onto GDEs (Sigracet 39BC, SGL Carbon). Alternatively, a given volume of particle suspension was mixed with carbon black (ENSACO®, Imerys Carbon) under inert atmosphere to achieve a C/Cu ratio of 14 (0.1 M experiments) and electrode carbon loadings of ± 0.35 mg cm^{-2}. The suspension was sonicated under argon atmosphere and left to sediment for several minutes after which the hexane was removed by evaporation. An identical volume of anhydrous 2-propanol was then used to re-disperse the particles. The ink was then sonicated prior to drop casting. Total metal loadings were presented in Table S 6-1.

6.2.4 Electrochemical set-up

Electrochemical measurements were performed using an Autolab M204 potentiostat (Metrohm). Chronopotetiometric electrolysis experiments were conducted in a gas-fed hybrid flow-cell with a recycled catholyte stream (2 ml min^{-1}). The CO_2 (99.996%, Nippon Gases) flow rate, entering the channel, was controlled between 5-7.5 sccm by a mass flow controller (GF-080, Brooks Instruments). The backpressure in the gas channel was measured by a Gefran TK-series pressure sensor with an accuracy of ±2.5 mbar and range of 0-1 barg. Pressure readings were logged using an I/O device (National instruments, NI6000) which was interfaced with MATLAB® R2016a for data recording. A 1 mm Ag/AgCl leak-free electrode (W3-690053, Harvard Apparatus) was used as reference in the cell. Catholyte and anolyte were separated by a Selemion® DSVN anion exchange membrane (AEM). On the anode side, a carbon cloth was used as counter electrode with conductive Al foil as current collector. The uncompensated resistance (iR) and the resulting ohmic drop (IR) were determined using current interrupt and electrochemical impedance spectroscopy. All potentials are reported versus the RHE, unless stated otherwise.

Product analysis was done by (i) feeding the reacted gas stream to an in-line thermo trace 1300 gas chromatograph (GC) equipped with a TCD detector and a micropacked column (ShinCarbon ST 100/120, 2 m, 1 mm ID, Restek) and (ii) quantifying the liquid products by means of high-performance liquid chromatography (HPLC) and GC equipped with a flame ionization detector (FID).

6.3 Results and discussion

6.3.1 Tuning the product selectivity during the eCO_2R

In this work Cu-Ag bimetallic nanoparticles synthesized and characterized in Chapter 5 were used.

6.3.1.1 *Influence of the electrolyte during the eCO_2R*

To investigate the influence of the cation, two different electrolytes were chosen. The first one is $KHCO_3$, which is a very common used electrolyte in literature and was compared to $CsHCO_3$. The use of Cs^+ as a cation has a clear influence on the CO production, which increased significantly from 57.2% to 82.5 % in $KHCO_3$ and $CsHCO_3$, respectively (Figure 6-1). An original hydrogen production of 20.3 % was suppressed to 7.7 % in the presence of Cs^+. Additionally, the enhanced CO production was at the expense of primarily methane, ethanol and ethylene (full FE presented in Table S 6-2).

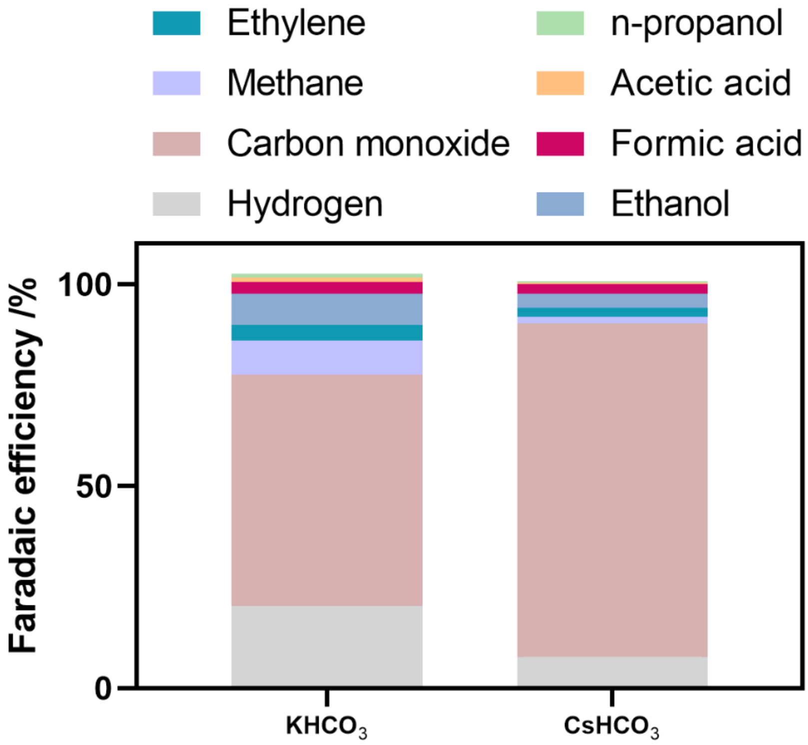

Figure 6-1: CO_2 reduction reaction selectivity of as-prepared Cu0.1Ag17 at 0.1 A cm^{-2} in 0.1 M $KHCO_3$ and $CsHCO_3$

It is clear that the use of Cs^+ as a cation, instead of K^+, proved to be beneficial for the CO production, which is in accordance to literature [196]. The reason behind this is the following: since Cs^+ has a greater radius and thus smaller relative charge compared to K^+, the hydration shell is therefore smaller. This results in a smaller repulsion of Cs^+ in the vicinity of the electrode, resulting in a higher concentration of Cs^+ ions at the electrode surface, since large hydrated cations are energetically more favorable at the Helmholtz plane [197], [198]. This in turn results in a stronger interfacial field, enabling an improved stabilization of surface intermediates with a strong dipole moment such as CO_2. This stabilization decreases the energy necessary for the reduction of adsorbed CO_2.

6.3.1.2 *Influence of the NP structure on the product distribution during eCO₂R*

All further electrochemical experiments were conducted in 0.1 M $CsHCO_3$ because of the promoting role of Cs^+ in multicarbon and carbon monoxide formation over Ag and Cu surfaces [196]. Unsupported Cu-Ag bimetallic nanoparticles are used to study the effect between nanodimers and core-shells.

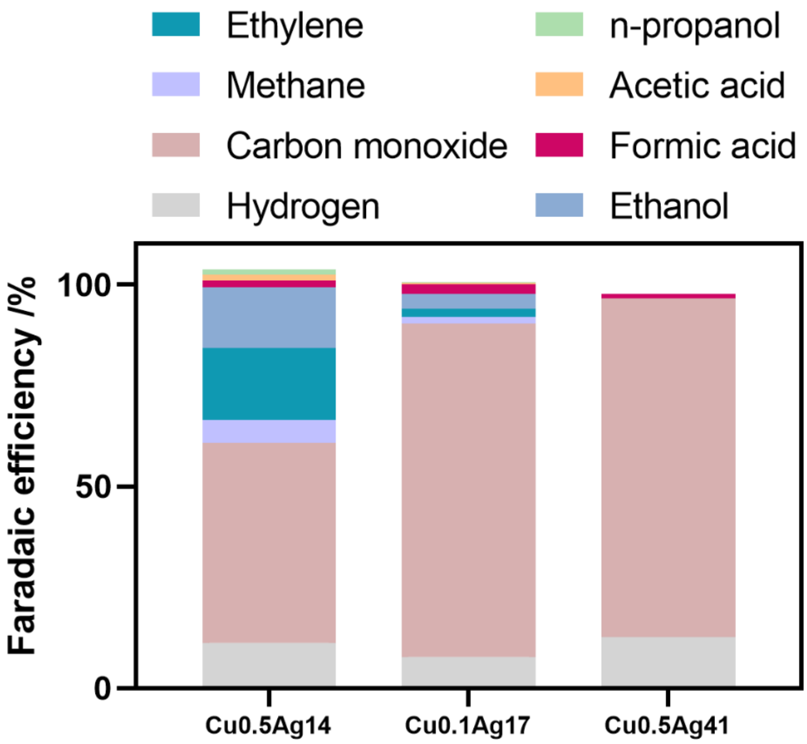

Figure 6-2: eCO_2R reaction selectivity of as-prepared Cu-Ag NPs-based GDEs at 0.1 A cm^{-2} in 0.1 M $CsHCO_3$

Figure 6-2 shows that the transition from partial (Cu0.5Ag14, nanodimer) to complete (Cu0.1Ag17 and Cu0.5Ag41, core-shell) coverage of the Cu cores by Ag was accompanied by an increase of CO_2 reduction selectivity towards CO, the major product typically formed over Ag surfaces. Whereas Cu0.5Ag41 recorded the highest CO selectivity (83.8 %) at -1.2 V_{RHE} (Table S 6-3), Cu0.1Ag17 was not far off with 82.5 % at -1.14 V_{RHE}. Since Cu0.1Ag17 has a complete Ag shell, in contrast to Cu0.5Ag14, the FE towards CO is larger than over Cu0.5Ag14.

Liquid product analysis by HPLC revealed that several C2 and C3 products, such as ethanol, acetate and n-propanol, were formed over Cu0.5Ag14 and to a lesser extent over Cu0.1Ag17, whereas formate was the only measurable liquid product in experiments involving Cu0.5Ag41 electrodes (full FE presented in Table S 6-3).

To further boost the CO_2 reduction and inhibit the HER over Cu-Ag nanocatalysts, we aimed at improving the initial spatial distribution of the Cu-Ag NPs. In the specific case of CO_2 reduction over sub-10-nm spherical Cu NPs, inter-particle distance and packing density (i.e. loading) are known to be crucial parameters for controlling CO_2 reduction selectivity [199]–[201]. Therefore, we tried to at ameliorate the initial spatial distribution of Cu-Ag NPs at the electrode surface by physically mixing nanoparticle suspensions with carbon black.

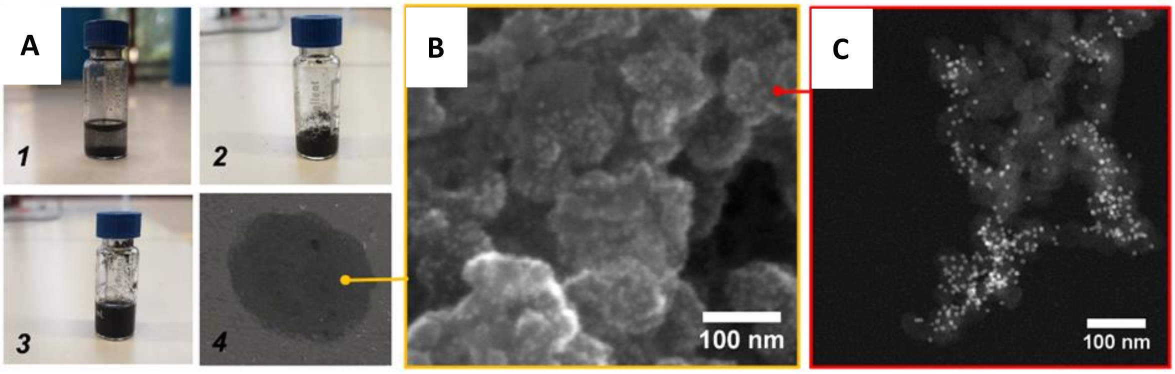

Figure 6-3: (A) Outline of the dispersion procedure: (A1) mixing of C with a Cu-Ag suspension results in adsorption of the particles onto the surface of carbon black after which the Cu-Ag-supporting carbon sediments. (A2) slurry obtained after evaporation of hexane under inert conditions (A3) suspension after mild sonication in anhydrous 2-propanol without binder addition. (A4) drop-cast film on a gas diffusion electrode with a cross-section of ~1 cm^2. (B) SEM image of 11 wt.% Cu0.5Ag14/C (C) HAADF-STEM image of Cu0.1Ag17 NPs on a carbon black nanoaggregate.

The mixing procedure is outlined in Figure 6-3(A), and representative overview SEM and HAADF-STEM images are shown in Figure 6-3(B-C). The SEM and HAADF-STEM images show the distribution of Cu-Ag nanoparticles on the carbon black substrate. Compared to the HAADF-STEM images of the Cu-Ag series in Chapter 5, they are less closely packed, resulting in an improved spatial distribution.

The selectivity profile as a function of at.% Ag is shown in Figure 6-4. The major products formed for all Ag contents were hydrogen, carbon monoxide, methane, ethylene and ethanol. Only small amounts of formic acid, acetic acid and n-propanol were detected.

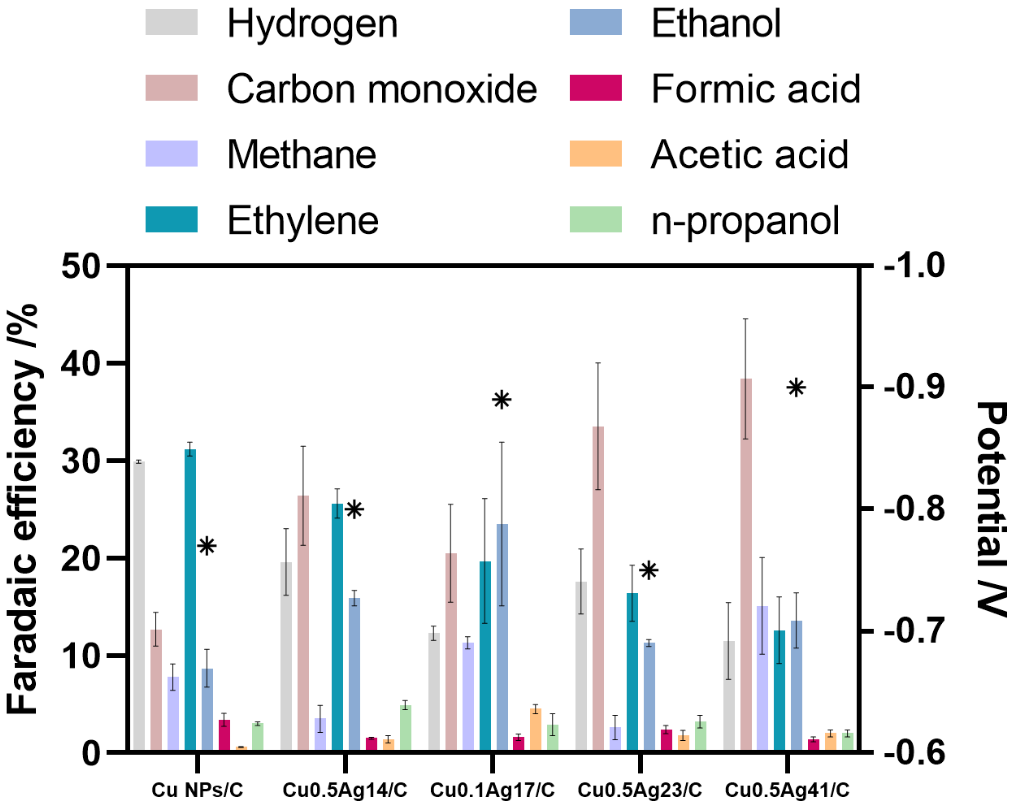

Figure 6-4: Selectivity profile as a function of Ag at.% for Cu-Ag/C electrodes. Experiments were performed at 25°C in 0.1 M $KHCO_3$. A current density of 0.1 A cm^{-2} was applied for a duration of 1 hour. Error bars give the standard deviation of two-three experiments, in which the gas phase was sampled four times over the course of 1 hour and the liquid phase was sampled once after electrolysis ended.

In general, it is clear that hydrogen suppression is occurring on Cu-Ag/C catalysts as compared to the monometallic Cu NPs/C. Ag enrichment in the Cu-Ag thus causes a decrease in hydrogen production. The decrease in HER over Cu-Ag electrodes could be attributed to a reduced H binding strength on Cu surfaces generated upon introduction of Ag [55]. Comparing Cu/Ag nanodimers (Cu0.5Ag14 and Cu0.5Ag23) with Cu@Ag core-shells

(Cu0.1AG17 and Cu0.5Ag41), it is clear that hydrogen production is suppressed even more in case of core-shell catalysts. Increasing the Ag concentration in Cu/Ag nanodimers as well as in Cu@Ag core-shells, reduced the HER.

As for the CO production, a clear improvement is observed upon addition of Ag, which further increased with Ag loading up to a FE of 38.4 % in case of Cu0.5Ag41/C with the exception of Cu0.1Ag17. According to Chang et al. [66], the increased CO production could be attributed to the tensile strain occurring in the Ag surface leading to an improved *CO adsorption at higher Ag contents.

The increased CO production was accompanied by a decrease in ethylene production over Cu-Ag electrodes. The higher the Ag content, the lower the FE to ethylene. Whereas pure Cu NPs/C gave a FE of 31.2%, Cu0.5Ag0.41/C only resulted in a $FE_{Ethylene}$ of 12.6%. Additionally, the share of methane appears to grow at the expense of ethylene in the Cu-Ag series, with the exception of Cu0.5Ag23 (due in part to its lower electrode potential) where it decreased again. The reduction of ethylene as a function of increasing Ag concentration was already observed in literature [38], [95]. They showed that there is a balance between Cu core and Ag shell for the electrochemical CO_2 reduction performance. They hypothesize Cu-Ag nanoparticles operate as a tandem catalyst where the CO_2 reduction will pursuit as a two-step reaction process. CO_2 will first adsorb and convert to CO on the Ag surface, and subsequently be converted to C_{2+} products on the Cu surface. If the concentration of Ag is too high, the rate of the CO production is much bigger than the rate of the C-C coupling.

Furthermore, it was noted that the ethanol and acetic acid production were promoted when Ag was added to the catalyst and this at the expense of the ethylene production. Researchers have demonstrated that the selectivity determining intermediate between ethanol and ethylene is likely $*CH_2CHO$, which is claimed to bond weakly through an oxygen atom to the surface of Cu and even more weakly to Ag and Au [46]. According to Clark et al. [45], the enhanced oxygenate production along with the suppression of the HER over Cu-Ag catalysts could be attributed to the reduced oxophilicity and H binding strength of Cu surface atoms, which is induced by compressive strain, imposed by the larger neighboring Ag atoms. Alternatively, Li et al. [47] calculated that doping Cu(111) with Ag increases the number of different binding sites 4-fold, yielding Cu atoms in the vicinity of Ag with a lower affinity to carbon, rather than to oxygen, which was claimed to destabilize the ethylene pathway and thus to promote ethanol formation. Enhanced ethanol selectivity was also linked to a higher local *CO concentration and to CO spillover from Ag ensembles to Cu ensembles [89], [94].

6.4 Conclusions

The performance of the Cu-Ag bimetallic catalysts, synthesized in Chapter 5, was investigated. First, the influence of the electrolyte was demonstrated. Replacing K^+ with Cs^+ led to a shift in selectivity which increased the CO production, whereas the selectivity towards hydrogen, methane and ethanol decreased.

Secondly, dispersing the nanoparticles on carbon black at high packing densities, facilitated considerably the mapping of the composition-selectivity relationship in the range of Ag atomic percentages between 14 and 41 at.%. Consequently, the Ag/Cu ratio can be regarded as an imaginary slider button that lowers the average binding energy of *CO in the entire system, resulting in an increased CO production when increasing the Ag concentration. This was accompanied by the suppression of the HER. Subsequently, CO_2 reduction reaction selectivity shifted from ethylene formation to ethanol between Cu NPs/C and Cu-Ag/C based electrodes. Remarkably, the production of methane was boosted over Cu@Ag core-shell nanoparticles, in contrast to Cu/Ag nanodimers.

To conclude, variations of the Ag concentration in Cu-Ag nanocatalysts could alter the product selectivity. By tuning the Cu-Ag nanocatalysts, the product distribution can be shifted between CO and C_{2+} products, which highlights their great application potential. In addition, integration of sub-10 nm Cu-Ag nanocrystals into more advanced carbon-based CO_2 reduction interfaces could enable further optimization of the product selectivity over Cu-Ag nanocatalysts.

6.5 Supporting information

Table S 6-1: Overview of Cu and Ag loading measured by ICP-MS

Sample	Cu loading /µg cm^{-2}	Ag loading /µg cm^{-2}
Cu NPs/C	29	-
Cu0.5Ag14/C	36	7
Cu0.5Ag23/C	28	28
Cu0.5Ag41/C	19	13
Cu0.1Ag17/C	18	5

Table S 6-2: Performance of Cu@$Ag_{0.17}$ electrodes in 0.1 M $CsHCO_3$ and $KHCO_3$ at 0.1 A cm^{-2}

	Faradaic efficiency (%)									
Catalyst	Gas phase				Liquid phase					
	H_2	CO	CH_4	C_2H_4	EtOH	Formate	Acetate	PrOH	Acetaldehyde	Glyoxal
$KHCO_3$	20.3	57.2	8.4	4.0	7.6	3.0	1.0	1.0	-	-
$CsHCO_3$	7.7	82.5	1.7	3.6	3.6	2.4	0.3	0.3	-	-

Table S 6-3: Performance of Cu-Ag electrodes in 0.1 M $CsHCO_3$ at 0.1 A cm^{-2}

		Faradaic efficiency (%)									
Catalyst	|E| (V_{RHE})	Gas phase				Liquid phase					
		H_2	CO	CH_4	C_2H_4	EtOH	Formate	Acetate	PrOH	Acetaldehyde	Glyoxal
Cu0.5Ag14	1.08	11.2	49.5	5.7	17.9	15.0	1.6	1.4	1.4	0.7	traces
Cu0.1Ag17	1.14	7.7	82.5	1.7	3.6	3.6	2.4	0.3	0.3	-	-
Cu0.5Ag41	1.2	12.7	83.8	-	-	-	1.2	-	-	-	-

Table S 6-4: Performance of Cu-Ag/C electrodes in 0.1 M $KHCO_3$ at 0.1 A cm^{-2}

		Faradaic efficiency (%)									
Catalyst	|E| (V_{RHE})	Gas phase				Liquid phase					
		H_2	CO	CH_4	C_2H_4	EtOH	Formate	Acetate	PrOH	Acetaldehyde	Allyl alcohol
Cu NPs/C	0.77	29.9	12.7	7.8	31.2	8.7	3.4	0.6	3.0	0.7	-
Cu0.5Ag14/C	0.8	19.6	26.4	3.5	25.6	15.9	1.5	1.4	4.9	-	-
Cu0.1Ag17/C	0.89	12.3	20.5	11.3	19.7	23.5	1.6	4.5	2.9	-	-
Cu0.5Ag23/C	0.75	17.6	33.5	2.6	16.4	11.3	2.4	1.8	3.2	-	1.4
Cu0.5Ag41/C	0.9	11.5	38.4	15.1	12.6	13.6	1.4	2.0	2.0	-	-

PART III

Stability of Cu-Ag bimetallic electrocatalysts

CHAPTER 7:

Structural transformation of Cu@Ag core-shell nanoparticles under CO_2 operating conditions

This chapter elucidates the structural tranformation mechanism of Cu@Ag core-shell NPs during the eCO_2R. The Cu@Ag core-shell NPs are analyzed under CO_2 operating conditions. The structural changes are mapped by electron tomography at different stages during operation. Accordingly, the performance of the electrocatalyst is linked to the morphological transformation observed within the electron tomography series.

This chapter is in preparation to be submitted as: Daniel Arenas-Esteban[§], Lien Pacquets[§], Daniel Choukroun, Saskia Hoekx, Jonathan Schalck, Nick Daems, Tom Breugelmans, Sara Bals, 3D characterization of the structural transformation undergone by Cu@Ag core-shell nanoparticles during CO_2 reduction reaction, ACS Nano, 2022, submitted

[§]*These authors contributed equally to this work. Daniel Arenas-Esteban performed the microscopic, Lien Pacquets conducted the electrochemical analysis, Daniel Choukroun designed the hybrid flow cell and assisted with the synthesis of the NPs, Saskia Hoekx performed the TEM analysis of the Cu NPs, Jonathan Schalck designed the batch cell.*

7.1 Introduction

In Chapter 5, the differences between core-shells and nanodimers and the influence of electrolyte cation and the concentration of Ag were investigated. By switching between a fully and a partially covered Ag shell, the selectivity towards CO could be tuned. Upon increasing the Ag concentration, the CO production was promoted and the core-shell structure yielded the highest amount of CO. Additionally, introduction of these NPs into a carbon structure has led to the decrease of the HER.

Despite the promising research on altering the product selectivity and boosting the activity of the Cu-Ag bimetallic electrocatalysts, the morphological changes and the their effect on the electrochemical performance of the bimetallic electrocatalyst remains underexplored [202]. These structural changes can cause unreliable electrocatalytic performances, which is why the correlation between selectivity and morphology of the electrocatalyst is of crucial importance to create insights into structural transformation pathways in order to potentially anticipate on this and be able to progress towards highly stable electrocatalysts.

It is already known that catalysts used during electrochemical experiments exerience destabilization [200], [203], [204] and recent literature showed the crucial role of CO formation in the degradation of Cu-based catalysts [205]. Nevertheless, the 3D characterization of the core-shell particles and the link with the changing selectivity profile is still missing. Therefore this chapter has been devoted to investigate the effect of electrochemical stress on Cu@Ag core-shell NPs morphology/structure by electron tomography at different stages of the electrochemical CO_2 reduction. Their morphological/structural changes were analyzed in 3D and linked to the selectivity profile of the CO_2 reduction. These new insights allow a better understanding on how this type of NPs behave during its catalytic performance and how this restructuring can potentially be prevented.

7.2 Experimental

7.2.1 Chemicals

Copper(II) acetate monohydrate (Cu(II)OAc, p.a., Janssen Chimica), Trioctylamine (TOA, 97%, Acros Organics), Tetradecylphosphonic acid (TDPA, 98%, Sigma Aldrich), Isoamyl ether (IAE, 99%, Sigma Aldrich), silver trifluoroacetate (Ag-TFA, 99.99%, trace metal basis, Sigma

Aldrich), Ethanol (99.5% Extra Dry, AcrosSeal®, Acros Organics), iso-propanol (99.5%, AcrosSeal® Acros Organics), Potassium bicarbonate (Chem-Lab, 99,5%), Sigracet® 39BC (SGL Carbon) and Selemion® DSVN anion exchange membrane (AGC Engineering Co., Japan) were used during this research. All solutions were prepared with ultra-pure water (MQ, Milli-Q grade, 18.2 MΩcm).

7.2.2 Preparation of Cu@Ag core-shell NPs

A detailed description of the preparation can be found in Chapter 5.

7.2.3 Grid preparation

The electrochemical degradation of Cu@Ag core-shell NPs under CO_2 reduction environment, caused by applying a current, was explored. Therefore, charges of 17.8 mC, 23.5 mC and 70.6 mC were imposed onto a TEM grid in an in-house made electrochemical batch set-up (Figure 7-1) to analyze the intermediate steps.

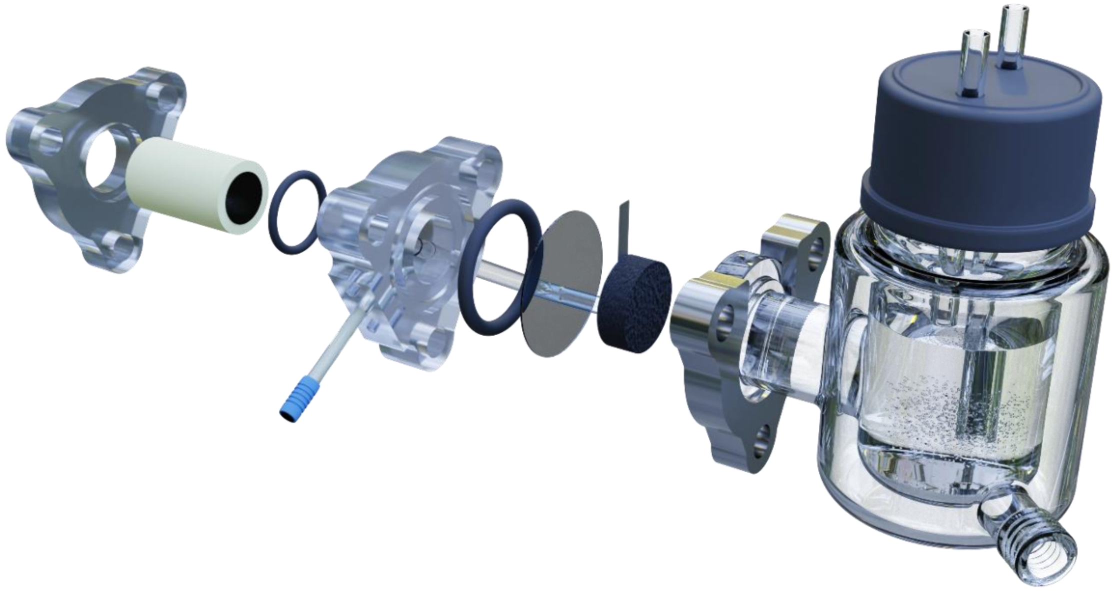

Figure 7-1: Electrochemical batch set-up

This set-up can be divided into two compartments of which a cathodic and anodic one. The cathodic compartment consisted of a glassy carbon WE with a, Cu@Ag core-shell NPs containing, TEM grid attached. The RE was placed in the vicinity of the WE to limit the ohmic resistance. CO_2 gas was fed into the catholyte (1 M $KHCO_3$) at 7.5 sccm, where it could react on the Cu@Ag catalyst. The anodic compartment consisted of an H-type half-cell with a carbon cloth serving as a CE. A Selemion® DSVN anion exchange membrane separated the anolyte (1 M $KHCO_3$) and catholyte. Afterwards, the TEM grid was washed with Milli Q and dried with an Ar flow.

7.2.4 Electron microscopic investigation

HAADF-STEM has been performed on an aberration-corrected cubed FEI Titan microscope operating at 300 kV. Electron tomography tilt series were acquired using a Fischione 2020 tomography holder between -75° and 75° with a tilt step of 3°. The projection images were acquired using 5 frames at 0.5 µs dwell time, while the image resolution was set to 2048x2048 pixels. The obtained series were aligned using cross-correlation and 3D reconstructions were obtained using the Expectation Maximization (EM) algorithm, as implemented in Astra Toolbox [206], [207]. EDS analysis were performed by acquiring at least 100 frames at a higher dosage of $2 \cdot 10^4$ e/A^2 to ensure enough counts.

7.2.5 Electrochemical investigation

The electrochemical behavior of the as-prepared Cu@Ag core-shell NPs was investigated in first instance by cyclic voltammetry with a multi Autolab n204 potentiostat. A three electrode system was used employing a glassy carbon (GC) with dropcasted Cu@Ag core-shell WE, an Ag/AgCl$_{sat}$ RE and a carbon cloth CE. All potentials in this work will be presented vs the RHE. A stated potential range was scanned at 100 mV s^{-1} between 0.21 V_{RHE} and 1.7 V_{RHE}, which comprises the different oxidation states of Cu and Ag in an Ar saturated 0.1 M KOH solution at room temperature.

The degradation of Cu@Ag core-shell was electrochemically evaluated by a CP experiment, using the in-house made hydrid flow cell as described in Chapter 6. 1 M $KHCO_3$ was used as anolyte and catholyte, with a catholyte flow of 0.2 mL min^{-1}. CO_2 was fed in flow-by mode at a flow rate of 7.5 sccm.

7.3 Results

7.3.1 Electron microscopic characterization

Sub-10 nm Cu@Ag core-shell NPs were successfully synthesized using a TOA thermal decomposition method with subsequently two galvanic displacement reaction steps. As discussed in Chapter 5, the thermal decomposition allowed the formation of highly monodisperse sub-10 nm Cu NPs, as presented in Figure 7-2.

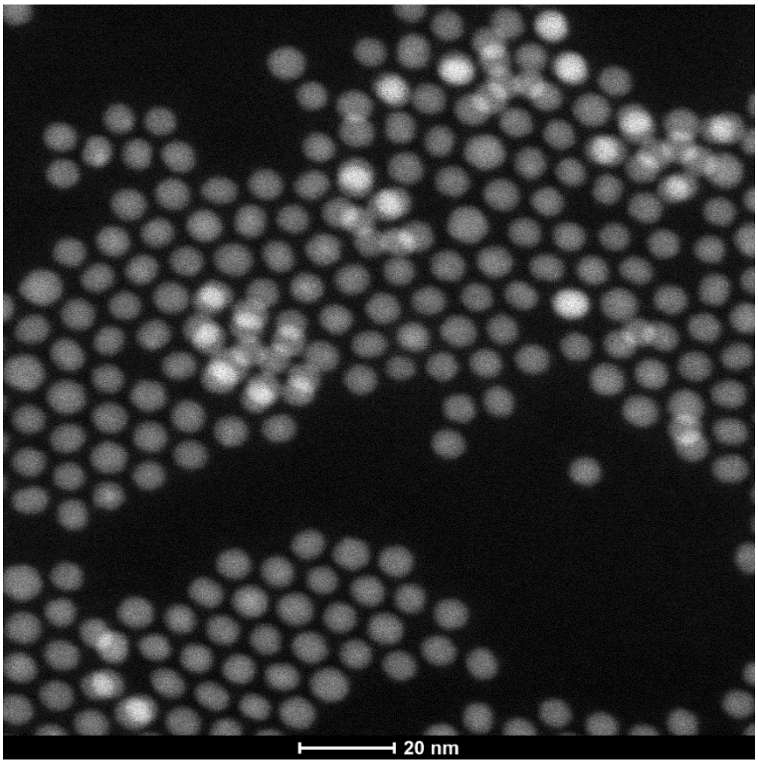

Figure 7-2: HAADF-STEM image of monodisperse sub-10 nm Cu NPs

Subsequently, a first galvanic displacement step was performed at room temperature for two hours and was ensued by a second replacement with Ag at 90 °C. The latter reaction ensured the formation of a core-shell structure with a composition determined by EDS of 40 at% and 60 at% of Ag and Cu, respectively.

The core-shell nanoparticles obtained, following the abovementioned method, show a high degree of homogeneity in shape and size as can be observed in the low magnification HAADF-STEM image as well as in the particle size distribution analysis presented in Figure 7-3a, showing a narrow average particle size of 6,27 nm.

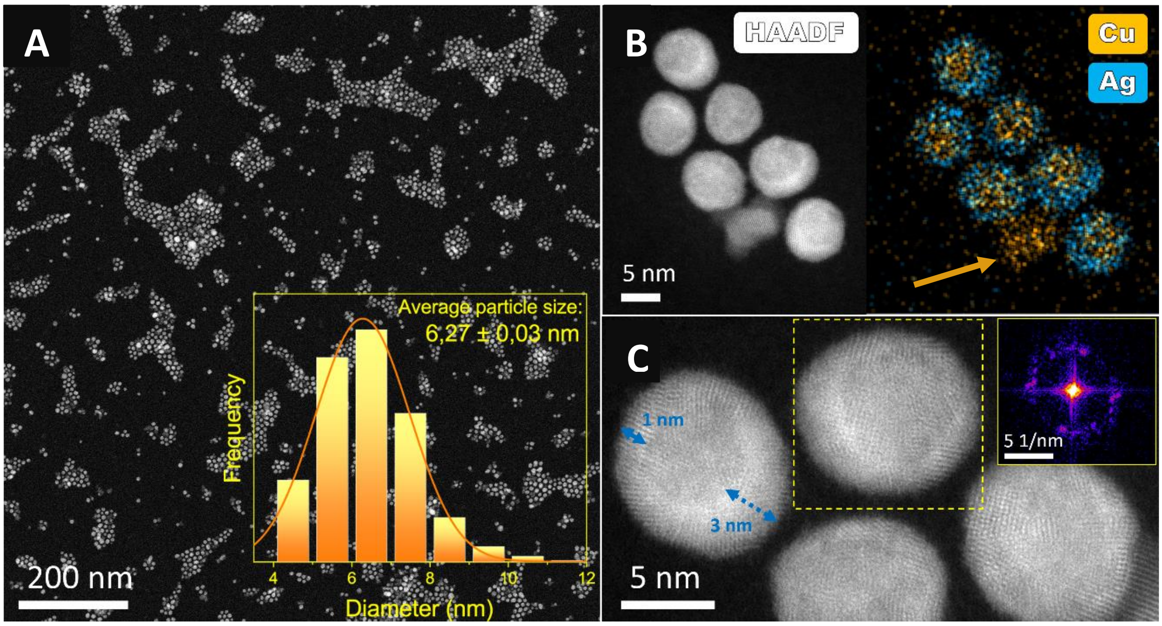

Figure 7-3: (A) Low magnification HAADF-STEM image of the Cu@Ag NPs and particle size distribution analysis. (B) EDS analysis performed on few Cu@Ag NPs demonstrating its core-shell element distribution. (C) Atomic resolution detail and inset FFT performed over the nanoparticle marked by a yellow square where the uneven and polycrystalline Ag shell can be visualized.

The EDS maps in Figure 7-3 (B) show that most NPs indeed yield a core-shell structure although occasionally, bare Cu NPs are observed (indicated with the orange arrow). The high resolution HAADF-STEM image in Figure 7-3 (C) clearly shows a polycrystalline Ag shell. This observation is confirmed by the FFT of the part of the image marked with a yellow square, in which a quasi-circular diffraction diagram can be observed. In addition, we observed that the polycrystalline Ag shells yield a non-uniform thickness. For example, the blue arrows in Figure 7-3 (C). indicate parts of a shell with a thickness of 3 nm versus 1 nm.

7.3.2 Electrochemical performance

The performance of the Cu@Ag core-shell nanoparticles was tested for the electrochemical CO_2 reduction (eCO_2R) by performing a chronopotentiometry experiment at 75 mA cm^{-2} for 600 s in a hybrid-flow reactor. The corresponding selectivity profile is depicted in Figure 7-4, along with the potential distribution during the experiment.

Initially, a potential of -2.06 V_{RHE} was recorded after 10 s of measuring and remained stable until 30 s. The potential then increased up to -2.45 V_{RHE} at 60 s and finally after 600 s, a potential of -2.53 V_{RHE} was recorded as presented in Figure 7-4. The increase in potential by 0.47 V_{RHE}, can possibly be attributed to structural changes in the initial Cu@Ag structure (e.g. changing availability of Cu at the surface of the NP, changing size due to possible agglomeration,..), as Cu is known to have a higher resistivity compared to Ag [208].

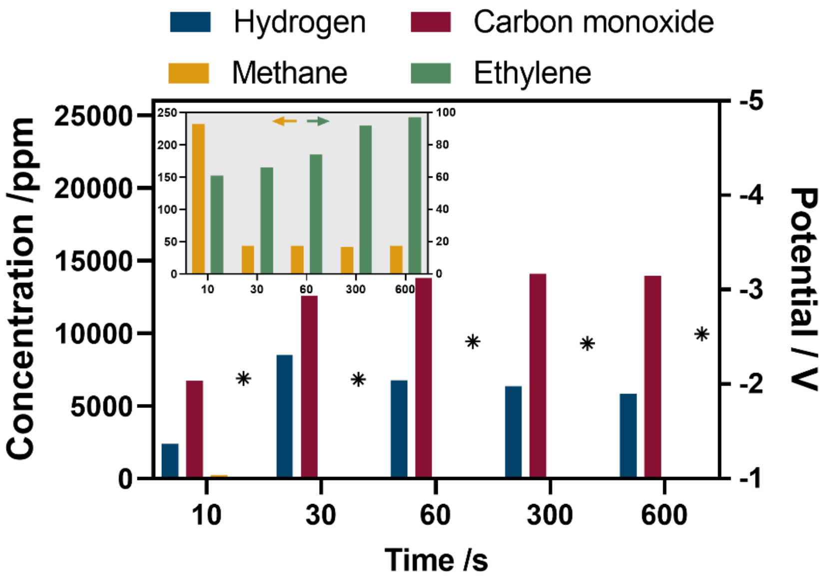

Figure 7-4: Evolution of the gas-phase selectivity of unsupported Cu@Ag core-shell NPs at 75 mA cm^{-2} during a 600 s long experiment with gas-phase analysis at 10 s, 30 s, 60 s, 300 s and 600 s. Experiments were performed in 1 M $KHCO_3$ with a CO_2 flow rate of 7.5 sccm and a catholyte recycle flow of 0.2 mL min^{-2}.

After 10 s of applying a current density of 75 mA cm^{-2} in a CO_2 reduction environment, hydrogen and CO accounted for 2403 ppm and 6747 ppm, respectively. Their concentrations increased after 30 s without any major changes in potential (0.01 V_{RHE} difference). Thereafter, no major concentration changes for CO were observed, whereas the hydrogen concentration kept decreasing slowly to 5835 ppm after 600 s.

Remarkably, these Cu@Ag core-shells can produce up to 232 ppm of methane during a short time window. Nevertheless, the concentration dropped to 44 ppm after 30 s and remained stable during the remaining time of the experiment. Finally, an increase in the ethylene production can be observed from 61 ppm (10 s) to 97 ppm (600 s).

To explain the evolution in performance for the eCO_2R and potentially link the impact of electrochemical stress with core-shell structural changes, their behavior was further analyzed using cyclic voltammetry. The experiment was performed in an Ar saturated 0.1 M KOH solution, scanning in a potential window from 0.68 V_{RHE} to 1.78 V_{RHE} at a scan rate of 100 mV s^{-1}. These boundaries were chosen such that they contain the different oxidation states of Cu and Ag, as presented in Figure 7-3.

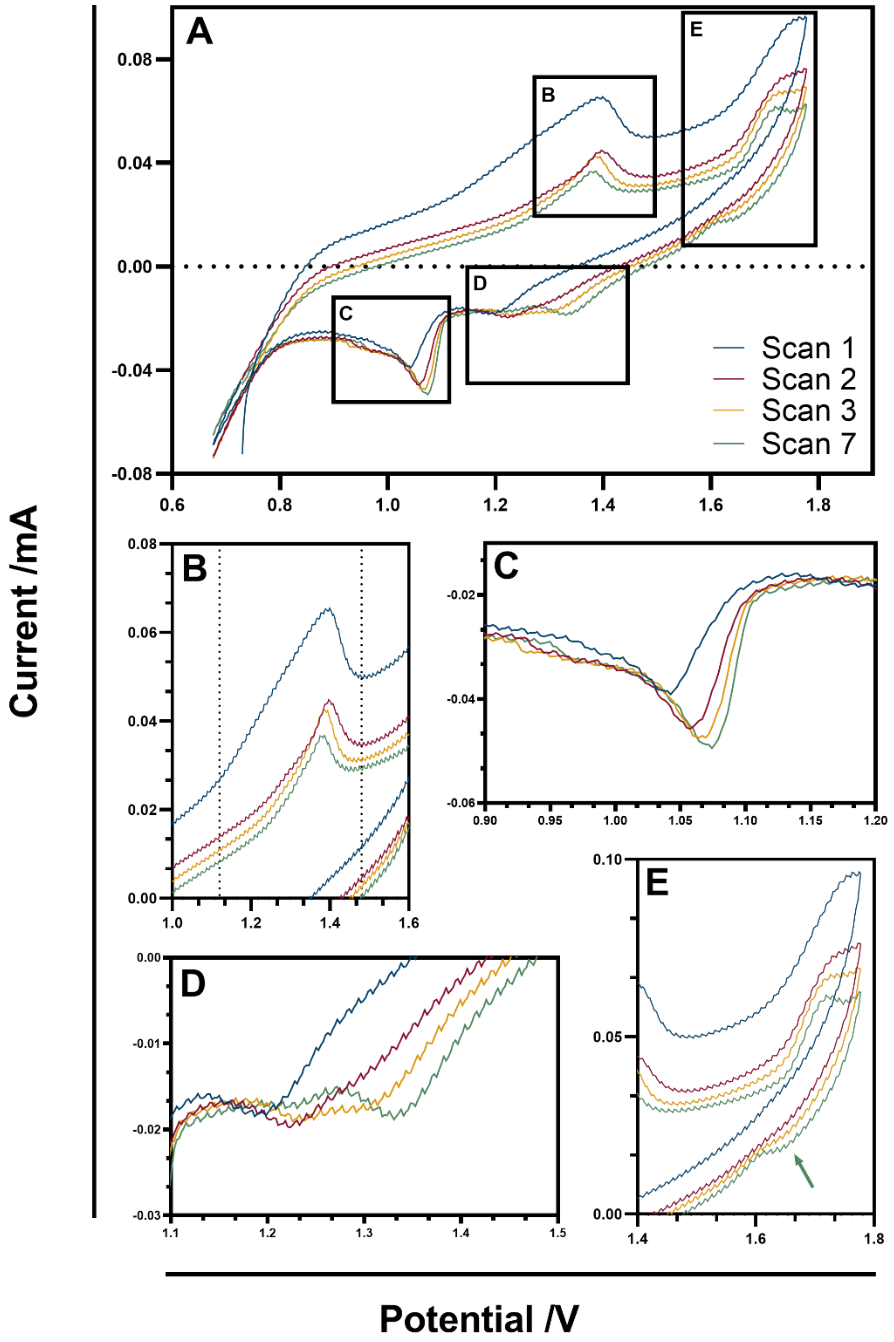

Figure 7-5: Cyclic voltammogram of Cu@Ag core-shell in Ar-saturated 0.1 M KOH at 100 mV s^{-1} within a range of 0.68 V_{RHE} to 1.78 V_{RHE} of the first (blue), second (red), third (orange) and seventh (green) scan. The oxidation/reduction of Ag (B) and the reduction peaks of Cu (C) and (D) are highlighted.

Unsupported nanoparticles were used, which means they are free to move across the surface of the electrode when the experiment is performed, which is preferred to accurately study the structural transformation pattern of the nanoparticles, eliminating the influence of an additional (typically carbon) support.

During the first scan, a broad convoluted oxidation peak appeared between 1.13 V_{RHE} and 1.47 V_{RHE} (presented in Figure 7-3 (B)), indicating the formation of Cu^+ and Cu^{2+}, consisting of the formation of Cu^+ and Cu^{2+}, as observed previously in sub-10 nm Cu@Ag core-shell NPs [54]. In addition, a very weak anodic feature appeared at 1.72 V_{RHE}, corresponding to the oxidation of Ag. This anodic feature increased in strength as the number of scans increased to seven, as shown in Figure 7-3 (E). This, in turn, provoked the presence of a Ag reduction shoulder around 1.65 V_{RHE} with increased scan number (indicated by the green arrow).

In the cathodic scan, the Cu reduction peak at 1.04 V_{RHE} (highlighted in Figure 7-3 (C)) was preceded by a smaller one at 1.20 V_{RHE} (presented in Figure 7-3 (D)), representing the reduction of the Cu^+ to metallic Cu^0 and Cu^{2+} to Cu^+, respectively. Both cathodic peaks encountered an anodic shift with increased cycle number. The reduction peak at 1.20 V_{RHE}, present in the first scan, lost its intensity already in the second scan. Moreover, during the third scan, the reduction peak was preceded by a cathodic shoulder, which increased in intensity when reaching the seventh cycle. Finally, the reduction peak located at 1.04 V_{RHE} increased in magnitude at higher scan number. This evolution in cathodic peaks can potentially be attributed to the reconstruction of the Cu^+ surface [209] and possible Cu enrichment at the surface [45]. This is a first indication that electrochemical stress causes the Cu@Ag core-shell structure to change. However, the investigation of structural details such as crystallinity and interface strain require a 3D characterization of these complex core-shell nanoparticles at the atomic level.

7.3.3 Structural transformation of Cu@Ag core-shell nanoparticles under CO_2 operating conditions

To couple the observations obtained by cyclic voltammetry with possible restructuring of the Cu@Ag core-shell structure, an in-depth 3D characterization by TEM was performed. First, the initial Cu@Ag core-shell structure was reconstructed in 3D by electron tomography. A high resolution HAADF-STEM tilt series was acquired over a tilt range between ±75° with a tilt increment of 3°. In order to obtain atomic resolution in 3D, a recently developed approach was used for which we acquired a time series of images for every tilt angle at a short dwell time [210]. Next, we used these images as input for a non-rigid registration method in combination with a convolutional neural network (CNN) [210].

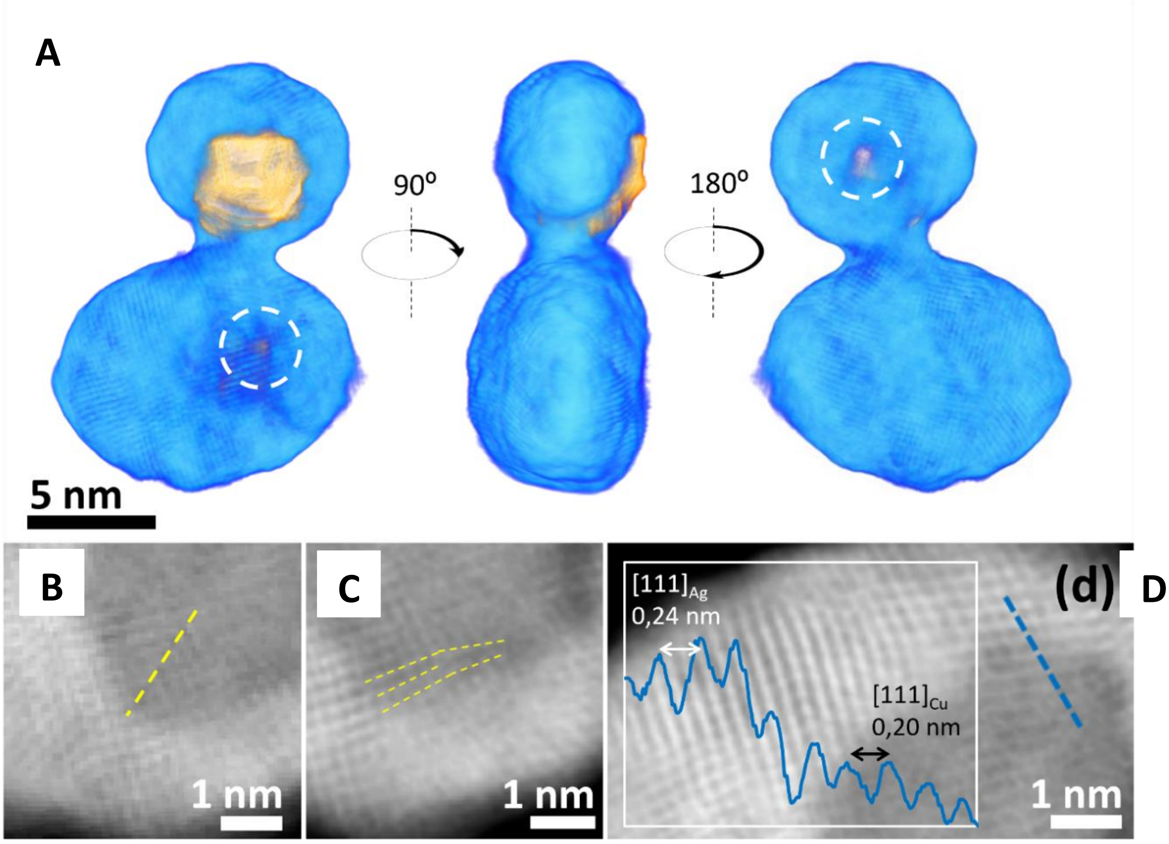

Figure 7-6: (A) 3D visualizations of an electron tomography reconstruction of two connected Cu@Ag core-shell NPs imaged along different viewing directions. (B) Orthoslices through the 3D reconstruction reveal the presence of defects such as twin planes or (C) edge dislocations in the Cu core. (D) An intensity line scan acquired from an orthoslice across the core-shell interface shows different distances along the 111 direction corresponding to the fcc crystal structure of Ag and Cu.

After aligning all projection images, a 3D reconstruction was obtained by using the EM algorithm. 3D visualizations of the reconstructed data set are presented in Figure 7-6 (A) and Supporting movie 7-1. These results show that the Cu NPs appear to be spherical, but because of the non-uniformity of the Ag shell, the Cu@Ag core-shell system yields an oval shape. Moreover, we observed that for some nanoparticles, the Ag shell is not uniform and small pin holes in the Ag shell were present as highlighted in the image by white dashed circles. These findings are consistent with theoretical studies, which indicated that Ag can form a complete stable shell around Cu nanoparticles, despite the fact that the construction of a perfect Janus core shell structure is not energetically favored [211]. From orthoslices through the 3D reconstruction of one of the Cu@Ag NP, the atomic lattice of the core and shell could be visualised. The orthoslices moreover show several crystal defects that were present in the interior of the Cu core, such as twin planes and edge dislocations (Figure 7-6 (B) and (C), respectively). It is likely that these defects induced the polycrystalline character of the Ag shell. From one of the orthoslices, an intensity line profile across the Ag-Cu interface was acquired as illustrated in Figure 4d. For uncoated Cu, oxidation is likely to occur after exposure to air, leading to the formation of CuO. The (111) interplanar distance of CuO is close to that of Ag (i.e. 0.24 nm, Fm-3m). However, from Figure 7-6 (D), a (111) interplanar distance was observed that corresponds to the expected distance for metallic Cu (i.e. 0.20 nm, Fm-3m). These observation suggest that the presence of the pinholes is insufficient to oxidize the core of the Cu@Ag NP.

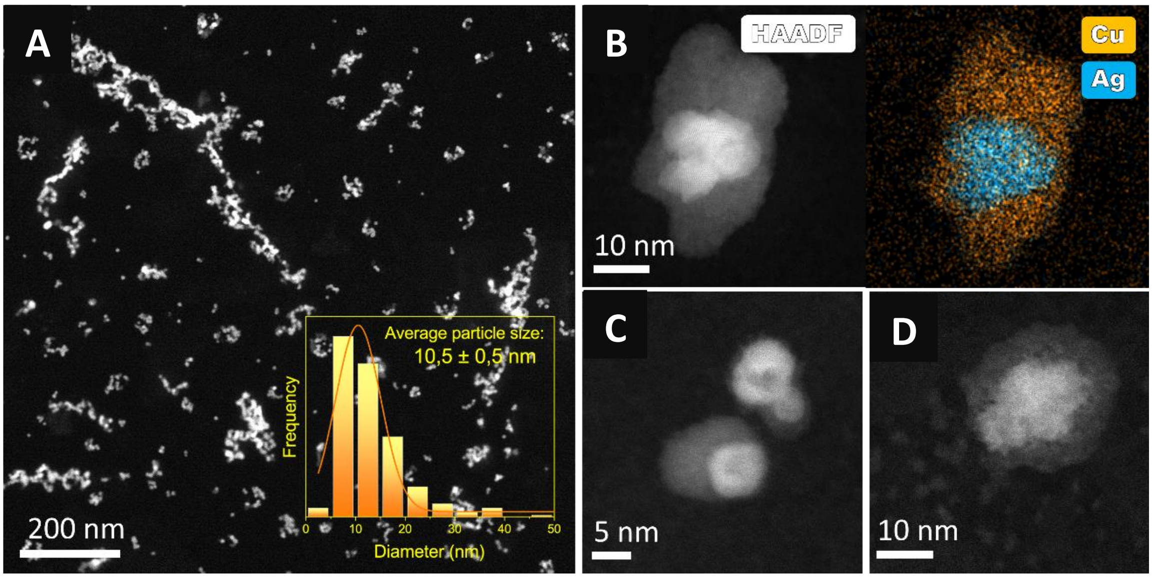

Figure 7-7: (A) Low magnification HAADF-STEM image and particle size distribution analysis of the Cu@Ag NPs from figure 1 after being exposed to a total charge of 70.6 mC. (B) EDS analysis performed on one of the new structures where the elementary distribution in the core shell seems to be inverted, identifying the Cu as the low intensity material in the HAADF-STEM image. (C) High resolution detail of the NPs showing Cu leaching, and (D) an agglomeration of solid Ag NPs where Cu can be detected scattered around it.

In order to understand the evolution of the Cu@Ag core-shell nanostructure during electrocatalysis, a total charge of 70.6 mC was applied to the same TEM grid as used for the characterization in Figure 7-3 and Figure 7-6**Error! Reference source not found.**. The low magnification HAADF-STEM image in Figure 7-7 (A) shows a higher degree of agglomeration between NPs as compared to their initial appearance shown in Figure 7-3. Consequently, the particle size distribution is much broader than in the previous case resulting in a mean particle size of 10.5 nm. A more detailed investigation of the sample revealed that different nanostructure transformations had occurred. The EDS map in Figure 7-7 (B) shows a NP fow which the core-shell elemental distribution was inverted. It can be seen that the Cu (low intensity in the HAADF-STEM image) was covering an Ag solid core (high intensity in the HAADF-STEM image). Moreover, different structures were also found where Cu was partially leaching from the original core-shell structures (Figure 7-7 (C)) and was segregating from the core-shell structure as smaller nanoparticles (Figure 7-7 (D)).

From these observations, we conclude that the transformation of Cu@Ag nanoparticles under electrical current did not occur in a synchronized manner. To obtain further insights, we again performed atomic resolution electron tomography, in this case for different selected nanoparticles.

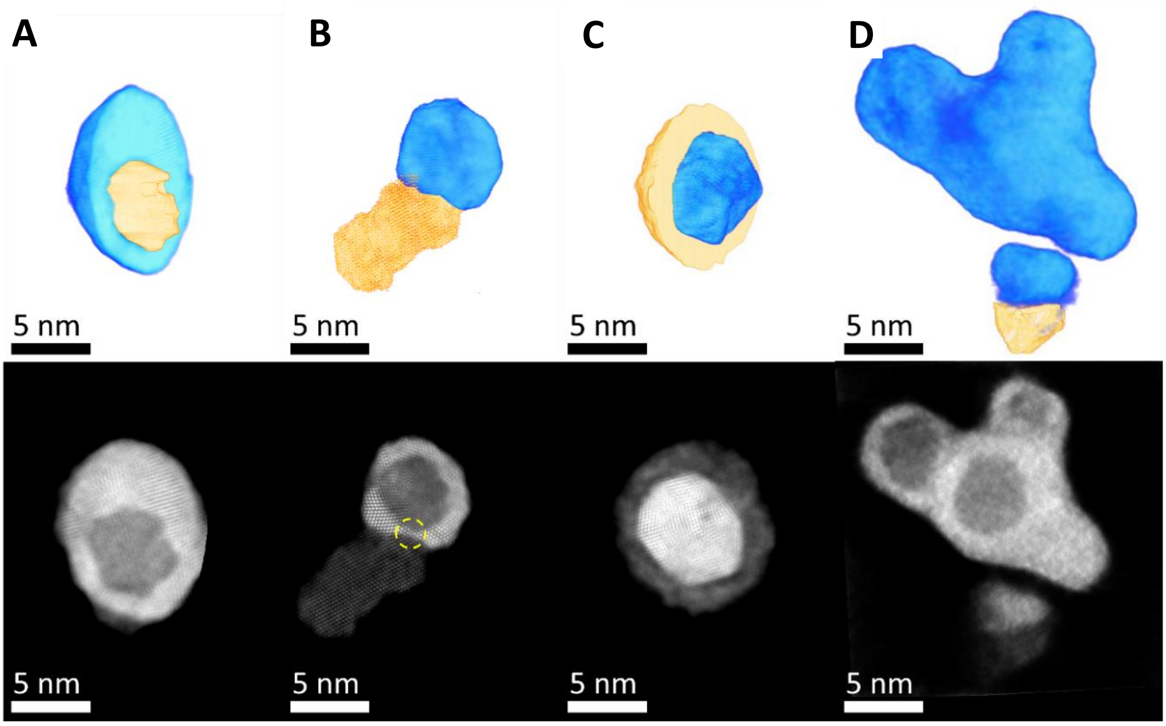

Figure 7-8: 3D reconstruction and their respective orthoslices for the Cu@Ag NPs proposed degradation mechanism. The pinhole area where the leaching starts is highlighted by a yellow dashed circle.

The results are presented in Figure 7-8 and in Supporting movie 7-2. Starting from the previously characterized Cu@Ag core-shell structure with high shell coverage (Figure 7-8 (A), before electrocatalysis), the transformation process seems to start with the Cu leaching from the nanoparticle core through one of the thinner Ag shell areas where atomic size pinholes where observed (Figure 7-8 (B)). The Cu later oxidizes on the outside forming CuO as can be observed in the crystallographic analysis shown in the Supporting Information (Figure 7-9) carried out in the projection image corresponding to 0 degrees from the tilt series.

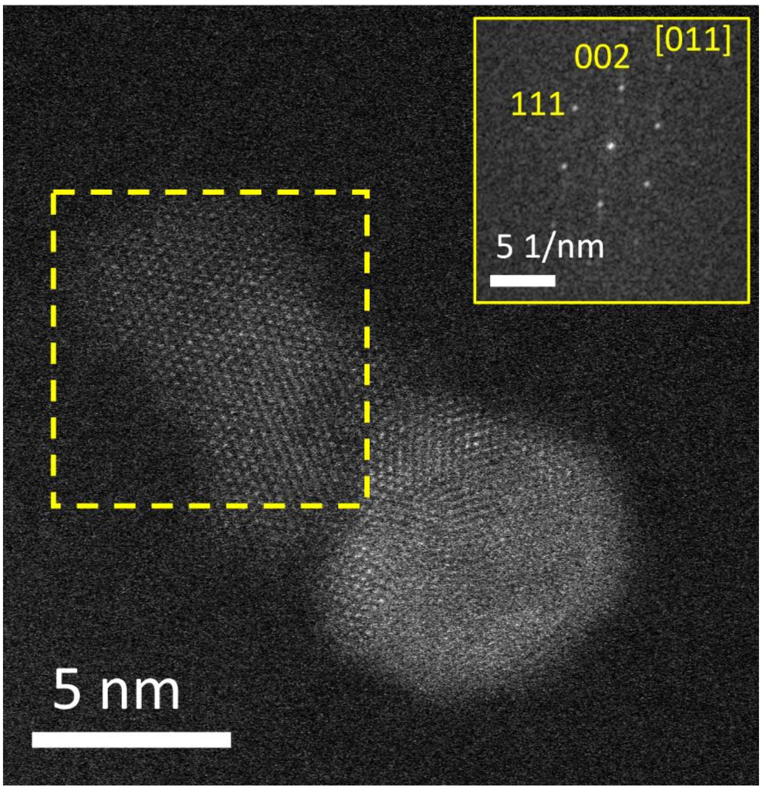

Figure 7-9: HAADF-STEM image projection obtained at 0 degrees for the reconstruction shown on Figure 5b where the FFT performed over the Cu area (low intensity) highlighted by a yellow dashed square show the 011 zone axis for the CuO structure.

Hereafter, CuO rearranges to cover the Ag nanoparticle in a completely inverted Ag@Cu core-shell structure (Figure 7-8 (C)). If close to other Ag nanoparticles, merging of the Ag@Cu core-shell structures was observed (Figure 7-8 (D)). This conversion pathway is supported by the 2D images from Figure 7-7, which show that Cu will eventually fragment into nanoclusters throughout the substrate (Figure 7-7 (D)), meanwhile, the Ag will continue to agglomerate and self-sinter into long chains (Figure 7-7 (A)) [19].

7.3.4 Discussion

It is clear that the transformation of Cu@Ag core-shell nanoparticles occured in two stages. The first stage is characterized by the leaching of Cu from the core-shell through pinholes in the Ag shell . Recent studies showed CO adsorption to be the key factor in destabilization of Cu [212]–[214]. Since the formation of a complete homogeneous Ag shell is not energetically stable, CO molecules (generated on the Ag shell) can always find their way to the Cu surface, where their negative Cu-CO interface energy represents a strong driving force towards Cu leaching and hereafter CuO is formed [203]. The second stage of the transformation is the agglomeration of the Ag shells. Such a two-step process has recently been observed for CuZn nanoparticles under CO_2 reaction conditions, where Cu degrades immediately, Zn degradation progresses slowly [215].

This two-step conversion mechanism could potentially be the cause for the changes observed during the eCO_2R (Figure 7-4) and the CV (Figure 7-5) experiment. The ethylene production increased along the course of the experiment due to the modification of the Cu/Ag interface and the increased availability of Cu at the surface [54], [66], which is crucial for the C-C coupling [45], [216]. The rapid decrease in methane production can be related to the changing Ag/Cu ratio along the experiment. During the first stages of the experiment, the Ag/Cu ratio decreases rapidly, due to leaching of Cu to the surface, increasing its share at the surface. Recent research showed that increasing the concentration of Cu, in Cu-Ag as well as Cu-Au, suppressed the methane formation [54], [217]. Note that the changes in methane production can also be attributed to the availability of CO at the electrocatalyst surface. Low local CO concentration promote the methane production. The CO production increased after 10 s, which led to the drop in methane. CO production remained stable after 300 s, which could potentially be explained by the already good performance of monometallic Ag catalysts towards CO. This will ensure a certain amount of CO to be produced even after structural conversion occurred at this early stage of the CO_2 reduction process. By combining electron microscopy and electrochemistry we were able to obtain a more in-depth study on structural transformation of core-shell NPs and its effect on the electrocatalyst performance. Here we found that despite the morphological transformation, electrocatalyst performance towards CO was promoted, whereby this destabilization can actually be interpreted as some sort of activation of these core-shell NPs.

7.4 Conclusions

Cu@Ag core-shell nanoparticles have been successfully obtained by Ag galvanic replacement on thermal decomposed Cu nanoparticles. EDS analysis and dose-controlled electron tomography demonstrate their core-shell structure and oval shapes, which can potentially be attributed to the heterogeneity of the Ag shell coverage. The 3D structural transformation pathway of Cu@Ag core-shells during the electrochemical CO_2 reduction has been investigated at atomic resolution level by electron tomography, and the results were correlated with the electrochemical insights observed. The key factor causing the transformation changes was found to be the heterogeneous coverage of the Ag shell on the nanostructures, as it was observed that Cu leached from the atomic-size pinholes of the Ag shell. This Cu leaching potentially caused an increased ethylene production and a decreased methane production, both effects originating from the changing Cu/Ag interface and Cu enrichment at the surface. Remarkably, the transformed Cu-Ag core-shell structure practically doubles the production of CO, which is the mean product generated on monometallic Ag surfaces. These observations can contribute significantly to state-of-the-art research on morphological transformation, since it has been established that metal leaching is the commence of the structural transformation. Often in literature the focus of improving electrocatalyst stability is preventing agglomeration. In order to take the new insights of this study into account, metal leaching must be studied in conjunction with agglomeration prevention. This way, a proper and dependable tailored approach can be created enabling the study of the original electrocatalyst structures for the eCO_2R. This will be elaborated more in Chapter 8.

7.5 Supporting information

Supporting movie 7-1: 3D reconstruction of Cu@Ag core-shell nanoparticle before electrochemical stress is applied (https://drive.google.com/file/d/1zI9IUHRrPwlFEl4pUhcrOQY4yWXt-rTg/view?usp=sharing)

Supporting movie 7-2: 3D reconstruction of degradation process of Cu@Ag core-shell NPs due to electrochemical stress (https://drive.google.com/file/d/10JxvQKQ8TMK2TCVIQ-qHV0bJbH2mSHC2/view?usp=sharing)

CHAPTER 8:

HER inhibition and stability strategy using a nanoscale carbon layer

In this chapter, the effect of an amorphous carbon layer on the HER inhibition and catalyst stability during the eCO_2R was investigated. Ag-based gas diffusion electrodes were used as a proof of concept and the carbon layer thickness was optimized. Hereafter, the best performing catalyst was subjected to stability measurements.

This chapter has been submitted as: L. Pacquets, J. Van den Hoek, D. Arenas-Esteban, R. Ciocarlan, P. Cool, K. Baert, T. Hauffman, N. Daems, S. Bals and T. Breugelmans, The Use of Nanoscale Carbon Layers on Ag-Based Gas Diffusion Electrodes to Promote CO Production, ACS Applied Nano Materials, 2022, 5, 7723-7732.

Lien Pacquets performed the electrochemical, contact angle, SEM and EDS experiments, Järi Van den Hoek designed the flow reactor and assisted with the stability measurements, Daniel Arenas-Esteban performed the TEM and EELS analyses, Radu Ciocarlan performed the Raman measurements and Kitty Baert performed the XPS measurements.

8.1 Introduction

Up until today, the challenge remains to develop a catalyst to efficiently reduce CO_2 by lowering the large overpotential necessary for this reduction along with the inhibition of the competing HER and therefore tuning the selectivity in aqueous environments [218]. Various studies have been conducted to suppress the HER by catalyst structure [219], alloying catalyst metals [220], [221], electrolysis in alkaline media [222], [223], reactor design [224], electrode design [224] and catalyst protective layers [62], [63], [225]–[227]. The latter are often surface modifiers which primarily aim for changes in selectivity by effectively modifying the electrocatalytic surface properties. Ahn et al. tuned the selectivity of Cu foam by adsorption of poly-amides and thereby stabilizing the CO dimer which is essential for the formation of C_2 products [63]. Buckley et al. applied organic modifiers on Cu surfaces in order to alter the selectivity between CO, H_2 and formic acid [225]. Hsieh et al. used halide anions at Ag surfaces influencing the rate-determining step [228]. Recently, researchers started to explore the applications of carbon films and the effect on product distributions, but they mainly focused on high layer thicknesses [229], [230].

In this chapter, we demonstrate the effect of an ultrathin protective layer based on amorphous carbon without additional functional groups. By using a carbon layer, the chemical nature and the EASA of the electrocatalyst does not change, which is in contrast to previously mentioned literature. Additionally, by the application of a carbon layer, difficult synthesis methods that add functional groups to tune the product distribution, can be avoided.

As a proof of concept, we investigate the effect of the carbon layer and its thickness on Ag-based GDEs for the CO_2 electrochemical reduction to CO. Afterwards, the ideal layer thickness was selected to investigate its performance over a longer period of time, showing the beneficial role of the carbon layer on the durability of Ag-based GDEs.

8.2 Experimental

8.2.1 Chemicals

Potassium bicarbonate (Chem-Lab, 99,5%), potassium hydroxide (Chem-Lab, 85%), Sigracet® 39BB (SGL Carbon), Selemion® DSVN anion exchange membrane (AEM, AGC Engineering Co., Japan), Nafion 117 (Fuel Cell Store) cation exchange membrane (CEM) were used during this research. All solutions were prepared with ultra-pure water (MQ, Milli-Q grade, 18.2 MΩ cm)

8.2.2 Electrode preparation

Ag is a well-explored electrocatalyst in literature and is therefore selected for this proof of concept study. Consequently, a 70 nm thick Ag layer was deposited by magnetron sputter coating onto a gas diffusion electrode (GDE, sigracet), using a Leica EM ACE600 employing 35 mA of current, 4.0 .10^{-2} mbar of Ar pressure. Subsequently, a nanoscale carbon layer was added by pulse mode evaporation with thicknesses varying between 0 nm and 30 nm referred to as Ag70Cx (with x indicating the carbon layer thickness on top of the Ag-based GDE) in all experiments (a schematic representation of the synthesis approach and photographs of the different samples can be found in Figure S 8-1 and Figure S 8-2, respectively). The source was angled 25° towards the sample stage.

The samples were neither cooled nor heated during the depositions, while the sample stage continuously rotated during the sputtering/evaporation and the target-to-substrate distance was maintained at 50 mm.

8.2.3 Electrochemical set-up

Electrochemical measurements were performed with a multi Autolab M204. CP measurements of one hour were conducted using an in-house made hybrid flow cell where the anolyte performs in batch and the catholyte is recirculated through a gas-liquid divider (a more detailed configuration can be found in Figure S 8-4 and Figure S 8-6). Both compartments were separated by a Selemion® DSVN anion exchange membrane, this membrane was chosen to allow hydroxyl ions (formed at the cathode) to migrate to the anode and avoid CO_2 consumption. CO_2 was fed into the gas channel at the cathode in a flow-by configuration at 7.5 sccm controlled by a mass flow controller (GF-080, Brooks Instruments) with a catholyte flow of 0.2 mL min^{-1}. The back pressure was measured by a Gefran TK-series pressure sensor and logged by a I/O device (National instruments, NI6000), which was automatically read out with MATLAB® R2016a. The reacted gas stream was fed to an in-line thermo trace 1300 gas chromatograph (GC) equipped with a TCD detector and a micropacked column (ShinCarbon ST 100/120, 2 m, 1 mm ID, Restek). Finally, the gas stream was fed to a mass flow indicator to record the outlet flow, which was used for FE calculations. For both catholyte and anolyte, 1 M of $KHCO_3$ was used as the electrolyte.

A carbon cloth served as CE and a leak-free Ag/AgCl electrode (W3-690053, Harvard Apparatus) was used as a reference electrode (RE) to control the applied current and to measure the corresponding potential in a three electrode set-up where the Ag-based GDE functioned as a WE. During all measurements, the ohmic resistance in the set-ups remained between 6 and 8 ohms, evidencing that the additional carbon layer does not significantly alter the resistance of the cell. The iR-drop was measured at the end of the experiment by the current interrupt method (CI) which applies a lower current and measures the corresponding potential. All potentials are reported versus the RHE, unless stated otherwise.

The accessibility of water at the Ag surface was investigated using CV. The Ag70C15 sample was submersed in a 0.5 M KOH solution and analyzed within a potential range of -0.5 V and 0.7 V at a scan rate 50 mV s^{-1}. The reduction and oxidation peaks of Ag were investigated.

8.2.4 Electrode surface analysis

Contact angle measurements were performed with a Krüss GmbH DSA 10-mk2 device by drop-casting 2 µL of Milli-Q at a rate of 24.79 µL min^{-1} with a syringe plunger on the electrode surface at room temperature. The angle between the catalyst surface and the water droplet was measured by a drop-shape analysis software, repeated for several times and thereafter the average of these measurements was calculated.

The sample was further investigated from 2 different morphological perspectives. First, the surface was analyzed with a SEM (FEI Quanta 250) at 20 kV using secondary electrons. Subsequently, cross-sections were taken from the Ag-based GDE electrodes using a focused ion beam dual beam microscope (FIB, ThermoFischer Scientific FEI Helios Nanolab 650). Primarily, a Pt protective layer was deposited (by ion beam induced platinum deposition at 30 kV with 0.23 nA) onto the different Ag-based GDEs in order to prevent any FIB induced damage. Thereafter, three subsequent thinning steps were performed at 30 kV, 8 kV and 2 kV, respectively, to obtain a FIB lamella. HAADF-STEM and electron energy loss spectroscopy (EELS) measurements were performed using an aberration-corrected cubed ThermoFischer Scientifc Titan electron microscope, operated at 300 kV.

Next, Raman spectra were recorded in air at room temperature using a Micro-Raman Horiba (Xplora Plus Microscope) equipped with a green 532 nm laser, in the range of 100 cm^{-1} to 3000 cm^{-1} Raman shift. This technique was used to indicate the presence of an amorphous carbon layer and investigate the evolution of the carbon layer thickness. All samples were sputtered on a glass substrate to eliminate the contribution of the GDE (carbon based).

Finally, XPS measurements were performed using a PHI - VersaProbe III using an Al X-ray source (1486.6 eV) and an automatic electron neutralizer. The samples were analyzed across an area of 100 µm in diameter. High resolution scans were recorded with a pass energy of 26 eV and a step size of 0.05 eV. Due to the low penetration depth of XPS, Ag70 and Ag70C5 were the only two samples investigated, as thicker carbon layers would block the Ag signal.

8.2.5 Stability measurements

Electrochemical durability measurements were conducted using an in-house made flow set-up, allowing to operate in a three-electrode configuration (a schematic overview is presented in Figure S 8-5 and Figure S 8-6). A CO_2 flow of 25 sccm, controlled by a Brooks Instrument GF-40/100 mL min^{-1} mass flow controller, entered the cell in flow-by mode at the cathode side. Both the catholyte and anolyte flows were set to 2.6 mL min^{-1} containing respectively 0.5 M aqueous $KHCO_3$ and 2 M aqueous KOH solutions, with a total volume of 100 mL catholyte and 500 mL anolyte, which were recycled during the experiment. A 1 cm^2 Ag-based GDE functioned as the WE, while the cathodic current was controlled by a leak-free Ag/AgCl reference electrode (Innovative Instruments, Inc.) with a multichannel Autolab potentiostat M204. A Nafion® 117 cation exchange membrane (CEM) was used to separate the cathode from the anode. Since a KOH solution was used as anolyte for the stability measurements (as opposed to the one hour CP measurements where $KHCO_3$ was used on both sides), a cation exchange membrane was preferred as otherwise hydroxyl ions would transport to the cathode and react with gaseous CO_2. The alkaline anolyte was preferred because of its benefits towards the oxygen evolution reaction (counter reaction). The reacted CO_2 stream traveled through the catholyte buffer container which served as a gas-liquid divider (G/L divider) to prevent liquid from entering the GC, an in-line Shimadzu 2014 series GC equipped with a TCD detector and a micropacked column (Restek Shincarbon ST, 2 m length, 1 mm internal diameter, 100/120 mesh). The reacted CO_2 stream was sampled into the GC every 20 minutes throughout the entire experiment.

8.3 Results and discussion

8.3.1 Physical properties of the catalyst

To perform efficient and selective eCO_2R tests, a 70 nm Ag layer was deposited onto a GDE (Ag70) by magnetron sputter coating using ionized Ar. SEM images showing the planar view of the sample are depicted in Figure 8-1 (A-C). The Ag sputtered layer showed a rather uniform appearance with an interconnected micro-pore structure [231]–[233] (indicated by the red circles in Figure 8-1(C)), even on a large scale.

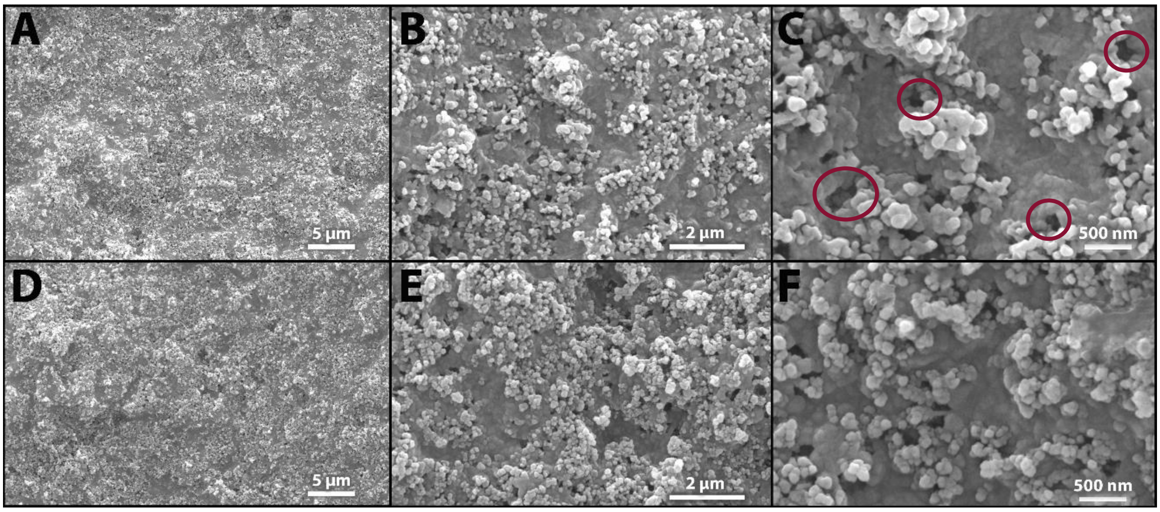

Figure 8-1: SEM images of a sputtered Ag-based GDE with a thickness of 70 nm and with a 15 nm thick carbon layer at different magnifications

A nanoscale carbon layer was deposited through carbon evaporation. Layer thicknesses of 5, 15, 20 and 30 nm (Ag70C5, Ag70C15, Ag70C20 and Ag70C30, respectively) on top of the Ag sputtered layer were obtained. Using the SEM for a top-down comparison between the Ag70 sample (Figure 8-1 (A-C)) and the Ag70C15 (Figure 8-1 (D-F)) did not show clear differences before and after the application of the carbon layer. As a result, the microporous Ag architecture remained visible even after applying the carbon coating. SEM-EDS data (Table S 8-1) of the resulting structures however clearly indicated a difference between Ag70 and Ag70C15 in terms of the Ag/C ratio. The latter resulted in a ratio of 0.027 in contrast to the Ag70 sample where a ratio of 0.045 was obtained. This is a clear indication of a carbon layer being present at the surface of Ag70C15. In conclusion, the planar view of AG70 and Ag70C15 indicated that the addition of a carbon layer did not affect the structure of the Ag coating itself.

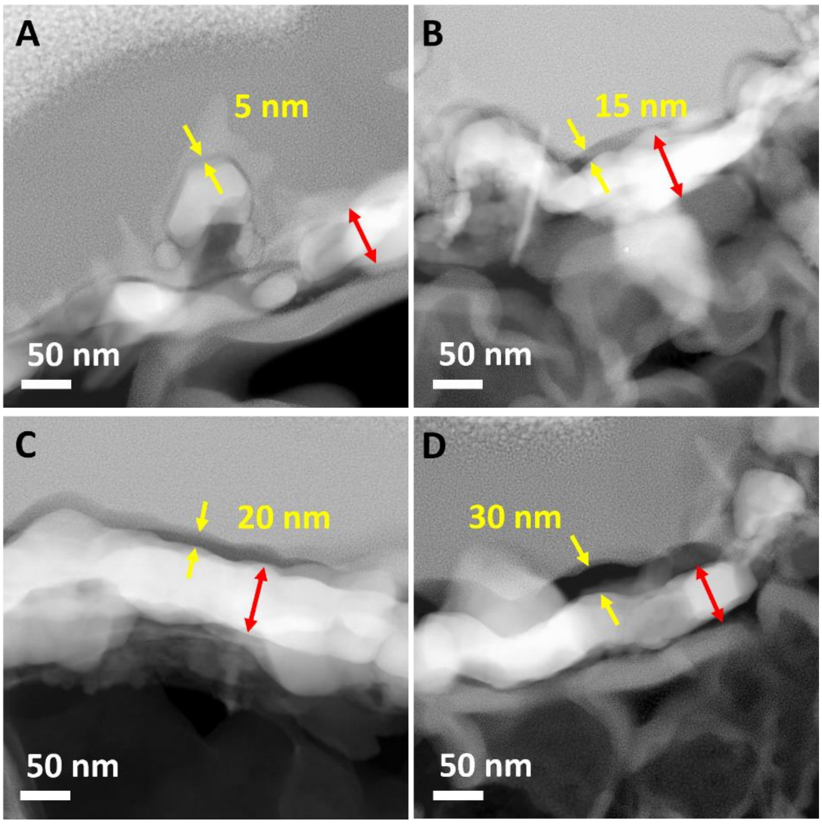

Figure 8-2: Cross-sectional HAADF-STEM images of sample (A) Ag70C5, (B) Ag70C15, (C) Ag70C20 and (D) Ag70C30, indicating the Ag layer with the red arrow and the increased thickness of the carbon layer in each sample with yellow arrows

To further confirm the presence of the carbon layer, a cross-section of each sample was prepared by FIB milling (Figure 8-2 and Figure S 8-3). Although the electrode surface appears to be quite rough, an homogeneous Ag layer of ~70 nm is clearly observed in each sample, as well as a carbon layer with increased thickness of 5, 15, 20 and 30 nm for the Ag70C5, Ag70C15, Ag70C20 and Ag70C30 samples respectively. Importantly, for the thinner layers an inhomogeneous distribution of the carbon layer over the rough Ag surface was observed. Underneath the Ag layer, the porous GDE (carbon paper) was visible in the HAADF-STEM cross-sectional images.

To investigate the graphitization degree of the carbon layers, EELS measurements were performed on sample Ag70C30 (Figure 8-3(A)). As it has the thickest carbon layer, it is easier to obtain a reliable measurement of the carbon layer without other possible contributions from the background. The obtained EELS spectrum is shown in Figure 8-3(B) where the characteristic shape of a sp^2-rich amorphous carbon can be observed [234]. The well-defined π peak indicate the presence of sp^2 C, whereas the broad σ peak indicates a lower level of crystallinity. From these results, it can be concluded that the carbon layers are composed of disordered graphene-like carbon, which are well known for their high degree of porosity [235], [236]. This high porosity is preferred, as it allows H^+ carriers to travel to the Ag catalyst layer.

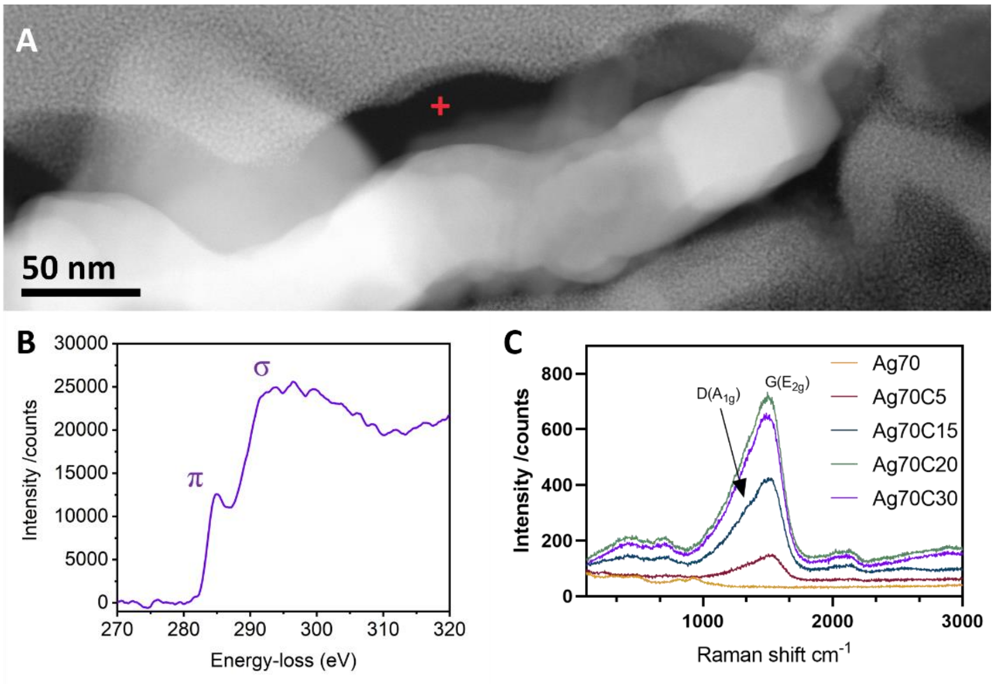

Figure 8-3: (A) High-resolution HAADF-STEM image of the carbon layer from the Ag70C30 sample and (B) EELS spectrum obtained from the red cross point indicated in the image on A, where the π and σ contribution of the C–K edge for sp^2 amorphous carbons can be observed. (C) Raman spectrum of Ag70Cx before electrochemical CO2 reduction giving insight on the graphitization degree of the carbon layers.

Figure 8-3(C) illustrates the Raman spectrum of the as-deposited carbon layer onto the Ag-based GDE electrode before the eCO_2R. As shown in the graph, one main peak appears at 1568 cm^{-1} and one shoulder at 1361 cm^{-1}, which correspond to the G (E_{2g}) and D (A_{1g}) bands, respectively [237]–[240] and are visible in all carbon samples. The D maximum originates from the movement of neighboring atoms in radial directions in the plane and is caused by structural defects, often called the disorder-induced mode. The G maximum corresponds to the movements of atoms in opposite directions perpendicular to the plane and causes C-C bond stretching [241], [242]. These two bands are typical features present in amorphous carbon materials and combined with the absence of the 2D band (at about 2700 cm^{-1}, characteristic to bulk or multilayer graphite/graphene-related materials) [238], [243], clearly indicate that a thin amorphous carbon surface layer is present at the Ag-based GDE electrode. In addition, upon increasing the carbon layer thickness, the intensity of the carbon related maxima increased, an observation which confirms the trend already proven by the HAADF-STEM experiments. It however appears that at a certain point saturation of the signal occurs as the maxima of Ag70C20 and Ag70C30 were similar. From this spectrum it can also be noted that metallic Ag is Raman insensitive as it is not polarizable during the molecular vibration. The signal that was visible during the measurements originated from the glass substrate.

To further confirm this, a CV measurement of Ag70C15 in 0.5 M KOH was performed to investigate the porosity of the carbon layer. The oxidation and reduction of Ag manifests itself in Figure S 8-10. This demonstrates that the Ag catalyst layer is accessible for an electrochemical reaction.

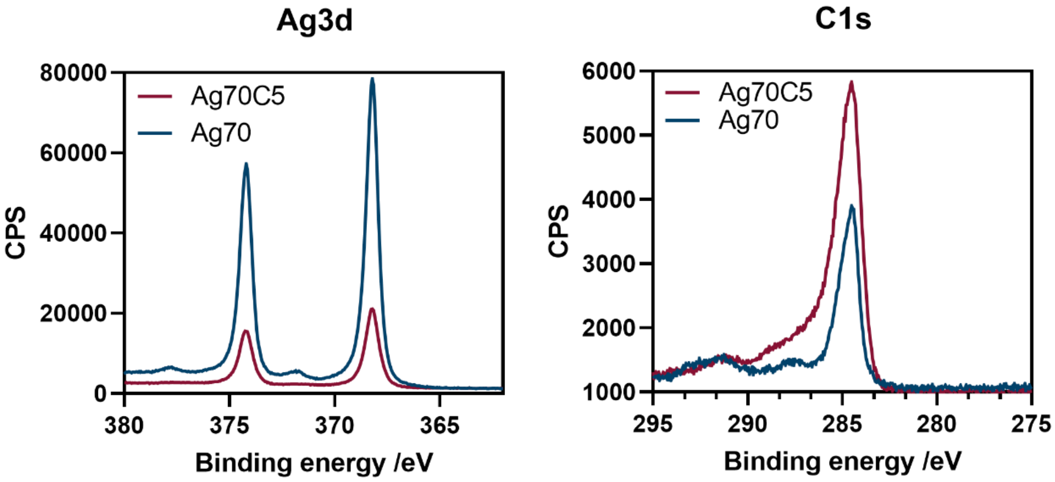

Figure 8-4: High-resolution spectra of Ag3d and C1s. Ag70C5 is represented in red and Ag70 in blue

In order to investigate the nature of the Ag catalyst layer and the influence of the carbon layer on Ag, XPS measurements were performed. Figure 8-4 shows the XPS spectra of Ag3d and C1s, respectively. Two asymmetric Ag peaks, separated by 6 eV, at 368.5 eV (Ag3d$_{5/2}$) and 374.5 eV (Ag3d$_{3/2}$) could be observed. This indicates that Ag0 is predominantly present in the sample of each spin-orbit component for Ag metal. These peaks were both accompanied by low loss features to their higher binding energy side. Comparing both samples, the Ag signal was more pronounced for the Ag70 sample, whereas the carbon signal was increased in the Ag70C5 sample.

Nevertheless, no clear difference between the two samples can be observed (Figure S 8-9), which most likely means that Ag and C do not bind directly to each other. This is further confirmed by the absence of additional peaks at lower binding energies in the Ag3d spectrum, as they typically occur in literature reports where Ag-C bonds are formed.[244] These findings thus support our hypothesis that the Ag catalyst is not chemically bonded to the carbon layer and that the carbon layer will not interfere with the selectivity of the Ag layer towards eCO_2R but rather solely serves as a protective layer.

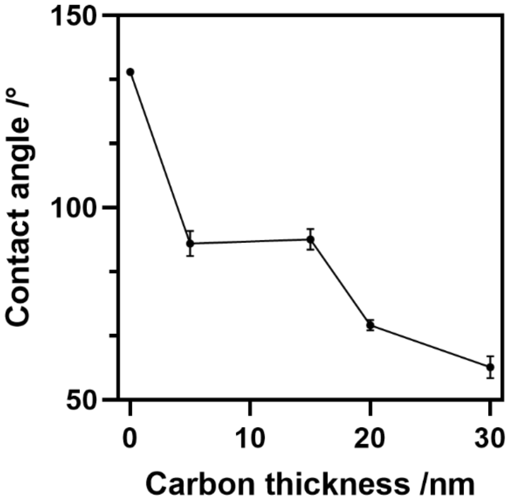

Figure 8-5: Contact angles as a function of the amorphous carbon layer thickness on Ag-based GDEs prior to CO_2 reduction experiments with layer thicknesses reaching from 0 nm to 30 nm

Contact angles of Ag70, Ag70C5, Ag70C15, Ag70C20 and Ag70C30 were measured prior to the electrochemical CO_2 reduction reaction. A contact angle of 135.3° was measured at Ag70, where a carbon coating was absent. This angle decreased upon addition of a 5 nm carbon layer to 90.6° and declined to 58.5° at 30 nm of carbon coating, as shown in Figure 8-5 (images of the corresponding contact angles are depicted in Figure S 8-7). We hypothesize that the difference in contact angle between Ag70 and the Ag70Cx can be due to (i) the varying roughness of the surface [245]–[248]. When the surface roughness increases, the contact angle increases as well, as was reported by Wenzel on non-wettable surfaces [249]. The GDE substrate is known to be a rough surface and by depositing the Ag layer by sputtering, this layer also expressed a certain roughness. Upon addition of a carbon layer, the roughness however decreased, which might seem a contradiction but can be explained as follows. The carbon layer was applied by evaporation, which is a different method compared to the Ag layer deposition (which was deposited by sputtering). This type of method is typically used to obtain better 'step coverage' with a smoother surface as a result. At first the carbon layer is very thin (only 5 nm thick), but increasing the layer thickness, created a better step coverage, leading to an even smoother surface yielding lower contact angles [250], [251]; or (ii) the sputtered Ag film did not fully cover the hydrophobic GDE, whereby the influence of the GDE during the contact angle measurements was not completely eliminated. After applying an additional carbon layer, the influence of the GDE diminished.

8.3.2 Nanoscale carbon layers and their effect on the performance of Ag-based GDEs

Electrochemical experiments were executed in a hybrid flow reactor as depicted in Figure S 8-4. The FEs of compounds in the gas phase were recorded during a period of 1 hour with intermediate sampling every 15 min, starting at 5 min after applying a current of 100 mA cm^{-2}. The evolution of the FE over time of the Ag-based GDEs with altering carbon layer thickness are shown in Figure 8-6.

Considering the electrolysis experiment of Ag70, a pronounced amount of H_2 was already formed at the beginning of the measurement. The H_2 increased over time from 19.6 % at the beginning to 31.4 % after 50 min of running time. The gradual increase in H_2 production impacted the CO formation with a consequent reduction in its FE over time. Initially, the FE of CO reached up to 79.5 % which waned to 69.0 %. Additionally, methane was also detected as a reaction product and along with the H_2 experienced an increase in FE up to 4.5 % after 50 min of electrolysis. We hypothesize that this development in methane production is related to the migration of Cu to the surface during electrolysis, which was already reported in literature on Cu-Ag bimetallic surfaces [205]. Ethylene was also present in the reacted flow, but only in very low amounts resulting in a FE of 0.3 % (not represented in the graph). The production of methane and ethylene can be attributed to the trace amount of Cu (originating from the sputter equipment) present inside the Ag layer, as shown in Figure S 8-8.

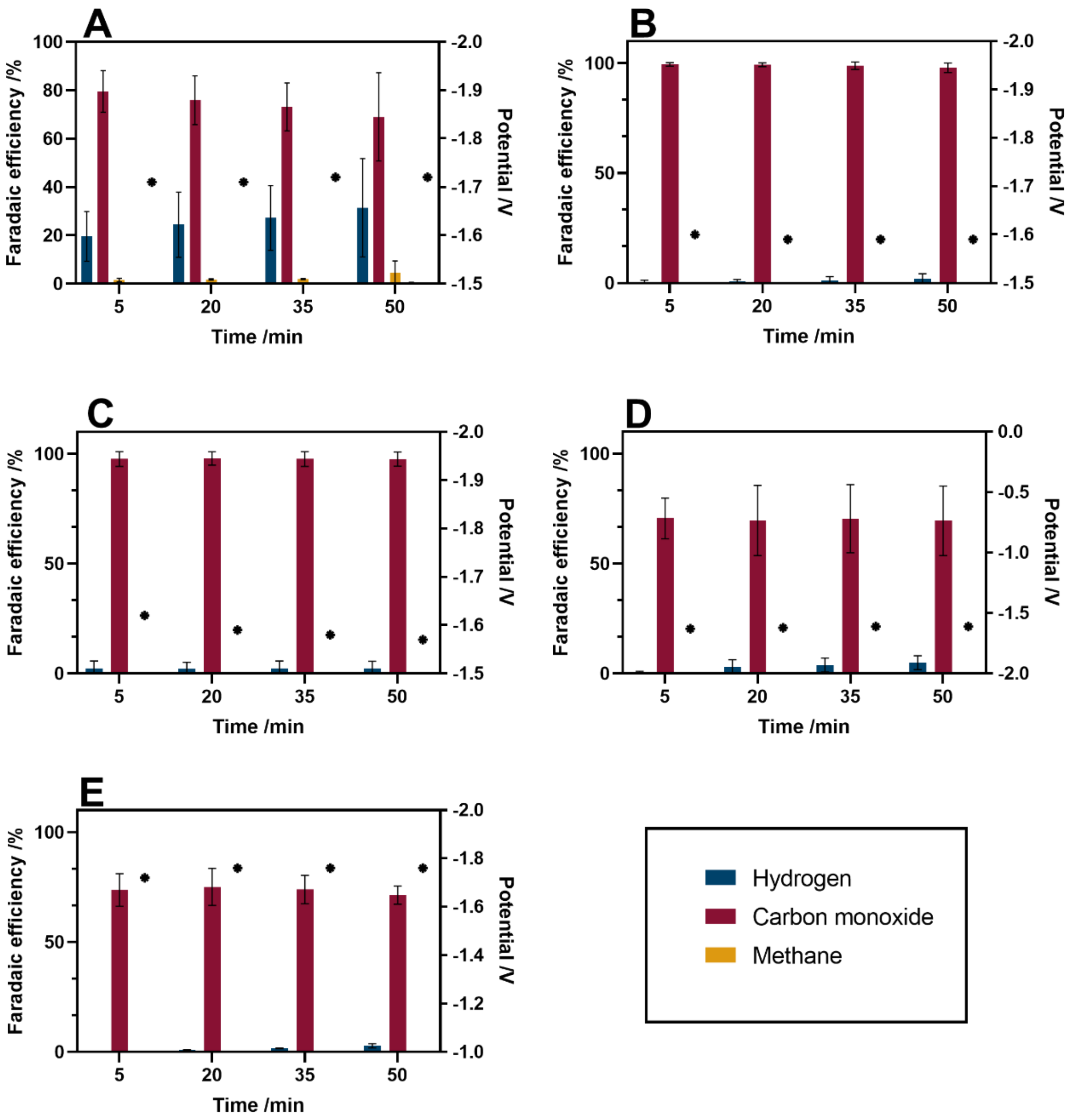

Figure 8-6: Evolution in FE of H_2 (blue); CO (red); CH_4 (orange) and C_2H_4 (green) during an 1 h electrolysis experiment for samples (A) Ag70; (B) Ag70C5; (C) Ag70C15; (D) Ag70C20 and (E) Ag70C30

Compared to the literature of Ag-based GDEs [252]–[256], the FE of CO was rather low and a considerable amount of H_2 was produced at the end of the experiment. This can be attributed to the intensive flooding occurring throughout the experiment, as a consequence of the lower Ag loading present on the substrate compared to literature. Flooding is a well-known problem within this field of research. Literature states that this is due to electro-wetting [257], [258], which is a possible cause for the increasing amount of

H_2 produced during the electrolysis. It is known that the passage of faradaic current accelerates flooding and is consistently reported in literature [257], [259]. Increasing the current density seemed to be beneficial for appearance of flooding, which initiates carbonate precipitation and eventually can lead to GDE failure [257].

In order to inhibit the production of hydrogen, an amorphous carbon layer was deposited onto the existing Ag-based GDEs with altering layer thicknesses. The amorphous carbon layers in this paper differentiate themselves from other studies in terms of their simplicity and thickness. Often, the chemical nature of the catalyst surface was modified by either additives during the catalyst synthesis [63] or by modifying the existing electrode surface [62], [76], [225], [226], [260]. These catalyst adaptions severely influenced the hydrophobicity of the surface and participate in the stabilization of the intermediates, altering the product distribution. On the contrary, here, only a very nanoscale amorphous carbon layer was deposited and additional functional groups were absent preserving the intrinsic function of the electrocatalyst. This is a cost-efficient, easy and faster way to prepare electrocatalysts with HER inhibiting properties.

As a result, as shown in Figure 8-6 (B), only a 5 nm thick carbon layer was necessary to inhibit the HER. At the beginning of the measurement, hydrogen formation was reduced to a FE of 0.5 % leading to a FE of 99.5 % of CO. Throughout the experiment, the FE of H_2 increased slowly and eventually accounted for 2.1 % which was accompanied by a small decrease in FE of CO to 97.9 %. The HER suppression could be attributed to the diffusion-selective carbon layer [261]. This porous carbon layer acts as a physical barrier between the catalyst layer and the electrolyte, preventing direct contact. The carbon layer drastically lowers the diffusion of proton carriers to the Ag catalyst surface. The CO_2 molecules are supplied from the backside of the GDE and can easily reach the Ag catalyst layer. Due to the limited amount of protons at the Ag interface, CO_2 reduction is promoted and the HER is suppressed [262]. In addition, liquid passing through the outlet gas channel was absent. Despite the contradiction of the decrease in contact angle, the carbon layer seems to prevent flooding (this difference was elucidated in 3.1). Nevertheless, since carbon is more hydrophobic than Ag, a decrease in flooding is observed. This flooding was visible with the naked eye in all experiments in the hybrid cell where the carbon layer was absent and disappeared upon deposition of a carbon layer

Depositing a carbon layer of 15 nm resulted in a FE of 2.4 % for H_2 and 97.6 % for CO, which were thus within the same range as the previous layer thicknesses. Interestingly, the addition of an amorphous carbon layer also lowered the cathodic working potential from -1.71 V (Ag70) to -1.60 V (Ag70C15), which is a reduction of 0.16 V comparing both GDEs.

Increasing the thickness even further, entailed a decrease in the FE towards CO and in addition the total FE no longer reached 100 %. Total FE's of around 69.5 % and 71.3 % were observed when depositing 20 nm and 30 nm of carbon, respectively. This discrepancy could not be accounted for by analyzing the liquid phase, as only traces of formate were observed. Since these layer thicknesses underperformed, they were not considered for further investigation.

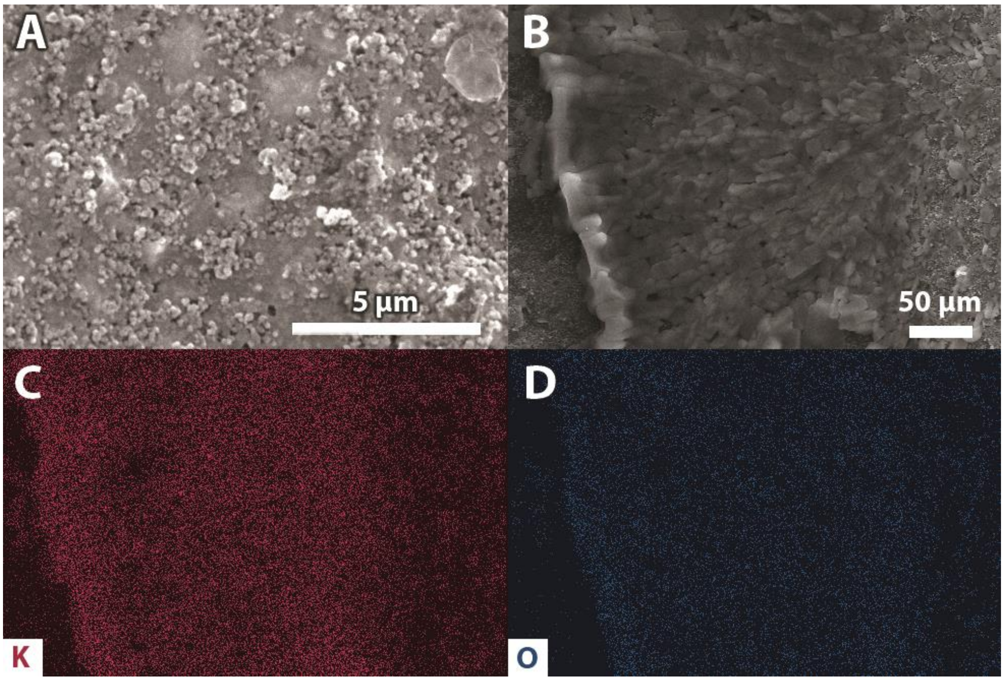

Figure 8-7: SEM images of AG70C20 (A) before and (B) after 1 h of electrolysis and the corresponding SEM-EDS maps of (C) potassium and (D) oxygen after 1 h electrolysis

Additionally, Figure 8-7 (A-B) depict the SEM images of the Ag70C20 sample before and after the electrolysis experiment and after thoroughly rinsing the electrode with milliQ at the end of the measurement. Comparing both SEM images, it is clear that still an additional layer exists after using the Ag-based GDE in the hybrid flow cell. To confirm the presence of $KHCO_3$ deposits, SEM-EDS maps (Figure 8-7(C-D)) were recorded. These maps indeed indicated that the additional layer consisted of potassium and oxygen, which was absent prior to the experiment. This indicates the precipitation of salt from the electrolyte onto the electrocatalyst surface.

In addition, Raman spectra were collected on the same sample to support the SEM and SEM-EDS data. The Raman spectra, depicted in Figure 8-8, show a clear difference between the two samples which supported the SEM and SEM-EDS data from Figure 8-7. The Ag70C20 sample before the experiment was in accordance with Ag70C15 (Figure 8-3 (C)) when comparing both Raman spectra. Nevertheless, investigating the sample after the electrolysis, a clear difference could be observed (Figure 8-8). In this case, the presence of CO_3^{2-} could be confirmed due to the characteristic peaks at 681 cm^{-1} and 1047 cm^{-1}, which were absent before electrolysis [263]. These results, in combination with the SEM-EDS maps, prove the presence of an electrolyte salt layer deposited on top of the Ag70C20 sample.

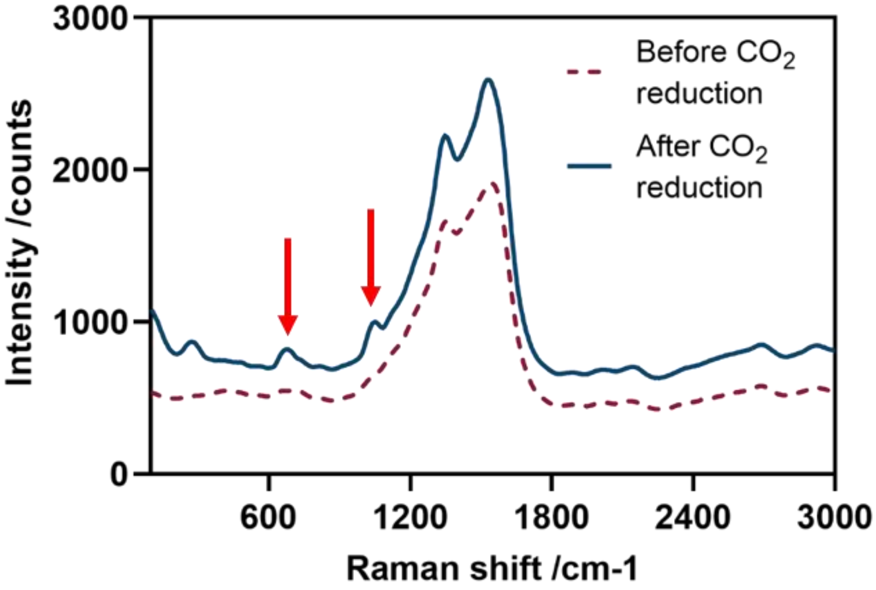

Figure 8-8: Raman spectra of Ag70C20 (dashed – red) before and (solid – blue) after 1 h electrolysis

In conclusion, the amorphous carbon layer seemed to be beneficial for the inhibition of the HER and CO formation, at least in terms of FE. A decrease in overpotential was ensured and the EASA was preserved, despite the deposition of an additional layer on top of the Ag catalyst layer. A carbon layer thickness beyond 15 nm resulted in a decrease in total FE which could not be accounted for by analyzing the liquid phase. A thickness of 15 nm was selected to be most ideal to pursue further experiments because of the persistence in FE compared to the other layers.

8.3.3 Superior durability of carbon coated Ag-based GDEs

Ag70 and Ag70C15 were both subjected to more industrially relevant conditions over a longer period of time. The production of H_2 and CO were logged every 20 min during 6 hours.

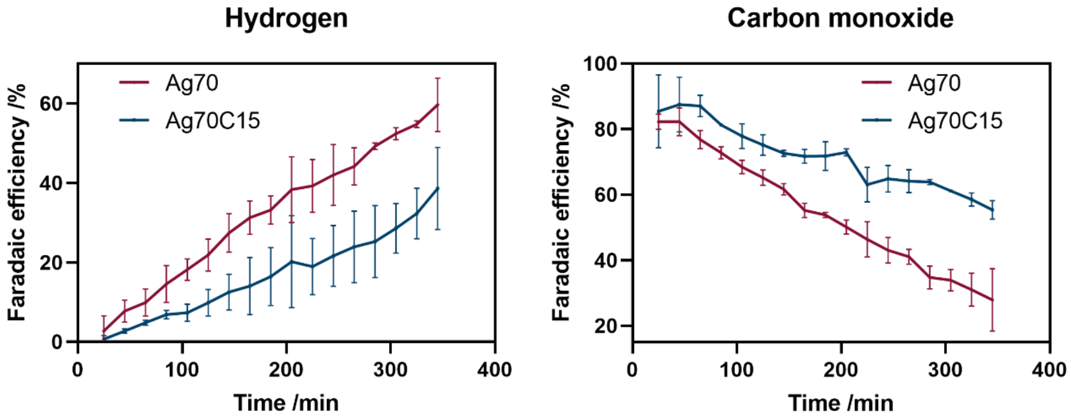

Figure 8-9: Inhibition of H_2 by an nanoscale carbon layer on Ag-based GDEs expressed in the evolution of the faradaic efficiency of CO and H_2 during the experiment

Figure 8-9 depicts the evolution in H_2 and CO production over time. A distinct difference existed between Ag70 and Ag70C15. Ag70 showed a precipitous increase in H_2 production, which consequently led to a faster decrease in CO production. At Ag70C15, the HER was inhibited by the additional carbon layer on the Ag-based GDE. A difference of 21 % in FE of H_2 was present between Ag70 and Ag70C15 at the end of the 6 hours of measurement, with FE reaching 60 % and 39 % for Ag70 and Ag70C15, respectively. The FE of CO decreased to 55 % over Ag70C15 and 28 % over Ag70, which is a difference of 27 % between the two electrocatalysts. The FE of CO diminished by 54.4 % at Ag70 compared to 30.2 % at Ag70C15. Additionally, an overall increase in HER of 56.9 % was observed at Ag70, which was only 37.9 % at Ag70C15. It is clear that the amorphous carbon layer inhibits the HER production over longer periods of time.

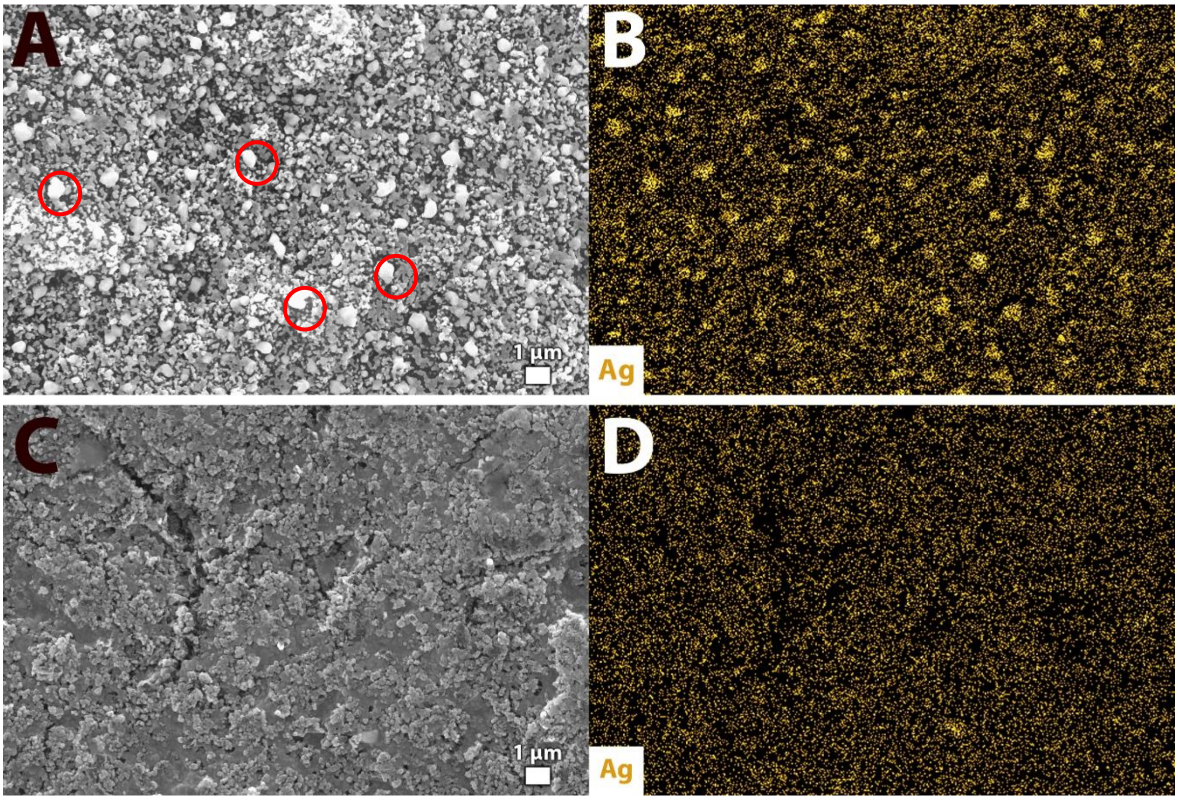

Figure 8-10: SEM image of (A) Ag70 after 3 hours of experiment, (C) Ag70C15 after 5 hours of experiment and (B and D) their corresponding SEM-EDS map.

Comparing the surfaces of Ag70 and Ag70C15 after 3 h and 5 h of the experiment, respectively, clearly indicated a difference between the two electrodes. As depicted in Figure 8-10, clustering of Ag on the surface of the electrode, indicated by the red circles, was visible. This clustering is absent on the Ag70C15 surface. This proves the stabilizing effect of the amorphous carbon layer, since it inhibits the movement of the Ag particles on the surface and thereby prevents the clustering of the Ag on the surface.

8.4 Conclusions

In this study we investigated the inhibition of the HER by applying a carbon top layer on a typical CO_2 reduction catalyst as it typically lowers the overall energy efficiency of the process. At the same time, we also explored the stabilizing effect of porous low loading electrocatalysts (~70 µg cm^{-2}). As most studies use surface modifiers to alter the chemical nature of the surface and use very thick protective layers, we investigated the effect of nanoscale amorphous carbon layers on the HER and stability, preserving the chemical nature of the electrocatalyst itself. In comparison with previously mentioned literature, this is a straightforward and fast modification that can be done after catalyst synthesis and deposition on the GDE.

In this investigation, we used Ag-based GDEs as a benchmark, which were synthesized by magnetron sputtering. Additionally, porous amorphous carbon was added by carbon evaporation. By using Ag-based GDEs, we were able to highlight the effect of carbon on the HER inhibition since they are not prone to produce products other than H_2 and CO. In addition, the porous carbon layer allows the H^+-carriers to diffuse to the Ag catalyst layer, without any excess of protons. Since the CO_2 is supplied from the backside of the GDE, it is sufficiently available at the Ag catalyst surface.

Upon applying a porous amorphous carbon layer onto the Ag-based GDEs, we noticed that the Ag catalyst is attainable, since Ag oxidation and reduction could be observed during the CV measurements. It has also been perceived during the XPS measurement that the Ag catalyst layers was not chemically bonded to the carbon layer. This carbon layer resulted in the inhibition of the HER and preventing the catholyte from traveling through the GDE.

Carbon layers thinner than 15 nm already showed to be less stable after 1 hour. Increasing the layer thickness to 30 nm or even 50 nm led to a decrease in total faradaic efficiency. Considering the above, a layer thickness of 15 nm is most ideal to perform long term experiments.

By comparing the bare Ag-based electrode, after a measurement of 6 hours, against the carbon coated Ag-based GDE, a remarkable difference in the pronounced amount of hydrogen produced was obtained. The HER accounted for 39 % on the latter electrode in contrast to 60 % at the former electrode. This is an increase in FE of 56.9 % using the Ag70 catalyst and only 37.9 % when carbon was applied. Additionally, the carbon layer ensured that the distribution of Ag catalyst across the electrocatalyst surface was maintained throughout the experiment. This is in contrast to the bare Ag electrode, which encountered destabilization due to sintering.

As this nanoscale carbon layer was able to prevent agglomeration of the electrocatalyst, along with its ability to inhibit HER, it highlights its potential as protective layer during electrochemical conversion of CO_2. This approach can potentially be extended to other electrocatalytic processes.

8.5 Supporting information

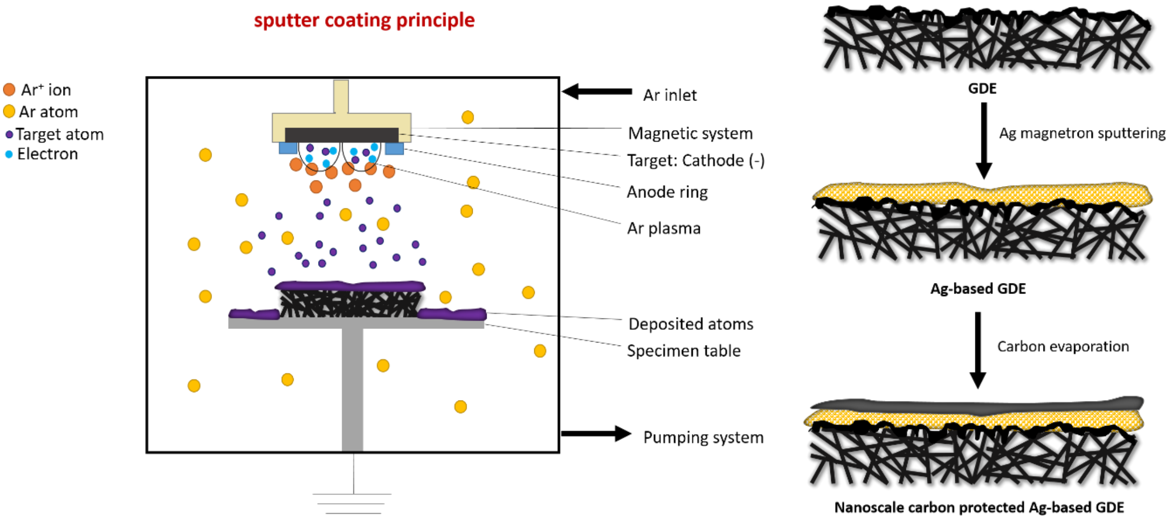

Figure S 8-1: Illustration of the sputter coating principle and the formation of nanoscale carbon protected Ag-based GDEs by Ag magnetron sputtering and carbon evaporation.

Figure S 8-2: Ag70Cx samples used during electrochemical experiment. Note the difference in color upon increasing the carbon layer thickness.

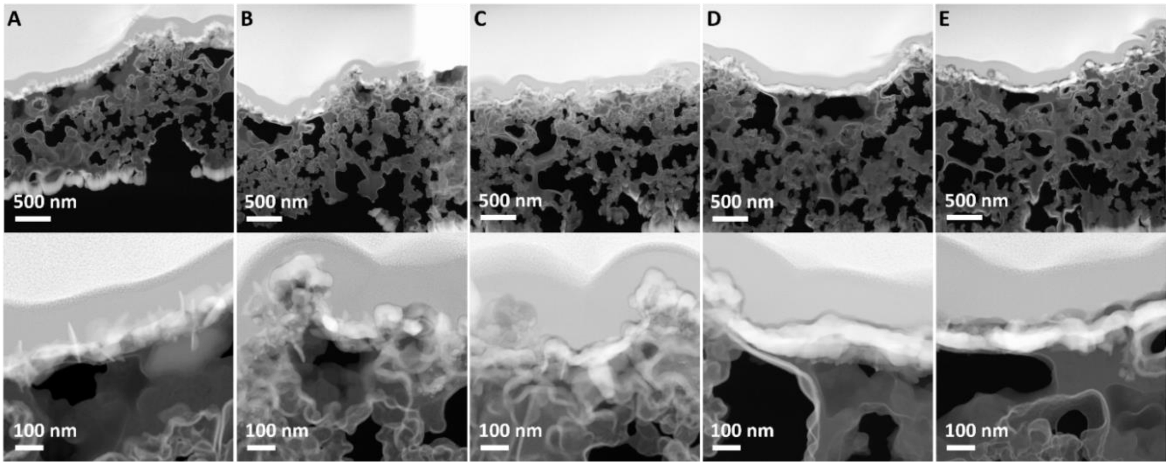

Figure S 8-3: (top) Low and (bottom) high magnification cross sectional HAADF-STEM images of samples (A) Ag70, (B) Ag70C5, (C) Ag70C15, (D) Ag70C20 and (E) Ag70C30. The cross-sectional images show the layered structure of the Ag-based GDE electrodes with altered carbon layer thicknesses.

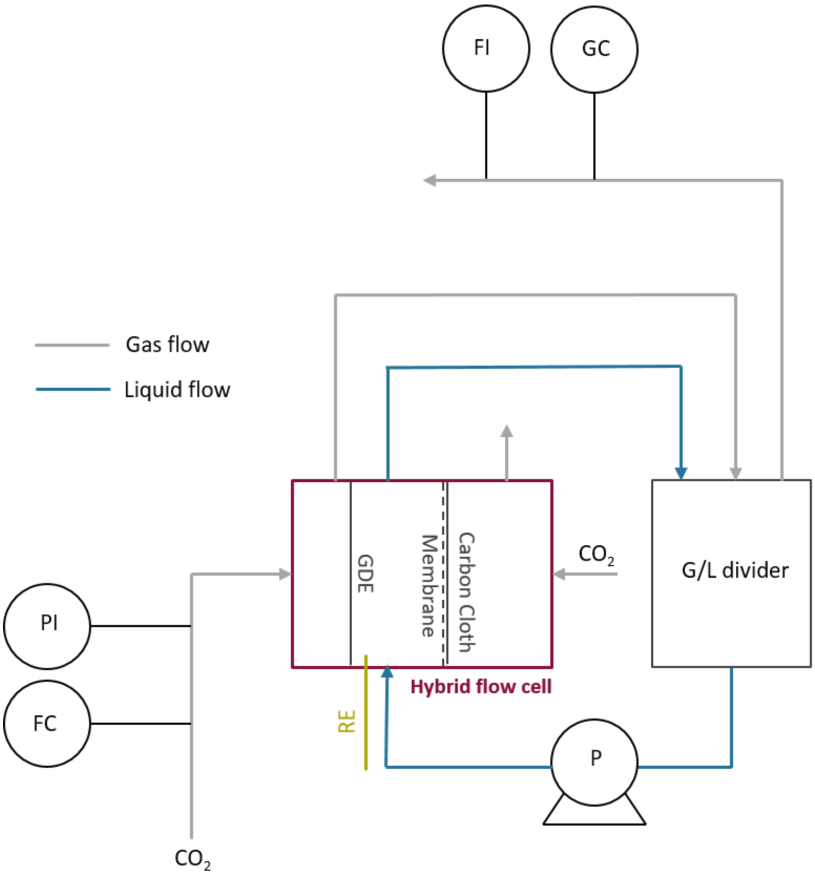

Figure S 8-4: Schematic representation of the hybrid flow cell. With FC being the (mass) flow controller, PI the pressure indicator, FI the (mass) flow indicator and GC the in-line gas chromatograph.

The hybrid flow cell contains three compartments which are (i) the gas channel where CO_2 is provided as feedstock; (ii) the cathode chamber which is filled with a CO_2 saturated $KHCO_3$ solution and (iii) the anolyte compartment containing a CO_2 saturated $KHCO_3$ solution. An Ag-based GDE operates as the WE and is connected to a graphite current collector. This GDE separates the CO_2 flow from the catholyte and allows CO_2 to travel to the electrocatalyst. A carbon cloth is used as a CE which is connected to an Al current collector. The CE is pressed together with the AEM (Selemion DSVN) to reduce the ohmic resistance. The catholyte is recycled using a gas-liquid divider (G/L divider) which is also used to separate liquid from the reacted CO_2 stream and the anode compartment performs in batch mode.

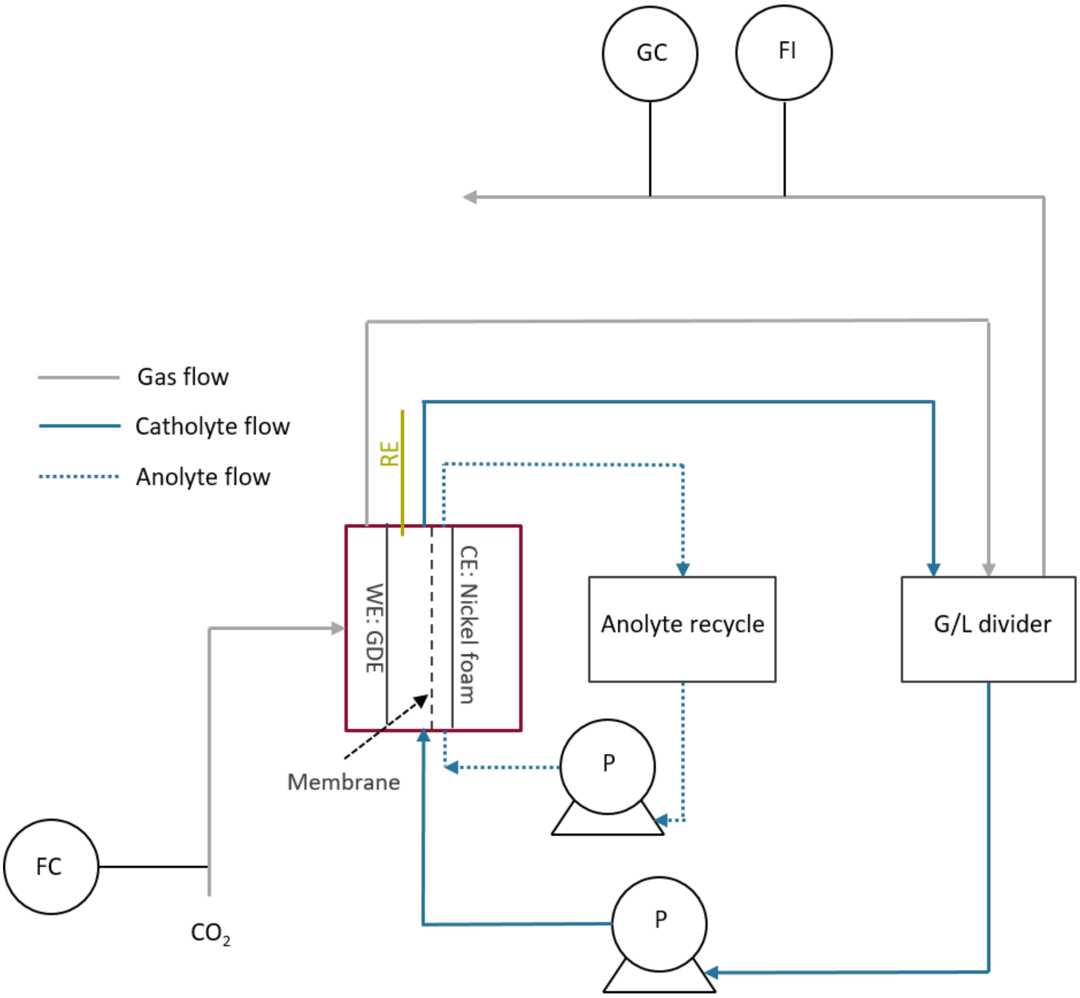

Figure S 8-5: Schematic representation of the flow reactor used during the durability measurements. With FC being the (mass) flow controller, FI the (mass) flow indicator and GC the in-line gas chromatograph.

This set-up has a three electrode flow-by configuration where WE and CE are separated by a CEM (Nafion). The Ag-based GDE (WE) is connected to a copper current collector, whereas the CE consists of a nickel foam which is electrically connected to another copper current collector. A CO_2 flow is fed into the gas channel in flow-by mode and subsequently into the G/L divider before being injected into the GC to prevent liquid from entering the column of the GC. Catholyte as well as anolyte are being recycled.

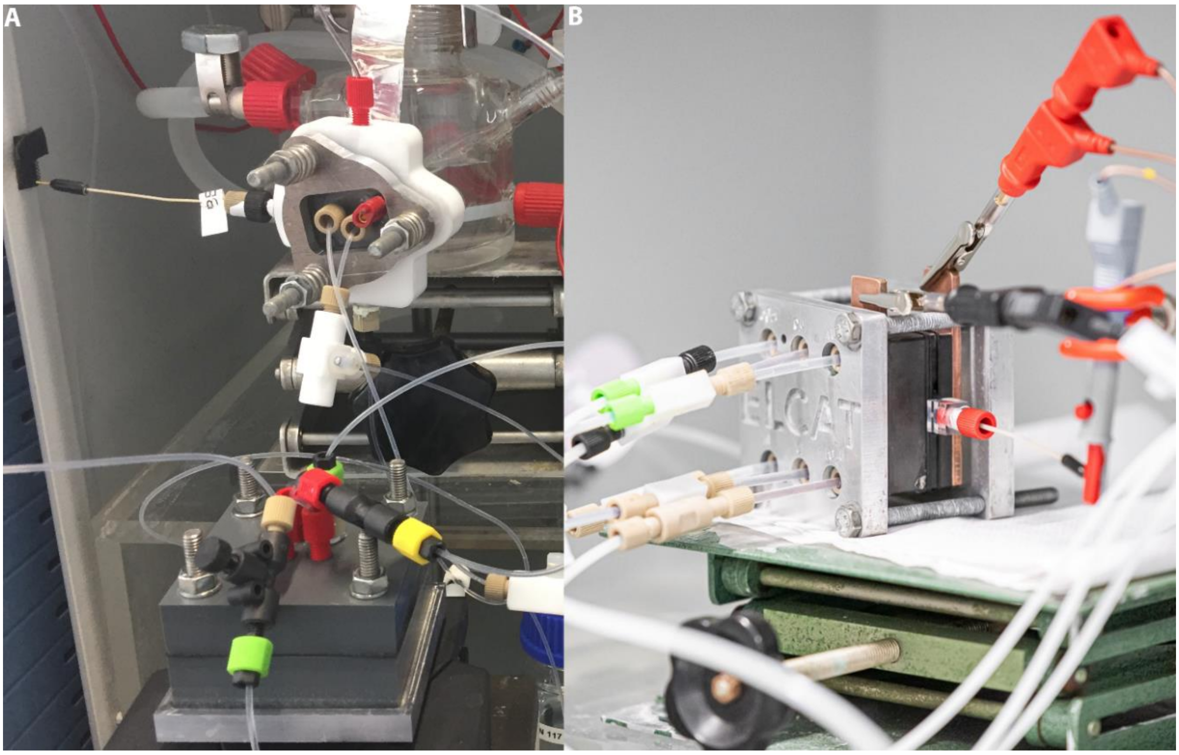

Figure S 8-6: Photograph of (A) the hybrid flow cell land (B) the flow reactor used for the 1 h experiment and the stability measurements, respectively.

Table S 8-1: Comparison of the at% of Ag and carbon between Ag-based catalysts Ag70 and Ag70C15 effecting the Ag/C ratio

Catalyst	At% Ag (%)	At% C (%)	Ag/C ratio
Ag70	3.75	84.00	0.045
Ag70C15	2.34	88.00	0.027

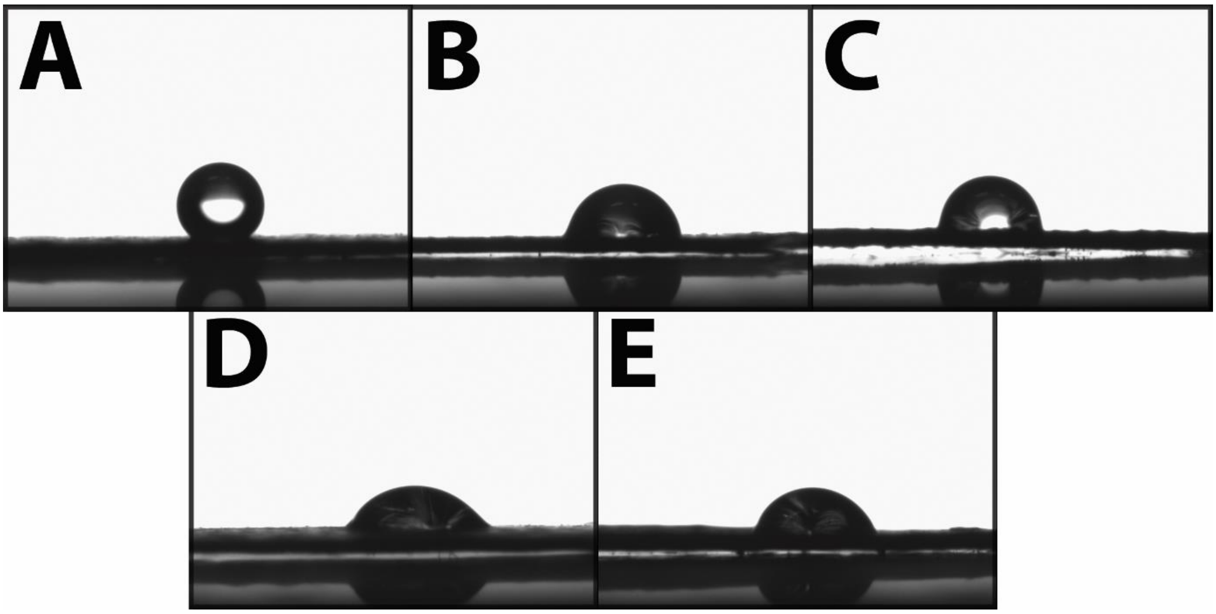

Figure S 8-7: Images taken during contact angle measurements of the sessile droplets of MilliQ on top of the Ag-based GDEs prior to the CO_2 reduction reaction with (A) 0 nm, (B) 5 nm, (C) 15 nm, (D) 30 nm and (E) 50 nm of carbon

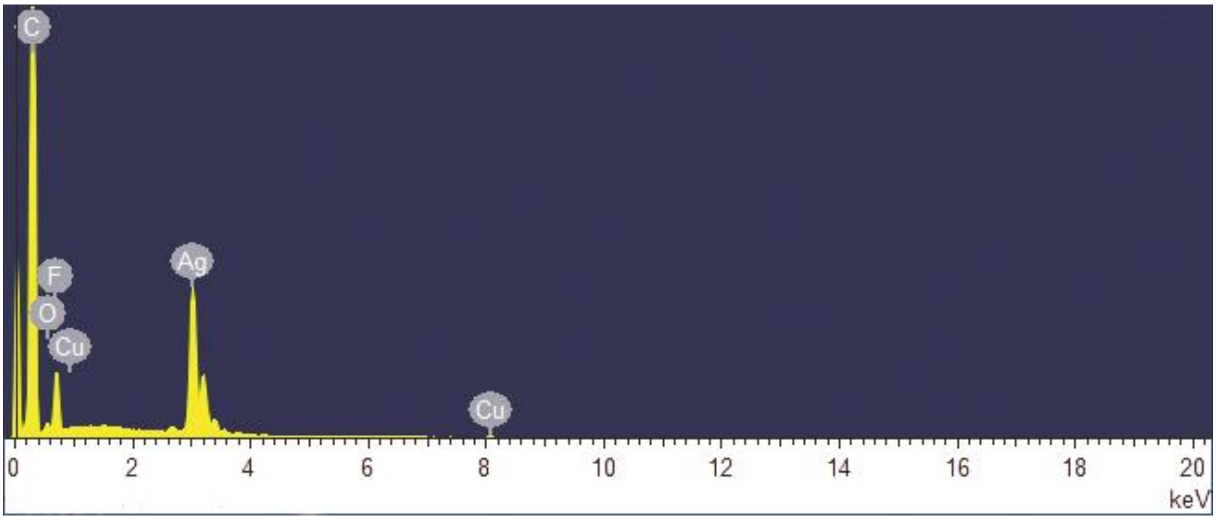

Figure S 8-8: SEM-EDS spectrum of the Ag70 sample depicted in Fig. 1C indicating the presence of Cu impurities inside the Ag layer

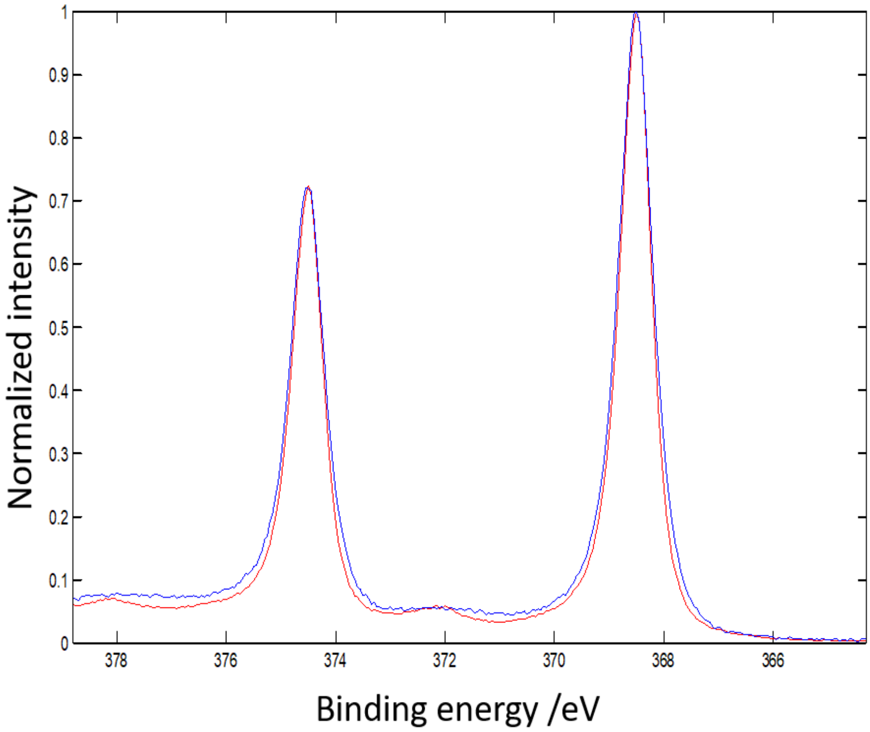

Figure S 8-9: : Normalized high resolution spectra of Ag3d. Ag70 presented in red and Ag70C5 presented in blue.

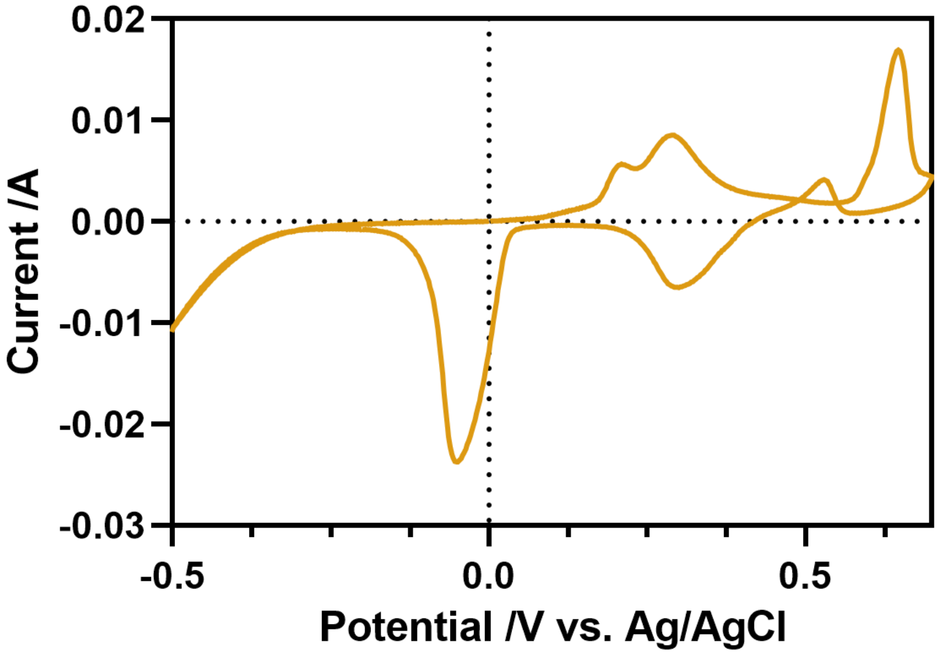

Figure S 8-10: CV measurement (10th scan) of Ag70C15 in 0.5 M KOH, at a scan rate of 50 mV s^{-1}

PART IV

Conclusions and future perspectives

CHAPTER 9:

Conclusions and future perspectives

The final chapter of this work summarizes the scientific conclusions of this doctoral dissertation. The different synthesis methods used in this work, their electrochemical CO_2 reduction performance, the stability of Cu@Ag core-shell nanoparticles and a possible stability strategy are evaluated. Finally, some perspectives on future research are presented.

9.1 Conclusions

The disastrous effects of global warming are catching up on us. As the sense of urgency seeps in, one has been striving to find new technologies. One very promising strategy to combat global warming, is the electrochemical conversion of CO_2 to value-added products. In order to efficiently convert CO_2, the design of an electrocatalyst is of essence since this enables tuning of the final product. Therefore, a reliable synthesis method is key to obtain good control over morphology, size and composition. The behavior of electrocatalysts, more specific bimetallic ones, is not fully understood up until today. In addition, it has been observed that electrocatalysts suffer from stability problems under electrochemical reaction conditions. Hence, the aim of the work was to optimize the synthesis routes towards reproducible electrocatalysts (in this work we focused on Cu and Ag) to be able unveil the structure-performance relationships of bimetallic nanoparticles. Furthermore, the structural transformation pattern was investigated in order to be able to improve the electrochemical performance of electrocatalysts in general. To pursuit this goal, the experimental section of this dissertation was divided into two parts: (I) Cu-Ag bimetallic catalysts for the CO_2 reduction and (II) stability.

This work focused on exploring possible synthesis routes to design different electrocatalysts in a reproducible manner. As discussed in Chapter 1, Cu-Ag bimetallic catalysts are promising candidates for the CO_2 reduction towards CO as well as hydrocarbons and alcohols.

In Chapter 4, the electrodeposition was investigated to deposit Cu nanoparticle electrocatalysts on rough surfaces. Electrodeposition is known for its outstanding control over electrocatalyst design, since various parameters can be tuned. Nevertheless, this technique is primarily used on smooth surfaces, whereas in Chapter 4, a gas diffusion electrode was used as deposition substrate. This entailed several challenges:

- The hydrophobicity of the substrate complicated the deposition of Cu. The hydrophobicity can be altered by pre-treating the surface, inducing differences in surface charge, as evidenced by the CV measurements where a peak potential shift was observed. These changes instigated differences in nucleation modes, thereby leading to differences in morphology and size of the Cu particles.

- The roughness of the substrate surface hampered the reproducibility of the synthesis of Cu particles when using analogous parameters. Despite the fact that the particle size and density could be adjusted by varying the nucleation potential, growth charge and electrolyte composition, electrodeposition remains inconsistent on rough surfaces. Apparently, the surface roughness is an additional parameter that needs to be accounted for during the electrocatalyst synthesis by means of electrodeposition.

As electrodeposition on rough surfaces has shown to be inconsistent, another approach was explored in Chapter 5. Thermal decomposition was used to synthesize highly monodisperse Cu nanoparticles. Various Cu-Ag bimetallic nanoparticles (e.g. different compositions and configurations) could be obtained by applying a Ag shell, using galvanic displacement. Several parameters, listed below, influence the synthesis of these nanoparticles.

- The role of the ligand: Since TDPA (the preferred ligand during the Cu nanoparticle synthesis) interacts strongly with the Cu-precursor, it ensured monodispersity and good self-assembling. Nevertheless, experiments showed the concentration has an influence on the size focusing of the nanoparticles as well as on the particle size. An optimum TDPA:Cu ratio was found at 0.5. Higher ratios resulted in the production of bigger nanoparticles, which exceeded 10 nm. Lower ratios, on the other hand, resulted in NPs with a broad size distribution.

- The Ag concentration: The Cu:Ag ratio in the bimetallic particles can be tuned by changing the initial concentration of Ag during the galvanic displacement. Depending on the initial size of the Cu core nanoparticle, one or two galvanic replacement steps are required, which is attributed to the altered interfacial energy.

- The temperature and heat distribution: The galvanic displacement can also be performed at elevated temperatures. It is of crucial importance that the applied heat is properly distributed in the entire sample. If not, elevated temperatures result in the formation of an inhomogeneous shell with local Ag enrichment on the nanoparticles.

In this work, Cu0.5Ag45 bimetallic nanoparticles showed to be stable during storage for over 12 months despite the large lattice misfit between Cu and Ag, making these configurations prone to degradation over time. The improved stability could possibly be attributed to:

- The solvent, in which these nanoparticles were stored. A solvent should be selected in which the preferred ligand is poorly soluble. In this work hexane is preferred because TDPA is poorly soluble in this solvent.

- The high Ag concentration in the bimetallic nanoparticles. The presence of an increased amount of Ag in the shell could be able to release the strain in the core-shell resulting in a more stable core-shell configuration

- The multi-step galvanic displacement, where in the first step a stable intermediate is formed. Afterwards the formation of the shell is completed by a second galvanic displacement.

The thermal decomposition and subsequent galvanic displacement allowed the synthesis of Cu-Ag bimetallic nanoparticles differing in size, morphology and composition. The effect on their performance was elucidated in Chapter 6. It was shown that the CO production could be boosted when considering the effect of:

- Ag concentration: Introducing Ag in the bimetallic system resulted in an increase in CO production, which improved even further upon Ag enrichment. It is evident that the Ag:Cu ratio can be regarded as an imaginary slider button that lowers the average binding energy of *CO in the entire system, enhancing the production of CO. The increase in CO production was accompanied by a suppression of the HER, which could be attributed to a reduced H binding strength on Cu surfaces generated upon introduction of Ag. In addition, the share of methane appeared to grow at the expense of ethylene in the Cu-Ag series.

- Ag coverage: Comparing Cu/Ag nanodimer and Cu@Ag core-shell structures with comparable Ag:Cu ratio it was evident that core-shell structures were generally more selective towards CO than nanodimers. Accordingly, production of ethylene, methane and ethanol was lower on core-shell structures compared to the nanodimers.

- The electrolyte: Literature recently showed that the electrolyte can influence the product distribution. When $CsHCO_3$ instead of $KHCO_3$ was used during the electrochemical CO_2 reduction over Cu@Ag core-shell nanoparticles, a selectivity shift towards CO occurred. On the other hand, the selectivity towards hydrogen, methane and ethanol decreased.

The Cu-Ag series experienced structural changes during the CO_2 reduction due to electrocatalyst reconstruction. Nevertheless, the exact structural tranformation pathway remained indistinct, which is key in postulating a proper strategy to prevent these changes and enable the investigation of the original electrocatalyst structures. Therefore, Chapter 7 was devoted to unravel the early stages of structural transformation and its effect on the eCO_2R over Cu@Ag core-shell NPs. In this chapter electron tomography at atomic resolution was used to investigate the Cu@Ag core-shell structure. Since Cu and Ag were beam sensitive, it imposed some challenges concerning beam-induced reconstruction. Consequently, decreasing the dwell time and increasing the scan rate enabled the acquisition of the tilt series for tomography and avoided damaging the nanoparticles.

3D reconstructions demonstrated an oval Cu@Ag core-shell structure due to the inhomogeneous shell ranging from 2.5 nm to 1 nm, in contrast the literature reports that were based on 2D projections images. Investigation of the orthoslices revealed several defects in the interior of the Cu core, which most probably induced the polycrystalline character of the Ag shell. Applying electrochemical stress under CO_2 reaction conditions revealed that electrocatalyst reconstruction proceeded in two consecutive steps. Firstly, the Cu leached from the core through the thinner parts of the Ag shell, where pinholes were located. This leaching was caused by the adsorption of CO, inducing the reconstruction of the Cu surface and eventually leading to the formation of an inverted core-shell structure. Subsequently, the nanoparticles agglomerated to form bigger nanoparticles. Nanoparticle reconstruction could also be derived from the CV measurements, where the Cu reduction peak current increased and an anodic peak shift was observed. In addition, Cu leaching promoted the production of ethylene and suppressed the production of hydrogen.

Given the unique and multistep electrocatalyst reconstruction pathway and the persistent production of hydrogen, Chapter 8 focused on the use of nanoscale carbon layers to prevent electrocatalyst reconstruction and inhibit the HER. To evaluate the behavior of these carbon layers, Ag-based electrodes were used to serve as a benchmark. Remarkably, the nanoscale carbon layer served as an excellent HER inhibitor and preserved a homogeneous distribution of the catalyst layer over time.

To conclude, this thesis showed that the synthesis approach is crucial in obtaining proper electrocatalysts particles and depending on which application, a different synthesis method should be addressed. In addition, electrochemistry and electron microscopy prove to be complementary techniques which allows the in-depth study of electrochemical processes. This enables to combat electrocatalytic challenges, such as electrocatalyst reconstruction, in a tailored way.

9.2 Future perspectives

This thesis has demonstrated the successful design of spherical-like electrocatalysts in Chapter 5, with altered composition and size. Despite the improvements on the synthesis method in terms of particle/composition control, the environmental aspects still have to be considered. As discussed in 5.1, often toxic components are employed. In this respect, a first step has already been taken, as TDPA was used as stabilizing agent during the Cu synthesis. Nevertheless, there is still room for improvement since for example TOA is a toxic solvent. Alternatives such as plant-based components are currently being described in literature [264].

The synthesized nanostructures where analyzed by combining the use of electrochemistry and electron tomography. The latter field rapidly evolved during the last decade. Electron tomography was primarily used to obtain information about a nanostructure which could not be obtained in performing 2D analysis. Nevertheless, even for seemingly simple structures, valuable information (e.g. how the structure actually looks like, interior information) is still missing. The time required to obtain a tilt-series is the major limitation when using electron tomography, which can be quite challenging when using beam sensitive materials as used in this thesis. Tremendous efforts have been made to analyze such materials by (i) reducing the electron dose when using undersampling (using higher tilt increment, measuring randomly selected pixels); (ii) decreasing the acquisition time fast tomography (continuous image acquisition with intermediate refocusing and repositioning). The latter also enables the analysis of dynamic processes such as NP reconstruction during electrocatalysis.

In addition, it should be stressed out that the product distribution during the CO_2 reduction can, apart from size and composition, also be tuned by morphology. It is therefore worthwhile to investigate the possibility of modifying the existing synthesis route to be able to obtain for example cubic and octahedral structures. Note that the surfactant can play a key role in designing different electrocatalyst structures. By incorporating different ligands, the shape can be altered since some ligands preferentially bind to a crystal facet. In addition, by changing the ligand-to-Cu ratio in the existing synthesis method the dispersity and size can be tuned even further.

In this work, the performance of various Cu-Ag series were tested in a hybrid flow reactor. Despite the relatively small gas and liquid volume, the analysis of primarily liquid products remained challenging. A next step in future research could be the investigation of the electrocatalyst performance using differential electrochemical mass spectrometry (DEMS). This technique combines electrochemistry and spectroscopy and enables the detection of electrochemically synthesized products by mass spectroscopy. This technique allows in-situ detection of gaseous or volatile reaction products. The set-up that is used consists of an electrochemical half-cell that is separated from a vacuum system by a membrane. The products are ionized and separated by their mass-to-charge ratio. The advantage of this technique is the usage of a 25 µL cell, which allows real-time analysis of the products. In addition, small amounts of product can be detected that were maybe undetectable in the current reactor. This approach will allow a more accurate detection of all products that can possibly be synthesized by using a Cu-Ag bimetallic electrocatalyst.

DEMS analysis could also be an asset in determining the evolution of product distribution in the early stages of electrocatalyst restructuring. In Chapter 7, the effect of catalyst restructuring on the product distribution was investigated. Nevertheless, the analysis was currently hampered by the relatively large liquid and gas volume in the reactor. Therefore, it is suggested to use DEMS in order to obtain insights in the product distribution during the first few seconds of the electrolysis. This could determine the selectivity of the initial Cu@Ag core-shell nanoparticles.

Nanoscale carbon layers proved to be an excellent HER inhibitor and improved the stability of Ag-based electrocatalysts. The effect of a carbon layer on Cu-Ag bimetallic nanoparticles should be further explored. Recently published research showed the benefit of a carbon shell in preventing Cu restructuring. The carbon layer used in this work, could potentially avert the leaching of Cu from the bimetallic nanoparticles and prevent agglomeration.

List of figures

List of tables

Bibliography

[1] J. A. Bell, “Benchtop Global-Warming Demonstrations Do Not Exemplify the Atmospheric Greenhouse Effect, but Alternatives Are Available,” *J. Chem. Educ.*, vol. 96, no. 10, pp. 2352–2354, 2019, doi: 10.1021/acs.jchemed.8b01057.

[2] T. Gr *et al.*, “Evaluation of Methane Emissions Originating from LNG Ships Based on the Measurements at a Remote Marine Station Tiia,” *Environ. Sci. Technol.*, 2021, doi: 10.1021/acs.est.1c03293.

[3] O. et al. Edenhofer, “Climate Change 2014 Mitigation of Climate Change,” 2014.

[4] M. et al. Allen, “GLOBAL WARMING OF 1.5 ° C an IPCC special report on the impacts of global,” 2018.

[5] IPCC, “Climate Change 2021: The Physical Science Basis,” 2021. doi: 10.1002/2014GL06106.

[6] L. Glowka, “Second conference of the parties,” *Environ. Policy Law*, vol. 26, no. 2–3, pp. 71–75, 1996.

[7] U. Nations, “COP26 the Glasgow climate pact,” 2021.

[8] European Union, “Long-term low greenhouse gas emission development strategy of the European Union and its Member States,” 2020. [Online]. Available: http://www4.unfccc.int/submissions/INDC/Published Documents/Latvia/1/LV-03-06-EU INDC.pdf

[9] D. E. H. J. Gernaat, H. S. De Boer, V. Daioglou, S. G. Yalew, C. Müller, and D. P. Van Vuuren, “Climate change impacts on renewable energy supply,” *Nat. Clim. Chang.*, vol. 11, pp. 119–125, 2021, doi: 10.1038/s41558-020-00949-9.

[10] INTERNATIONAL ENERGY AGENCY, “World Energy Outlook 2017,” 2017.

[11] et al Ram, M., *GLOBAL ENERGY SYSTEM BASED ON 100 % RENEWABLE ENERGY*. 2019.

[12] M. Z. Jacobson, M. A. Delucchi, M. A. Cameron, and B. V Mathiesen, “Matching demand with supply at low cost in 139 countries among 20 world regions with 100%

intermittent wind, water, and sunlight (WWS) for all purposes," *Renew. Energy*, 2018, doi: 10.1016/j.renene.2018.02.009.

[13] S. Teske, *Achieving the Paris Climate Agreement Goals*. 2018.

[14] A. B. Gallo, J. R. Simões-Moreira, H. K. M. Costa, M. M. Santos, and E. Moutinho dos Santos, "Energy storage in the energy transition context: A technology review," *Renew. Sustain. Energy Rev.*, vol. 65, pp. 800–822, 2016, doi: 10.1016/j.rser.2016.07.028.

[15] P. Denholm and M. Hand, "Grid flexibility and storage required to achieve very high penetration of variable renewable electricity," *Energy Policy*, vol. 39, no. 3, pp. 1817–1830, 2011, doi: 10.1016/j.enpol.2011.01.019.

[16] A. Evans, V. Strezov, and T. J. Evans, "Assessment of utility energy storage options for increased renewable energy penetration," *Renew. Sustain. Energy Rev.*, vol. 16, no. 6, pp. 4141–4147, 2012, doi: 10.1016/j.rser.2012.03.048.

[17] K. Van Kranenburg, E. Schols, H. Gelevert, R. De Kler, Y. Van Delft, and M. Weeda, "EMPOWERING THE CHEMICAL INDUSTRY OPPORTUNITIES FOR," 2016.

[18] European and Council, "Report on the functioning of the European carbon market," 2020.

[19] European Commission, "EU ETS Handbook," 2015. [Online]. Available: http://ec.europa.eu/clima/publications/docs/ets_handbook_en.pdf

[20] C. Federsel, R. Jackstell, and M. Beller, "State-of-the-art catalysts for hydrogenation of carbon dioxide," *Angew. Chemie - Int. Ed.*, vol. 49, no. 36, pp. 6254–6257, 2010, doi: 10.1002/anie.201000533.

[21] F. Orsini and P. Marrone, "Approaches for a low-carbon production of building materials: A review," *J. Clean. Prod.*, vol. 241, p. 118380, 2019, doi: 10.1016/j.jclepro.2019.118380.

[22] T. Wich, W. Lueke, G. Deerberg, and M. Oles, "Carbon2Chem®-CCU as a Step Toward a Circular Economy," *Front. Energy Res.*, vol. 7, no. January, pp. 1–14, 2020, doi: 10.3389/fenrg.2019.00162.

[23] A. Wieckowski, *Catalysis in Electrochemistry From Fundamental Aspects to Strategies for Fuel Cell Development*. 2011.

[24] P. B. Balbuena and V. R. Subramanian, *Theory and Experiment in Electrocatalysis*. 2010.

[25] Q. Shao, P. WAng, S. Liu, and X. Huang, “Advanced Engineering of Core/Shell Nanostructures for Electrochemical Carbon Dioxide Reduction,” *J. Mater. Chem. A*, 2019, doi: 10.1039/C9TA07016H.

[26] P. Sabatier, “Hydrogénations et déshydrogénations par catalyse,” p. 1984, 1911.

[27] K. P. seem. like the best candidate Kuhl, T. Hatsukade, E. R. Cave, D. N. Abram, J. Kibsgaard, and T. F. Jaramillo, “Electrocatalytic conversion of carbon dioxide to methane and methanol on transition metal surfaces,” *J. Am. Chem. Soc.*, vol. 136, no. 40, pp. 14107–14113, 2014, doi: 10.1021/ja505791r.

[28] J. T. Feaster *et al.*, “Understanding Selectivity for the Electrochemical Reduction of Carbon Dioxide to Formic Acid and Carbon Monoxide on Metal Electrodes,” *ACS Catal.*, vol. 7, no. 7, pp. 4822–4827, 2017, doi: 10.1021/acscatal.7b00687.

[29] M. E. Royer, “-,” *Comptes rendus hebdomadaires des séances de l´Académie des science*, vol. 70, 1870.

[30] Y. Y. Birdja, E. Pérez-Gallent, M. C. Figueiredo, A. J. Göttle, F. Calle-Vallejo, and M. T. M. Koper, “Advances and challenges in understanding the electrocatalytic conversion of carbon dioxide to fuels,” *Nat. Energy*, vol. 4, no. 9, pp. 732–745, 2019, doi: 10.1038/s41560-019-0450-y.

[31] Y. Hori, A. Murata, and R. Takahashi, “Formation of hydrocarbons in the electrochemical reduction of carbon dioxide at a copper electrode in aqueous solution,” *J. Chem. Soc. Faraday Trans. 1 Phys. Chem. Condens. Phases*, vol. 85, no. 8, pp. 2309–2326, 1989, doi: 10.1039/F19898502309.

[32] N. Hoshi, M. Kato, and Y. Hori, “Electrochemical reduction of CO_2 on single crystal electrodes of silver Ag(111), Ag(100) and Ag(110),” 1997. doi: 10.1016/S0022-0728(97)00447-6.

[33] Y. Hori, “Selective formation of C_2 compounds from electrochemical reduction of CO,” *J. Phys. Chem. B*, vol. 106, pp. 15–17, 2002, doi: 10.1021/jp013478d.

[34] Y. Hori, I. Takahashi, O. Koga, and N. Hoshi, “Electrochemical reduction of carbon dioxide at various series of copper single crystal electrodes,” *J. Mol. Catal. A Chem.*, vol. 199, no. 1–2, pp. 39–47, 2003, doi: 10.1016/S1381-1169(03)00016-5.

[35] Y. Hori, H. Wakebe, T. Tsukamoto, and O. Koga, “Electrocatalytic process of CO selectivity in electrochemical reduction of CO_2 at metal electrodes in aqueous media,” *Electrochim. Acta*, vol. 39, no. 11–12, pp. 1833–1839, 1994, doi: 10.1016/0013-4686(94)85172-7.

[36] X. G. Zhang, X. Jin, D. Y. Wu, and Z. Q. Tian, “Selective Electrocatalytic Mechanism of CO_2 Reduction Reaction to CO on Silver Electrodes: A Unique Reaction Intermediate,” *J. Phys. Chem. C*, vol. 122, no. 44, pp. 25447–25455, 2018, doi: 10.1021/acs.jpcc.8b08170.

[37] K. J. P. Schouten, Y. Kwon, C. J. M. der Ham, Z. Qin, and M. T. M. Koper, “A new mechanism for the selectivity to C_1 and C_2 species in the electrochemical reduction of carbon dioxide on copper electrodes,” *Chem. Sci.*, vol. 2, no. 10, pp. 1902–1909, 2011.

[38] K. P. Kuhl, E. R. Cave, D. N. Abram, and T. F. Jaramillo, “New insights into the electrochemical reduction of carbon dioxide on metallic copper surfaces,” *Energy Environ. Sci.*, vol. 5, no. 5, pp. 7050–7059, 2012, doi: 10.1039/c2ee21234j.

[39] Y. Y. Birdja and M. T. M. Koper, “The importance of cannizzaro-type reactions during electrocatalytic reduction of carbon dioxide,” *J. Am. Chem. Soc.*, vol. 139, no. 5, pp. 2030–2034, 2017, doi: 10.1021/jacs.6b12008.

[40] E. L. Clark, J. Wong, A. J. Garza, Z. Lin, M. Head-Gordon, and A. T. Bell, “Explaining the Incorporation of Oxygen Derived from Solvent Water into the Oxygenated Products of CO Reduction over Cu,” *J. Am. Chem. Soc.*, vol. 141, no. 10, pp. 4191–4193, 2019, doi: 10.1021/jacs.8b13201.

[41] S. Gao *et al.*, “Atomic layer confined vacancies for atomic-level insights into carbon dioxide electroreduction,” *Nat. Commun.*, vol. 8, pp. 1–9, 2017, doi: 10.1038/ncomms14503.

[42] F. Yu, P. Wei, Y. Yang, Y. Chen, L. Guo, and Z. Peng, “Material design at nano and atomic scale for electrocatalytic CO_2 reduction,” *Nano Mater. Sci.*, vol. 1, no. 1, pp. 60–69, 2019, doi: 10.1016/j.nanoms.2019.03.006.

[43] and G. Z. Yuhang Wang, Junlang Liu, “Designing Copper-Based Catalysts for Efficient Carbon Dioxide Electroreduction.pdf.”

[44] Y. Ye *et al.*, “Dramatic differences in carbon dioxide adsorption and initial steps of reduction between silver and copper,” *Nat. Commun.*, vol. 10, no. 1, pp. 1–9, 2019, doi: 10.1038/s41467-019-09846-y.

[45] E. L. Clark, C. Hahn, T. F. Jaramillo, and A. T. Bell, “Electrochemical CO_2 Reduction over Compressively Strained CuAg Surface Alloys with Enhanced Multi-Carbon Oxygenate Selectivity,” *J. Am. Chem. Soc.*, vol. 139, no. 44, pp. 15848–15857, 2017, doi: 10.1021/jacs.7b08607.

[46] S. Hanselman, M. T. M. Koper, and F. Calle-Vallejo, “Computational Comparison of Late Transition Metal (100) Surfaces for the Electrocatalytic Reduction of CO to C_2 Species,” *ACS Energy Lett.*, vol. 3, no. 5, pp. 1062–1067, 2018, doi: 10.1021/acsenergylett.8b00326.

[47] Y. C. Li *et al.*, “Binding Site Diversity Promotes CO_2 Electroreduction to Ethanol,” *J. Am. Chem. Soc.*, pp. 8584–8591, 2019.

[48] A. Vasileff, C. Xu, Y. Jiao, Y. Zheng, and S. Z. Qiao, “Surface and Interface Engineering in Copper-Based Bimetallic Materials for Selective CO_2 Electroreduction,” *Chem*, vol. 4, no. 8, pp. 1809–1831, 2018, doi: 10.1016/j.chempr.2018.05.001.

[49] Y. Yang, S. Ajmal, Y. Feng, K. Li, X. Zheng, and L. Zhang, “Insight into the Formation and Transfer Process of the First Intermediate of CO_2 Reduction over Ag-Decorated Dendritic Cu,” *Chem. - A Eur. J.*, vol. 26, no. 18, pp. 4080–4089, 2020, doi: 10.1002/chem.201904063.

[50] H. Zhang *et al.*, “Computational and experimental demonstrations of one-pot tandem catalysis for electrochemical carbon dioxide reduction to methane,” *Nat. Commun.*, vol. 10, no. 1, pp. 1–9, 2019, doi: 10.1038/s41467-019-11292-9.

[51] R. Kortlever, J. Shen, K. J. P. Schouten, F. Calle-Vallejo, and M. T. M. Koper, “Catalysts and Reaction Pathways for the Electrochemical Reduction of Carbon Dioxide,” *J. Phys. Chem. Lett.*, vol. 6, no. 20, pp. 4073–4082, 2015, doi: 10.1021/acs.jpclett.5b01559.

[52] H. Zhang, X. Chang, Q. Lu, J. G. Chen, and W. A. G. Iii, “Computational and experimental demonstrations of one-pot tandem catalysis for electrochemical carbon dioxide reduction to methane,” *Nat. Commun.*, pp. 1–9, 2019, doi: 10.1038/s41467-019-11292-9.

[53] Y. Lum and J. W. Ager, “Sequential Catalysis Controls Selectivity in Electrochemical CO_2 Reduction on Cu,” *Energy Environ. Sci.*, 2018, doi: 10.1039/C8EE01501E.

[54] D. Choukroun *et al.*, “Mapping Composition − Selectivity Relationships of Supported Sub-10 nm Cu − Ag Nanocrystals for High-Rate CO_2 Electroreduction,” *ACS Nano*, 2021, doi: 10.1021/acsnano.1c04943.

[55] E. L. Clark, C. Hahn, T. F. Jaramillo, and A. T. Bell, “Electrochemical CO_2 Reduction over Compressively Strained CuAg Surface Alloys with Enhanced Multi-Carbon Oxygenate Selectivity,” *J. Am. Chem. Soc.*, pp. 15848–15857, 2017, doi: 10.1021/jacs.7b08607.

[56] R. Reske, H. Mistry, F. Behafarid, B. R. Cuenya, and P. Strasser, “Particle Size Effects in the Catalytic Electroreduction of CO_2 on Cu Nanoparticles,” *J Amer Chem Soc*, vol. 136, no. 3, pp. 6978–6986, 2014, doi: 10.1021/ja500328k |.

[57] Q. Lu *et al.*, “A selective and efficient electrocatalyst for carbon dioxide reduction,” *Nat. Commun.*, 2014, doi: 10.1038/ncomms4242.

[58] M. Yang *et al.*, “Facet Sensitivity of Capping Ligand-Free Ag Crystals in CO_2 Electrochemical Reduction to CO,” *ChemCatChem*, 2018.

[59] A. Bagger, W. Ju, A. S. Varela, P. Strasser, and J. Rossmeisl, “Electrochemical CO_2 Reduction: Classifying Cu Facets,” *ACS Catal.*, vol. 9, no. 9, pp. 7894–7899, 2019, doi: 10.1021/acscatal.9b01899.

[60] G. O. Larrazábal, A. J. Martín, S. Mitchell, R. Hauert, and J. Pérez-Ramírez, “Synergistic effects in silver–indium electrocatalysts for carbon dioxide reduction,” *J. Catal.*, vol. 343, pp. 266–277, 2016, doi: 10.1016/j.jcat.2015.12.014.

[61] C. Kim *et al.*, “Achieving Selective and Efficient Electrocatalytic Activity for CO_2 Reduction Using Immobilized Silver Nanoparticles,” *J. Am. Chem. Soc.*, vol. 137, no. 43, pp. 13844–13850, 2015, doi: 10.1021/jacs.5b06568.

[62] C. Kim *et al.*, “Insight into Electrochemical CO_2 Reduction on Surface-Molecule-Mediated Ag Nanoparticles,” *ACS Catal.*, vol. 7, no. 1, pp. 779–785, 2017, doi: 10.1021/acscatal.6b01862.

[63] S. Ahn *et al.*, “Poly-Amide Modified Copper Foam Electrodes for Enhanced Electrochemical Reduction of Carbon Dioxide,” *ACS Catal.*, vol. 8, no. 5, pp. 4132–4142, 2018, doi: 10.1021/acscatal.7b04347.

[64] E. Irtem *et al.*, “Ligand-mode directed selectivity in Cu–Ag core–shell based gas diffusion electrodes for CO_2 electroreduction,” *ACS Catal.*, pp. 13468–13478, 2020.

[65] J. Zhang, Q. Shao, P. Wang, J. Guo, and X. Huang, “Catalytic Hydrogen Production by Janus CuAg Nanostructures,” *ChemNanoMat*, vol. 4, no. 5, pp. 477–481, 2018, doi: 10.1002/cnma.201800057.

[66] Z. Chang, S. Huo, W. Zhang, J. Fang, H. Wang, and J. Accepted, “The Tunable and Highly Selective Reduction Products on Ag @ Cu Bimetallic Catalysts Towards CO_2 Electrochemical Reduction Reaction,” *J. Phys. Chem. C*, 2017.

[67] D. Higgins *et al.*, “Guiding Electrochemical Carbon Dioxide Reduction toward Carbonyls Using Copper Silver Thin Films with Interphase Miscibility,” *ACS Energy Lett.*, vol. 3, no. 12, pp. 2947–2955, 2018, doi: 10.1021/acsenergylett.8b01736.

[68] A. Tamilvanan, K. Balamurugan, K. Ponappa, and B. M. Kumar, “Copper Nanoparticles: Synthetic Strategies, Properties and Multifunctional Application,” *Int. J. Nanosci.*, vol. 13, no. 02, p. 1430001, 2014, doi: 10.1142/S0219581X14300016.

[69] E. Gross, “Tuning Product Selectivity by Changing the Size of Catalytically Active Metallic Nanoparticles,” *Stud. Surf. Sci. Catal.*, vol. 177, pp. 57–84, 2017, doi: 10.1016/B978-0-12-805090-3.00002-4.

[70] J. A. Van Bokhoven and J. T. Miller, “D Electron Density and Reactivity of the D Band As a Function of Particle Size in Supported Gold Catalysts,” *J. Phys. Chem. C*, vol. 111, no. 26, pp. 9245–9249, 2007, doi: 10.1021/jp070755t.

[71] B. Hammer, “Adsorbate-Oxide Interactions during the NO + CO Reaction on MgO(100) Supported Pd Monolayer Films,” *Phys. Rev. Lett.*, vol. 89, no. 1, pp. 1–4, 2002, doi: 10.1103/PhysRevLett.89.016102.

[72] B. Hammer, “Special sites at noble and late transition metal catalysts,” *Top. Catal.*, vol. 37, no. 1, pp. 3–16, 2006, doi: 10.1007/s11244-006-0004-y.

[73] A. Sengupta and C. K. S. Sarkar, *Introduction to Nano*. 2015.

[74] B. S. Murty, P. Shankar, B. Raj, B. B. Rath, and J. Murday, *Textbook of Nanoscience and Nanotechnology*. 2013.

[75] A. Salehi-Khojin *et al.*, “Nanoparticle silver catalysts that show enhanced activity for carbon dioxide electrolysis,” *J. Phys. Chem. C*, vol. 117, no. 4, pp. 1627–1632, 2013, doi: 10.1021/jp310509z.

[76] Y.-C. Hsieh, S. D. Senanayake, Y. Zhang, W. Xu, and D. E. Polyansky, “Effect of Chloride Anions on the Synthesis and Enhanced Catalytic Activity of Silver Nanocoral Electrodes for CO_2 Electroreduction,” *ACS Catal.*, vol. 5, no. 9, pp. 5349–5356, 2015, doi: 10.1021/acscatal.5b01235.

[77] S. E. Habas, H. Lee, V. Radmilovic, G. A. Somorjai, and P. Yang, “Shaping binary metal nanocrystals through epitaxial seeded growth,” *Nat. Mater.*, vol. 6, no. 9, pp. 692–697, 2007, doi: 10.1038/nmat1957.

[78] J. R. Kitchin, J. K. Norskov, M. A. Barteau, and J. G. Chen, “Role of strain and ligand effects in the modification of the electronic and chemical Properties of bimetallic surfaces,” *Phys. Rev. Lett.*, vol. 93, no. 15, pp. 4–7, 2004, doi: 10.1103/PhysRevLett.93.156801.

[79] M. B. Gawande *et al.*, “Core-shell nanoparticles: synthesis and applications in catalysis and electrocatalysis,” *Chem. Soc. Rev.*, vol. 44, no. 21, pp. 7540–7590, 2015, doi: 10.1039/c5cs00343a.

[80] H. Baltruschat, S. Ernst, and N. Bogolowski, “Electrocatalysis at Bimetallic Surfaces Obtained by Surface Decoration,” in *Catalysis in Electrochemistry: From Fundamentals to Strategies for Fuel Cell Development*, 2011, pp. 297–337. doi: 10.1002/9780470929421.ch9.

[81] C. Wei *et al.*, “Surface Composition Dependent Ligand Effect in Tuning the Activity of Nickel−Copper Bimetallic Electrocatalysts toward Hydrogen Evolution in Alkaline,” *J. Am. Chem. Soc.*, 2020, doi: 10.1021/jacs.9b12005.

[82] S. Nitopi *et al.*, “Progress and Perspectives of Electrochemical CO_2 Reduction on Copper in Aqueous Electrolyte,” *Chem. Rev.*, 2019, doi: 10.1021/acs.chemrev.8b00705.

[83] S. Alayoglu, A. U. Nilekar, M. Mavrikakis, and B. Eichhorn, “Ru – Pt core – shell nanoparticles for preferential oxidation of carbon monoxide in hydrogen,” *Nature*, pp. 333–338, 2008, doi: 10.1038/nmat2156.

[84] D. M. Mott and S. Maenosono, “Manipulation of the electronic properties of gold and silver core-shell nanoparticles,” *ACS Symp. Ser.*, vol. 1112, pp. 327–358, 2012, doi: 10.1021/bk-2012-1112.ch013.

[85] B. Hammer and J. K. Nørskov, “Electronic factors determining the reactivity of metal surfaces,” *Surf. Sci.*, vol. 343, no. 3, pp. 211–220, 1995, doi: 10.1016/0039-6028(96)80007-0.

[86] L. Tang *et al.*, “Novel Interface in CuAg Nanostructure Induced by Size Effect,” *J. Phys. Chem. Lett.*, vol. 10, pp. 1973–1980, 2019, doi: 10.1021/acs.jpclett.9b00484.

[87] H. Lee and S. H. Ahn, “Ag Displacement on Cu Foam with Additives for

Electrochemical Reduction of Carbon Dioxide to Carbon Monoxide,” *Bull. Korean Chem. Soc.*, vol. 38, no. 9, pp. 1085–1090, 2017, doi: 10.1002/bkcs.11225.

[88] C. Chen *et al.*, “Report Cu-Ag Tandem Catalysts for High-Rate CO_2 Electrolysis toward Multicarbons Cu-Ag Tandem Catalysts for High-Rate CO 2 Electrolysis toward Multicarbons,” *Joule*, vol. 4, no. 8, pp. 1688–1699, 2020, doi: 10.1016/j.joule.2020.07.009.

[89] T. T. H. Hoang *et al.*, “Nano Porous Copper-Silver Alloys by Additive-Controlled Electro- deposition for the Selective Electroreduction of CO_2 to Ethylene and Ethanol,” *J. Am. Chem. Soc.*, 2018, doi: 10.1021/jacs.8b01868.

[90] A. N. Kuhn *et al.*, “Engineering Silver-Enriched Copper Core-Shell Electrocatalysts to Enhance the Production of Ethylene and C_{2+} Chemicals from Carbon Dioxide at Low Cell Potentials,” *Adv. Funct. Mater.*, vol. 2101668, pp. 2–11, 2021, doi: 10.1002/adfm.202101668.

[91] R. P. Jansonius, L. M. Reid, C. N. Virca, and C. P. Berlinguette, “Strain Engineering Electrocatalysts for Selective CO_2 Reduction,” *ACS Energy Lett.*, pp. 980–986, 2019, doi: 10.1021/acsenergylett.9b00191.

[92] C. Cui, L. Gan, M. Heggen, S. Rudi, and P. Strasser, “nanoparticles and their structural behaviour during electrocatalysis,” *Nat. Mater.*, no. June, pp. 1–7, 2013, doi: 10.1038/nmat3668.

[93] M. Luo and S. Guo, “Strain-controlled electrocatalysis on multimetallic nanomaterials,” *Nat. Publ. Gr.*, vol. 2, pp. 1–14, 2017, doi: 10.1038/natrevmats.2017.59.

[94] J. Huang, M. Mensi, E. Oveisi, and V. Mantella, “Structural Sensitivities in Bimetallic Catalysts for Electrochemical CO_2 Reduction Revealed by Ag–Cu Nanodimers,” *J. Am. Chem. Soc.*, 2019, doi: 10.1021/jacs.8b12381.

[95] S. Zhang, S. Zhao, D. Qu, X. Liu, Y. Wu, and Y. Chen, “Electrochemical Reduction of CO_2 Toward C_2 Valuables on Cu@Ag Core-Shell Tandem Catalyst with Tunable Shell Thickness,” vol. 2102293, pp. 1–7, 2021, doi: 10.1002/smll.202102293.

[96] Y. Wang *et al.*, “Ensemble Effect in Bimetallic Electrocatalysts for CO_2 Reduction,” *J. Am. Chem. Soc.*, pp. 16635–16642, 2019, doi: 10.1021/jacs.9b05766.

[97] C. M. Brett and A. M. O. Brett, *Electrochemistry: Principles, Methods and Applications*. Oxford University Press, 1994.

[98] A. J. Bard, L. R. Faulkner, N. York, C. @bullet, W. Brisbane, and S. E. Toronto, *ELECTROCHEMICAL METHODS Fundamentals and Applications*. 1944. doi: 10.1016/B978-0-12-381373-2.00056-9.

[99] K. Gerhard, O. Ken-ichiro, and S. Robert, *Encyclopedia of Applied Electrochemistry*. 2014.

[100] B. J. Inkson, "Scanning Electron Microscopy (SEM) and Transmission Electron Microscopy (TEM) for Materials Characterization," in *Materials Characterization Using Nondestructive Evaluation (NDE) Methods*, Elsevier Ltd, 2016, pp. 17–43. doi: 10.1016/B978-0-08-100040-3.00002-X.

[101] J. I. Goldstein, D. E. Newbury, J. R. Michael, N. W. M. Ritchie, J. H. J. Scott, and D. C. Joy, *Microscopy and X-Ray Microanalysis*. 2018.

[102] A. A. T. Bui and J. Cong, "GENERAL CONVERGENT EXPECTATION MAXIMIZATION (EM)-TYPE ALGORITHMS FOR IMAGE RECONSTRUCTION Ming," *Inverse Probl. Imaging Vol.*, vol. X, no. 0, pp. 1–23, doi: 10.3934/ipi.xx.xx.xx.

[103] A. Ul-Hamid, *A Beginners' Guide to Scanning Electron Microscopy*. 2018. doi: 10.1007/978-3-319-98482-7.

[104] C. E. Lyman *et al.*, *Scanning Electron Microscopy, X-Ray Microanalysis, and Analytical Electron Microscopy Plenum Press @BULLET New York and London*. 1990.

[105] D. B. Williams and C. B. Carter, *Transmission Electron Microscopy: A Textbook for Materials Science*. 2009.

[106] S. J. Pennycook, *Scanning transmission electron microscopy imaging and analysis*. 2011.

[107] A. B. Hungría, J. J. Calvino, and J. C. Hernández-Garrido, "HAADF-STEM Electron Tomography in Catalysis Research," *Top. Catal.*, vol. 62, no. 12–16, pp. 808–821, 2019, doi: 10.1007/s11244-019-01200-2.

[108] J. Frank, *Electron Tomography: Methods for Three-Dimensional Visualization of Structures in the Cell*, vol. 3. 2015.

[109] J. A. Seibert, "Iterative reconstruction: how it works, how to apply it," *Pediatr. Radiol.*, vol. 44, no. 3, pp. 431–439, 2014, doi: 10.1007/s00247-014-3102-1.

[110] F. J. Sigworth, P. C. Doerschuk, J. M. Carazo, and S. H. W. Scheres, “An introduction to maximum-likelihood methods in cryo-EM,” *Methods Enzymol.*, vol. 482, no. C, pp. 263–294, 2010, doi: 10.1016/S0076-6879(10)82011-7.

[111] N. Claes, “3D CHARACTERIZATION OF COATED NANOPARTICLES AND SOFT - HARD NANOCOMPOSITES,” 2018.

[112] P. W. Hawkes, “The electron microscope as a structure projector,” *Electron Tomogr. Methods Three-Dimensional Vis. Struct. Cell*, vol. 9780387690, pp. 83–111, 2006, doi: 10.1007/978-0-387-69008-7_4.

[113] J. Radon, “No Title,” *Ber Verh K Sachs Ges Wiss Leipzig, Math-Phys Kl*, vol. 69, pp. 262–277, 1917.

[114] W. J. Lorenz, *Electrochemical Phase Fomation and Growth Keep up to date with VCH ’ s book series . . . Advances in Electrochemical Science and Engineering*. 1990.

[115] B. Vanrenterghem, B. Geboes, S. Bals, J. Ustarroz, A. Hubin, and T. Breugelmans, “Influence of the support material and the resulting particle distribution on the deposition of Ag nanoparticles for the electrocatalytic activity of benzyl bromide reduction,” *Appl. Catal. B Environ.*, vol. 181, pp. 542–549, 2016, doi: 10.1016/j.apcatb.2015.08.026.

[116] L. L. Hung, C. K. Tsung, W. Huang, and P. Yang, “Room-temperature formation of hollow Cu_2O nanoparticles,” *Adv. Mater.*, vol. 22, no. 17, pp. 1910–1914, 2010, doi: 10.1002/adma.200903947.

[117] Y. Hashimoto *et al.*, “In-plane oriented highly ordered lamellar structure formation of poly(: N -dodecylacrylamide) induced by humid annealing,” *RSC Adv.*, vol. 7, no. 11, pp. 6631–6635, 2017, doi: 10.1039/c6ra27994e.

[118] K. Ebata *et al.*, “Molecular-weight dependence of the formation of highly ordered lamellar structures of poly(: N -dodecyl acrylamide) by humid annealing,” *Polym. Chem.*, vol. 10, no. 7, pp. 835–842, 2019, doi: 10.1039/c8py01660g.

[119] J. M. Wolska, A. Błażejewska, M. Tupikowska, D. Pociecha, and E. Górecka, “Gold nanoparticles grafted with chemically incompatible ligands,” *RSC Adv.*, vol. 11, no. 16, pp. 9568–9571, 2021, doi: 10.1039/d1ra00547b.

[120] T. Mokari, M. Zhang, and P. Yang, “Shape , Size , and Assembly Control of PbTe Nanocrystals,” *J. Am. Chem. Soc.*, pp. 9864–9865, 2007.

[121] P. K. Chu, G. S. Wu, and H. Kong, *Surface design of biodegradable magnesium alloys for biomedical applications*. 2015. doi: 10.1016/B978-1-78242-077-4.00003-6.

[122] Y. Hori, "Electrochemical CO 2 Reduction on Metal Electrodes," no. 42, pp. 89–189.

[123] R. Kas, R. Kortlever, H. Yilmaz, M. T. M. Koper, and G. Mul, "Manipulating the Hydrocarbon Selectivity of Copper Nanoparticles in CO_2 Electroreduction by Process Conditions," *ChemElectroChem*, vol. 2, no. 3, pp. 354–358, 2015, doi: 10.1002/celc.201402373.

[124] W. Tang *et al.*, "The importance of surface morphology in controlling the selectivity of polycrystalline copper for CO_2 electroreduction," *Phys. Chem. Chem. Phys.*, vol. 14, no. 1, pp. 76–81, 2012, doi: 10.1039/c1cp22700a.

[125] H. Cao, T. Hang, H. Ling, and M. Li, "Behaviors of Chloride Ions in Methanesulfonic Acid Bath for Copper Electrodeposition of Through-Silicon-Via," *J. Electrochem. Soc.*, vol. 160, no. 4, pp. D146–D149, 2013, doi: 10.1149/2.052304jes.

[126] K. Manthiram, B. J. Beberwyck, and A. P. Alivisatos, "Enhanced electrochemical methanation of carbon dioxide with a dispersible nanoscale copper catalyst," *J. Am. Chem. Soc.*, vol. 136, no. 38, pp. 13319–13325, 2014, doi: 10.1021/ja5065284.

[127] A. E. W. Horst, K. M. Mangold, and D. Holtmann, "Application of gas diffusion electrodes in bioelectrochemical syntheses and energy conversion," *Biotechnol. Bioeng.*, vol. 113, no. 2, pp. 260–267, 2016, doi: 10.1002/bit.25698.

[128] A. Kaisheva, I. Iliev, R. Kazareva, S. Christov, U. Wollenberger, and F. W. Scheller, "Enzyme/gas-diffusion electrodes for determination of phenol," *Sensors Actuators, B Chem.*, vol. 33, no. 1–3, pp. 39–43, 1996, doi: 10.1016/0925-4005(96)01930-2.

[129] I. Merino-Garcia, J. Albo, and A. Irabien, "Tailoring gas-phase CO_2 electroreduction selectivity to hydrocarbons at Cu nanoparticles," *Nanotechnology*, vol. 29, no. 1, p. 14001, 2018, doi: 10.1088/1361-6528/aa994e.

[130] N. S. Romero Cuellar, K. Wiesner-Fleischer, M. Fleischer, A. Rucki, and O. Hinrichsen, "Advantages of CO over CO_2 as reactant for electrochemical reduction to ethylene, ethanol and n-propanol on gas diffusion electrodes at high current densities," *Electrochim. Acta*, vol. 307, pp. 164–175, 2019, doi: 10.1016/j.electacta.2019.03.142.

[131] Y. L. Qiu, H. X. Zhong, T. T. Zhang, W. Bin Xu, X. F. Li, and H. M. Zhang, "Copper Electrode Fabricated via Pulse Electrodeposition: Toward High Methane Selectivity

and Activity for CO_2 Electroreduction," *ACS Catal.*, vol. 7, no. 9, pp. 6302–6310, 2017, doi: 10.1021/acscatal.7b00571.

[132] H. Guo *et al.*, "Controllable synthesis of Cu–Ni core–shell nanoparticles and nanowires with tunable magnetic properties," *Chem. Commun.*, vol. 52, no. 42, pp. 6918–6921, 2016, doi: 10.1039/C6CC02868C.

[133] K. R. Lee, J. H. Lim, J. K. Lee, and H. S. Chun, "Reduction of Carbon Dioxide in 3-Dimensional Gas Diffusion Electrodes," *Korean J. Chem. Eng.*, vol. 16, no. 6, pp. 829–836, 1999, doi: 10.1007/BF02698360.

[134] H. Xiang, S. Rasul, K. Scott, J. Portoles, P. Cumpson, and E. H. Yu, "Enhanced selectivity of carbonaceous products from electrochemical reduction of CO_2 in aqueous media," *J. CO2 Util.*, vol. 30, no. December 2018, pp. 214–221, 2019, doi: 10.1016/j.jcou.2019.02.007.

[135] M. Nagar, A. Radisic, K. Strubbe, and P. M. Vereecken, "The Effect of the Substrate Characteristics on the Electrochemical Nucleation and Growth of Copper," *J. Electrochem. Soc.*, vol. 163, no. 12, pp. D3053–D3061, 2016, doi: 10.1149/2.0081612jes.

[136] W. Shao, G. Pattanaik, and G. Zangari, "Electrochemical Nucleation and Growth of Copper from Acidic Sulfate Electrolytes on n-Si(001)," *J. Electrochem. Soc.*, vol. 154, no. 7, p. D339, 2007, doi: 10.1149/1.2733813.

[137] R. L. Harniman, D. Plana, G. H. Carter, K. A. Bradley, M. J. Miles, and D. J. Fermín, "Real-time tracking of metal nucleation via local perturbation of hydration layers," *Nat. Commun.*, vol. 8, no. 1, 2017, doi: 10.1038/s41467-017-01087-1.

[138] K. AOTANI and H. SUMIYA, "Studies on Electrodeposition of Copper from Methanesulphonic Acid Bath," *J. Met. Finish. Soc. Japan*, vol. 8, no. 1, pp. 12–18, 2011, doi: 10.4139/sfj1950.8.12.

[139] M. D. Gernon, M. Wu, T. Buszta, and P. Janney, "Environmental benefits of methanesulfonic acid," *Green Chem.*, vol. 1, no. 3, pp. 127–140, 1999, doi: 10.1039/a900157c.

[140] S. Ki Cho, M. Jun Kim, and J. Jeong Kim, "MSA as a Supporting Electrolyte in Copper Electroplating for Filling of Damascene Trenches and Through Silicon Vias," *Electrochem. Solid-State Lett.*, vol. 14, no. 5, p. D52, 2011, doi: 10.1149/1.3557758.

[141] M. Hasan and J. F. Rohan, "Cu Electrodeposition from Methanesulfonate Electrolytes

for ULSI and MEMS Applications," *J. Electrochem. Soc.*, vol. 157, no. 5, p. D278, 2010, doi: 10.1149/1.3332729.

[142] K. Singh, R. Bharose, S. K. Verma, and V. K. Singh, "Potential of powdered activatedmustard cake for decolorising raw sugar," *J. Sci. Food Agric.*, vol. 93, no. 1, pp. 157–165, 2013, doi: 10.1002/jsfa.5744.

[143] L. Thi Mai Hoa, "Characterization of multi-walled carbon nanotubes functionalized by a mixture of HNO_3/H_2SO_4," *Diam. Relat. Mater.*, vol. 89, no. May, pp. 43–51, 2018, doi: 10.1016/j.diamond.2018.08.008.

[144] L. Fan *et al.*, "Effects of surface modification on the reactivity of activated carbon in direct carbon fuel cells," *Electrochim. Acta*, vol. 284, pp. 630–638, 2018, doi: 10.1016/j.electacta.2018.07.196.

[145] Y. C. Chiang, W. H. Lin, and Y. C. Chang, "The influence of treatment duration on multi-walled carbon nanotubes functionalized by H_2SO_4 /HNO_3 oxidation," *Appl. Surf. Sci.*, vol. 257, no. 6, pp. 2401–2410, 2011, doi: 10.1016/j.apsusc.2010.09.110.

[146] M. T. Pise, S. Srinivas, A. Chatterjee, B. P. Kashyap, R. N. Singh, and S. S. V. Tatiparti, "Influence of surface condition on the current densities rendering nucleation loop during cyclic voltammetry for electrodeposition of Pd thin films," *Surfaces and Interfaces*, vol. 20, p. 100525, 2020, doi: 10.1016/j.surfin.2020.100525.

[147] M. Rezaei, S. H. Tabaian, and D. F. Haghshenas, "A kinetic description of Pd electrodeposition under mixed control of charge transfer and diffusion," *J. Electroanal. Chem.*, vol. 687, pp. 95–101, 2012, doi: 10.1016/j.jelechem.2012.10.007.

[148] A. Radisic, F. M. Ross, and P. C. Searson, "In situ study of the growth kinetics of individual island electrodeposition of copper," *J. Phys. Chem. B*, vol. 110, no. 15, pp. 7862–7868, 2006, doi: 10.1021/jp057549a.

[149] S. Wu, Z. Yin, Q. He, G. Lu, Q. Yan, and H. Zhang, "Nucleation mechanism of electrochemical deposition of Cu on reduced graphene oxide electrodes," *J. Phys. Chem. C*, vol. 115, no. 32, pp. 15973–15979, 2011, doi: 10.1021/jp201667p.

[150] R. Tolosa, "Electrochemical Deposition Mechanism for ZnO Nanorods: Diffusion Coefficient and Growth Models," *J. Electrochem. Soc.*, vol. 158, no. 11, pp. E107–E110, 2011, doi: 10.1149/0.020111jes.

[151] X. Zhou, Y. Wang, Z. Liang, and H. Jin, "Electrochemical deposition and

nucleation/growth mechanism of Ni-Co-Y_2O_3 multiple coatings," *Materials (Basel).*, vol. 11, no. 7, 2018, doi: 10.3390/ma11071124.

[152] B. Scharifker, "Theoretical and experimental studies of multiple nucleation," *Electrochim. Acta*, vol. 28, no. 7, pp. 879–889, 1982.

[153] G. Gunawardena, G. Hills, I. Montenegro, and B. Scharifker, "Electrochemical nucleation. Part I. General considerations," *J. Electroanal. Chem.*, 1982, doi: 10.1016/0022-0728(82)85080-8.

[154] A. Pei, G. Zheng, F. Shi, Y. Li, and Y. Cui, "Nanoscale Nucleation and Growth of Electrodeposited Lithium Metal," *Nano Lett.*, vol. 17, no. 2, pp. 1132–1139, 2017, doi: 10.1021/acs.nanolett.6b04755.

[155] B. Geboes, B. Vanrenterghem, J. Ustarroz, and D. Pauwels, "Influence of the Morphology of Electrodeposited Nanoparticles on the Activity of Organic Halide Reduction," *Chem. Eng. Trans.*, vol. 41, pp. 73–78, 2014, doi: 10.3303/CET1441013.

[156] J. Ustarroz, X. Ke, A. Hubin, S. Bals, and H. Terryn, "New Insights into the Early Stages of Nanoparticle Electrodeposition," *J. Phys. Chem. C*, vol. 116, no. 3, pp. 2322–2329, 2012, doi: 10.1021/jp210276z.

[157] D. R. Ely and R. E. García, "Heterogeneous Nucleation and Growth of Lithium Electrodeposits on Negative Electrodes," *J. Electrochem. Soc.*, vol. 160, no. 4, pp. A662–A668, 2013, doi: 10.1149/1.057304jes.

[158] L. Huang, E. S. Lee, and K. B. Kim, "Electrodeposition of monodisperse copper nanoparticles on highly oriented pyrolytic graphite electrode with modulation potential method," *Colloids Surfaces A Physicochem. Eng. Asp.*, vol. 262, no. 1–3, pp. 125–131, 2005, doi: 10.1016/j.colsurfa.2005.03.023.

[159] Y. Oztekin *et al.*, "Copper nanoparticle modified carbon electrode for determination of dopamine," *Electrochim. Acta*, vol. 76, pp. 201–207, 2012, doi: 10.1016/j.electacta.2012.04.105.

[160] L. Xi, D. Shou, and F. Wang, "Electrodeposition of monodispersed Cu nanoparticles on poly-p-aminobenzene sulfonic acid functionalized glassy carbon electrode and the electrocatalytic reduction toward H_2O_2," *J. Electroanal. Chem.*, vol. 747, pp. 83–90, 2015, doi: 10.1016/j.jelechem.2015.04.006.

[161] A. E. Bolzán, "Electrodeposition of copper on glassy carbon electrodes in the presence of picolinic acid," *Electrochim. Acta*, vol. 113, no. 2, pp. 706–718, 2013, doi:

10.1016/j.electacta.2013.09.132.

[162] O.A. Baturina, “CO_2 electroreduction to hydrocarbons on carbon-supported Cu nanoparticles.,” pp. 5–6, 2008.

[163] M. Cazayous, C. Langlois, T. Oikawa, C. Ricolleau, and A. Sacuto, “Cu-Ag core-shell nanoparticles : A direct correlation between micro-Raman,” *Phys. Rev. B*, 2006, doi: 10.1103/PhysRevB.73.113402.

[164] Z. Chen, D. Mochizuki, M. M. Maitani, and Y. Wada, “Facile synthesis of bimetallic Cu – Ag nanoparticles under microwave irradiation and their oxidation resistance,” *Nanotechnology*, vol. 24, 2013, doi: 10.1088/0957-4484/24/26/265602.

[165] R. Bernasconi, J. L. Hart, A. C. Lang, L. Magagnin, L. Nobili, and M. L. Taheri, “Structural properties of electrodeposited Cu-Ag alloys,” *Electrochim. Acta*, vol. 251, pp. 475–481, 2017, doi: 10.1016/j.electacta.2017.08.097.

[166] K. P. Almtoft, A. M. Ejsing, J. Bøttiger, and J. Chevallier, “The dependence of the nanostructure of magnetron sputtered Cu – Ag alloy films on composition and temperature,” *J. Mater. Res.*, vol. 22, no. 4, pp. 1018–1023, 2007, doi: 10.1557/JMR.2007.0121.

[167] B. L. Cushing, V. L. Kolesnichenko, and C. J. O. Connor, “Recent Advances in the Liquid-Phase Syntheses of Inorganic Nanoparticles,” *Chem. Rev.*, vol. 1385, no. 504, pp. 3893–3946, 2004, doi: 10.1021/cr030027b.

[168] J. Park, J. Joo, S. G. Kwon, Y. Jang, and T. Hyeon, “Synthesis of Monodisperse Spherical Nanocrystals Angewandte,” *Nanostructures*, pp. 4630–4660, 2007, doi: 10.1002/anie.200603148.

[169] K. Mallikarjuna and H. Kim, “Synthesis of shape and size-dependent CuAg bimetallic dumbbell structures for organic pollutant hydrogenation,” *Phys. E Low-dimensional Syst. Nanostructures*, vol. 102, no. January, pp. 44–49, 2018, doi: 10.1016/j.physe.2018.04.033.

[170] M. Grouchko, A. Kamyshny, and S. Magdassi, “Formation of air-stable copper – silver core – shell nanoparticles for inkjet printing,” *J. Mater. Chem.*, pp. 3057–3062, 2009, doi: 10.1039/b821327e.

[171] G. Yang *et al.*, “Towards understanding the facile synthesis of well-covered Cu-Ag core-shell nanoparticles from a complexing model,” *J. Alloys Compd.*, vol. 874, p. 159900, 2021, doi: 10.1016/j.jallcom.2021.159900.

[172] A. P.- Swierzy, Y. Farraj, A. Kamyshny, and S. Magdassi, “Colloids and Surfaces A : Physicochemical and Engineering Aspects Air stable copper-silver core-shell submicron particles : Synthesis and conductive ink formulation,” *Colloids Surfaces A Physicochem. Eng. Asp.*, vol. 521, pp. 272–280, 2017, doi: 10.1016/j.colsurfa.2016.08.026.

[173] W. G. Choe, D. Y. Kim, and O. O. Park, “Morphology control and temporal growth of a continuous silver shell on core– shell spheres,” *CrystEngComm*, pp. 5142–5149, 2014, doi: 10.1039/c4ce00351a.

[174] X. He *et al.*, “A Facile Fabrication of Silver-Coated Copper Nanowires by Galvanic Replacement,” *J. Nanomater. Nanomater.*, 2016.

[175] S. Levi, C. Rousse, V. Mancier, and J. Michel, “Synthesis and characterization of copper – silver core – shell nanowires obtained by electrodeposition followed by a galvanic replacement reaction in aqueous solution ; comparison with a galvanic replacement reaction in ionic media,” *J. Mater. Res.*, vol. 30, no. 22, pp. 3518–3527, 2015, doi: 10.1557/jmr.2015.335.

[176] B. Zhang *et al.*, “Large-Scale and Galvanic Replacement Free Synthesis of Cu@Ag Core−Shell Nanowires for Flexible Electronics,” *inorganc Chem.*, 2018, doi: 10.1021/acs.inorgchem.8b03460.

[177] W. T. Osowiecki, X. Ye, P. Satish, K. C. Bustillo, E. L. Clark, and A. P. Alivisatos, “Tailoring Morphology of Cu-Ag Nanocrescents and Core-Shell Nanocrystals Guided by a Thermodynamic Model,” *J. Am. Chem. Soc.*, vol. 140, no. 27, pp. 8569–8577, 2018, doi: 10.1021/jacs.8b04558.

[178] Y. Hwan, D. Keun, B. Gi, J. Hean, and Y. Soo, “Synthesis of oleate capped Cu nanoparticles by thermal decomposition,” *Colloids Surfaces A Physicochem. Eng. Asp.*, vol. 285, pp. 364–368, 2006, doi: 10.1016/j.colsurfa.2005.10.067.

[179] Z. Lin, D. Han, and S. Li, “Study on thermal decomposition of copper (II) acetate monohydrate in air,” *J. Therm. Anal. Calorim.*, pp. 471–475, 2012, doi: 10.1007/s10973-011-1454-4.

[180] A. Y. Obaid, A. Al-youbi, and S. Al-thabaiti, “Kinetics of Thermal Decomposition of Copper (II) Acetate Monohydrate,” *J. Therm. Anal. Calorim.*, vol. 61, no. September, pp. 985–994, 2000, doi: 10.1023/A.

[181] A. Singhal, M. R. Pai, R. Rao, K. T. Pillai, I. Lieberwirth, and A. K. Tyagi, “Copper (I) Oxide Nanocrystals – One Step Synthesis , Characterization , Formation Mechanism

, and Photocatalytic Properties," *Eur. J. Inorg. Chem.*, pp. 1–13, 2013, doi: 10.1002/ejic.201201382.

[182] R. B. V. Mantella, M. Strach, K. Frank, J. R. Pankhurst, D. Stoian, C. Gadiyar, B. Nickel, "Polymer Lamellae as Reaction Intermediates in the Formation of Copper Nanospheres as Evidenced by In Situ X-ray Studies," *Angew. Chemie - Int. Ed.*, pp. 11627–11633, 2020.

[183] E. Szłyk, P. Piszczek, M. Chaberski, and A. Golin, "Studies of thermal decomposition process of Ag (I) perfluorinated carboxylates with temperature variable IR and MS," *Polyhedron*, vol. 20, pp. 2853–2861, 2001.

[184] G. A. Kamat, C. Yan, W. T. Osowiecki, I. A. Moreno-Hernandez, M. Ledendecker, and A. P. Alivisatos, "Self-Limiting Shell Formation in Cu@Ag Core-Shell Nanocrystals during Galvanic Replacement," *J. Phys. Chem. Lett.*, vol. 11, no. 13, pp. 5318–5323, 2020, doi: 10.1021/acs.jpclett.0c01551.

[185] A. Loiudice *et al.*, "Tailoring Copper Nanocrystals towards C_2 Products in Electrochemical CO_2 Reduction Angewandte," vol. 94720, pp. 5789–5792, 2016, doi: 10.1002/anie.201601582.

[186] W. Y. Ko, W. H. Chen, C. Y. Cheng, and K. J. Lin, "Architectural growth of Cu nanoparticles through electrodeposition," *Nanoscale Res. Lett.*, vol. 4, no. 12, pp. 1481–1485, 2009, doi: 10.1007/s11671-009-9424-5.

[187] M. Yin *et al.*, "Copper Oxide Nanocrystals," *J. Am. Chem. Soc.*, no. 12, pp. 9506–9511, 2005.

[188] B. Abécassis *et al.*, "Real-Time in Situ Probing of High-Temperature Quantum Dots Solution Synthesis," *Nano Lett.*, pp. 2620–2626, 2015, doi: 10.1021/acs.nanolett.5b00199.

[189] J. Zhao, B. Chen, and F. Wang, "Shedding Light on the Role of Misfit Strain in Controlling core-shell nanocrystals," *Adv. Mater.*, vol. 2004142, pp. 1–20, 2020, doi: 10.1002/adma.202004142.

[190] H.-H. F. and C.-N. L. Wei-Lun Weng, Chin-Yu Hsu, Jheng-Syun Lee, "Twin-mediated epitaxial growth of highly lattice-mismatched Cu/Ag core-shell nanowires," *Nanoscale*, 2018, doi: 10.1039/C8NR02875C.

[191] M. G. and M. B.J., "Growth and Ripening Kinetics of Crystalline Polymorphs," *Cryst. GROWTH &DESIGN*, vol. 3, no. 6, pp. 981–990, 2003.

[192] A. Muzikansky *et al.*, “Ag Dewetting in Cu @ Ag Monodisperse Core-Shell Nanoparticles Ag Dewetting in Cu @ Ag Monodisperse Core-Shell Nanoparticles,” *J. Phys. Chem. C*, 2012, doi: 10.1021/jp3109545.

[193] C. W. Yuan *et al.*, “Structure map for embedded binary alloy nanocrystals Structure map for embedded binary alloy nanocrystals,” *Appl. Phys. Lett.*, vol. 193114, no. 2008, pp. 21–24, 2013, doi: 10.1063/1.3027066.

[194] Y. Wang, D. Wang, C. J. Dares, S. L. Marquard, M. V. Sheridan, and T. J. Meyer, “CO_2 reduction to acetate in mixtures of ultrasmall $(Cu)_n$,$(Ag)_m$ bimetallic nanoparticles,” *Proc. Natl. Acad. Sci. U. S. A.*, vol. 115, no. 2, pp. 278–283, 2017, doi: 10.1073/pnas.1713962115.

[195] C. Yang *et al.*, “Overcoming immiscibility toward bimetallic catalyst library,” *Sci. Adv.*, vol. 6, no. 17, pp. 1–10, 2020, doi: 10.1126/sciadv.aaz6844.

[196] M. R. Singh, Y. Kwon, Y. Lum, J. W. Ager, and A. T. Bell, “Hydrolysis of Electrolyte Cations Enhances the Electrochemical Reduction of CO_2 over Ag and Cu,” *J. Am. Chem. Soc.*, vol. 138, no. 39, pp. 13006–13012, 2016, doi: 10.1021/jacs.6b07612.

[197] S. Ringe *et al.*, “Understanding cation effects in electrochemical CO_2 reduction,” *Energy Environ. Sci.*, vol. 12, no. 10, pp. 3001–3014, 2019, doi: 10.1039/c9ee01341e.

[198] J. Resasco *et al.*, “Promoter Effects of Alkali Metal Cations on the Electrochemical Reduction of Carbon Dioxide,” *J. Am. Chem. Soc.*, vol. 139, no. 32, pp. 11277–11287, 2017, doi: 10.1021/jacs.7b06765.

[199] H. Mistry, F. Behafarid, R. Reske, A. S. Varela, P. Strasser, and B. Roldan Cuenya, “Tuning Catalytic Selectivity at the Mesoscale via Interparticle Interactions,” *ACS Catal.*, vol. 6, no. 2, pp. 1075–1080, 2016, doi: 10.1021/acscatal.5b02202.

[200] W. T. Osowiecki *et al.*, “Factors and Dynamics of Cu Nanocrystal Reconstruction under CO_2 Reduction,” *ACS Appl. Energy Mater.*, vol. 2, no. 11, pp. 7744–7749, 2019, doi: 10.1021/acsaem.9b01714.

[201] D. Kim, C. S. Kley, Y. Li, and P. Yang, “Copper nanoparticle ensembles for selective electroreduction of CO_2 to C_2 –C_3 products,” *Proc. Natl. Acad. Sci.*, vol. 114, no. 40, pp. 10560–10565, 2017, doi: 10.1073/pnas.1711493114.

[202] J. Park *et al.*, “Hollow nanoparticles as emerging electrocatalysts for renewable energy conversion reactions,” *Chem. Soc. Rev.*, 2018, doi: 10.1039/C8CS00336J.

[203] J. Huang *et al.*, “Potential-induced nanoclustering of metallic catalysts during electrochemical CO2 reduction,” *Nat. Commun.*, vol. 9, no. 1, pp. 1–9, 2018, doi: 10.1038/s41467-018-05544-3.

[204] D. Göhl *et al.*, “Engineering stable electrocatalysts by synergistic stabilization between carbide cores and Pt shells,” *Nat. Mater.*, 2019, doi: 10.1038/s41563-019-0555-5.

[205] P. Wilde *et al.*, “Is Cu instability during the CO_2 reduction reaction governed by the applied potential or the local CO concentration?,” *Chem. Sci.*, vol. 12, no. 11, pp. 4028–4033, 2021, doi: 10.1039/d0sc05990k.

[206] W. van Aarle *et al.*, “The ASTRA Toolbox: A platform for advanced algorithm development in electron tomography,” *Ultramicroscopy*, vol. 157, no. 2015, pp. 35–47, 2015, doi: 10.1016/j.ultramic.2015.05.002.

[207] W. van Aarle *et al.*, “Fast and flexible X-ray tomography using the ASTRA toolbox,” *Opt. Express*, vol. 24, no. 22, p. 25129, 2016, doi: 10.1364/oe.24.025129.

[208] C. Lee, N. R. Kim, J. Koo, and Y. J. Lee, “Cu-Ag core – shell nanoparticles with enhanced oxidation stability for printed electronics,” *Nanotechnology*, vol. 26, no. 45, p. 455601, 2015, doi: 10.1088/0957-4484/26/45/455601.

[209] V. D. Jović and B. M. Jović, “Surface reconstruction during the adsorption/desorption of OH- species onto Cu(111) and Cu(100) in 0.1 M NaOH solution,” *J. Serbian Chem. Soc.*, vol. 67, no. 7, pp. 531–546, 2002, doi: 10.2298/JSC0207531J.

[210] T. Altantzis *et al.*, “Three-Dimensional Quantification of the Facet Evolution of Pt Nanoparticles in a Variable Gaseous Environment,” *Nano Lett.*, vol. 19, no. 1, pp. 477–481, 2019, doi: 10.1021/acs.nanolett.8b04303.

[211] N. Eom, M. E. Messing, J. Johansson, and K. Deppert, “General Trends in Core-Shell Preferences for Bimetallic Nanoparticles,” *ACS Nano*, vol. 15, no. 5, pp. 8883–8895, 2021, doi: 10.1021/acsnano.1c01500.

[212] C. M. Gunathunge, X. Li, J. Li, R. P. Hicks, V. J. Ovalle, and M. M. Waegele, “Spectroscopic Observation of Reversible Surface Reconstruction of Copper Electrodes under CO2 Reduction,” *J. Phys. Chem. C*, vol. 121, no. 22, pp. 12337–12344, 2017, doi: 10.1021/acs.jpcc.7b03910.

[213] H. Li, P. Wei, D. Gao, and G. Wang, “In situ Raman spectroscopy studies for electrochemical CO_2 reduction over Cu catalysts,” *Curr. Opin. Green Sustain. Chem.*,

vol. 34, p. 100589, 2022, doi: 10.1016/j.cogsc.2022.100589.

[214] S. H. Lee *et al.*, “Oxidation State and Surface Reconstruction of Cu under CO_2 Reduction Conditions from in Situ X-ray Characterization,” *J. Am. Chem. Soc.*, vol. 143, no. 2, pp. 588–592, 2021, doi: 10.1021/jacs.0c10017.

[215] H. S. Jeon *et al.*, “Operando insight into the correlation between the structure and composition of CuZn nanoparticles and their selectivity for the electrochemical CO_2 reduction,” *J. Am. Chem. Soc.*, vol. 141, no. 50, pp. 19879–19887, 2019, doi: 10.1021/jacs.9b10709.

[216] S. Ma *et al.*, “Electroreduction of carbon dioxide to hydrocarbons using bimetallic Cu-Pd catalysts with different mixing patterns,” *J. Am. Chem. Soc.*, vol. 139, no. 1, pp. 47–50, 2017, doi: 10.1021/jacs.6b10740.

[217] X. Wang *et al.*, “Gold-in-copper at low *CO coverage enables efficient electromethanation of CO_2,” *Nat. Commun.*, vol. 12, no. 1, pp. 1–7, 2021, doi: 10.1038/s41467-021-23699-4.

[218] D. T. Whipple and P. J. A. Kenis, “Prospects of CO_2 Utilization via Direct Heterogeneous Electrochemical Reduction Devin,” *J. Phys. Chem. Lett.*, pp. 3451–3458, 2010.

[219] H. Lee *et al.*, “Concave Rhombic Dodecahedral Au Nanocatalyst with Multiple High-Index Facets for CO_2 Reduction,” *ACS Nano*, no. 8, pp. 8384–8393, 2015.

[220] M. Valenti *et al.*, “Suppressing H_2 Evolution and Promoting Selective CO_2 Electroreduction to CO at Low Overpotentials by Alloying Au with Pd,” *ACS Catal.*, vol. 9, pp. 3527–3536, 2019, doi: 10.1021/acscatal.8b04604.

[221] J. He, N. J. J. Johnson, A. Huang, and C. P. Berlinguette, “Electrocatalytic Alloys for CO_2 Reduction,” *ChemSusChem*, pp. 48–57, 2018, doi: 10.1002/cssc.201701825.

[222] G. Marcandalli, A. Goyal, and M. T. M. Koper, “Electrolyte Effects on the Faradaic Efficiency of CO_2 Reduction to CO on a Gold Electrode,” *ACS Catal.*, 2021, doi: 10.1021/acscatal.1c00272.

[223] B. Kim, S. Ma, H. M. Jhong, and P. J. A. Kenis, “Influence of dilute feed and pH on electrochemical reduction of CO_2 to CO on Ag in a continuous flow electrolyzer,” vol. 166, pp. 271–276, 2015, doi: 10.1016/j.electacta.2015.03.064.

[224] J. Vennekoetter, R. Sengpiel, and M. Wessling, "Beyond the catalyst : How electrode and reactor design determine the product spectrum during electrochemical CO_2 reduction," *Chem. Eng. J.*, vol. 364, no. September 2018, pp. 89–101, 2019, doi: 10.1016/j.cej.2019.01.045.

[225] A. K. Buckley *et al.*, "Electrocatalysis at organic-metal interfaces: Identification of structure-reactivity relationships for CO_2 reduction at modified cu surfaces," *J. Am. Chem. Soc.*, vol. 141, no. 18, pp. 7355–7364, 2019, doi: 10.1021/jacs.8b13655.

[226] N. Sakamoto and T. Arai, "Enhanced electrochemical CO_2 reduction selectivity by application of self-assembled polymer microparticles to a silver electrode," *Chem. Commun.*, vol. 55, no. 77, pp. 11623–11625, 2019, doi: 10.1039/c9cc05921k.

[227] P. Yue *et al.*, "Triple-phase electrocatalysis for the enhanced CO_2 reduction to HCOOH on a hydrophobic surface," *Chem. Eng. J.*, vol. 405, no. June 2020, p. 126975, 2021, doi: 10.1016/j.cej.2020.126975.

[228] Y. C. Hsieh *et al.*, "Modification of CO_2 reduction activity of nanostructured silver electrocatalysts by surface halide anions," *ACS Appl. Energy Mater.*, vol. 2, no. 1, pp. 102–109, 2019, doi: 10.1021/acsaem.8b01692.

[229] X. Han and V. S. Thoi, "Non-Innocent Role of Porous Carbon Towards Enhancing C_{2-3} Products in Electroreduction of Carbon Dioxide," *ACS Appl. Mater. Interfaces*, 2020, doi: 10.1021/acsami.0c10591.

[230] C. Dinh *et al.*, "CO_2 electroreduction to ethylene via hydroxide-mediated copper catalysis at an abrupt interface," *Electrochemistry*, vol. 787, no. May, pp. 783–787, 2018.

[231] P. J. Kelly, J. O'Brien, and R. D. Arnell, "The production of porous and chemically reactive coatings by magnetron sputtering," *Vacuum*, vol. 74, no. 1, pp. 1–10, 2004, doi: 10.1016/j.vacuum.2003.11.002.

[232] R. Alvarez *et al.*, "Growth regimes of porous gold thin films deposited by magnetron sputtering at oblique incidence: From compact to columnar microstructures," *Nanotechnology*, vol. 24, no. 4, 2013, doi: 10.1088/0957-4484/24/4/045604.

[233] R. Dedoncker, H. Rijckaert, and D. Depla, "Sputter deposition of porous thin films from metal/NaCl powder targets," *Appl. Phys. Lett.*, vol. 115, no. 4, 2019, doi: 10.1063/1.5112822.

[234] N. Bernier *et al.*, "A methodology to optimize the quantification of sp2 carbon

fraction from K edge EELS spectra," *J. Electron Spectros. Relat. Phenomena*, vol. 164, no. 1–3, pp. 34–43, 2008, doi: 10.1016/j.elspec.2008.04.006.

[235] Y. Wang, Y. Zhu, and H. Wu, "Porous characteristics of three-dimensional disordered graphene networks," *Crystals*, vol. 11, no. 2, 2021, doi: 10.3390/cryst11020127.

[236] J. W. Martin, C. De Tomas, I. Suarez-Martinez, M. Kraft, and N. A. Marks, "Topology of disordered 3D graphene networks," *Phys. Rev. Lett.*, vol. 123, no. 11, p. 116105, 2019, doi: 10.1103/PhysRevLett.123.116105.

[237] X. Jin, R. He, and S. Dai, "Electrochemical Graphitization: An Efficient Conversion of Amorphous Carbons to Nanostructured Graphites," *Chem. - A Eur. J.*, vol. 23, no. 48, pp. 11455–11459, 2017, doi: 10.1002/chem.201701620.

[238] B. S. An *et al.*, "Characteristics of an Amorphous Carbon Layer as a Diffusion Barrier for an Advanced Copper Interconnect," *ACS Appl. Mater. Interfaces*, vol. 12, no. 2, pp. 3104–3113, 2020, doi: 10.1021/acsami.9b15562.

[239] A. V. Kesavan *et al.*, "Work Function-Tunable Amorphous Carbon-Silver Nanocomposite Hybrid Electrode for Optoelectronic Applications," *ACS Appl. Mater. Interfaces*, vol. 13, no. 3, pp. 4284–4293, 2021, doi: 10.1021/acsami.0c13937.

[240] N. Daems, X. Sheng, I. F. J. Vankelecom, and P. P. Pescarmona, "Metal-free doped carbon materials as electrocatalysts for the oxygen reduction reaction," *J. Mater. Chem. A*, vol. 2, no. 12, pp. 4085–4110, 2014, doi: 10.1039/c3ta14043a.

[241] A. Dychalska, P. Popielarski, W. Franków, K. Fabisiak, K. Paprocki, and M. Szybowicz, "Study of CVD diamond layers with amorphous carbon admixture by Raman scattering spectroscopy," *Mater. Sci. Pol.*, vol. 33, no. 4, pp. 799–805, 2015, doi: 10.1515/msp-2015-0067.

[242] S. Gupta and J. Narayan, "Reduced Graphene Oxide/Amorphous Carbon P-N Junctions: Nanosecond Laser Patterning," *ACS Appl. Mater. Interfaces*, vol. 11, no. 27, pp. 24318–24330, 2019, doi: 10.1021/acsami.9b05374.

[243] I. Childres, J. L.A., W. Park, H. Cao, and J. P. Chen, "Raman spectroscopy of graphene and related materials," *New Dev. Phot. Mater. Res.*, 2013.

[244] D. W. Boukhvalov, I. S. Zhidkov, E. Z. Kurmaev, E. Fazio, S. O. Cholakh, and L. D'Urso, "Atomic and electronic structures of stable linear carbon chains on Ag-nanoparticles," *Carbon N. Y.*, vol. 128, pp. 296–301, 2018, doi: 10.1016/j.carbon.2017.11.044.

[245] Hideo Nakae, Ryuichi Inui, Yosuke Hirata, and Hiroyuki Saito, “Effects of surface roughness on wettability,” *Acta Mater.*, vol. 46, no. 7, pp. 2313–2318, 1998, doi: 10.1016/s1359-6454(98)80012-8.

[246] K. J. Kubiak, M. C. T. Wilson, T. G. Mathia, and P. Carval, “Wettability versus roughness of engineering surfaces,” *Wear*, vol. 271, no. 3–4, pp. 523–528, 2011, doi: 10.1016/j.wear.2010.03.029.

[247] B. Xiong *et al.*, “Effect of pore morphology and surface roughness on wettability of porous titania films,” *Mater. Res. Express*, vol. 7, no. 11, 2020, doi: 10.1088/2053-1591/abc770.

[248] H. Gu, C. Wang, S. Gong, Y. Mei, H. Li, and W. Ma, “Investigation on contact angle measurement methods and wettability transition of porous surfaces,” *Surf. Coatings Technol.*, vol. 292, pp. 72–77, 2016, doi: 10.1016/j.surfcoat.2016.03.014.

[249] A. B. D. Cassie and S. Baxter, “Wettability of Porous Surfaces,” *Trans. Faraday Soc.*, vol. 40, pp. 546–551, 1944.

[250] W. K. Han *et al.*, “Complete filling of 41 nm trench pattern using Cu seed layer deposited by SAM-modified electroless plating and electron-beam evaporation,” *Appl. Surf. Sci.*, vol. 256, no. 8, pp. 2649–2653, 2010, doi: 10.1016/j.apsusc.2009.11.012.

[251] A. Marmur, C. Della Volpe, S. Siboni, A. Amirfazli, and J. W. Drelich, “Contact angles and wettability: Towards common and accurate terminology,” *Surf. Innov.*, vol. 5, no. 1, pp. 3–8, 2017, doi: 10.1680/jsuin.17.00002.

[252] S. Verma, X. Lu, S. Ma, R. I. Masel, and P. J. A. Kenis, “The effect of electrolyte composition on the electroreduction of CO_2 to CO on Ag based gas diffusion electrodes,” *Phys. Chem. Chem. Phys.*, vol. 18, no. 10, pp. 7075–7084, 2016, doi: 10.1039/c5cp05665a.

[253] C. T. Dinh, F. P. García De Arquer, D. Sinton, and E. H. Sargent, “High rate, selective, and stable electroreduction of CO_2 to CO in basic and neutral media,” *ACS Energy Lett.*, vol. 3, no. 11, pp. 2835–2840, 2018, doi: 10.1021/acsenergylett.8b01734.

[254] R. Wang *et al.*, “Maximizing Ag Utilization in High-Rate CO_2 Electrochemical Reduction with a Coordination Polymer-Mediated Gas Diffusion Electrode,” *ACS Energy Lett.*, vol. 4, pp. 2024–2031, 2019, doi: 10.1021/acsenergylett.9b01509.

[255] S. Ma, R. Luo, J. I. Gold, A. Z. Yu, B. Kim, and P. J. A. Kenis, “Carbon nanotube

containing Ag catalyst layers for efficient and selective reduction of carbon dioxide," *J. Mater. Chem. A*, 2016, doi: 10.1039/C6TA00427J.

[256] B. Endrodi, C. Bencsik, F. Darvas, R. Jones, K. Rajeshwar, and C. Janaky, "Continuous-flow electroreduction of carbon dioxide," *Prog. Energy Combust. Sci.*, vol. 62, pp. 133–154, 2017, doi: 10.1016/j.pecs.2017.05.005.

[257] M. E. Leonard, L. E. Clarke, A. Forner-Cuenca, S. M. Brown, and F. R. Brushett, "Investigating Electrode Flooding in a Flowing Electrolyte, Gas-Fed Carbon Dioxide Electrolyzer," *ChemSusChem*, vol. 13, no. 2, pp. 400–411, 2020, doi: 10.1002/cssc.201902547.

[258] T. Burchardt, "An evaluation of electrocatalytic activity and stability for air electrodes," *J. Power Sources*, vol. 135, no. 1–2, pp. 192–197, 2004, doi: 10.1016/j.jpowsour.2004.03.072.

[259] S. Verma *et al.*, "Insights into the Low Overpotential Electroreduction of CO_2 to CO on a Supported Gold Catalyst in an Alkaline Flow Electrolyzer," *ACS Energy Lett.*, vol. 3, no. 1, pp. 193–198, Jan. 2018, [Online]. Available: https://pubs.acs.org/doi/10.1021/acsenergylett.7b01096

[260] N. N. Nguyen, A. V. Nguyen, K. M. Steel, L. X. Dang, and M. Galib, "Interfacial Gas Enrichment at Hydrophobic Surfaces and the Origin of Promotion of Gas Hydrate Formation by Hydrophobic Solid Particles," *J. Phys. Chem. C*, vol. 121, no. 7, pp. 3830–3840, 2017, doi: 10.1021/acs.jpcc.6b07136.

[261] D. V. Esposito, "Membrane-Coated Electrocatalysts - An Alternative Approach to Achieving Stable and Tunable Electrocatalysis," *ACS Catal.*, vol. 8, no. 1, pp. 457–465, 2018, doi: 10.1021/acscatal.7b03374.

[262] A. Thevenon, A. Rosas-Hernández, A. M. Fontani Herreros, T. Agapie, and J. C. Peters, "Dramatic HER Suppression on Ag Electrodes via Molecular Films for Highly Selective CO_2 to CO Reduction," *ACS Catal.*, vol. 11, no. 8, pp. 4530–4537, 2021, doi: 10.1021/acscatal.1c00338.

[263] N. Buzgar and A. Apopei, "THE RAMAN STUDY OF CERTAIN CARBONATES," *Analele Stiint. Univ. A.I. Cuza din Iasi*, vol. 2, no. 5, 2009, [Online]. Available: ???

[264] G. Pal, P. Rai, and A. Pandey, *Green synthesis of nanoparticles: A greener approach for a cleaner future*. Elsevier Inc., 2019. doi: 10.1016/b978-0-08-102579-6.00001-0.

Personal information

A1 Publications in international peer-reviewed journals included in the Web of Science

1. **L. Pacquets**, E. Irtem, S. Neukermans, N. Daems, S. Bals, T. Breugelmans, Size-controlled electrodeposition of Cu nanoparticles on gas diffusion electrodes in methanesulfonic acid solution, Journal of Applied Electrochemistry, (51) 2021, 317-330.
2. C. Li, A. P. Tardajos, D. Wang, D. Choukroun, K. Van Daele, T. Breugelmans, S. Bals, A simple method to clean ligand contamination on TEM grids, ultramicroscopy, 221 (2021) 113195.[1]
3. D. Choukroun, **L. Pacquets**, C. Li, S. Hoekx, S. Arnouts, K. Baert, T. Hauffman, S. Bals, and T. Breugelmans, Mapping Composition–Selectivity Relationships of Supported Sub-10 nm Cu–Ag Nanocrystals for High-Rate CO2 Electroreduction, ACS Nano, 2021, 15, 9, 14858–14872.
4. N. Daems, D. Choukroun, P. Merino, C. Rettenmaier, **L. Pacquets**, Arno Bergmann, G. Santoro, L. Vázquez, L. Martínez, B. R. Cuenya, J. A. M. Gago, T. Breugelmans, Electroreduction over Soft-Landed CuO_x Nanoparticle-Functionalized Gas Diffusion Electrodes, ACS Applied Materials and Interfaces, 2022, 14, 2, 2691–2702.
5. **L. Pacquets**, J. Van den Hoek, D. Arenas-Esteban, R. Ciocarlan, P. Cool, K. Baert, T. Hauffman, N. Daems, S. Bals and T. Breugelmans, The Use of Nanoscale Carbon Layers on Ag-Based Gas Diffusion Electrodes to Promote CO Production, ACS Applied Nano Materials, 2022, 5, 7723-7732.

---

[1] Sub-10 nm Cu@Ag core-shell NPs analyzed in this paper where synthesized by Lien Pacquets with the assistance of Daniel Choukroun.

Oral Presentations and posters at international conferences

1. Presentation: **Lien Pacquets**, Nick Daems, Sara Bals and Tom Breugelmans. Tuning the selectivity of CuAg core-shell nanoparticles towards CO through a combination of high-end electrochemistry and electron microscopy. 71st annual online meeting event (ISE), 31/08/2020-04/09/2020.
2. Poster: Daniel Choukroun, **Lien Pacquets**, Chen Li, Sara Bals, Tom Breugelmans. Composition Selectivity Relationships and Accumulation of Liquid Products over Supported sub 10 nm Cu Ag Nanocrystals. Elcorel, 29-31/03/2021.
3. Presentation: **Lien Pacquets**, Nick Daems, Sara Bals and Tom Breugelmans. Tuning Cu@Ag core-shell nanoparticles for the conversion of CO_2 towards CO. 72th annual hybrid meeting event (ISE), 30/08/2020-03/09/2020.